UCRL-53943-89
Distribution Category UC-700

UCRL--53943-89

DE91 000510

1988–1989

# Chemistry & Materials Science Department

## Annual Report

Lawrence Livermore National Laboratory
University of California
Livermore, California 94551

# Acknowledgments

Christopher Gatrousis is the Associate Director for the Chemistry & Materials Science Directorate. Thomas T. Sugihara is the Deputy Associate Director for Research, and Larry L. Schwartz is the Deputy Associate Director for Administration. The three Division Leaders are: Jeffery H. Richardson, Chemical Sciences Division; Michael J. Fluss, Condensed Matter and Analytical Sciences Division; and Jeffrey N. Kass, Materials Division.

The following people formed the publication staff for the 1988–1989 Chemistry & Materials Science Department Annual Report:

| | |
|---|---|
| **Scientific Editors** | Richard J. Borg<br>Thomas T. Sugihara |
| **C&MS Department Coordinator** | Linda M. Brown |
| **Publication Editors** | Jay C. Cherniak<br>Cara W. Corey |
| **Designer and Art Coordinator** | Ellen L. Baldwin |
| **Composition Coordinator and Proofreader** | Rebecca M. Cowan |
| **Proofreader** | Jill S. Sprinkle |

# Contents

# Overview

This is the first annual report of the Chemistry & Materials Science (C&MS) Department. The principal purpose of this report is to provide a concise summary of our scientific and technical accomplishments for fiscal years 1988 and 1989. The report is also intended to become part of the archival record of the Department's activities. We plan to publish future editions annually.

As a disciplinary department of Lawrence Livermore National Laboratory (LLNL), the mission of the C&MS Department is to provide scientific and technical expertise and leadership in the chemical and materials sciences in support of the Laboratory's many programs. In accomplishing this mission, the Department seeks to advance the frontiers of science, develop a qualified and responsive scientific and technical staff, be innovative in advancing technologies with end applications, and expand its interactions with scientists in universities, government laboratories, and industry.

The activities of the Department can be divided into three broad categories. First, C&MS staff are assigned by the matrix system to work directly in a program. These programmatic assignments typically involve short deadlines and critical time schedules. A second category is longer-term research and development in technologies important to Laboratory programs. The focus and direction of this technology-base work are generally determined by programmatic needs. Finally, the Department manages its own research program, mostly long-range in outlook and basic in orientation. These three categories are not mutually exclusive but form a continuum of technical activities. Representative examples of all three are included in this report.

The principal subject matter of this report has been divided into six sections:

1. Innovations in Analysis and Characterization
2. Advanced Materials
3. Metallurgical Science and Technology
4. Surfaces and Interfaces
5. Energetic Materials and Chemical Synthesis
6. Energy-Related Research and Development

These six sections reflect the range of C&MS research and development interests. The articles in the sections describe projects for which results were obtained in FY 1988 and FY 1989. Section 7 lists Department personnel along with publications, presentations, and patents. A list of universities and other organizations with which the C&MS Department collaborates is also included. Finally, C&MS budget information is given in Sec. 8.

## The C&MS Department

Chemistry as a discipline has been identified by a separate organization since the beginning of the Laboratory in 1952. At various times, the organization has been called the Chemistry Group, the Chemistry Division, the Chemistry Department, and, since 1973, the Chemistry & Materials Science Department. Until 1985, the chief executive was called the Department Head, and he reported to Laboratory management through an Associate Director whose responsibilities typically included other areas, such as computing, in addition to chemistry.

In April 1985, Christopher Gatrousis was named Associate Director for Chemistry & Materials Science. He reports to the Director of the Laboratory.

Figure 1 shows the current organizational structure of the C&MS Department. Activities that span the Department spectrum, such as administration, research, quality assurance and safety, liaison with the Weapons Program, and operation of critical facilities are placed in the Associate Director's office. Operational activities are

**Figure 1.** Organizational structure of the C&MS Department.

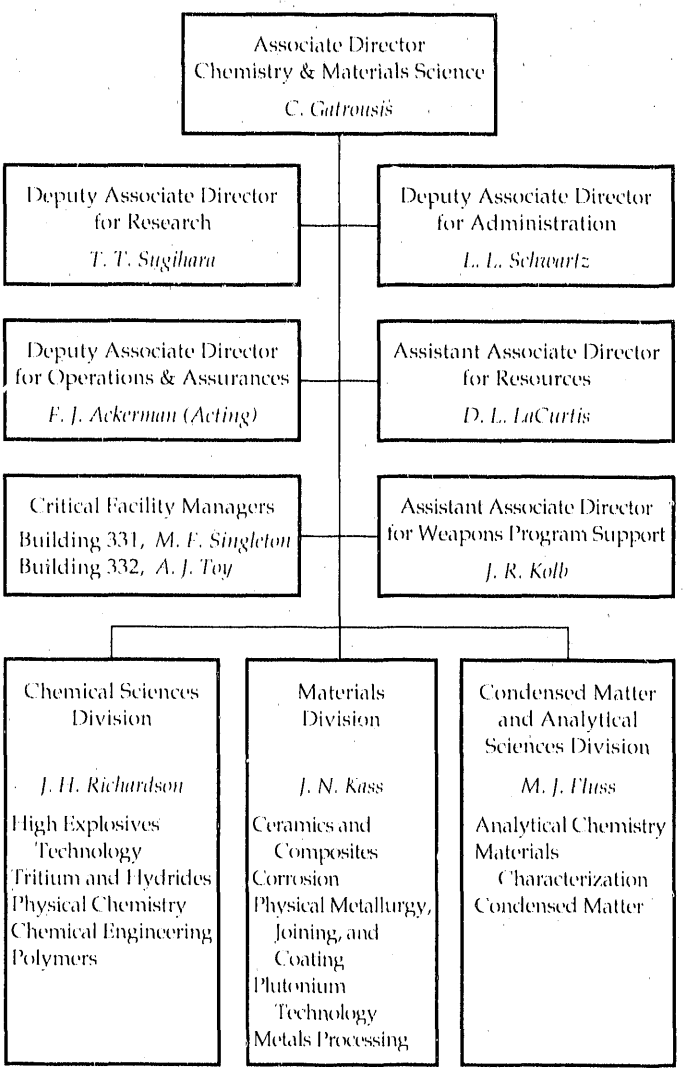

assigned to the three divisions: the Chemical Sciences Division, Condensed Matter and Analytical Sciences Division, and Materials Division. The personnel assigned to each division are listed in Sec. 7 of this report.

On September 30, 1989, the Department consisted of 402 persons (head count, corresponding to 360 FTE). Of these, 60% were professionals, 29% were technicians and in crafts, and 11% were administrative and clerical. Of the 240 professionals, 53% were chemists, 21% engineers, 14% metallurgists, and 12% physicists. More than 60% of the professionals hold a Ph.D. degree. The Department currently has 13 postdoctoral associates, and 19 graduate students are conducting their thesis research under the guidance of C&MS staff.

## Funding and Budgets

Funding of the C&MS Department comes in two forms. In the first, dollars are allocated to the Department for specific purposes: direct programs, distributed services, and indirect activities. Direct programs are those over which the Department has jurisdiction, such as specific projects in Weapons Supporting Research, Departmental and Laboratory Institutional Research and Development, DOE/Basic Energy Sciences, and the Department of Defense and other federal agencies. Distributed services are those that the Department provides the Laboratory in managing and operating the Plutonium Facility and the Tritium Facility. Indirect activities include general Departmental administration and the maintenance of buildings for which the Department has responsibility. In FY 1989, funding was $13.7 million for direct programs, $6.9 million for distributed services, and $11.8 million for indirect activities, for a total of $32.4 million.

The second category of Departmental support is in the form of manpower allocations rather than dollars. For example, Defense Systems allocated 107.6 FTE to the C&MS Department in FY 1989 to support various projects, and the Laser Program allocated 48.9 FTE. The number allocated to the Department from all sources totaled 255.9 FTE. The dollar equivalent of 255.9 FTE is about $39 million. Thus the total dollar budget of the Department in FY 1989 was the equivalent of about $71 million. Details of the budget are given in Sec. 8.

## Research and Development

Since this annual report is concerned mostly with our research and development activities, it may be useful in this, our first annual report, to describe the context in which these activities are carried out and how they are organized and administered. The major sources of discretionary funds for basic research are Weapons Supporting Research (WSR) and Institutional Research and Development (IR&D).

**WSR.** Funds for WSR are allocated to the Department by the Director of the Laboratory. In FY 1988 and FY 1989, WSR funding for the C&MS Department was $6840K and $6949K, respectively. The purpose of WSR is to provide the scientific and technical base that is required in the longer term for the success of the Weapons Program.

In the C&MS Department, resources are allocated principally to block-funded programs ("thrust areas") and to projects led by individual investigators. Some of the WSR funds are also used to provide discretionary resources for Division Leaders. A thrust area is expected to provide a coordinated approach to a focused scientific or technological area. Several senior scientists are typically involved, and the program is expected to last several years. Individual projects result from proposals by a principal investigator and are generally limited in scope and duration. The thrust areas and projects active in FY 1988 and FY 1989 are listed in Sec. 8 (Table 2). Many of the results described in this annual report were obtained as part of a thrust area, but this relationship has not been explicitly cited.

In the case of both thrust areas and individual projects, the principal criteria for their selection are the quality of the proposed science and the qualifications of the investigators. Relevance to the mission of the Weapons Program is also an important consideration. All WSR projects are reviewed internally at least twice a year and by an external review committee at approximately 18-month intervals.

**IR&D.** At the Laboratory level, IR&D is administered by a special assistant to the Director. Funding is divided among three general categories: a lump-sum allocation to a department ("Departmental IR&D"), a Director's Initiative, and a Laboratory-wide competition among proposals from individual investigators ("Laboratory IR&D"). The general purpose of IR&D is to broaden the exploratory research base of the Laboratory by funding forefront science and technology in fields related to the Laboratory's defense and energy missions.

In the C&MS Department, the lump sum is divided among projects that emphasize new ideas, new concepts, or new experimental devices or methods. One of the Department's programs, in spin polarization of DT, qualified as a Director's Initiative. Several individual projects competed successfully for Laboratory IR&D support. Projects active in FY 1988 and FY 1989 are listed in Sec. 8 (Table 3).

## State of the Department

A substantial portion of the C&MS Department's discretionary resources is concentrated in areas of recognized priority with a focus toward fulfilling the Laboratory's mission. As an equal priority, we attempt to maintain a flexibility that encourages adventurous new directions with a potential yet to be recognized. Indeed, many of

the Department's most far-reaching developments, both in concept and application, have come from unexpected directions. Thus, an essential element of our scientific mission is the support of creative scientists who decide independently where the best prospects lie for acquiring significant new knowledge. We describe a few examples here from the currently recognized priority frontiers as well as from the new avenues out of which future priority lists will be drawn.

New materials, new processing technologies, and new concepts for manipulating materials at the atomic level are all critical to the Laboratory's future programs and to this nation's competitiveness and national security. A vital goal of our research is to design, synthesize, and fabricate, in high yield, new materials with properties that can be predicted, varied, and controlled. Achieving this goal is often an empirical process, but the research is most effective when the structure and stability of materials are known well enough on the atomic and molecular scale to predict their macroscopic physical properties. Although single-component crystalline solids remain an active subject of study, our emphasis is shifting toward more complex materials and systems: important examples are surfaces, interfaces, thin films, submicron structures, and systems with intricate microstructures. Complex materials with artificial periodic structures fabricated by multilayer deposition technology are the basis for unique x-ray optics: mirrors, diffraction gratings, and x-ray microscopes. The future for such atomically engineered materials—in which specific atomic, electronic, magnetic, or mechanical properties might be achieved—will ultimately depend on our understanding of the fundamental physics and chemistry of the multilayer interface itself. The development of new bicrystal synthesis methods will soon permit us to more fully understand one of the most ubiquitous interfaces, the grain boundary, from which many materials derive their macroscopic properties.

Not only are these materials new, but so are the techniques used to examine them. Synchrotron-based x-ray sources have led to new spectroscopies, including extended x-ray absorption fine structure (XAFS), for monitoring interfacial chemistry as single atomic layers are deposited. The coupling of characterization methods to the fabrication process permits control of the resultant product and the tailoring of material properties to specific physical requirements for fundamental studies or practical applications.

We are developing a vast array of new diagnostic tools that can probe physical and chemical properties on an atomic scale. The scanning tunneling microscope (STM) is one of our instruments that has achieved atomic resolution for the first time. A team of LLNL chemists, materials scientists, and biologists, along with a group of surface scientists from Lawrence Berkeley Laboratory, recently used this newly invented method to achieve a unique high-resolution image of the DNA molecule. Our biologists and materials scientists are continuing this work by developing methods for "tying" molecules to surfaces to atomically image their functional groups. This work promises to contribute to the success of one of the grand scientific challenges of the coming decade: the mapping of the human genome.

Polymer and physical chemists in the C&MS Department are world leaders in the study of aerogels. They have invented a new, rigid, inorganic material whose low density approaches that of air. This silica aerogel, or "frozen smoke," provides extraordinary surface area in a small volume and will lead to opportunities in a wide variety of applications, including as a catalyst substrate, a new insulating material, and a dispersing medium for atomically fine powders. Since its announcement, LLNL scientists have received hundreds of requests from colleagues and industry for samples of this extraordinary material.

The C&MS Department has traditionally provided the scientific and technical expertise for developing and utilizing high-explosive materials. Our emphasis has always been on safety, and the invention of insensitive high explosives has now made even higher levels of safety possible. A fundamental understanding of the atomistic details of the explosive process is of paramount importance because this process is affected not only by stored chemical energy but also by crystal structure, defects, and electron transport. By utilizing x-ray microtomography, modeling, and new paths of synthesis, new phenomena are slowly being uncovered, and a fundamental understanding of insensitivity is within our grasp.

Among the services we provide to the Laboratory is the operation of the Plutonium and Tritium Facilities. Besides utilizing these facilities to provide direct support services to LLNL programs, Department scientists carry out unusual research of importance to future Laboratory programs. The dream of controlled fusion is being brought closer to reality by chemists and physicists who are developing schemes to produce a "super" fusion DT fuel in which the spins of tritium are polarized. This new condensed state of matter is being developed using high magnetic fields and cryogenics.

The discovery of high-temperature superconductivity has challenged our understanding of the fundamental aspects of electron delocalization and electron-electron correlation. The Department is leading a Laboratory-wide effort to characterize the electron structure of the Cu-O superconductor, to discover the mechanism of correlation, and to identify critical technological implications of importance to the Laboratory's national security mission. Strong collaborations with the University of California faculties and with sister laboratories have

characterized the interaction of this effort with the outside scientific community.

The historical gap between a fundamental understanding of simple systems and practical applications to complex materials is narrowing, and in some cases, it is being bridged by the increasing capability of theory to deal with more complex materials and phenomena. In the area of "alloy design," our theorists are in the forefront in developing new formalisms that deal with systems of low periodicity, such as grain boundaries, and with the role of short-range correlations and dynamical properties in phase stability. This effort is concentrated on the design of new alloys with specific and predictable properties, such as a superior class of materials that meet the demanding requirements for safe containment of weapons materials in the event of aircraft fuel fires.

It is clear from the foregoing discussion that the research conducted in the C&MS Department includes a wide variety of scientific disciplines, ranging from organic chemistry to physical metallurgy. In spite of this diversity, there is considerable interaction and collaboration between members of different groups. For example, the uses of analytical instruments and techniques such as synchrotron radiation or microprobe analysis transcend disciplinary boundaries, and frequently help to create fruitful interdisciplinary research. Also, the Department strongly encourages theorists and experimentalists to work on the same problems. This approach has the obvious benefit of keeping our theoretical efforts within the scope of the programmatic goals. It also has the desirable effect of increasing our depth of understanding beyond that acquired from experimentation alone.

The evolution of new technologies and devices will depend for its success mainly upon the corresponding inventiveness and discoveries of chemists and materials scientists. We are continuing to build an organization of scientists and equipment that will meet the future needs of all LLNL programs.

## Overview

The research programs in the C&MS Department have specialized requirements for analysis and materials characterization. Although Departmental activities are emphasized in the following pages, the Department provides this function for the entire Laboratory. A list of the tools and methods available includes electron and optical microscopy, mechanical-properties measurements, particle-size and porosity determinations, electron- and ion-beam microprobe analysis, x-ray crystallography, and differential thermal analysis. Diagnostic imaging methods range in resolving power from the nanometer level of scanning tunneling microscopy (STM) to the micrometer scale of x-ray tomography.

In addition to using well established methods for analysis and characterization, we engage in research and development to solve unusual or nonrecurrent problems. Our efforts at addressing such problems are described in this section.

While most equipment is purchased or constructed in-house with programmatic goals in mind, it is also chosen to suit the research activities of the C&MS division in which it resides. New techniques and apparatus are selected to match the skills and interests of their operators, ensuring competent handling and innovative application. This equipment and the associated scientists ultimately become a resource available to the entire Laboratory.

## Innovations

The C&MS Department has a substantial program in which a broad spectrum of solid state structures is investigated with synchrotron-produced x rays. The importance of short-range atomic order on the bulk physical properties of solids is becoming increasingly apparent, and synchrotron radiation is ideally suited to the study of this phenomenon. We have also used synchrotron radiation to elucidate the complex crystal structure of doped beta-boron by both x-ray absorption fine structure (XAFS) measurements and x-ray absorption near edge structure (XANES) measurements. The National Synchrotron Light Source at Brookhaven National Laboratory was the source of the x rays. In other research, we used a Stanford Synchrotron Radiation Laboratory beamline to develop an x-ray tomographic technique with a resolution of 5 μm. This new method will prove extremely useful for delineating structural details in a variety of bulk materials and interfaces. Until now, tomography has lacked the necessary resolution, while electron optical methods lacked sufficient penetration.

The morphology of DNA was clearly seen for the first time by STM. This research demonstrates that STM is both relatively simple in operation and low in cost. It provides resolution beyond that of conventional electron microscopy decoration techniques for biological molecules.

The C&MS Department conducts research into almost every aspect of the chemical and physical properties of high explosives. Our development of advanced analytical techniques allows us to positively identify the nature of the parent explosive from minute amounts of detonation products. The method reported here links on-line gas chromatography with mass spectroscopy. These tools can also be combined with thermal-energy analysis for the identification of nitrogen-containing compounds.

Finally, we report on our success in producing a multilayer substrate that serves as the optics (effectively, a lens) for a pseudo-Cassegrain telescope. The substrate was produced by sputtering. Other items made in this manner were multilayer diffraction gratings that can be tailored to operate in the x-ray, soft-x-ray, and extreme ultraviolet regions. All these developments have important implications for solar system astrophysics.

The C&MS Department has made recent progress in areas not described in this section. We improved our electron microscopy by installing a brighter electron source and a high-resolution electron-energy-loss spectrometer (EELS), for the determination of low-Z elements. A photoelectron spectroscope became operational and is being used for the band mapping of large untwinned crystals of superconducting $YBa_2Cu_3O_{7-x}$. We expanded our XAFS capability so that now we can perform time-resolved analyses of solid state reactions, which will lead to an understanding of their kinetics. We also improved the resolution of our STM nearly five-fold, achieving atomic resolution on the scale of organic molecules.

The laser chemistry program began an investigation of the decomposition of adsorbed layers of high explosives induced by an innovative shock technique. The shock waves not only induce the decomposition reaction but also expel the products from the surface, where they are characterized by spectroscopic analysis.

We also studied the photodissociation of $H_2O$ by laser light by using spectrometric methods to determine the relative concentrations of the various excited states of the dissociation products. This information is pertinent to some of the problems arising from the combustion of fossil fuels and the mechanisms of chemical explosive detonation.

Section I

# Innovations in Analysis and Characterization

Topographic image of DNA obtained by scanning tunneling microscopy

# State- and Bond-Selective Laser Chemistry

W. E. Conaway and
C. G. Stevens

***A full understanding of the properties and behavior of highly energized molecules is important to a number of industrial processes and technologies. These include the production and combustion of fossil fuels and the development of safer and more efficient high explosives. We are developing and applying new laser techniques that stimulate and interrogate high-energy chemical transformations. In this study, we are exploring the state-to-state photodissociation of $H_2O$ from highly excited vibrational states and have demonstrated the feasibility of a new and promising approach to bond-selective chemistry.***

## Introduction

A proper description of the structure and dynamics of highly energized molecules forms the basis for understanding and controlling a number of important energy technologies, including fossil fuel production and the combustion and development of safer, more efficient explosives. Lasers have been used in a variety of ways to energize molecules and to interrogate the subsequent molecular dynamics by multiphoton excitation up the vibrational quantum ladder a step at a time or, more recently, by single-photon excitation directly to vibrational overtone states.

Direct overtone transitions (up to $\Delta v = 7$) are seen in molecules having X–H bonds (X = carbon, nitrogen, or oxygen), and apparently the energy is localized in a single X–H bond for an observable period of time before it migrates into the other available energy states of the molecule.[1] This observation offers a possible means of achieving bond-selective chemistry through capturing the localized bond energy before it dissipates. We are researching a promising technique to accomplish this.

A laser excites the molecule into a single vibrational overtone state of the electronic ground state that has a large component of X–H stretching motion.[2] We then follow this bond "priming" step with a second laser pulse to break that same bond before the localized excitation dissipates into the other vibrational degrees of freedom of the molecules. The large bond extension gives this second threshold photon access to a dissociative potential surface away from the ground-state equilibrium geometry and down into the dissociative channel associated with breaking the selected X–H bond. Quantum state-specific detection of the molecular-product fragment is accomplished by a third probe using laser-induced fluorescence or resonance-ionization techniques.

The success of this approach relies upon several factors: (1) an understanding of the structure of overtone transitions in polyatomic molecules,[3] (2) the rate of intramolecular vibrational-energy transfer in the molecule, and (3) an accurate description of excited-state, potential-energy surfaces.

As a candidate system, we have chosen to examine the state-to-state photodissociation of highly excited vibrational levels of water molecules via the lowest excited electronic state. Bond-selective photochemical

**Figure 1.** Potential energy surfaces for the two lowest electronic states of water, showing the two-step photodissociation process leading to the selective breaking of the O–H bond. A visible laser near 592 nm selects a single rotational level from the $v_{OH} = 5$ vibrational state. A second laser pulse selectively promotes the vibrationally excited bond to a dissociative electronic state, leading to state- and bond-selective chemistry.

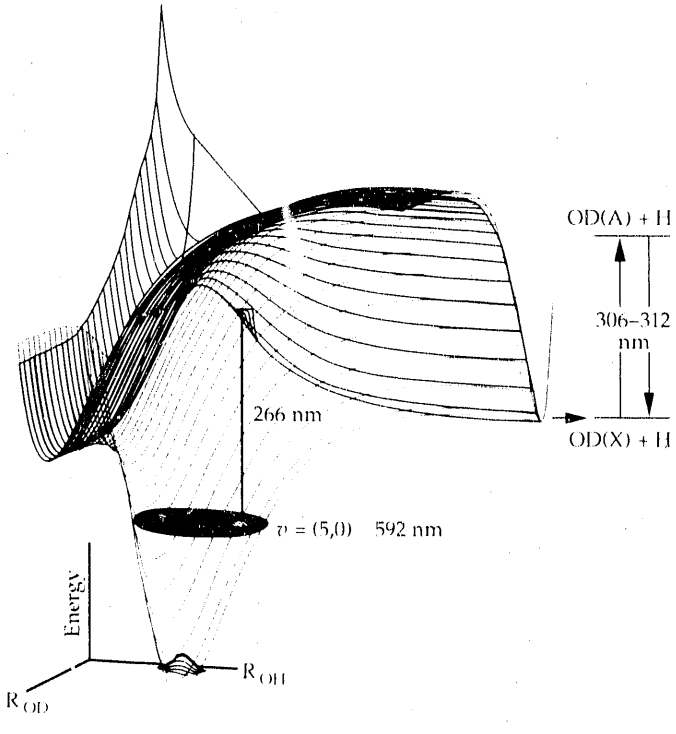

studies will ultimately be carried out on HOD (deuterated water), where the deuterium substitution allows us to distinguish between the two possible dissociation channels. We have concentrated our initial efforts to date on the complete characterization of the two-step photodissociation of $H_2O$, via the fifth O–H bond-stretching state. The pertinent potential energy surfaces of water are shown in Fig. 1, along with representative laser wavelengths for the three laser steps required for this photodissociation.

## Experimental Methods

The method of generating the three laser frequencies and the overall experimental schematic is illustrated in Fig. 2. The path delays of the three lasers are adjusted so that the overtone pumping laser pulse and the dissociation laser pulse are coincident in time. The laser-induced fluorescence (LIF) probe laser follows 15 to 20 ns later. The fluorescence is generated by laser excitation from the $v = 0$ ground vibrational state of the product OH molecules.

In addition to the LIF cell, a separate static gas cell equipped with a sensitive microphone is used to locate the water overtone transitions by pulsed photoacoustic spectroscopy (PAS). A number of strong, unblended rotational transitions are available experimentally for pumping molecules to the 5 $v_{OH}$ stretching region. Rotational levels up to angular-momentum quantum number $J = 5$ can be populated appreciably in a sample at room temperature. We estimate that up to 10 percent of a single initial rotational-state population can be excited to the upper overtone level by our present laser setup.

## Results and Discussion

We have measured the population distributions in OH following photodissociation of four single rovibrational states of water, characterized by the angular-momentum quantum number $J = 0$, 2, 3, and 4 in the fifth vibrational-stretch quantum state. Rotational-state distributions obtained for the state $J = 0$ are shown in Fig. 3. The angular momentum possibilities in the product OH are rather complex, resulting in four electronic states, labeled $^2\Pi_{1/2}(A')$, $^2\Pi_{1/2}(A'')$, $^2\Pi_{3/2}(A')$ and $^2\Pi_{3/2}(A'')$. These resolved state-to-state data represent the first such obtained from a vibrational overtone state and only the second successful state-to-state measurement of a direct photodissociation process.[4]

A number of interesting observations can be made regarding these results. Each electronic manifold shows a distinct population distribution (shown as bars on each level in Fig. 3) among the rotational quantum states. The populations cannot be described by a Boltzman distribution because we observe the nascent population before collisional equilibration has time to take place. In fact, a number of population inversions are seen, creating the

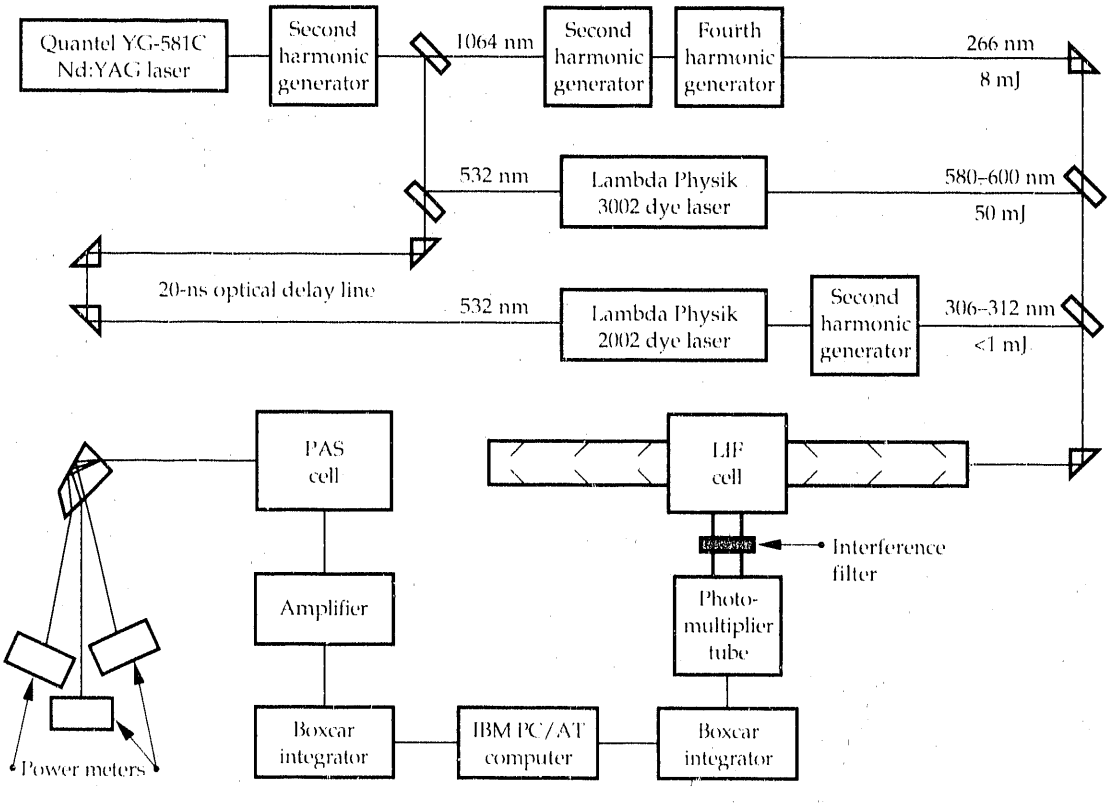


**Figure 2.**

**Schematic of experimental setup, showing the generation of the three laser wavelengths required, their respective energies, and the general data acquisition modes. Nd:YAG is neodymium:yttrium-aluminum-garnet.**

conditions for stimulated emission. Observed interstellar OH masers have been attributed to the direct photodissociation of water located near ultraviolet-emitting stars.

The observation of rather small distributions of rotational levels seen in the products and the large population inversions is surprising in that roughly 10,000 times more energy has been placed into the dissociating molecule than the energy difference between these levels. These observations can be quantitatively accounted for by the conservation of angular momentum and an assumption that no additional torque is added to OH as the molecule slides down the final exit channel[5] (see Fig. 1). The predictions of this model are shown in Fig. 3 and successfully recreate most of the details we observe.

**Figure 3.** State-to-state population distributions in product OH molecules following two-step photodissociation of $H_2O$. The four lowest electronic states of OH are shown, each with its manifold of molecular rotation quantum levels, designated by *J*. The relative populations of each product's rotational level are given by the height of the bars. A number of population inversions that are directly related to the mechanism of interstellar maser action are seen. Theoretical calculations based on a wave function projection model (solid bars) reproduce the trends in population.

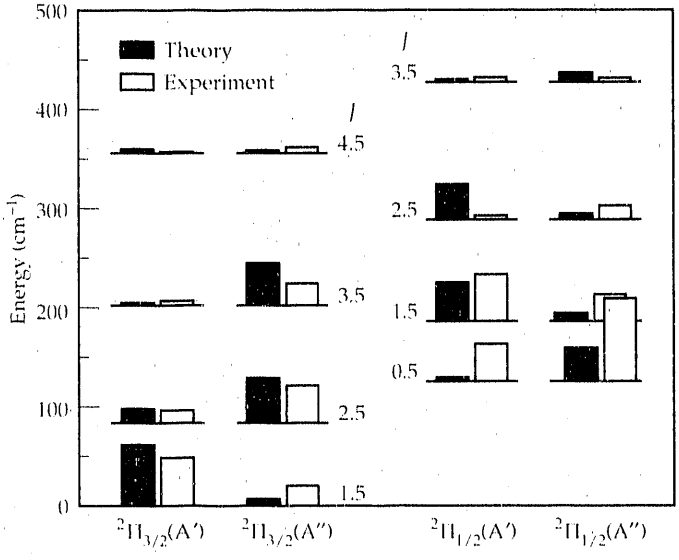


## Summary

We are now planning experiments on HOD in anticipation of selective breaking of the O–H bond. This will be a demonstration of a simple, selective reaction and a first step toward a long and fruitful exploration of photon-mediated chemistry. Recent theoretical modeling by Imre lends quantitative support to this selective bond-breaking concept.[6] A number of molecular systems have been identified as fulfilling the basic requirements of this approach: (1) localized *X*–H stretching states, and (2) purely dissociative electronic states. These include simple alcohols, amines, and selected hydrocarbons. Future experiments will explore these possibilities.

*This work was supported by Weapons Supporting Research.*

## References

1. B. R. Henry, *Acc. Chem. Res.* **10**, 207 (1977).
2. W. E. Conaway, M. W. Crofton, S. Bosson, and C. G. Stevens, *Bull. Am. Phys. Soc.* **32**, 1617 (1987).
3. M. W. Crofton, C. G. Stevens, D. Klenerman, J. H. Gutow, and R. N. Zare, *J. Chem. Phys.* **89**, 7100 (1988).
4. P. Anderesen, V. Behausen, D. Häusler, H. W. Lülf, and E. W. Rothe, *J. Chem. Phys.* **83**, 1492 (1985).
5. G. G. Balint-Kurti, *J. Chem. Phys.* **84**, 4443 (1986).
6. J. Zhang, D. G. Imre, and J. H. Frederick, *J. Phys. Chem.* **93**, 1840 (1989).

# XANES and EXAFS Studies of Metal Sites in Beta-Rhombohedral Boron

J. Wong and
G. A. Slack*

***Beta-boron is an intrinsic semiconductor with a band gap of 1.5 eV; it is hard and refractory, and it has a very high melting point (about 2300 K). Beta-boron satisfies the criterion of being made up of small atoms with a large number of atoms (105) per unit cell, which is necessary for potentially high thermoelectric efficiency. We have applied synchrotron-radiation techniques to determine the local atomic configurations surrounding various metallic dopants as well as to investigate the nature of their bonding to the beta-boron matrix.***

## Introduction

Crystallographically, beta-boron is made up of compact $B_{10}$, $B_{12}$, and $B_{28}$ polyhedral units and isolated boron atoms, all linked together by strong, directional covalent bonds.[1] These structural and bonding features create a very open structure in beta-boron, as shown in Fig. 1. Assuming a radius of $r_B = 0.88$ Å, space filling is estimated to be only 36 percent. Consequently, the structure contains many holes that can interstitially accommodate a variety of metal atoms. The doped boron materials may be denoted $B_{100-x}M_x$, where $M$ may be a transition or nontransition metal and $x$ can vary from a fraction of a percent to a few atomic percent, depending on solubility and on the doping conditions of temperature and pressure.

Our experiments consisted of a combination of extended x-ray absorption fine-structure (EXAFS) measurements and x-ray absorption near-edge-structure (XANES) measurements, which were performed using intense synchrotron radiation. The purpose of the experiments was to determine the local atomic environment of the metal dopant(s) and their electronic interaction (bonding) with the boron host lattice, which is electron-deficient. Chemical and structural information of this kind is essential in understanding the physicochemical behavior that is directly relevant to improved and advanced thermoelectric applications of nuclear power.

## Experimental Procedure

The metal-doped boron materials were prepared at General Electric Corporate Research and Development Center using a melt-grown technique at a temperature above 2000°C in an argon ambient atmosphere at about 50 atm. X-ray absorption spectra were measured at room temperature on beamline X-11A at the National Synchrotron Light Source (NSLS) at Brookhaven National Laboratory, which operated with an electron energy of 2.5 GeV and an injection current of about 100 mA. The synchrotron x-ray beam from the NSLS x-ray ring was monochromatized with

**Figure 1.** Beta-rhombohedral boron is made up of compact $B_{12}$ and $B_{28}$ polyhedral units and isolated boron atoms, all linked by strong directional covalent bonds. The $B_{12}$ units form icosahedra located at the corners and mid-edges of the rhombohedral cell. The two $B_{28}$ units are located inside the cell and are joined by a single boron atom at the center of the cell. The structural and bonding features create a very open crystal lattice with about 60 percent interstitial space; consequently, the many interstitial holes can accommodate a variety of metal atoms.

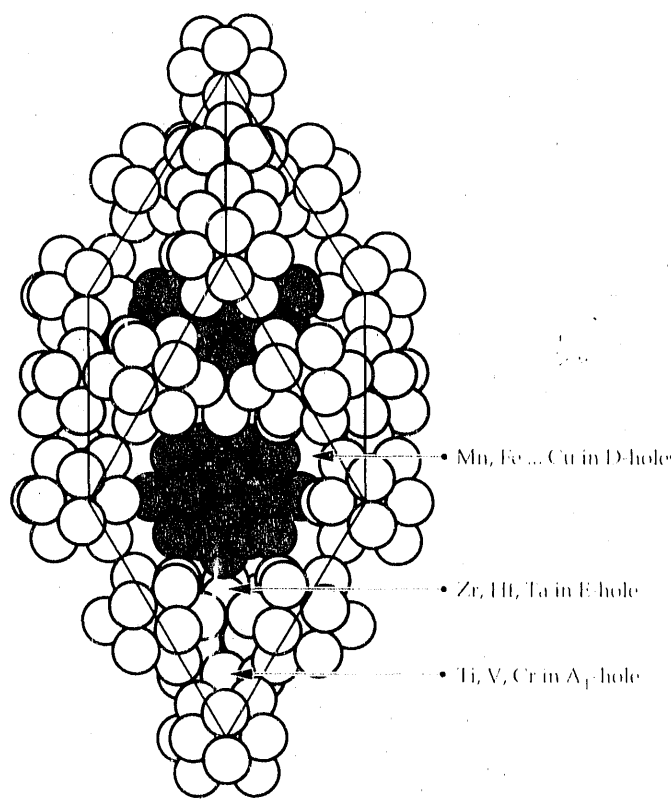

a double silicon (111) crystal and a 0.5-mm entrance slit, which yielded a resolution of about 0.5 and 1.5 eV at the titanium and copper K-edges, respectively. Details of spectral recording, XANES normalization, EXAFS analysis, and simulation have been described in other publications.[2,3]

Figure 2 shows the normalized XANES spectra for a series of 3d metals that are 1 percent in concentration and doped in beta-boron. For the early members (in particular, titanium, vanadium, and chromium), a number of well-resolved transitions up to 24 eV are evident. The pre-edge feature at 1 to 2 eV is a 1s → 3d transition, which is normally dipole-forbidden, but here it is rather strong, indicating appreciable overlap with the p-states of the metal dopants. Two well-defined bound states at 7 and 11 eV are also evident. As the d-states are progressively filled in, going across the 3d series from titanium to copper, the pre-edge feature at 1 to 2 eV becomes less well defined. This is evident from the spectra of manganese through copper. The spectral features at high energies are due to lattice scattering.

**Figure 2.** K-edge XANES spectra of 3d metals (1%) doped in beta-boron.

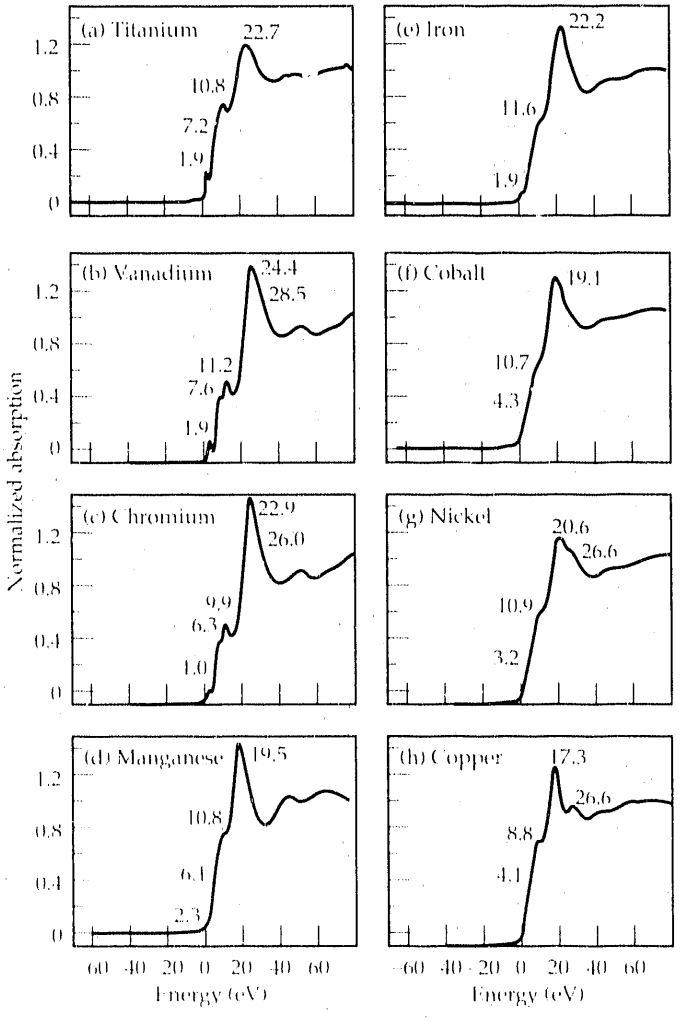


The XANES spectra of two systems, one double-doped with 1% vanadium and 1% copper and the other with 1% vanadium and 3% copper, are identical to those of the respective single-doped boron materials. This fact indicates that the local structure and electronic configuration around the vanadium atom are affected little by the presence of copper in the boron lattice, and vice versa. This result demonstrates conclusively that there is no interaction between two dissimilar dopants in the boron lattice (Figs. 3 and 4).

Concentration dependence and EXAFS analysis, which are described in the next section, show that both vanadium and chromium occupy the more symmetric $A_1$ site, with 12 boron neighbors at a bond distance of 2.15 Å, up to a doping concentration of 1 percent, while titanium, iron, and manganese occupy both $A_1$ and D sites. The latter has 14 boron atoms as neighbors. Above 0.5 percent, nickel goes into a second site, whereas copper undergoes multisite occupancy at 1 percent.

The $L_3$-edge spectra of hafnium and tantalum in boron are shown in Figs. 5 and 6, respectively. The $L_3$-edge arises from excitation of the core 2p state to some final d states, which for hafnium and tantalum (the early 5d elements) are quite empty (i.e., there is a high density of final states). The principal absorption maximum, the so-called "white line," is observed to be intense. The $L_3$ spectrum may be deconvoluted into a Lorentzian function and an arctangent step function (i.e., the edge jump) according to a procedure described by Horsley.[4]

**Figure 3.** K-edge XANES spectra of vanadium in vanadium/copper double-doped boron.

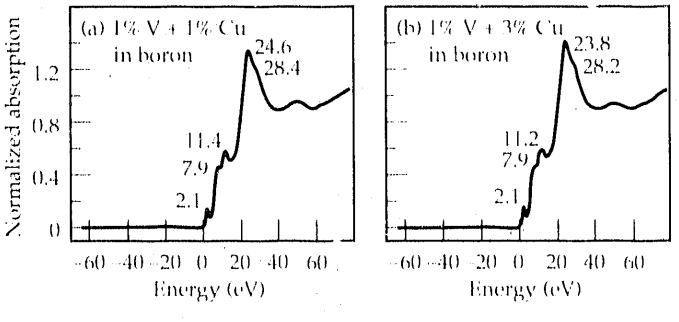


**Figure 4.** K-edge XANES spectra of copper in copper/vanadium double-doped boron.

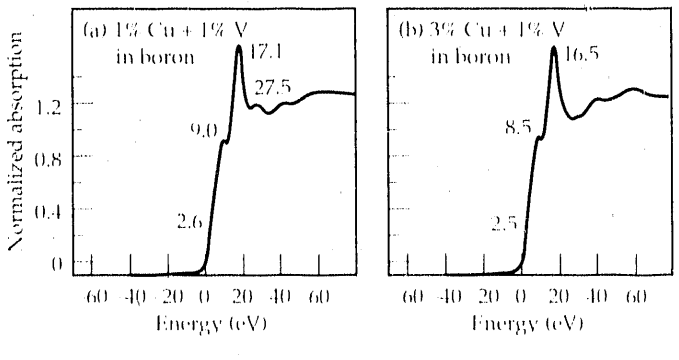

Hafnium diboride ($HfB_2$) and tantalum diboride ($TaB_2$) are isostructural to aluminum diboride ($AlB_2$): hexagonal, space group C6/mmm, with an atomic number of 1 $HfB_2$ or $TaB_2$ unit per primitive cell.[5] The structure consists of alternate layers of metal and boron stacked along the c axis. Each metal atom has six equidistant closest metal neighbors in its plane and twelve equidistant boron neighbors, six in the layer above and six in the layer below the metal atom. Correspondingly, each boron atom has three boron neighbors in its plane and forms six boron-metal bonds. Accordingly, the deconvoluted spectra of both $HfB_2$ and $TaB_2$ as well as those of the pure metals, shown as dashed lines in Figs. 5 and 6, yield a single Lorentzian function, which is indicative of a single crystallographic site. The corresponding deconvoluted spectra of metals in boron are best fitted with two Lorentzian functions, as shown in Fig. 5(b) and (c) for hafnium and Fig. 6(c) for tantalum. This spectral analysis suggests that there are multisites of these 5d metals in the boron lattice.

## EXAFS Results

As an example of the EXAFS results, we present an analysis of the vanadium EXAFS data to determine the metal coordination in beta-boron. In Fig. 7(a), the experimental vanadium K-edge EXAFS spectrum at room temperature for $VB_{\sim 165}$ is plotted as $I_F/I_0$ vs energy, where $I_F$ is the vanadium $K_\alpha$ fluorescence intensity and $I_0$ is the incident intensity. In Fig. 7(b), the normalized vanadium EXAFS for $VB_{\sim 165}$ is plotted as $\chi(k)$ vs $k$. The Fourier transform of this $k^1$-weighted signal yields a radial peak at just below 2 Å, as shown in Fig. 7(c). The inverse transform of the radial structure in the region of 0.8 to 2.2 Å yields a filtered $\chi^F$ signal in $k$ space [shown as a solid line in Fig. 7(d)].

To determine the vanadium–boron phase shift and boron envelope function, we use the diboride of vanadium, $VB_2$, as a model. Like $HfB_2$ and $TaB_2$, $VB_2$ belongs to the $AlB_2$-type structure. Correspondingly, each boron atom has three boron neighbors in its plane and forms six boron–vanadium bonds. We found that a one-shell fit yielded the best fit with physically meaningful parameters for the $VB_{\sim 165}$ alloy: $N = 12.2$, $r = 2.17$ Å, and $\sigma = -0.00347$ Å, where $N$ is the number of boron neighbors, $r$ is the average boron distance from a given vanadium atom, and $\sigma$ is the Debye-Waller factor. The simulated spectrum is shown in Fig. 7(d) as the dotted curve. The standard deviation in amplitude between the simulated and experimental spectra is 5.4 percent.

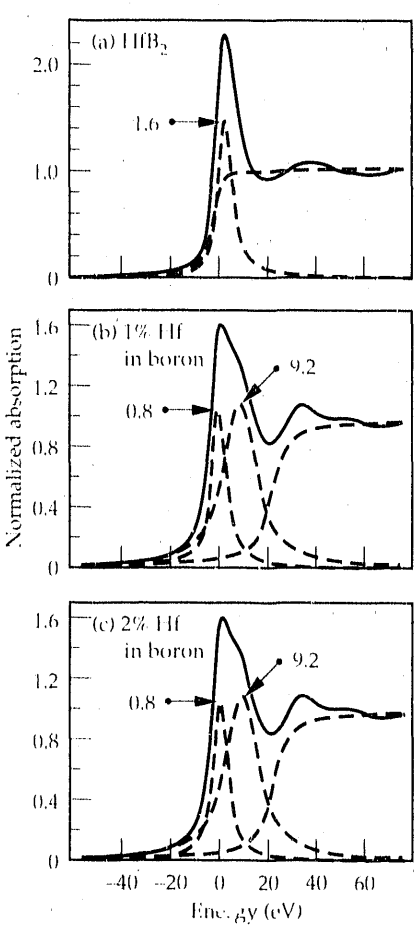


**Figure 5.**

**$L_3$-edge XANES spectra of hafnium in various systems. Deconvoluted spectra are shown as dashed lines.**

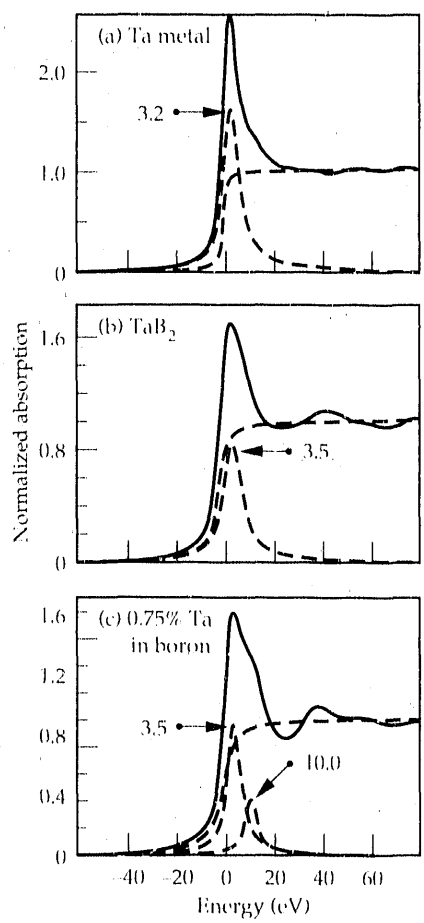


**Figure 6.**

**$L_3$-edge XANES spectra of tantalum in various systems. Deconvoluted spectra are shown as dashed lines.**

A recent single-crystal diffractometric study[6] shows that in $VB_{\sim 165}$, the vanadium atoms are found only at the 12-fold coordinated $A_1$ sites, which have six boron atoms at 2.167 Å, three at 2.133 Å, and three at 2.145 Å. Within the accuracy of the EXAFS technique ($r$, ±0.02 Å; and $N$, ±10%), the EXAFS results agree with those obtained by x-ray diffraction.

## Conclusions

We have demonstrated the usefulness of EXAFS and XANES, using synchrotron radiation as a light source to probe the local atomic structure and bonding of metal sites in beta-boron. Our structural results for the case of $VB_{\sim 165}$ agree well with x-ray diffraction data in terms of the vanadium–boron bond distance and coordination of the x-ray-absorbing vanadium center. In addition, bonding information and electronic interaction of the metal dopant with the alpha-boron lattice, not previously available, may now be deduced by analyzing the near-edge spectrum using appropriate model compounds.

With brighter and more intense synchrotron sources, such as the Advanced Light Source at Lawrence Berkeley Laboratory and the Advanced Photon Source at Argonne National Laboratory, similar structural studies can be carried out at much lower concentrations (less than parts per million) and smaller sample sizes (micrometers), as well as in the millisecond time domain of time-resolved studies, to elucidate the chemical dynamics and kinetics of reactions.

*This work was supported by Institutional Research & Development.*

*General Electric Corporate Research and Development Center, Schenectady, N.Y.

## References

1. J. L. Hoard, D. B. Sullen, C. H. L. Kennedy, and R. E. Hughes, *J. Solid State Chem.* **1**, 268 (1970).
2. J. Wong, F. W. Lytle, R. P. Messmer, and D. H. Maylotte, *Phys. Rev.* **B30**, 5596 (1984).
3. J. Wong and H. H. Lieberman, *Phys. Rev.* **B29**, 651 (1984).
4. J. Horsley, *J. Chem. Phys.* **76**, 1451 (1981).
5. B. Post, F. W. Glaswer, and D. Moskowitz, *Acta Metall.* **2**, 20 (1954).
6. M. F. Garbauskas, J. S. Kasper, and G. A. Slack, *J. Solid State Chem.* (in press).

**Figure 7.**

(a) Room-temperature experimental scan of vanadium K-edge XANES and EXAFS spectra in $VB_{\sim 165}$. The energy zero is taken to be the first inflection at 5465 eV [see Fig. (2b)]. (b) Normalized EXAFS spectrum plotted as $\chi$ vs $k$. (c) Fourier transform of $\chi$. (d) Experimental inverse transform $\chi^F$ (solid line) and simulated EXAFS spectrum (dotted line) in the region 0.8 to 2.2 Å about the central absorbing vanadium atom in $VB_{\sim 165}$.

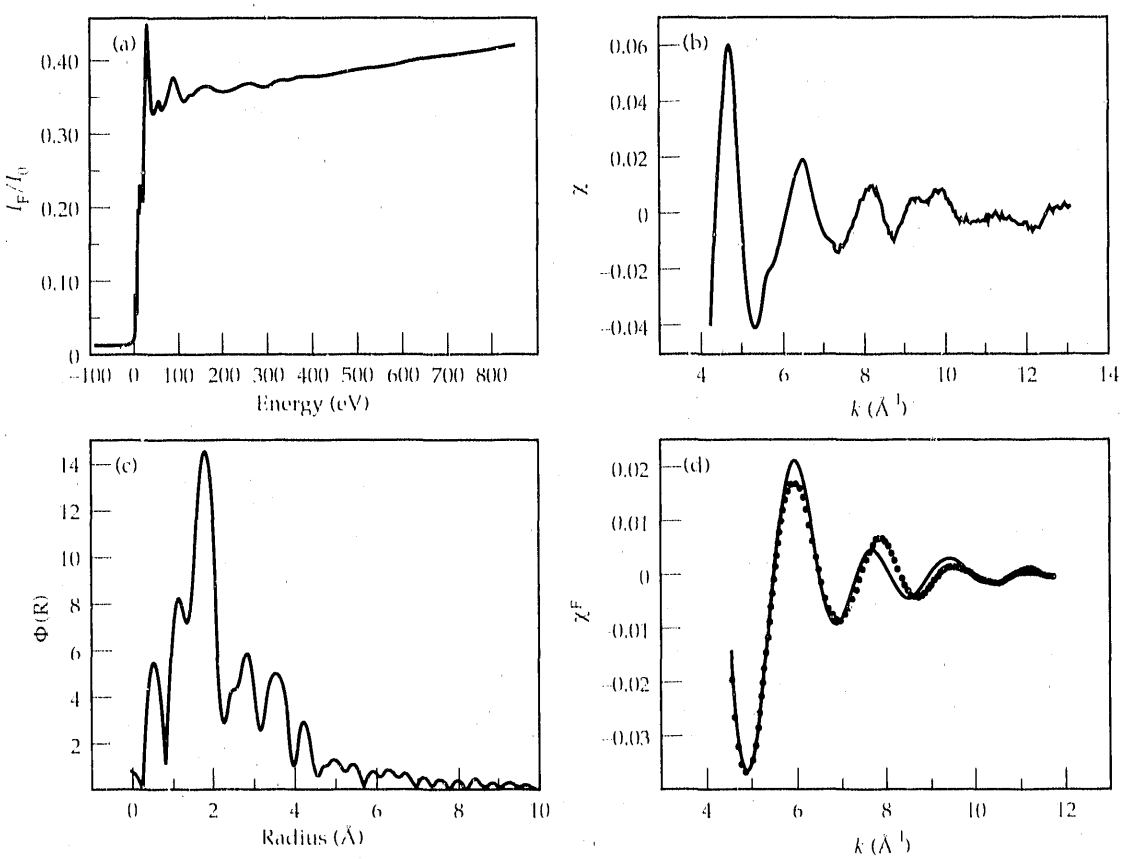

# Direct Observation of Native DNA Structures with the Scanning Tunneling Microscope

R. L. Balhorn,
T. B. Beebe, Jr.,
W. J. Siekhaus,
R. J. Tench, J. E. Katz,*
B. Marchon,*
D. F. Ogletree,*
M. B. Salmeron,* and
C. Ocal†

***Uncoated double-stranded DNA has been imaged for the first time with a scanning tunneling microscope (STM) operating in air. The resolution was such that the pitch of the DNA helix and its major and minor grooves could be observed. We have thus demonstrated that the STM can be useful for structural studies of a variety of uncoated and isolated biomolecules.***

## Introduction

The STM is becoming an essential tool at LLNL in the development of technology and in basic research in chemistry, materials science, and biology. In technology development, for example, higher-than-expected roughness (on the angstrom scale) was observed by STM on both diamond-turned surfaces and vapor-deposited multilayer x-ray-optics surfaces; this observation elucidated previously unknown details of the cutting and deposition processes. In chemistry and materials science research, STM revealed that what is seen with other techniques, such as low-energy electron diffraction, as a mono-atomic layer of sulfur atoms on a rhenium (0001) surface consists in reality of patches of nonuniform "hexagons" of sulfur separated by grain boundaries. This revelation helped to explain surface passivation in corrosion and catalysis.[1]

In support of biological research at LLNL, in particular the human genome project, we have used STM to image native DNA.[2] It is this observation that we report here in detail.

Earlier studies have shown that not only metals and semiconductors but also organic, inorganic, and biological molecules can be imaged by STM, both in air and a variety of other media.[3] These studies demonstrated the advantages of STM, viz, simplicity of operation, low cost, and angstrom resolution both laterally and normal to the surface. Imaging is possible in a wide variety of environments, including air and liquids, and sample-preparation conditions are not as harsh as those needed for most conventional electron-microscopy techniques, which generally require vacuum conditions and conducting coatings. This technique can be brought to bear on structural questions in the biological field, even if the nature of the electron energy levels that participate in the tunneling process in an organic molecule is not understood.

This article reports on the first high-resolution observations of DNA structures obtained with the STM in native (non-metal-shadowed) specimens. In these images, both the major and minor grooves of double-helix DNA were resolved, which implies a resolution of about 5 Å. Further, the distances between these grooves were measured.

## Experiment

We constructed an STM based on an earlier IBM design. Our STM used a micrometer-driven differential spring mechanism for sample movement and a tubular piezoelectric crystal rather than a tripod to scan the tip. We used mechanically cut tips consisting of a 60 percent platinum, 40 percent rhodium alloy. The typical tunneling conditions were a 150-mV sample bias (either polarity) and a few nanoamperes of tunneling current. No difference in the images was observed as a function of these parameters.

Solutions of calf thymus DNA were prepared as described in Ref. 4. A droplet of the aqueous solution (1 mg of DNA per ml in 10 m*M* KCl) was allowed to evaporate in air on a freshly cleaved, highly ordered pyrolytic graphite (HOPG) substrate, which provides a conductive surface with crystal planes atomically flat over thousands of angstroms. In the images we present, tunneling was initiated immediately after the last traces of water were observed to evaporate. Thus, the DNA was not subjected to particularly harsh or intricate sample-preparation procedures. Sample blanks exposed to 10-m*M* KCl solutions containing no DNA and subjected to identical treatments showed no topographic structure in the STM images other than the expected atomic features and occasional steps that are characteristic of cleaved graphite surfaces.

Some of the problems encountered with DNA prepared in this way include clumping into large unrecognizable aggregates that do not give stable tunneling conditions, and at the other extreme, the inability to find any DNA molecules within the scanning range of our microscope (our largest scans were 0.5 × 0.5 μm).

**Figure 1.**

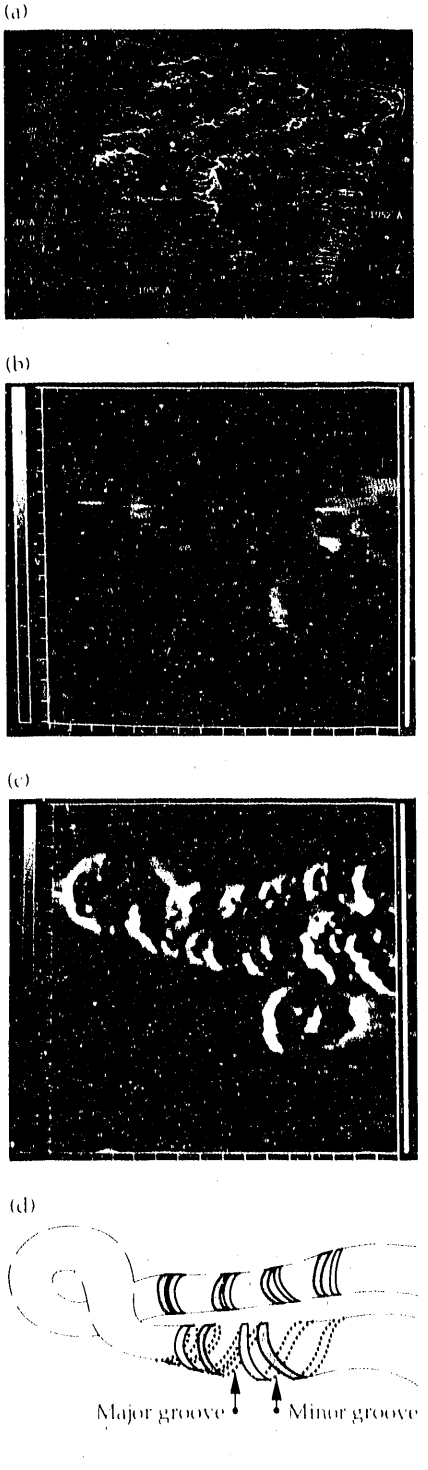


DNA deposited on graphite and imaged in air with the STM. All of the images were obtained at constant tunnel current (topographic images). (a) Sample area, 1050 × 1050 Å; total height, 49 Å; sample bias, −155 mV; current set point, 0.9 nA; acquisition time, 210 s (tip velocity 1300 Å/s). Postacquisition image processing consisted of digital band-pass filtering with the removal of all Fourier components greater than 0.097 $Å^{-1}$ and less than 0.0024 $Å^{-1}$. Variations of these values within reasonable ranges caused no significant changes in the images. The image is presented in a projected three-dimensional format with gray scale, as viewed from a perspective 45 deg above the plane and 20 deg clockwise in the plane. (b and c) Area 400 Å; total height range, 132 Å; sample bias, −97 mV; current set point, 3.3 nA; acquisition time, 42 s (tip velocity 2500 Å/s). (b) Raw image. (c) Postacquisition image processing consisted of nine-point two-dimensional smoothing applied once, followed by simulated light-source shading from a point 15 deg above the plane. (d) Schematic of the DNA structure in (b) and (c).

Movement or displacement of the DNA, although occasionally observed, was not found to be a problem. The complete evaporation of the DNA solution commonly left a 4-$mm^2$ area on the graphite surface consisting of a series of concentric rings, which were caused by the evaporation process and the salts that the shrinking droplet left behind. In the center of this area, there was usually a 1-$mm^2$ spot in which the last amounts of salt precipitated out of solution. This region was avoided because of the unstable tunneling conditions caused by the thick layer of nonconducting salt.

## Results

Figure 1 shows an image constructed from the topographic contours followed by the STM tip as it traversed the DNA adsorbed on the graphite, while the feedback-control electronics maintained a constant tunneling current. This image is typical of our large-area images in that it shows a double-stranded DNA molecule (DNA duplex) that makes many convolutions on the surface. The DNA consists both of segments that are isolated from the rest of the duplex as well as segments in which there are overlapping and apparently tangled DNA duplexes. The periodic bumps along the duplex occur with a range of spatial periodicities from 27 to 50 Å and correspond to the helix pitch. The DNA structures observed were stable and reproducible from scan to scan.

The apparent width of the DNA, which seems large in this image (about 60 Å) is actually broadened as a result of the finite size of the tip. This problem becomes more pronounced for structures with a large relief from the substrate, as tunneling from the side of the tip is possible. The apparent width is thus a convolution of the actual DNA structure with that of the tip. The height above the substrate, that is, variation in the z coordinate, is not affected in the same way, and this value is typically 20 to 30 Å, which is near the expected value.

In Fig. 1(b) and (c), an image is shown in which higher resolution was achieved that is typical of the others we have obtained [(b) is the raw image and (c) is processed]. The DNA duplex as imaged enters the figure in the upper right corner, makes a loop, and crosses over itself in the upper left corner, leaving an image in the upper half and an unresolved structure below this, possibly a DNA fragment. A schematic of the image is shown in Fig. 1(d). A long-short alternation occurs in the spacing of the ridges in the DNA duplex. These ridges are due to the phosphodiester backbone of DNA, which is composed of alternating deoxyribose sugar and phosphate groups. In Fig. 1(a), only the major groove could be observed, and each bump is due to the periodic double-stranded helix separated by the major grooves. In Fig. 1(b) and (c), where the resolution is higher, the additional structure due to the major-minor

groove alternation is seen. The distance of one major-minor pair is about 63 Å across the bottom duplex of the image and 49 Å across the top duplex. On average, this corresponds to about a 55 percent expansion in length compared with the crystalline state.

DNA may undergo length expansions by 25 to 50 percent when intercalated with ionic species in solution.[5] The DNA molecules that we examined have been subjected to the combined forces of the surface, dehydration, and possibly, intercalation with ionic species, so that we are not surprised that the pitch periodicities vary as they do here.

## Conclusion

We have shown that STM can be used to analyze biological structures in air with a resolution approaching that of the best electron microscopes operating in vacuum. We have presented this detailed example to show that STM and related techniques, such as atomic force microscopy and scanning tunneling spectroscopy, will significantly contribute to research and development at LLNL.

*This work was supported by Institutional Research & Development.*

*Lawrence Berkeley Laboratory, Berkeley, Calif.
†University of Madrid, Madrid, Spain.

## References

1. B. Marchon, C. Ocal, D. F. Ogletree, M. B. Salmeron, and W. J. Siekhaus, "STM Study of the Structure of Sulfur on Rhenium (0001) at Saturation Coverage," *J. Vac. Sci. Tech.* (in press).
2. T. P. Barbee, Jr., T. E. Wilson, D. F. Ogletree, J. E. Katz, R. L. Balhorn, M. B. Salmeron, and W. J. Siekhaus, "Direct Observation of Native DNA Structures with the Scanning Tunneling Microscope," *Science* **243**, 370 (1989).
3. P. K. Hansma and J. Tersoff, *J. Appl. Phys.* **61**, R1 (1987).
4. Highly polymerized calf thymus DNA (Worthington Biochemical Corp., Freehold, N.J.) was dissolved overnight in aqueous 10 m*M* KCl at a concentration of 4.5 mg/ml. Aliquots of this stock solution were subsequently diluted with 10 m*M* KCl to a working concentration of 1 mg/ml.
5. C. R. Cantor and P. R. Schimmel, in *Biophysical Chemistry, Part III: The Behavior of Biological Macromolecules* (Freeman, New York, 1980), p. 1252.

# X-Ray Tomographic Microscopy for Materials Characterization

J. H. Kinney,
Q. C. Johnson,
R. A. Saroyan,*
W. N. Massey,†
U. Bonse,‡ R. Nusshardt,‡
and M. C. Nichols§

*We have developed a method for characterizing materials in three dimensions with a spatial resolution of 5 μm. This method is known as x-ray tomographic microscopy (XTM). Though XTM does not yet have the spatial resolution afforded by electron-optical methods, the superior penetrating power of x rays allows fully three-dimensional characterization of materials in situ. We therefore expect XTM to be a technique that is complementary to electron microscopy.*

## Background

X-ray computed tomography (CT) is a powerful tool in diagnostic radiology. CT is performed by measuring x-ray absorption through a material from several viewing angles. This absorption information leads to an x-ray mass attenuation coefficient, $\mu$, for each volume element sampled by the beam. With proper knowledge of the x-ray energy, $\mu$ can be used to map directly the sample density and the chemical composition with an accuracy of better than 1 percent.

In medical practice, CT is a powerful tool for mapping the interior structures of the human body. It is superior to radiography because the interior structures can be imaged without being obscured by surrounding variations in tissue density. Unfortunately, the resolution of medical CT (~0.25 mm) is inadequate for most applications in materials characterization. The development of complex composite materials, as well as increased interest in the materials community in studies of interfaces, adhesion, and bonding, has led to renewed interest in the nondestructive x-ray inspection of materials, especially to obtain three-dimensional information of materials with a spatial resolution of a few micrometers.

Electron-optical methods, though possessing great spatial resolution, cannot yield three-dimensional information on samples without destructive thin sectioning of the material. Furthermore, many materials, especially nonconductive polymers, cannot be easily imaged by electron techniques without applying coatings of a conductive overlayer. We sacrifice spatial resolution to obtain three-dimensional, nondestructive characterization of samples, including their interiors.

XTM requires a well-collimated x-ray beam or a position-sensitive detector. Collimation was the first technique used to perform high-resolution CT because

**Figure 1.**

Artist's rendering of the XTM instrumentation. A parallel beam of synchrotron radiation is made nearly monochromatic using a double-crystal monochromator. The sample is positioned using precision stages accurate to better than 1000 Å. A second monochromator behind the sample eliminates scattered radiation and can be used to magnify the x-ray image. The x rays are converted to visible light and then optically imaged with a CCD array detector.

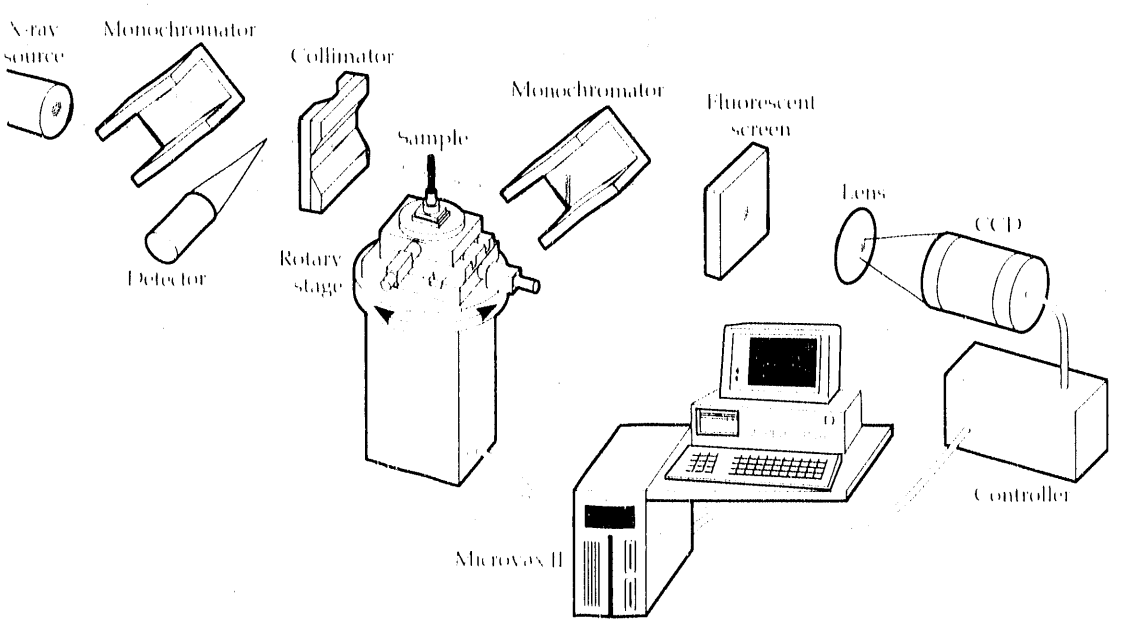

it does not require any extension of conventional radiography practices. Such techniques are very time consuming, because each projection for each viewing angle is measured sequentially. Using a synchrotron-radiation source with the collimation method, it required several hours to obtain enough absorption data to reconstruct a single 5-μm-thick cross section of the sample. Such a long time effectively precludes three-dimensional imaging using collimation.

As a result, we have developed a detector system in which all the projection data in horizontal and vertical dimensions can be taken in parallel. This method enables us to make measurements with high resolution on volumes of several cubic millimeters with great speed. The XTM requires a source of parallel x rays, such as synchrotron radiation, and consists of a sample stage, a detector system, and an analyzing computer.

In operation, a double-crystal monochromator selects a narrow energy range of x rays from the primary beam. The x rays pass through a sample positioned on a rotation stage and, if further magnification and filtering are desired, through a second magnifying x-ray optic. The x rays are then converted to visible light by means of a single-crystal scintillator. The visible-light image is magnified and recorded on a low-noise, two-dimensional, charge-coupled-device (CCD) detector. The sample is rotated by a small angle, and another two-dimensional absorption image is obtained.

This process continues until data from 180 deg of sample rotation have been recorded and stored in a computer. Tomographic software converts the x-ray absorption profile data into two-dimensional reconstructions of the linear attenuation coefficients in the sample interior. These values are rendered into a three-dimensional view using high-speed digital image-processing computers. The instrumentation is shown in Fig. 1.

The present XTM has a three-dimensional resolution of 5 μm, and the next generation of x-ray optics and synchrotron storage rings is expected to allow micrometer and submicrometer resolution. In addition, when elemental or phase-mapping details are desired, excellent chemical contrast can be obtained by recording data at two x-ray wavelengths—usually above and below a characteristic absorption edge—and performing image subtraction to enhance chemical or phase-specific information.

Since its development, XTM has been used to investigate coatings in supported catalysts, and porosity in oil shale and coal. Nevertheless, only with the recent advances in XTM technology has it been possible to successfully image complex composite materials.

## Application to Metal Matrix Composites

In a recent study, a 1.5 × 1.5 × 10-mm specimen of a composite consisting of an aluminum matrix and aligned silicon-carbide fibers was examined with XTM on the 31-pole wiggler beamline at the Stanford Synchrotron Radiation Laboratory. An x-ray energy of 21 keV was selected for good sample transparency and x-ray contrast between silicon carbide and aluminum.

Figure 2 shows a single XTM slice of the composite from a set of 97 contiguous cross sections obtained with the XTM. The projection width and slice thickness are 5.6 μm, and the spatial resolution is much better than 10 μm. Measurements were made with 5-s exposure times at 1-deg intervals. The 32-μm graphite cores and surrounding 140-μm-diameter silicon-carbide sheaths are clearly visible. The slight mottling observed in the aluminum matrix in Fig. 2 could be caused by either the statistical noise in the image (~2%) or actual variations in the materials composition.

Cracks running longitudinally in the plane of the fiber plies are evident in Fig. 2. These cracks, which do not penetrate the fibers, are believed to be a result of processing. Figure 3 shows a planar cut through the sample parallel to the fibers. In this ply, the fibers are regularly arranged, and the cracks tend to run along

**Figure 2.**

XTM cross section of an as-fabricated aluminum-matrix/silicon-carbide-fiber composite. Matrix microcracking is due to incomplete consolidation and to a mismatch in the coefficient of the thermal expansion between the silicon carbide and aluminum.

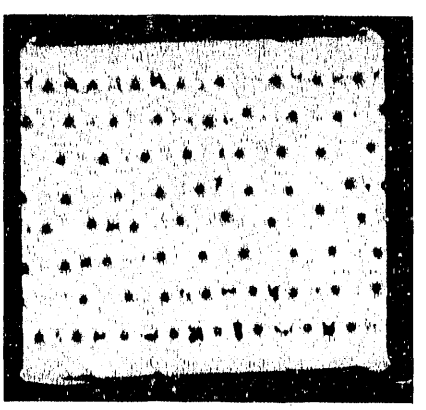

**Figure 3.** XTM section in the plane of the fibers. The fibers are clearly shown, as are cracks at the ceramic/metal interface. Because not all fibers are aligned with the numerically sectioned plane, variations in the fiber contrast (seen in the image) are created.

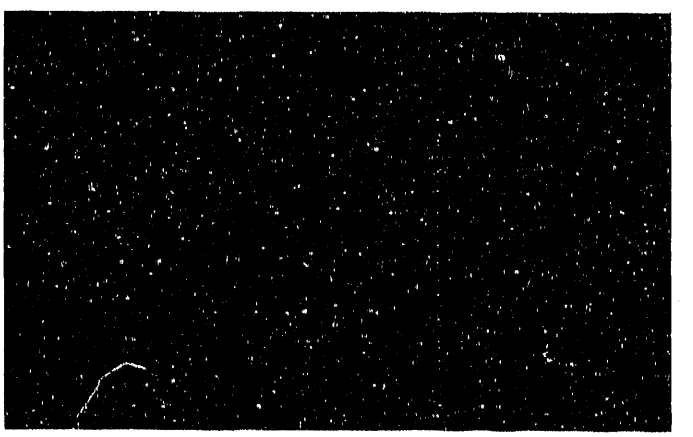

the fiber-matrix interface and between nearest-neighbor fibers rather than across the plies of the composite.

Values of μ, as measured using XTM, are given in Table 1 for the various parts of the composite. No corrections or normalizations have been made. These data are compared with two sets of tabulated x-ray attenuation coefficients. These calculations assumed all constituents to be fully dense, and the silicon carbide is presumed to be stoichiometric.

Agreement of the XTM data with the calculated values is excellent, and the differences between calculation and experiment are likely a result of slight departures from the nominal compositions of each phase, as well as inaccuracies in the tabulated cross sections. This agreement gives us confidence that XTM can be made very sensitive to subtle changes in alloy composition. Therefore, it should be possible to use XTM to study, at least in coarse detail, interfacial chemistry in situ.

**Table 1.** Calculated and observed values of the linear absorption coefficient $\mu$.

| Material | $\mu_{calc}$[a,b] ($cm^{-1}$) | $\mu_{obs}$ ($cm^{-1}$) | $\mu_{calc}/\mu_{obs}$ ($cm^{-1}$) |
|---|---|---|---|
| Crack | 0 | 0.07 ± 0.045 | — |
| Graphite | 0.85 (0.86) | 0.88 ± 0.44 | 0.97 (0.98) |
| Aluminum (pure) | 7.90 (7.95) | 8.09 ± 0.21 | 0.98 (0.98) |
| Aluminum (6061)[c] | 7.96 (8.26) | 8.15 ± 0.18 | 0.98 (1.01) |
| Silicon carbide | 9.21 (8.85) | 8.70 ± 0.73 | 1.06 (1.02) |

[a] E. F. Plechaty, *Tables and Graphs of Photon-Interaction Cross Sections*, Lawrence Livermore National Laboratory, Livermore, Calif., UCRL-50400, vol. 6, Rev. 3 (1981).

[b] *International Tables for X-Ray Crystallography* (Kynoch Press, Birmingham, England, 1972), vol. 4, Table 2.1C, pp. 61–66.

[c] The nominal composition of this alloy is from *Metals Handbook Desk Reference* (American Society for Metals, Metals Park, Ohio, 1961), 8th ed., vol. 1, p. 945.

## Future Directions

Efforts are now being focused on improving the resolution and sensitivity of XTM. Achieving a spatial resolution of 1 μm will require improved sample-positioning capabilities and larger CCD formats. The design of in situ tensile stages and environmental chambers for imaging samples under load or high temperature is also planned; presently, all measurements are made at room temperature and ambient conditions. If a sample is stressed or a crack is introduced, it must first be removed from the XTM stage for stressing and then be replaced in the XTM for characterization. Because cracks may close in the absence of an applied load, direct visualization of damage prior to failure may be difficult unless in situ load cells are used. The development of these stages and chambers is under way.

*This work was supported by Weapons Supporting Research and the Weapons Program.*

*Computation Directorate, LLNL.
†Engineering Department, LLNL.
‡Physics Department, University of Dortmund, Dortmund, FRG.
§Sandia National Laboratory, Livermore, Calif.

# Advanced Multilayer X-Ray Optics

T. W. Barbee, Jr.

***Multilayer optics for the x-ray, soft x-ray, and extreme ultraviolet spectral regimes is a rapidly expanding and maturing field. Most of the effort in this field is directed at improving the quality of multilayer structures by developing a better understanding of synthesis-structure-property relationships. Although the quality of simple multilayer structures may be improved, there are now significant instrumental applications for these reflecting structures and opportunities for developing new optics. A new class of diffraction grating (the multilayer grating) and a multilayer Cassegrain astronomical telescope are discussed.***

## Introduction

The basic physics and technology of simple multilayer structures for the extreme ultraviolet (15–100 eV), soft x ray (100–3000 eV), and x ray (3000–100,000 eV) were established 4 to 5 years ago.[1] It was apparent then that multilayers had the potential to greatly extend and simplify the experimental techniques available in these spectral ranges. Although this potential was clear, only a few demonstration experiments had been performed in which multilayer structures were an integral element of an optic system.

This article gives a short description of multilayer structure as it relates to extreme ultraviolet, soft x-ray, and x-ray optics. A new class of diffraction grating, the multilayer grating, is described. This optic extends the capabilities of simple reflecting diffraction gratings and makes possible efficient, high-resolution dispersion elements. Experimental performance of a multilayer-based imaging instrument is also described.

## Simple Multilayers

Multilayer-based optic elements are direct analogs to standard quarter-wave elements that are applied at longer wavelengths with the requirement that absorption be included. They are man-made, periodic-layered structures of high enough quality to be considered synthetic crystals.[1] Layers of materials A and B having significant differences in their scattering powers for x rays and being of uniform thicknesses $t_a$ and $t_b$, respectively, are combined to form a sample of uniform period $d_0 = t_a + t_b$.

Important multilayer parameters are the substrate quality (roughness and figure), the uniformity and thicknesses of the component layers, the x-ray optical constants of the component elements, the number of layers in the structure, the interface width or abruptness in atomic position and composition, and the interface roughness. These diffractive structures may be modeled using optical multilayer codes or the x-ray scattering approach typically applied to perfect crystalline Bragg diffractors.

Generally, multilayers may be synthesized using many of the naturally occurring elements. Optimized normal incidence reflectivities[2] that were calculated using tabulated optical constants for elements with atomic number ($Z$) greater than 5, and for the spectral range from 100 to 2000 eV, are all surprisingly large (40–80%), though only low resolution was predicted at the longer wavelengths. These reflectivities exceed by a factor of $10^4$ or more those typical of reflecting surfaces used in this energy range at high angles of incidence.

## Multilayer Diffraction Gratings

Simple multilayer structures have high reflectivity but low resolution. Increasing resolution by combining two diffractive structures—multilayers and diffraction gratings—is, therefore, important. Early work on multilayer gratings was devoted to using multilayers to enhance the reflectivity of the active grating surfaces, thereby increasing grating efficiency. Recent results[3–5] have shown that convolution of the properties of these two structures (multilayers and gratings) results in an optic having unique characteristics that greatly enhance the performance of both structures.

These new properties may be demonstrated by analysis[3] of a simple laminar-amplitude multilayer grating, shown schematically in Fig. 1. This grating structure is a laminar-amplitude grating as light is only diffracted

from the tops of the grating bars. The structure consists of flat-topped bars of width $d_g/2$ and has a period $d_g$. The multilayer structure is periodic in depth, with a period $d_0$, as shown.

Light incident at a grazing angle θ is diffracted by the multilayer at an exit angle θ in zeroth order. Interference of light diffracted by the multilayers on each grating bar results in intensity maxima (grating-dispersed, multilayer-diffracted light) at angles $\Phi_m$ relative to zeroth order, where $m = \pm1, \pm2, \pm3$, etc., are the grating orders. The relationship between the dispersion angle $\Phi_m$, the structural parameters $d_g$ and $d_0$, the angle of incidence θ, and the composition of the multilayer may be derived by analogy with a Young's slit structure or from the scalar grating equation, and is given as:

$$\sin\Phi_m = \sin\Phi_{m0}\,[1 - (2\delta - \delta^2)/\sin^2\theta]^{1/2}\ , \qquad (1)$$

where $\sin\Phi_{m0} = 2nd_0/nd_g$ and $n$ is the multilayer Bragg order. The term in brackets corrects for refraction of the multilayer-diffracted light resulting from the optical constants of the multilayer component materials, and is nearly constant over broad spectral ranges away from characteristic absorption edges of these materials. Therefore, $\Phi_m$ is essentially constant, being independent of θ and the energy of the light diffracted by the multilayer. It is defined by the multilayer period ($d_0$), the grating period ($d_g$), the order of the grating ($m$), and the multilayer Bragg order.

It is useful to consider the ramifications of Eq. (1). First, for multilayer gratings, higher Bragg-order contamination of the grating-dispersed orders is eliminated since $\Phi_m$ is inversely proportional to $n$. Second, the spectral range dispersed in any grating order is determined by the band-pass of the multilayer Bragg diffraction peak. This is always less than 10 percent, so that order overlap occurs only at very high order and, therefore, high resolutions are obtainable. Third, $\Phi_m$ is independent of the energy of the dispersed light and θ.

This has specific ramifications for laminar-amplitude gratings, true laminar-phase gratings, and blaze gratings. If the step height in a laminar-phase grating is matched to $d_0$ and $d_g$ as defined by Eq. (1), it will be on phase for all angles of incidence and, thus, for all Bragg-diffracted wavelengths. Also, if the blaze angle of a blaze grating is an integral multiple of $\Phi_1$, it may be operated on blaze at all angles of incidence and, thus, for all Bragg-diffracted wavelengths. This greatly extends the useful spectral ranges of these two optic structures and is a unique property of multilayer gratings. As a result of the limited band-pass of the multilayer Bragg diffraction peaks, these may be used in high order, so that very high resolutions are attainable.

The properties presented above have been observed experimentally for simple laminar-amplitude gratings,[3] laminar-phase gratings,[4] and blaze gratings.[5] In addition, concave-blaze and holographically ruled grating substrates have been multilayer-coated and characterized[6] at normal incidence. High resolution was demonstrated (~2500 for 15.0-nm light ), but efficiency was limited by the quality of the grating substrate.

In summary, multilayer gratings (laminar-amplitude, laminar-phase, and blaze) have demonstrated properties experimentally that greatly extend their utility and that evidence potential for very high resolution in high order. These characteristics are not limited to the x ray, soft x ray, and extreme ultraviolet, but will also be present with more traditional grating structures intended for use at lower energies. The characteristics described above for multilayer gratings are, therefore, general in nature and represent a new class of grating structure.

**Figure 1.** Schematic of a simple laminar-amplitude, multilayer-diffraction grating.[3]

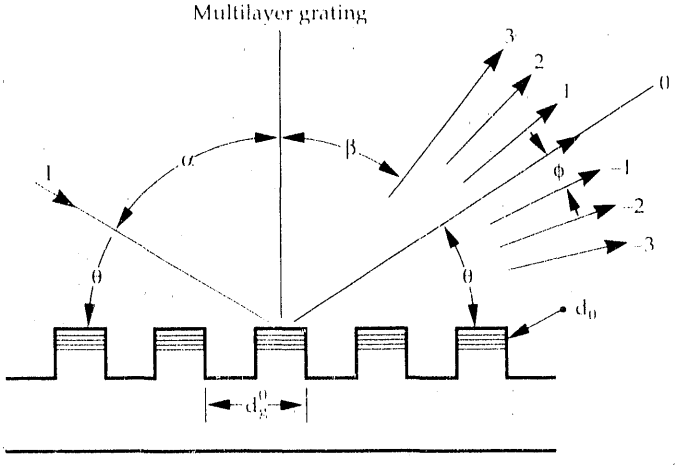


θ Bragg angle
0 Bragg-diffracted beam
+1, ±2, ±3 Grating-dispersed Bragg light

Variables θ, $d_0$, $d_g^0$, α, β, ϕ

## Multilayer Cassegrain Astronomical Telescopes

The application of figured multilayer structures in normal-incidence imaging systems represents an important area of instrument development. The most advanced applications in this area are to telescopes for solar astronomy. Several solar observations have been made using figured multilayer-optics-based instruments.

The most successful of these observations[7] were made with a pseudo-Cassegrain telescope constructed using multilayer, coated, superpolished, spherical, substrate optics. Images having a high spatial resolution (~1.2 arcsec) were obtained with a spectral resolution of

about 5 eV on a sounding rocket flight at the White Sands Proving Grounds in New Mexico. One of the solar corona images recorded on T-MAX 100 film is shown in Fig. 2. Note that the solar corona is imaged to at least 1.5 solar diameters, providing new information important to our understanding of the sun. It is expected that higher-quality images will be achieved at wavelengths greater than 4.0 nm with similar multilayer normal-incidence Cassegrain telescopes in the near future.

## Summary

The research and development results described above show that the potential of multilayer-reflecting optics is now being realized. Over a decade ago, when the first good x-ray and soft x-ray reflectivities were reported, new and improved optics and instruments based on multilayer structures were envisioned for the extreme ultraviolet, soft x ray, and x ray. These extrapolations were largely based on instrumentation characteristic of lower-energy regimes, and it was assumed that efficient, normal-incidence optics would be developed.

The field has now reached the stage at which this promise is being fulfilled, and new optics and instrumentation for these ranges are being developed. The most important technological result of our research is that the instruments have performed in a manner consistent with the standard analysis of geometric optics, indicating that the multilayer structures did not degrade their optic performance. Thus, neither the limits of spatial nor spectral resolution have been reached. It is, therefore, possible and appropriate to seek diffraction-limited performance from multilayer optic instrumentation in the soft x ray and extreme ultraviolet.

*This work was supported by Institutional Research & Development.*

## References

1. T. W. Barbee, Jr., *Opt. Eng.* **25**, 898 (1986).
2. A. E. Rosenbluth, *Revue Phys. Appl.* **23**, 1599 (1988).
3. T. W. Barbee, Jr., *Rev. Sci. Instrum.* **60**, 1588 (1989).
4. J. C. Rife, T. W. Barbee, Jr., W. R. Hunter, R. G. Cruddace, "Performance of a Tungsten/Carbon Multilayer Coated Blazed Grating from 80 to 1700 eV," *9th Int. Conf. Vacuum Ultraviolet Radiation Physics, 1989* (to be published in *Physica Scripta*).
5. R. G. Cruddace, T. W. Barbee, Jr., J. C. Rife, W. R. Hunter, "Measurements of the Normal Incidence X-ray Reflectance of a Molybdenum–Silicon Multilayer Deposited on a 2000 l/mm Grating," *9th Int. Conf. Vacuum Ultraviolet Radiation Physics, 1989* (to be published in *Physica Scripta*).
6. J. V. Bixler, T. W. Barbee, Jr., and D. D. Dietrich, *SPIE Proc.* **1160**, 648 (1989).
7. A. B. C. Walker, Jr., T. W. Barbee, Jr., R. B. Hoover, and J. F. Lindblom, *Science* **241**, 1781 (1988).

**Figure 2.**

**Photograph of the solar corona at 1,000,000°C, obtained with the normal-incidence, multilayer Cassegrain telescope.[7] The multilayers were molybdenum–silicon and were deposited using magnetron sputter-source, physical-vapor-deposition technology.[5]**

# Ultratrace Analysis of Explosive Residues

B. D. Andresen

***Analysis of explosives is an ongoing activity for many programs at LLNL. Not only are known explosives subjected to a variety of analytical techniques, but new synthetic explosives are analyzed, tested, and studied in great detail. In addition to methods for analyzing the parent explosive agents, methods are needed to analyze chemical binders, stabilizers, and impurities associated with explosives. We have designed a program to investigate new methods of explosive analysis.***

## Introduction

We* have initiated studies for detecting trace levels of explosives. A method is currently needed for analyzing environmental samples in order to identify explosives and their detonation residues that may be present only in complex mixtures at very low concentrations. The high sensitivity and specificity of analysis using computer-guided, gas-chromatography/mass-spectrometry (GC/MS) appears to make it a tool ideally suited for the identification of explosives. However, GC/MS alone was initially determined to be an analytical technique that is not readily amenable to thermally unstable and highly polar compounds.

All published methods of explosive analysis appear to center only on detection of the intact parent compound. These methods almost always ignore compounds very dissimilar to the parent explosive. In contrast, our approach has been to use unique derivatization schemes that make explosives and their residue products more amenable to GC/MS analysis. This new technique allows the simultaneous identification of very low levels of explosives, their detonation products, and other important compounds in complex mixtures, while utilizing the high sensitivity and unique analytical specificity of GC/MS.

**Figure 1.** Bottom trace: GC/MS total ionization plot of derivatized TATB. Upper trace: plot of only the molecular ion ($m/z$ 426) of the newly derivatized TATB compound (observed at 20.5 min; chromatographic conditions: 30-m, capillary, gas-chromatographic column; isothermal conditions: 70°C for 7 min, programmed to 300°C at a rate of 15°C/min).

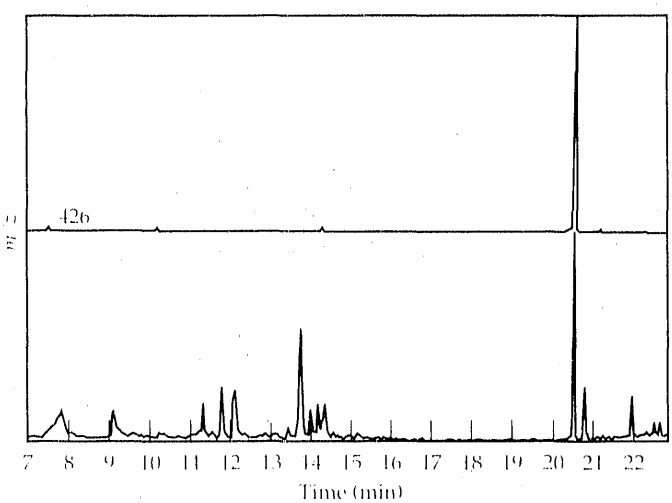


## Experimental Methods

Initial experiments with triaminotrinitrobenzene (TATB) support our preliminary hypothesis. This explosive cannot be easily identified using conventional chromatographic techniques.[1,2] Preliminary experiments have shown that a new derivatization procedure allows TATB to be analyzed using GC/MS. This process utilizes excess sodium dimethylsulfoxide (DMSO) as a combined solvent and strong base to remove the protons from the amino groups on TATB. The strongly basic solution is treated first with excess ethyl iodide and then with water, and the derivatized products are extracted into a suitable solvent. A microscale reaction, using only a few nanograms of material, appears to be complete in 15 min with mild heating.

The reaction seems to generate a nucleophilic TATB intermediate that reacts easily with ethyl iodide according to the following scheme:

$$R\text{–}NH_2 + Na\text{–}DMSO \rightarrow R\text{–}NH\text{–}Na^+ \quad , \tag{1}$$

$$R\text{–}NH\text{–}Na^+ + \text{ethyl–I} \rightarrow R\text{–}NH\text{–ethyl} \quad , \tag{2}$$

$$R\text{–}NH\text{–ethyl} \rightarrow R\text{–}N(\text{ethyl})_2 \quad . \tag{3}$$

We believe that the TATB molecule is fully derivatized by the addition of six ethyl groups. This may be due in part to the strong electron-withdrawing effects of three nitro groups symmetrically placed on the aromatic ring. This unique configuration allows the amino moieties to behave as weak acids.

Figure 1 shows analytical results of a 10-ng sample of TATB. The GC/MS total ionization plot (lower trace) reveals impurities and other compounds associated with the sample. The upper trace is a single mass plot that highlights only the new molecular ion (*m/z* 426) of the ethyl-derivatized TATB sample. The mass spectrum (Fig. 2) of the new TATB derivative reveals a characteristic fragmentation pattern and a unique and abundant molecular ion (base peak), which aids in trace-level measurements of TATB in complex environmental mixtures.

## Chemically Fingerprinting Explosive Residues

New techniques have also allowed us to chemically fingerprint trace levels of many common explosive residues. The experiments required the detonation of 300-g samples of pure explosives, collection of smoke and particles, isolation of trace levels of organic residues, derivatization, and GC/MS. The first phase of the work successfully identified unique fingerprint patterns associated with individual explosives. Figure 3 shows several GC/MS total ionization plots of explosives that will be useful for future work involving fingerprinting explosives in explosive residues and in environmental samples such as industrial waste, water, and air samples.[3]

We have also investigated a variety of derivatization schemes that appear to generate thermally stable compounds amenable to GC/MS and other types of chromatographic analysis. One of the important discoveries made during the course of this work was that major amounts of nonspecific explosive residues and side-reaction products were always present in the isolated explosive residues. This made identification of unique chemical fingerprint patterns difficult. It appeared that minor nitrogen-containing compounds associated with the explosive residues generated a more accurate fingerprint of the true parent explosive. However, these minor compounds are often completely obscured when major amounts of products derived from common plasticizers, binders, and moderators are present. A new nitrogen-specific analysis capable of providing additional fingerprinting data during GC/MS analyses is needed.

**Figure 2.** **Mass spectrum of the new derivative of TATB. A new molecular ion is seen at *m/z* 426, and a unique series of fragment ions that appears to be characteristic of TATB is observed. The fragment ion at *m/z* 380 appears to be the molecular ion minus one nitro group.**

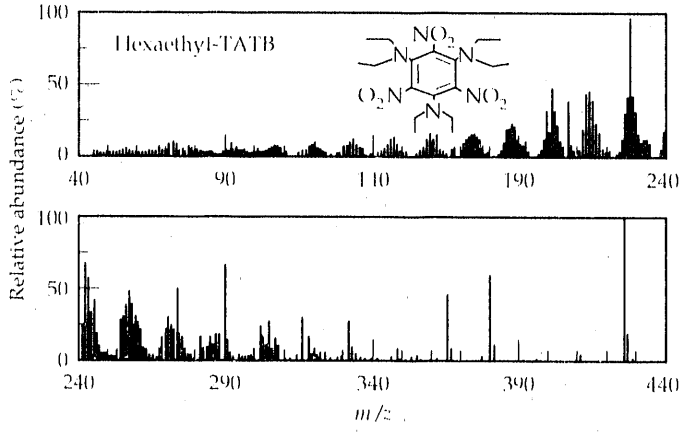


## Explosive-Residue Analyses Using GC/MS and Thermal-Energy Analysis

We are currently building new analytical capabilities using thermal-energy analysis (TEA).[4] The new TEA instrumentation will identify only nitrogen-containing chromatographic peaks during GC/MS analysis. The goal of this work has been to highlight more clearly the differences in the fingerprint patterns of nitrogen-containing compounds generated during analysis of trace levels of explosive residues.

During TEA analysis, nitrogen-containing gas-chromatographic components are pyrolyzed with oxygen at 700 to 850°C in a small furnace, which generates nitric oxides. Nitrogen gas is not pyrolyzed. The nitrosyl intermediates are immediately reacted with ozone. A gas-phase reaction generates chemiluminescence at 600 nm for each nitrogen-containing compound. Low-level light signals are easily measured with a high-gain photomultiplier assembly. Because all organic materials (including solvents) produce only $CO_2$ and $H_2O$ as pyrolysis products, the detection system is uniquely selective for those GC components that contained nitrogen.

**Figure 3.** **Total ionization plots generated from different explosive residues of smoke and particles. Each chemical fingerprint of explosive residue possesses characteristics that may be used to identify the parent explosive.**

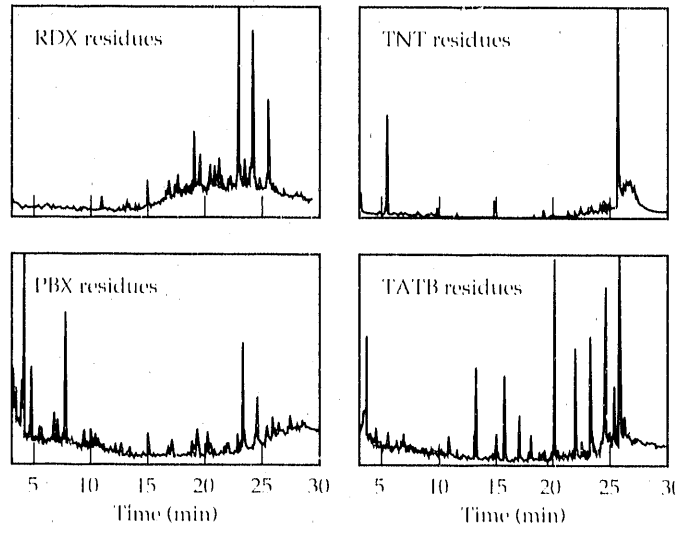

## Overview

The term "advanced materials" can be construed to include conventional materials whose performance has been significantly improved by a relatively minor alteration of structure or composition, or it can be limited to the designation of truly exotic substances. We confine ourselves to the latter definition here.

The reports in this section are divided almost equally between organic and inorganic substances, with particular emphasis on foams and gels. An ever increasing number of applications is being found for these materials. The number of journal articles dealing with them has more than doubled within the past year.

C&MS Department research also continues on the electronic and atomic structure of high-critical-temperature (high-$T_c$) superconductors. In addition to its inherent scientific value, this program makes another contribution to LLNL: it fosters considerable collaboration, which broadens the Laboratory's exposure to the academic community, sister laboratories, and industry.

Macroscopic superconducting properties are naturally a reflection of the underlying electronic makeup of each compound. In turn, the band structure is the product of this chemistry and the material's periodicity. Our research is aimed at unraveling the relations between these various factors. We report on determinations of the band structures of $La_2CuO_4$, $YBa_2Cu_3O_{7-\delta}$ (YBCO), and NiO made with angular correlation of positron annihilation radiation (ACPAR). The data show favorable agreement with our theoretical calculations based on simple molecular models.

It is well established that $T_c$ is a strong function of the oxygen stoichiometry of YBCO and the oxygen ordering. We made theoretical calculations of the energy of formation for the different allowable oxygen configurations while varying the oxygen concentration. Using such results, we computed the strengths of the critical pairwise interactions leading to an ab initio prediction of the phase diagram.

As stated above, one of the major research thrusts within the C&MS Department is the synthesis and characterization of gels and foams. Although most of this work is sponsored as Weapons Supporting Research, the materials are not considered to be classified. As a consequence, several unclassified uses have been identified for them, including uses as filters for the collection of cosmic dust outside the earth's atmosphere, insulation for homes and refrigerators, radiation detectors, chromatographic packings, adsorbents, acoustic couplers, frequency doublers for laser light, and many other applications. The densities of these materials are extremely low. For example, an $SiO_2$ aerogel has been produced with a density of 5 mg/cm$^3$, which is only about four times the density of the earth's atmosphere at sea level.

Aerogels can be made from either organic or inorganic reactants, and we pursue research within both categories. The organics have traditionally had a clear advantage when a foam of low atomic number is required. However, our recent development of a high-porosity LiH-$BeH_2$ foam with a density of 30 mg/cm$^3$ may challenge the preeminence of carbon-based foams for low-Z applications.

We also report on calculations related to planar flow driven by surface tension. This research is a theoretical adjunct to the experimental work being done on low-density materials.

The C&MS Department maintains both theoretical and experimental research in the field of fiber-reinforced composite materials. This year, our report deals only with theory and does not represent the entire program. The analysis described here generates quantitative criteria for the failure in shear of fibers and of the matrix. The goal of this research is to produce similar failure criteria that do not retain the artificial distinction between fibers and matrix, but account for the properties of the composite per se.

Section 2

# Advanced Materials

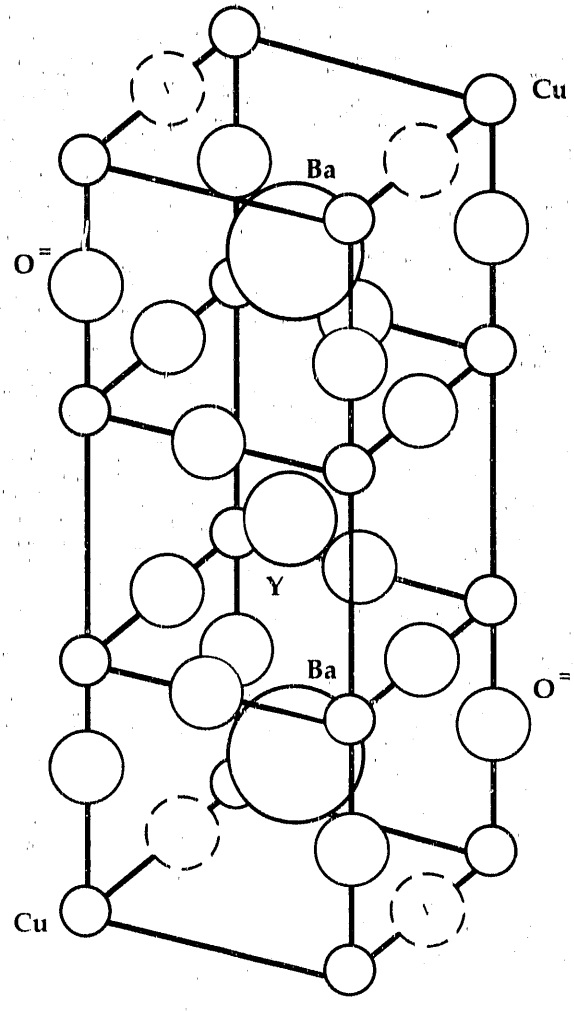


A high-$T_c$ superconducting compound

# Electron-Positron Momentum Distribution Measurements of High-$T_c$ Superconductors and Related Systems

A. L. Wachs,
P. E. A. Turchi,
R. H. Howell, Y. C. Jean,
M. J. Fluss, R. N. West,*
J. H. Kaiser,* S. Rayner,*
H. Haghighi,*
K. L. Merkle,†
A. Revcolevschi,‡
Z. Z. Wang§

***We have performed measurements of electron momentum density using two-dimensional angular correlation of positron annihilation radiation (ACPAR) in $La_2CuO_4$, $YBa_2Cu_3O_{7-\delta}$ (YBCO), and NiO. The data are compared with complementary theoretical calculations and with each other. We conclude that molecular-orbital features dominate the measured electron momentum densities.***

## Introduction

The positron-annihilation technique can be used to study the physics of the new high-$T_c$ superconductors. ACPAR techniques have been used to probe electron momentum densities. A consistent interpretation of the ACPAR results for high-$T_c$ and related systems is obtained from ACPAR measurements of high statistical quality performed on $La_2CuO_4$, YBCO, and NiO; our positron-lifetime studies; preliminary calculations of the positron wave function; and theoretical calculations based upon a linear combination of atomic orbitals/molecular orbital (LCAO/MO) model within the independent-particle model.

## Experiment

We performed measurements on single-crystal samples of $La_2CuO_4$, YBCO, and NiO at room temperature, and on NiO at 13 K. The sample-to-detector distance was 9.6 m for $La_2CuO_4$ and NiO, and the combined angular resolution of the detectors was 0.50 mrad; the corresponding values for YBCO were 11 m and 0.80 mrad. One milliradian corresponds to an electron-positron momentum of $10^{-3}$ $mc$, where $m$ is the electron rest mass. The $La_2CuO_4$ and NiO measurements consisted of 16 to 50 million counts, about $10^4$ counts in the peak channel, in a 256 × 256 square matrix with a bin width of (0.208 mrad)$^2$; for the YBCO measurements, a 128 × 128 square matrix was used with a bin width of (0.38 mrad)$^2$. Momentum integration directions were along high-symmetry sample crystalline axes (⟨100⟩ and ⟨110⟩).

The $La_2CuO_4$ and NiO samples have been described elsewhere.[1–4] The YBCO measurements were made upon an oriented mosaic of four crystals (~1 × 1 × .06 mm$^3$). Meissner-effect measurements of the crystals before and after the ACPAR experiments showed $T_c$ between 90 and 93 K, with $\Delta T \approx 0.5$ K. Positron annihilation lifetime measurements made upon these samples showed no evidence of defect trapping.[3,4]

## Results and Discussion

The ACPAR electron-positron momentum distributions were qualitatively similar for all the systems studied: highly isotropic with no statistically significant "Fermi breaks" due to partially filled band contributions. The highly isotropic nature of the distributions suggests a significant, perhaps 80 to 90%, "core state" contribution.[1–5] We have successfully modeled the small anisotropic valence-electron contribution to these distributions using an LCAO/MO formalism in conjunction with the independent-particle model. The positron wave function in a Bloch state with zero momentum is modeled using a variational procedure which formalistically takes into account the fairly localized electronic character of the material and also the relative affinity of the positron to the different chemical species.[1]

The statistically significant anisotropic components of the experimental distributions and their theoretical counterparts are in qualitative agreement. Their agreement illustrates the utility of this method for probing

selected details of the interatomic bonding in these systems. Figure 1 shows an example. The anisotropies in the experimental spectra reflect, in the main, the spatial distribution of the electron and positron charge densities rather than the fine details of the electronic band structure.

## Conclusions

Our ACPAR studies show that (1) positron-electron annihilations are dominated by nonconduction electrons in filled deep-lying bands, but that the details of the Cu-O MO bonding in high-$T_c$ materials and related systems can be observed, and (2) the contributions of the wave function of the probing positron to the ACPAR distributions are important and nontrivial. Such "positron wave-function" effects must be taken into account in future ACPAR studies. More annihilation events and higher-resolution ACPAR measurements are probably required to conclusively establish or refute the existence of a Fermi surface in YBCO using this technique.

*This work was supported by Weapons Supporting Research and Institutional Research & Development.*

[†]University of Texas, Arlington, Tex.
[‡]Argonne National Laboratory, Argonne, Ill.
[‖]University of Paris-Sud, Paris, France.
[§]Princeton University, Princeton, N. J.

## References

1. A. L. Wachs, P. E. A. Turchi, Y. C. Jean, K. H. Wetzler, R. H. Howell, and M. J. Fluss, *Phys. Rev. B* **38**, 913 (1988).
2. P. E. A. Turchi, A. L. Wachs, Y. C. Jean, R. H. Howell, K. H. Wetzler, and M. J. Fluss, *Physica C* **153–155**, 157–158 (1988).
3. P. E. A. Turchi, A. L. Wachs, K. H. Wetzler, Y. C. Jean, R. H. Howell, M. J. Fluss, J. H. Kaiser, and R. N. West, *J. Phys. CM* (in press).
4. A. L. Wachs, P. E. A. Turchi, R. H. Howell, Y. C. Jean, and M. J. Fluss, *Phys. Rev. B* **40**, 1 (1989).
5. H. Haghighi, J. H. Kaiser, S. Rayner, R. N. West, M. J. Fluss, R. H. Howell, P. E. A. Turchi, A. L. Wachs, Y. C. Jean, and Z. Z. Wang, *J. Phys. CM* (in press).

**Figure 1.** (a) Experimental, and (b) theoretical residual anisotropy surfaces for $YBa_2Cu_3O_7$. The momentum integration direction is the *c* axis. The values of $P_x$ and $P_y$ range between +21.8 mrad (a) and + 15 mrad (b).

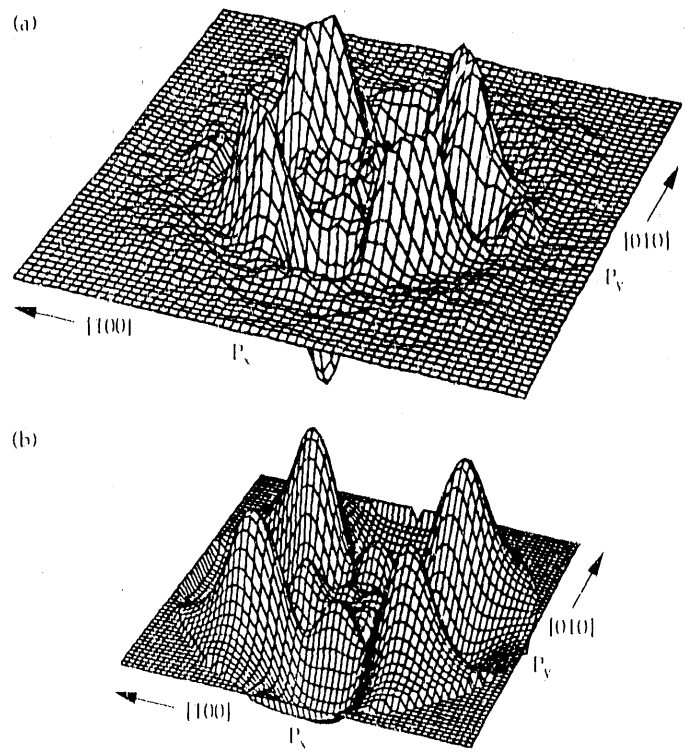

# Oxygen Ordering in $YBa_2Cu_3O_{7-y}$

P. A. Sterne and
L. T. Wille*

*We have performed first-principles total-energy calculations for $YBa_2Cu_3O_x$ with oxygen content x ranging from 6 to 7.5. The results of these calculations have been used to determine the effective pair interactions for the oxygen ordering in the basal plane. The phase diagram calculated with these "first-principles" pair interactions is in excellent agreement with experiment. The calculations also clearly indicate the thermodynamic stability of the double-cell phase.*

## Introduction

The high-temperature superconductor $YBa_2Cu_3O_7$ has an unusual crystal structure, with copper and oxygen atoms forming a copper-oxygen chain in the basal layer. The formation of these chains leads to a structural transition from tetragonal to orthorhombic symmetry which has been observed both in electron microscopy and neutron scattering.[1] The oxygen content of this layer can be varied from nearly zero to about one atom per unit cell by heating the material under varying oxygen partial pressures. By this means, the structure of the material with oxygen stoichiometry varying from the tetragonal $O_6$ phase to the orthorhombic $O_7$ phase can be studied. This simple experimental approach to mapping out the phase diagram is considerably complicated by the occurrence of many metastable phases, which leads to uncertainty in the true thermodynamic state of the system at a given temperature and oxygen concentration. Since a detailed knowledge of the phase diagram is potentially of great use in the manufacture of these superconductors, we have taken a theoretical approach to address the question of thermodynamic stability and to understand the physical origin of the oxygen-chain ordering in the basal plane.

**Figure 1.**

Diagram of the basal plane. Filled circles are copper atoms. Open circles are sites available to oxygen atoms. Half of these sites are occupied to form copper-oxygen chains for the $YBa_2Cu_3O_7$ superconductor. The pair interactions $V_1$, $V_2$, and $V_3$ are indicated.

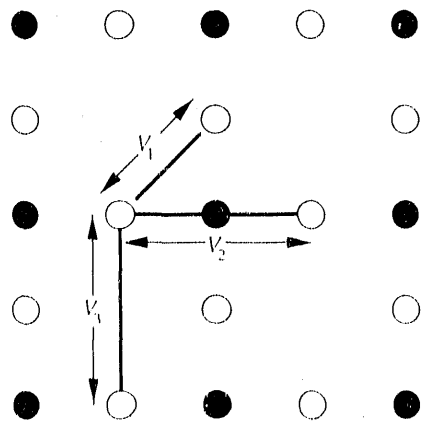


## Theoretical Model

Recently, de Fontaine, Wille, and co-workers have proposed a simple model to describe the oxygen ordering, casting the problem in the form of an equivalent Ising-like spin model.[2–4] The sites available to the oxygen atoms in the basal plane form a square lattice (Fig. 1). If there is an oxygen atom on a given site i, we assign that site a spin $\sigma_i = +1$, while a vacancy on site j is assigned a spin $\sigma_j = -1$. The Hamiltonian for this effective spin system can be written as:

$$H = \Sigma V_{ij}\sigma_i\sigma_j \quad , \qquad (1)$$

where the $V$s are effective pair interactions (EPIs) between the sites. It is assumed that these EPIs are sufficiently short-ranged so that only the first three $V$s are retained in Eq. (1): $V_1$, the interaction between neighboring sites; $V_2$, the next-neighbor interaction mediated by a copper atom; and $V_3$, the next-neighbor interaction with no intervening copper atom. This model can give a qualitative description of the phase diagram with an appropriate choice of parameters, but it provides no independent means of determining these $V_i$s, and alternative choices for the parameters can give qualitatively different phase diagrams.

## Calculations

The values of these parameters can be determined theoretically using the Connolly-Williams method.[5] In this approach, we compute the total energies of ordered structures containing different numbers and/or arrangements of oxygen atoms in the basal plane. We then equate the calculated total energy with the model total energy given in terms of $V_1$, $V_2$, and $V_3$ from Eq. (1), and once a sufficient number of structures are computed, we can solve the resulting set of simultaneous equations for the three interaction energies. The Linear Muffin Tin Orbital method has been used to perform the total-energy calculations. The entire unit cell is included in

these calculations since the total energy—and hence the stability of a structure—is affected by both the energy of the atoms in the basal plane and the interaction between these and all the other atoms in the system. Since the calculated total energies are of the order of 1000 Ry and the interaction parameters are only of order mRy, a great deal of care must be taken in determining these parameters.

The values obtained were

- $V_1 = 6.9$ mRy
- $V_2 = -2.4$ mRy
- $V_3 = 1.1$ mRy

$V_1$ is the largest of the parameters, and its positive sign indicates that the oxygen atoms do not tend to occupy nearest-neighbor sites. The negative $V_2$ term is the origin of the copper-oxygen chains; if an oxygen site on one side of a copper atom is occupied, the copper orbitals hybridize, making it more favorable to put an oxygen on the opposite side of the copper atom. The positive $V_3$ suggests a repulsion between the charge clouds of next-neighbor oxygen atoms that are not bonded through a copper atom.

The calculations immediately tell us that the double-cell phase,[1] with every second copper-oxygen chain missing, is thermodynamically stable. This is an important result, since it is very difficult to distinguish experimentally between a thermodynamically stable phase and a long-lived transient or metastable phase (cf diamond and graphite).

The phase diagram in Fig. 2 has been calculated from these parameters using the cluster variation method.[6] Agreement with experiment for the orthorhombic-to-tetragonal transition is excellent, considering that this is a first-principles calculation with no fitting to experiment. The double-cell phase, labeled Ortho II, is clearly seen around $O_{6.5}$, $y = 0.5$.

## Future Directions

The approach used here can be applied to address the question of thermodynamic stability for a whole range of related high-temperature superconductors. In particular, the $YBa_2Cu_4O_8$ and $Y_2Ba_4Cu_7O_{15}$ systems, which both have copper-oxygen chains, are potentially attractive for practical high-$T_c$ applications, because they tend to lose oxygen (and superconductivity) much less readily than the more common $YBa_2Cu_3O_7$. Phase separation into 1-2-3 and copper-oxygen is a problem, however, and a theoretical study of the thermodynamics of these systems could be very informative.

*This work was supported by Weapons Supporting Research and Institution Research & Development.*

[1]Physics Department, Florida Atlantic University, Boca Raton, Fla.

## References

1. R. Beyers and T. M. Shaw, *Solid State Phys.* **42**, 135 (1989).
2. D. de Fontaine, L. T. Wille, and S. C. Moss, *Phys. Rev. B* **36**, 5709 (1987).
3. L. T. Wille and D. de Fontaine, *Phys. Rev. B* **37**, 2227 (1988).
4. L. T. Wille, A. Berera, and D. de Fontaine, *Phys. Rev. Lett.* **60**, 1065 (1988).
5. J. W. D. Connolly and A. R. Williams, *Phys. Rev. B* **27**, 5169 (1983).
6. R. Kikuchi, *Phys. Rev.* **81**, 988 (1952).
7. Y. Kubo and H. Igarashi, *Phys. Rev. B* **39**, 725 (1989).
8. E. D. Specht et al., *Phys. Rev. B* **37**, 7246 (1988).

**Figure 2.**

**Phase diagram for $YBa_2Cu_3O_{7-y}$ calculated from the pair interactions derived from the total-energy calculations. The diamonds[7] and squares[8] are experimental data points.**

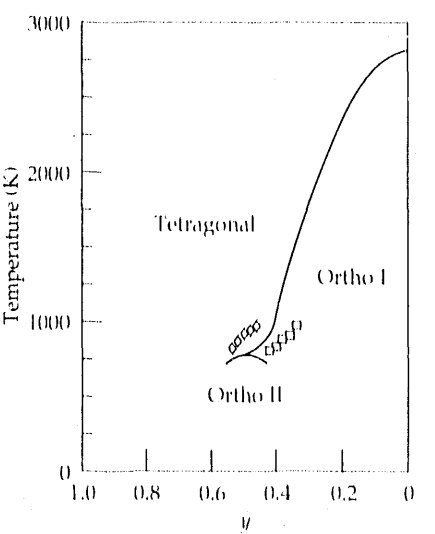

# Organic Aerogels

R. W. Pekala and F.-M. Kong

*The aqueous sol-gel polymerization of resorcinol with formaldehyde results in the formation of transparent gels that can be supercritically dried to form aerogels. These new low-density materials are the organic analogs of silica aerogels, with the advantage of having a lower average atomic number.*

## Introduction

Aerogels are a special class of foams that have an ultrafine cell/pore size (less than 1000 Å), high porosity (greater than 80 percent), and a microstructure composed of interconnected particles with characteristic dimensions less than 100 Å. This microstructure is responsible for the unusual thermal, optical, and acoustic properties of these materials.[1] In general, the hydrolysis and condensation of metal alkoxides, e.g., tetramethoxysilane and tetraisopropoxytitanate, has been the synthetic route for the production of inorganic gels, which are then supercritically dried to form aerogels.[2-4]

Although sol-gel chemistry has largely involved inorganic precursors, our research has focused on *organic* syntheses that proceed through a sol-gel transition and can be controlled to produce aerogels with varying properties. Potential applications for these low-density materials include thermal and phonic insulation, chromatographic packings, adsorbents, and catalyst supports.

**Figure 1.**

Transmission electron micrographs of RF aerogels synthesized at target densities of 0.05 g/cm$^3$ with two different catalyst concentrations. [Resorcinol]/[catalyst] ratios are (a) 50, and (b) 300. Note the larger particle sizes at the higher ratio.

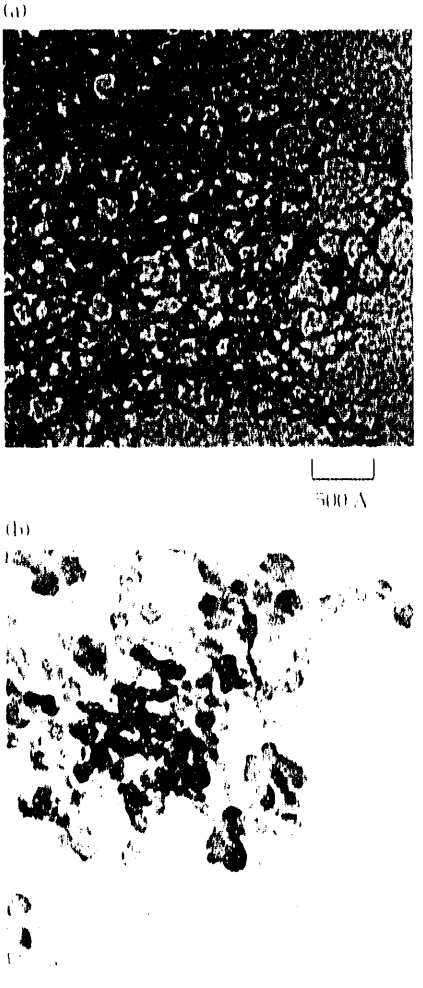


## Experimental Methods

Organic aerogels have been synthesized from the base-catalyzed aqueous reaction of resorcinol with formaldehyde.[5-7] In this reaction, resorcinol (1,3-dihydroxybenzene) serves as a trifunctional monomer capable of electrophilic aromatic substitution in the 2-, 4-, and/or 6-ring positions. This monomer is particularly reactive because of the electron-donating and ortho-para directing effects of the hydroxyl groups. The substituted resorcinol rings condense with each other to form polymeric clusters with diameters ranging from 30 to 175 Å. The resorcinol-formaldehyde (RF) clusters contain surface functional groups (e.g., $CH_2OH$) that lead to additional cross-linking and the formation of a transparent gel.

RF gels are supercritically dried using carbon dioxide ($T_c$ = 31 °C; $P_c$ = 1100 psi) to form organic aerogels. The RF aerogels are dark red and transparent, and have densities in the range of 0.03 to 0.30 g/cm$^3$. Their microstructure is similar to that of silica aerogels, yet their lower average atomic number offers many advantages in physics experiments.

Because RF aerogels are composed of a highly cross-linked aromatic polymer, they can be pyrolyzed in an inert atmosphere to form pure carbon aerogels. During the pyrolysis cycle, the aerogels undergo substantial shrinkage as gaseous by-products are evolved and the vitreous carbon matrix is formed. The carbon aerogels are black and opaque.

## Results and Discussion

The structure and properties of organic aerogels are largely controlled by the concentration of the catalyst (e.g., $Na_2CO_3$) used in the polymerization. The reaction must be conducted within a narrow initial pH window (6.0–7.5). Outside of this range, precipitates or opaque gels are generally formed.

The catalyst concentration affects the density, cell size, particle size, surface area, and modulus of the organic aerogels. At high catalyst concentrations, the clusters formed in solution are small and they cross-link into a fragile network that undergoes substantial shrinkage during supercritical drying. The resultant aerogel has a microstructure composed of interconnected 30-Å particles, a high surface area, and a final density about 80 percent higher than the target value. At low catalyst concentrations, the cross-linked network is composed of larger clusters that undergo much less shrinkage during supercritical drying. The resultant aerogel consists of interconnected particles with diameters of 170 Å, a lower surface area, and a density only 30 percent higher than the target value.

Figure 1 shows the microstructure of aerogels synthesized under the highest and lowest catalyst concentrations used in our research. In both cases, a network of interconnected particles is observed; however, the particle sizes are substantially different. By regulating the particle size, we can synthesize aerogels with surface areas varying over a wide range. Figure 2 shows the relationship between specific surface area and the [resorcinol]/[catalyst] ratio.

In order to improve the mechanical properties and thermal expansion coefficient of the aerogels, they are often carbonized. The carbonized aerogels exhibit a modulus about 15 times higher than that of the uncarbonized material at an equivalent density. The increased stiffness leads to improved machinability. In fact, carbonized aerogels are being machined into intricate shapes for inertial confinement fusion (ICF) applications. Figure 3 displays a carbonized aerogel machined into an ICF hemisphere.

## Summary

The polycondensation of resorcinol with formaldehyde under alkaline conditions follows a sol-gel pathway in which polymer clusters cross-link to form gels. These gels are then supercritically dried to form transparent organic aerogels. The structure and properties of these new materials are controlled through modifications of the polymerization conditions and/or heat treatment at high temperatures.

*This work was supported by Weapons Supporting Research and the Weapons Program.*

## References

1. J. Fricke, *Sci. Am.* **258**(5), 92 (1988).
2. S. J. Teichner, G. A. Nicolaon, M. A. Vicarini, and G. E. E. Gardes, *Adv. Coll. Interf. Sci.* **5**, 245 (1976).
3. D. W. Schaefer and K. D. Keefer, *Phys. Rev. Lett.* **56**(20), 2199 (1986).
4. *Aerogels*, J. Fricke, Ed. (Springer-Verlag, New York, 1986).
5. R. W. Pekala and F-M. Kong, *Revue De Physique Appliquée*, Colloque C4, Supplément au No. 4, Tome 24, C4-33 (1989).
6. R. W. Pekala and F-M. Kong, *Polym. Prpts.* **30**(1), 221 (1989).
7. R. W. Pekala and R. E. Stone, *Polym. Prpts.* **29**(1), 204 (1988).

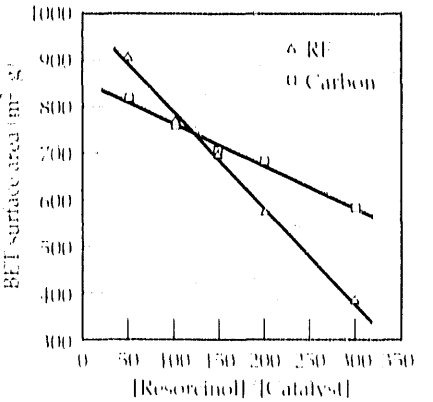


**Figure 2.**

BET surface areas of RF and carbon aerogels.

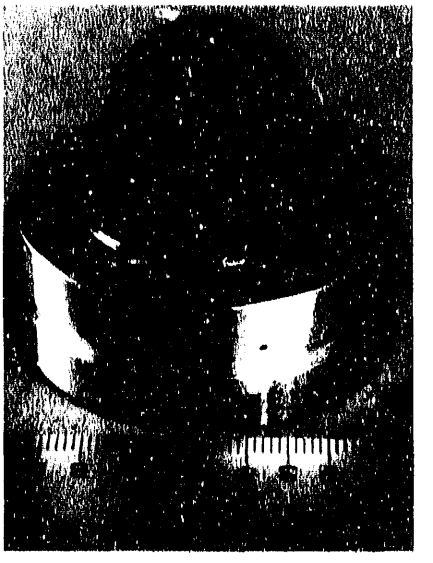

**Figure 3.**

A carbonized aerogel machined into a hemisphere for ICF target evaluation.

# Low-Density Polystyrene Foams from Inverse Emulsions

B. L. Haendler, R. C. Cook, S. A. Letts, and G. E. Overturf, III

***We have developed low-density polystyrene foams, synthesized from an inverse emulsion system, for use as direct-drive targets in laser inertial confinement fusion (ICF). These foams have cell sizes of 2 to 3 μm, can be made with densities as low as 30 mg/cm³, and have good wetting properties.***

## Introduction

Laser ICF is a promising approach to achieving a virtually inexhaustible supply of energy by recreating, through the power of the laser, the nuclear fusion process that goes on in the sun. The fuel for this process is a mixture of liquid deuterium and tritium (D-T) maintained in the liquid state at cryogenic temperatures (~20 K). For the fusion process to work, the liquid fuel must be held in a shape with near-perfect spherical symmetry, and there must be a container capable of holding it in this configuration.

A direct-drive target design that uses low-density polymer foams has been developed by Sacks and Darling[1] and is illustrated in Fig. 1. This foam is porous, or open-celled, and the liquid D-T should wet it and fill all empty spaces in order to maximize the amount of fuel per unit volume. Clearly, the lower the density of the foam, the better, but our density specification of 50 mg/cm³ means that 5% of the volume is foam and the remainder is D-T. To contain the D-T without leaking, the cell size has to be approximately 1 μm. The fusion process requires strict spherical symmetry; therefore, uniform density is a stringent requirement. Though the foam is of very low density, it has to be strong enough to be machined or molded.

A successful fusion process requires a foam with a low atomic number (Z). Carbon and hydrogen, which are the backbone of organic polymer materials, are prime candidates. An initial investigation revealed no suitable commercial polymers. We have developed a low-density polystyrene foam made by polymerization of an inverse emulsion system whose properties make it a good candidate for direct-drive laser ICF.

**Figure 1.** Use of a low-density, low-Z foam to define and stabilize the D-T shell allows an attractive single-shell, direct-drive target design. The foam saturated with liquid D-T provides both ablator and fuel. The D-T vapor in the capsule interior provides an ignition hot spot, and the capsule membrane provides a vapor barrier to prevent the D-T from boiling off.

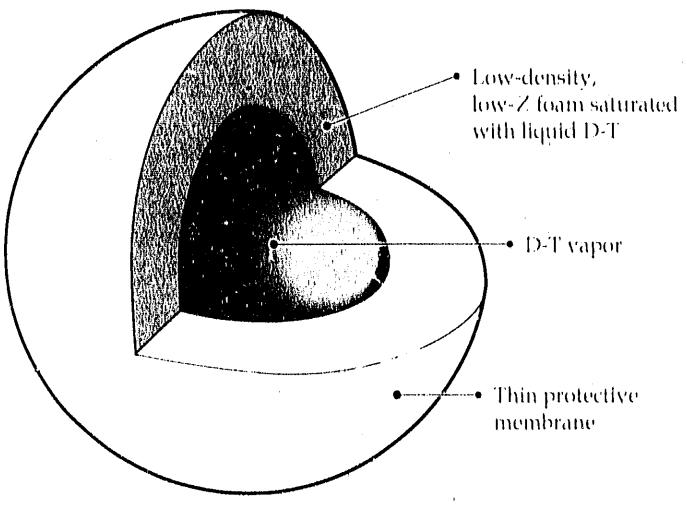


## Experimental Methods

An inverse emulsion[2–4] is a system like mayonnaise or cold cream, in which most of the material in the internal phase is in the form of droplets and the minor component is the external phase, which surrounds the droplets as a continuous and very thin interface. Two possible structures for these systems are shown in Fig. 2. The actual structure of the inverse emulsion used to make polystyrene foams is intermediate between these two cases, with some of the droplets being spherical and some polyhedral.

As shown in Fig. 2, the internal phase is water containing sodium persulfate ($Na_2S_2O_8$), and the external phase is an oil phase that is a mixture of two monomers, styrene and divinylbenzene (DVB), and an oil-soluble surfactant. The surfactant is sorbitan monooleate. The water phase constitutes 92 to 95% of the total material.

After mixing, the emulsion is heated to 50°C for 24 h, causing the $Na_2S_2O_8$ to initiate polymerization of the styrene and DVB. When polymerization is complete, all the thin interfacial regions have formed a solid

polystyrene material surrounding the water droplets. Oven-drying removes the water, producing a low-density (50–80 mg/cm$^3$) material. Further details on the procedures for making this system may be found in *Laser Program Annual Report 1985*.[5]

## Results and Discussion

Much of our early work with this system centered on finding the optimum formulation. As with most emulsion systems, the key to this process is the surfactant. The surfactant stabilizes the thin interfaces of the oil phase and keeps the system from coalescing into larger droplets or from breaking into separate phases. We have found that only sorbitan monooleate can accomplish this successfully, though the reasons for its uniqueness are still not completely understood.

Both theoretical and experimental studies have shown that the amount of sorbitan monooleate is also critical and that there is an interrelationship between cell size, density, and surfactant concentration. Lowering the cell size or the density requires more surfactant (to stabilize the oil phase) because it spreads more thinly as the cell size or density drops. Theoretical studies reveal a lower limit of approximately 2- to 3-μm cell size at the density that we require, where interfaces become too thin to maintain emulsion stability.

We have also investigated the effect of different mixing devices on the cell size of the emulsion. The most effective device is a development of ours, based on an idea from J. M. Williams of Los Alamos National Laboratory, called a syringe pump. The syringe pump mixes by forcing the emulsion back and forth between two syringes through a small orifice. We believe that the elongation of the droplets as they pass through the orifice causes them to break up into smaller ones, and the lack of high shear keeps the emulsion from breaking. This pump achieves the lower limit of 2- to 3-μm cell size.[6–8]

We have developed a process for extracting impurities from polystyrene foams without damaging the structure of the foams. Both the initiator and the surfactant leave decomposition products in the foam as undesirable impurities that contribute extra mass and increase the atomic number. X-ray diffraction studies of small crystallites observed by scanning electron microscopy have shown that the $Na_2S_2O_8$ decomposes into a mixture of $Na_2SO_4$ and $NaHSO_4$. These high-Z impurities interfere with the requirement of a uniform low-Z material. Studies by Fourier transform infrared spectroscopy have established that some surfactant remains as sorbitan monooleate, while some hydrolyzes to form oleic acid and sorbitol. We have developed an extraction apparatus that forces a mixture of isopropanol and water through the foams, removing virtually all of these impurities.

Our ability to remove the surfactant from the polystyrene foams led to an approach that was very successful in lowering foam density while maintaining the desired cell size. Increasing the amount of surfactant in the oil phase created more stable emulsions with less tendency to coalesce and form larger cells or voids. Removing this surfactant and its decomposition products after polymerization lowered the density even further. This approach eventually allowed us to achieve our target of 50 mg/cm$^3$. We could not lower the density past this point by this method, as there is an upper limit to how much surfactant can be incorporated into the oil phase without the undesirable development of closed cells.

Extending this idea, we tried incorporating ethylbenzene, which is the nonpolymerizable compound closest in structure to styrene, into the oil phase as a diluent. After polymerization, the same extraction procedure was found to remove the ethylbenzene, thus lowering the density still further. This process achieved a density of 30 mg/cm$^3$, which was the limit of this procedure, because the foam barely had enough mechanical strength to undergo the extraction process.

Figure 3 shows scanning electron micrographs of a foam with a density of 50 mg/cm$^3$ and a foam made using incorporation of ethylbenzene with a density of 30 mg/cm$^3$. An important feature of polystyrene foams from the standpoint of direct-drive laser ICF is that they are open-celled, with pores connecting the cells that are less than or equal to 1 μm in diameter. The open-celled structure of these foams leads to good D-T wetting properties. The size of the pores determines the wetting behavior.

**Figure 2.** **Two extremes of emulsion structure shown using spherical and polyhedral droplets. Geometric calculations show that spherical droplets must have a distribution of sizes, while polyhedral droplets can be uniform in size.**

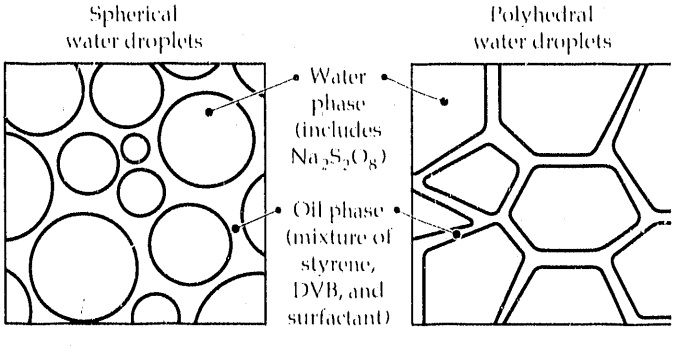

## Conclusions

Polystyrene foams are good candidates for direct-drive laser ICF. They have excellent machinability and are extremely easy to work with, and polystyrene is known to have good radiative stability. The D-T wetting behavior is quite satisfactory. The major disadvantage lies in the 2- to 3-μm cell size. Although it does not appear to degrade the wetting properties, it is virtually impossible to achieve the very fine surface finishes (~1 μm) that may be required.

*This work was supported by the ICF Program.*

## References

1. R. A. Sacks and D. H. Darling, "Direct Drive Cryogenic ICF Capsules Employing D-T Wetted Foam," *Nucl. Fusion* **27**, 447 (1987).
2. *Emulsion Process for Making Foams*, Unilever Research Laboratory, European Patent 60138 (Sept. 3, 1982).
3. J. M. Williams, "Toroidal Microstructures from Water-in-Oil Emulsions," *Langmuir* **4**, 44 (1988).
4. J. M. Williams and D. A. Wrobleski, "Spatial Distribution of the Phases in Water-in-Oil Emulsions. Open and Closed Microcellular Foams from Cross-Linked Polystyrene," *Langmuir* **4**, 656 (1988).
5. *Laser Program Annual Report 1985*, Lawrence Livermore National Laboratory, Livermore, Calif., UCRL-50021-85 (1986), pp. 3-18 to 3-21.
6. *Laser Program Annual Report 1986*, Lawrence Livermore National Laboratory, Livermore, Calif., UCRL-50021-86 (1987), pp. 5-2 to 5-11.
7. *Laser Program Annual Report 1987*, Lawrence Livermore National Laboratory, Livermore, Calif. UCRL-50021-87 (1988), pp. 4-1 to 4-34.
8. B. L. Haendler, L. M. Hair, and E-M. Kong, "The Application of Statistical Experimental Design to the Development of Low-Density Polymer Foams," *ACS Symp. Series 404, Computer Applications in Applied Polymer Science II: Automation, Modeling, and Simulation* (American Chemical Society, Washington, D.C., 1989), pp. 74–87.

**Figure 3.**

Scanning electron micrographs of polystyrene foams. Standard formula with a density of 50 mg/cm$^3$ is shown at (a) 500 ×, and (b) 10,000 ×. Ethylbenzene formula with a density of 30 mg/cm$^3$ is shown at (c) 500 ×, and (d) 15,000 ×.

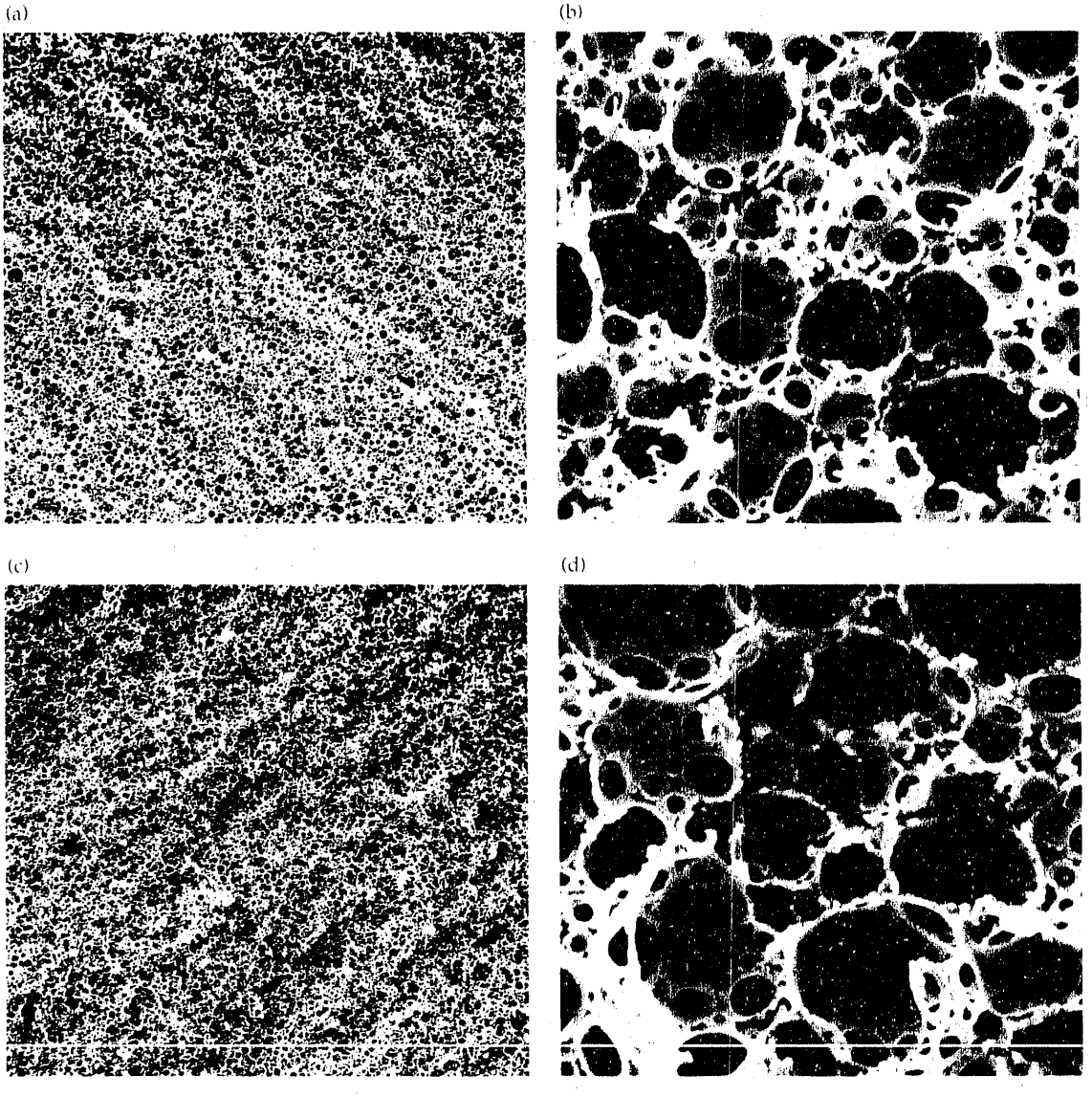

# Improvements in the Properties of Low-Density Carbon Foams

P. K. Shell and
S. S. Hulsey

*We have studied the fabrication of low-density foams made from pure carbon in order to improve several of their properties. Efforts this year have focused on improving homogeneity, reducing cell size, and studying the factors that affect surface properties, such as surface area and activation. Understanding these properties is important to improving the quality and performance of these foams. These studies will also increase our general understanding of the behavior of low-density carbon foams characterized by small cell sizes.*

## Introduction

The development of low-density foams is important for a variety of applications, such as catalytic supports, microporous membranes, and laser fusion targets. Carbon foams are potential candidates because they have many desirable characteristics, such as cell sizes ranging from several hundred angstroms to 35 μm, excellent machinability, and dimensional stability. The technique we use for making carbon foams is a replication process in which an inorganic substrate is infused with a carbonizable polymer.[1] After carbonization, the substrate is removed by leaching and the wet foam is dried. Foams prepared in this manner are referred to as replica carbon. The main problems in replica carbon studied at LLNL in 1988 and 1989 were homogeneity, effects of cell sizes on techniques used for drying wet foams, and surface properties.

## Experimental Methods

The homogeneity of replica carbon is affected by many factors, but perhaps the most important is the uniformity of the substrate used in preparation of the foam. In particular, particle segregation and agglomeration of the pore former are replicated as density gradients in the final foam. Proper preparation of the particles before pressing the substrates is necessary. We have been working with R&W Products of Auburn, Calif., to examine a variety of standard particle preparation techniques used by the ceramics industry to improve the homogeneity of compacts.

The raw substrate material, which is −400 mesh sodium chloride, was subjected to a variety of treatments in an attempt to improve its flowability prior to compaction. This included (1) mild sintering and ball-milling to increase the roundness of the salt grains, (2) dry blending with a variety of binders and lubricants, such as hydrophilic and hydrophobic polyethylene waxes and stearic acid, and (3) spray drying the substrate with a commercial binder, such as Dow Chemical Company's experimental ceramic binder XUS-40303.* Several substrates prepared from each of these treated powders and processed into foams using standard processing techniques[2] were evaluated radiographically for homogeneity.

It has long been thought that freeze drying or supercritical extraction were the only drying techniques that led to suitable cell sizes. We have found, however, that the water used to leach the salt substrate can be removed by soaking the particles alternately in isopropanol and Freon. After two such cycles, the particles are placed in a 40°C convection oven and allowed to air-dry overnight. This technique was repeated for foams of various densities (35 and 50 mg/cm$^3$) and cell sizes (average pore sizes of 3 and 12 μm). Nonuniform shrinkage and cracking of these foams were studied.

We characterized the surface properties of these highly porous, microcellular foams. Techniques that may reduce the surface area and degree of activation are of particular interest. Normally, the dry foams are heated in an inert atmosphere for 2 h at 1050°C in order to reduce the surface activation of the carbon. This treatment produces a foam with a typical surface area of 500 to 800 m$^2$/cm$^3$ that absorbs approximately 14 wt% water at ambient temperature and 55% relative humidity.

Experiments were performed to determine whether the surface area could be reduced by exposure to either higher temperatures or a reducing atmosphere during pyrolysis, or a combination of both. For the first test, two foams were each divided into halves, denoted A and B. The A halves were then heat-treated using the standard technique described above. One B half was heated at for 2 h at 1200°C in a pure argon atmosphere,

while the second B half was heated for 2 h at 1200°C in argon containing 5% hydrogen. The second test was performed by heating several foams for 1 h at 2200°C. Following heat treatment, the weight gain was determined after exposure to 55% humidity for several hours. The surface area of each sample was also determined by gas adsorption.

## Results and Discussion

**Homogeneity.** Neither sintering nor ball-milling the substrate powder proved to be of any value in eliminating localized inhomogeneities. Not only are both techniques too slow, but the tendency of the substrate powder to clump and agglomerate interferes with both techniques. Dry blending with various lubricants and binders was also unsuccessful, because dispersing the binders was difficult without agglomeration of the binder or the salt. Foams prepared by any of these techniques had inhomogeneities worse than those of the control samples.

Spray drying the salt appears to be the best method for minimizing segregation. During spray drying, individual substrate particles agglomerate into large (100 μm) prills. The size distribution of particles in a prill is approximately the same as that in the overall mix. Therefore, any prill segregation that occurs during compaction is irrelevant to the overall homogeneity. Furthermore, the prills do not clump or agglomerate prior to compaction but flow smoothly into the mold. Because the ceramic binder is burned out during sintering (the remaining residue is in the parts per million range), the substrate is basically identical to, though more uniform than, the standard, nonspray-dried substrates.

The yield of substrates during pressing is improved with spray-dried substrates. With untreated powder, substrates often delaminate and crack as they are released from the mold. Also, untreated salt often shows gross density gradients throughout the substrate, sometimes as large as 15%. Spray-dried powders seldom crack during compaction or show densities greater than 1%.

**Drying Techniques.** Foams with cell sizes greater than 3 μm survive air drying after solvent exchange with Freon. However, below foam densities of about 40 mg/cm$^3$ the parts warp or crack when dried with this technique. Parts of lower density must either be supercritically extracted for 2 to 3 days or freeze-dried for 7 days. Very low-density, replica carbon foams are unable to withstand the forces associated with air drying for any cell size examined to date.

**Surface Properties.** The heat treatment used to convert the activated carbon to a more glassy phase has a dramatic effect on the surface properties of these foams. Although the heating of the foam in an argon atmosphere at 1200°C had basically no effect on either surface area or water absorption, when 5% hydrogen was present, the resulting foam absorbed only 5% water as compared with the 14% absorbed by the control samples. There was no significant change in the surface area of this foam, indicating that water absorption probably depends on the presence of active sites that absorb water and that are destroyed in a reducing atmosphere. The part treated at 2200°C was also more inert, absorbing a negligible amount under the 55% relative humidity. The surface area of this part was reduced to 35 m$^2$/cm$^3$. X-ray diffraction indicated a small but definite presence of a graphitic phase in this sample.

## Conclusions

The quality of replica carbon foams does appear to improve with proper treatment of the substrate powder prior to compaction. In particular, spray drying with Dow's experimental ceramic binder, XUS-40303, provided foams with lower density gradients, fewer cracks, and fewer localized inhomogeneities than foams prepared from untreated salt. Spray drying was also preferable to sintering, ball milling, or dry blending other binders into the salt. The parameters used for spray drying the salt need to be optimized before the process is adopted for fabrication of high-quality, low-density carbon foams.

Although development of the faster drying technique involving exchange of leaching water with isopropanol and Freon makes a significant impact on the turnaround time in converting a substrate to a foam, it is limited to higher-density foams (>40 mg/cm$^3$). Also, this process requires the use of an environmentally sensitive chemical (Freon) and, thus, is unsuitable for further development.

Both surface area and activation of the carbon can be controlled by proper heat treatment of the foam. This fact is of interest in identifying potential applications for this material. However, unless a demand for more inert carbon foams is expressed, no further work is planned in this area.

*This work was supported by the Weapons Program.*

*XUS-40303 is a trademark of the Dow Chemical Company for poly(2-ethyl-2-oxazoline).

## References

1. R. W. Pekala and R. W. Hopper, "Low-Density Microcellular Carbon Foams," *J. Mater. Sci.* **22**, 1840 (1987).
2. P. K. Shell and S. S. Hulsey, *Technology Transfer Notes for Replica Carbon*, Lawrence Livermore National Laboratory, Livermore, Calif. (in press).

# Ultralow-Density Porous Glass

L. W. Hrubesh,
T. M. Tillotson, J. F. Poco,
W. E. Sunderland, and
J. D. LeMay

***We have developed methods for making silica "aerogel" monoliths over a range of densities from 0.02 to 0.6 g/cm$^3$ and have characterized their microstructures and measured their mechanical properties.***

## Introduction

We are developing porous silica glass by a sol-gel process to produce materials useful for numerous applications at LLNL. This porous glass material, called "aerogel" because it is mostly air, is commercially available in a limited range of densities. We have extended the range of densities from 99% void volume (~0.02 g/cm$^3$) to 73% void volume (~0.60 g/cm$^3$).

A large void volume, along with the extremely small pore and particle size in the glass, results in some very useful properties. For example, because it is made up mostly of air, aerogel is an excellent thermal insulator, yet it is almost as transparent as full-density glass. The silica solids are so finely distributed within the bulk material that it is especially homogeneous. The refractive index for aerogel is very near that of air; thus, aerogel can be used for applications requiring a minimum of reflection at the air/glass interface. Also, silica made by the sol-gel process is inherently pure and can be maintained as such when further processing converts it to full-density silica glass.

These and other properties have resulted in its use in such diverse applications as thermal-pane windows, Cerenkov radiation detectors, acoustic couplers, hypervelocity particle capture media, and catalyst substrates. Considerable research is in progress to understand the sol-gel-to-aerogel process and to study its extension to glasses other than silica.

Our main interest is the strength of aerogel at low density. We developed two methods that extend the density range to suit our needs: (1) controlled shrinkage to obtain higher densities, and (2) use of precondensed silica for both low and high densities.

## Experimental Methods

The common sol-gel process for making silica aerogel involves the hydrolysis reaction of silicon alkoxide compounds with water and the subsequent condensation reaction when the hydrolysis products polymerize. Either acidic or basic catalysts are added to stimulate the reactions. For example, for the commercial process[1] that uses the compound tetramethoxysilane (TMOS) and a basic catalyst ($NH_4OH$), the reactions are

$$Si(OCH_3)_4 + 4H_2O \xrightarrow{NH_4OH} Si(OH)_4 + 4CH_3OH \qquad \text{(Hydrolysis)}$$

$$Si(OH)_4 \xrightarrow{NH_4OH} SiO_2 + 2H_2O \qquad \text{(Condensation)}$$

Spheroidal macroparticles, grown from condensed silica, link to form a porous, skeletal microstructure surrounded by the alcohol solvent. Typical particle sizes range from 3 to 8 nm and void sizes from 30 to 100 nm. The gel is then typically dried in an autoclave by supercritical fluid extraction of the solvent, leaving a monolithic, air-filled aerogel. Supercritical fluid extraction is needed to prevent cracking caused by the large capillary forces that tend to collapse the gel's structure. The reaction rates for both the hydrolysis and condensation steps and the microstructure of the gel depend strongly on pH through the influence of the catalyst.[2,3]

The monolithic aerogels made are limited by stoichiometry to a maximum density of about 0.27 g/cm$^3$. Low densities, achieved by dilution with more solvent, are limited only by the long time needed for gelation of highly diluted solutions.

Our method for making aerogels with densities higher than the stoichiometric limit controls the shrinkage of the gel during extraction by varying the amount of basic catalyst used in the above reactions. The catalyst concentration affects the size of the primary silica particles and the strength of the bonds between them. We have found that the overall shrinkage from the wet gel to the aerogel is inversely related to the catalyst concentration. Thus, high aerogel densities (up to 0.60 g/cm$^3$) are achieved by including only very low concentrations of basic catalyst. Even though so little catalyst is used, gelation occurs within reasonable times (typically several days) because of the high concentration of TMOS.

We have determined an empirical formula that predicts the final density of the aerogel within a density range of 0.05 to 0.60 g/cm$^3$. Just two variables, the

number of moles of both TMOS and the catalyst, are needed to determine the density under conditions in which the water is in a constant ratio with regard to TMOS and the batch volume is constant. The relation is

$$D^{1/2} = 3.240 + 42.226T - 1.882CT + 0.036\,C^2 \quad ,$$

where $D$ is the aerogel bulk density in mg/cm$^3$, $T$ is the number of moles of TMOS, and $C$ is the number of micromoles of $NH_4OH$.

The density range is also extended by controlling the reactions to form a prehydrolyzed, partially condensed, stable sol that is subsequently processed to form a gel.[4] This condensed silica can be used as a precursor for either (1) high-density gels because it is a concentrated form of silica, or (2) low-density gels because it can be readily diluted, yet it is already partially condensed, so that the time to gel is rapid.

We make the condensed silica by using a substoichiometric amount of water and an acidic catalyst in the hydrolysis reaction, then removing all of the reaction-produced methanol by distillation. A nonalcohol solvent (e.g., acetone or ether) is added to the concentrated solution to prevent further condensation and gelation during storage.

## Results and Discussion

The microstructure of silica aerogels, resulting from controlled shrinkage through variations in basic catalyst concentrations, shows distinct particle-size differences. These differences can be seen in Fig. 1, which shows transmission electron micrographs of three aerogels with different densities. These were made using the same molar ratios of constituents (0.43 TMOS : 1.1 water : 0.5 methanol) but with different catalyst concentrations.

The average particle diameter obtained for each sample is shown in Table 1. Also shown are the results from two other types of measurements that confirm differences in the microstructures of the three aerogels. The surface area within the bulk material, as measured by nitrogen adsorption, correlates correctly with particle size. The quantity $Q^2$ is obtained from nuclear magnetic resonance spectra of dry, powdered aerogel and reflects the percentage of silicon atoms within the aerogel sample that have only two siloxane bonds. These are interpreted as silicon atoms in the neck between linked spheres. Thus, a higher $Q^2$ value suggests a higher degree of necking and a stronger, higher-density material. These measurements are all consistent with Keefer and Schaefer's theory[5] regarding the microstructure of base-catalyzed silica aerogel as a network-like

**Table 1.** Comparison of microstructural properties of aerogels made with different catalyst concentrations.

| Sample No. | $NH_4OH$ ($\mu M$) | Density (mg/cm$^3$) | Average particle diameter (nm) | Surface area (m$^2$/g) | $Q^2$ (%) |
|---|---|---|---|---|---|
| TT63-1-4 | 170 | 308 | 6.4 | 374 | 5.1 |
| TT64-4-10 | 120 | 330 | 5.3 | 520 | 5.8 |
| TT62-3-3 | 10 | 436 | 3.9 | 637 | 7.5 |

**Figure 1.** Transmission electron micrographs of three silica aerogels with different particle sizes. Left to right shows lower density/larger particle size to higher density/smaller particle size.

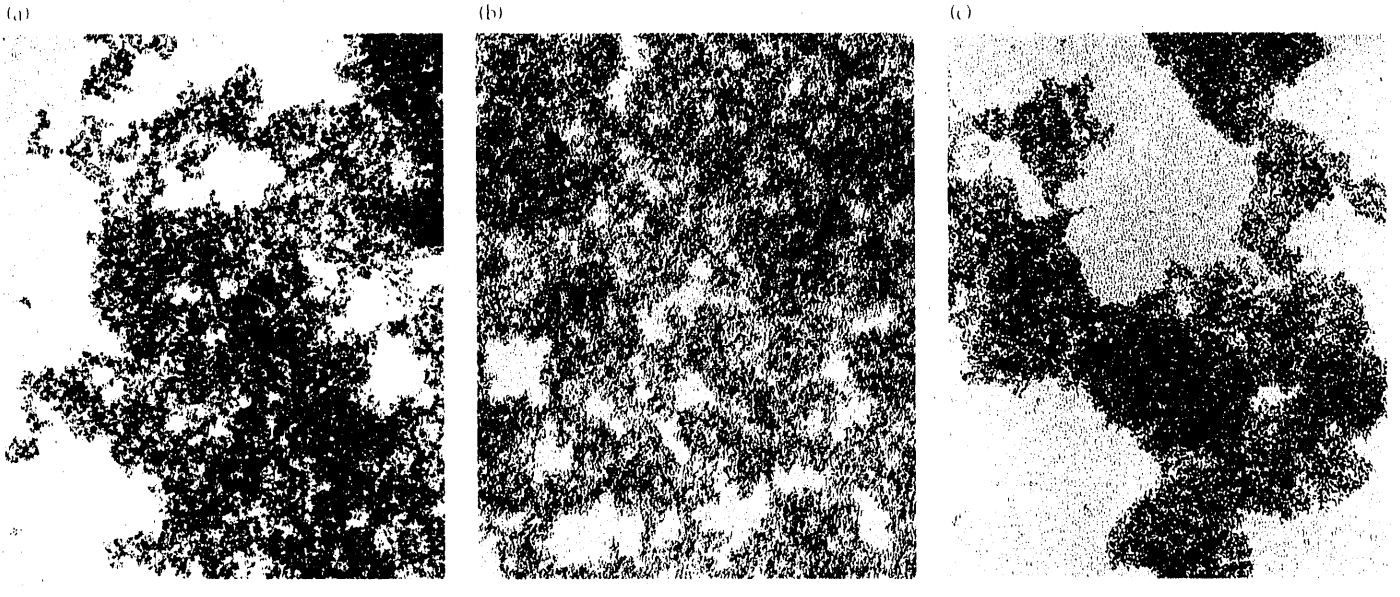

structure of compact colloidal particles whose strength is derived from the degree of cluster-monomer growth and cross-linking.

High-density aerogels made using the prehydrolyzed, partially condensed method show an even more highly compacted microstructure and are stronger than those obtained from one-step TMOS hydrolysis/condensation. Figure 2 shows the compressive modulus of both types of aerogels with respect to density. The factor-of-3 increase in modulus for the condensed silica aerogel is attributed to its more compacted microstructure. These data also show that the modulus of silica aerogel scales with nearly the fourth power of density, so that the strengths of the higher-density aerogels are more glass-like than foam-like.

We have successfully made aerogel foams with densities as low as 0.02 g/cm$^3$ using the condensed silica method. While the primary silica particle size in these aerogels is still less than 10 nm, the void size is several hundred nanometers, so that these aerogels are no longer optically transparent. A transition from transparent to opaque foam occurs for densities less than about 0.04 g/cm$^3$. These ultralow-density foams are typically highly elastic but very weak, having a modulus near only 10 psi.

## Conclusions

Two new methods can now be used routinely to make highly porous silica aerogel foams over an extended range of densities from 0.02 to 0.60 g/cm$^3$. An empirical formula derived from a statistical study of our process predicts the bulk density to within 5 percent of a target density in the range of 0.05 to 0.60 g/cm$^3$. Its use eliminates the iterative process formerly needed to produce specific densities.

The condensed-silica method has allowed us to make strong, high-density aerogels as well as highly transparent, ultralow-density aerogels. Variations of this method are being studied as a means of extending the range of available densities still further. The new materials made available by our work are in demand by those studying foam microstructures or the properties of these unusual materials and by those using aerogels in established or new applications.

*This work was supported by R Program and by NASA under interagency research contract agreements.*

## References

1. S. Henning and L. Svensson, *Phys. Scripta* **23**, 698 (1982).
2. R. K. Iler, *The Chemistry of Silica* (Wiley Interscience, New York, 1979).
3. D. W. Schaefer, *Science* **243**, 1023 (1989).
4. T. M. Tillotson, L. W. Hrubesh, and J. M. Thomas, *Mat. Res. Soc. Symp. Proc.* **121**, 685 (1988).
5. K. D. Keefer and D. W. Schaefer, *Phys. Rev. Lett.* **56**, 2376 (1986).

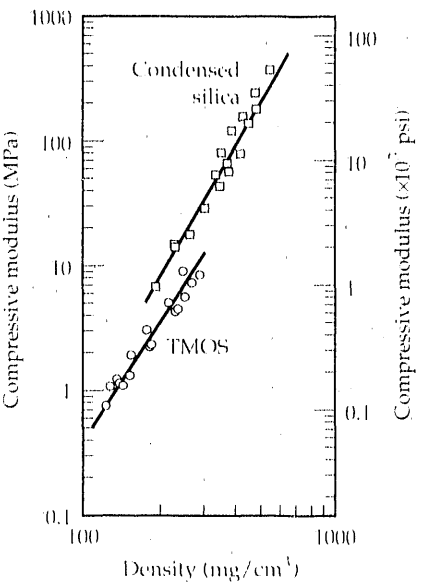


**Figure 2.**

**Compressive modulus for two types of silica aerogels.**

# Synthesis and Properties of a Low-Density, High-Porosity LiH-$BeH_2$ Foam

J. L. Maienschein and P. E. Barry

*We have developed a foam of low density and high porosity from LiH and amorphous $BeH_2$. This foam has applications as an x-ray scatterer in proposed space missions. The density of the foam ranges from 30 to 670 kg/m$^3$, and its porosity is as high as 97 percent. The pore-size distribution is centered on 400 nm for foams of 69 to 77 percent porosity, and on 4 μm for foams of 97 percent porosity. In addition, about 20 percent of the pores in the latter are larger than 130 μm. Hydrogen and organic compounds in the $BeH_2$ are evolved during the foaming reaction and apparently provide the force needed to expand the plastic reaction mass into a foam. The presence of $LiBeH_3$ as either a reaction intermediate or final product is suggested by the fact that the most vigorous foaming occurs with equimolar mixtures of LiH and $BeH_2$.*

## Introduction

We have developed a low-density solid foam made from LiH and amorphous $BeH_2$. The porosity can be varied from 0 to 96 percent, and densities are as low as 30 kg/m$^3$. This material is strong and machinable, even at 96 percent porosity, and it has a low $Z$ (<4). The combination of low density, high porosity, low atomic number, and high hydrogen content makes the foam attractive as an x-ray scattering material, e.g., in a Thomson-scattering polarimeter.[1] This article discusses the formation of the foam, physical properties such as porosity, density, and pore size, and our current understanding of the mechanism of foaming and the identity of reaction products.

## Formation of LiH-$BeH_2$ foams

The starting reagents are LiH powder from the Martin Marietta Y-12 plant, and $BeH_2$ powder (made in the 1960s by Ethyl Corporation). The LiH is typically 99.5 wt% polycrystalline LiH, with the major impurity being 0.3 wt% oxygen. The $BeH_2$ is amorphous, with a $BeH_2$ content of 90 to 96 wt%. Impurities in the $BeH_2$ include free beryllium metal (1–3 wt%), beryllium alkyls and alkoxides (2–3 wt%), beryllium chloride (0–0.2%), and beryllium oxide and hydroxide (0–2%) (Ref. 2). Both reagents are fine powders.

To make LiH-$BeH_2$ foam, we mix and grind the powdered reagents. The resulting powder is then pressed in a uniaxial compaction die with a hydraulic press at 393 K and 140 MPa for 15 min to form a pellet. In the final step, we heat the pellet to 478 K at 3 to 4 K/min, hold it at 478 K for 1 h, and cool it over 4 h. Foaming begins as the pellet reaches 443 to 453 K and is essentially complete at 473 K. The 1-h soak at 478 K allows complete reaction and thermal annealing of the foam.

Careful grinding of the mixed powders is required to optimize the foaming process. Three different methods of grinding and mixing were used: grinding by hand in a boron carbide mortar and pestle for several minutes; grinding 50-g batches in a Fritsch Pulverisette 5 planetary ball mill for 1 h; and grinding 2-g batches in a Spex Model 8000 ball mill for 1 h. The mean particle size of the ground powder produced by the various methods was 1 μm as measured by nitrogen adsorption analysis, but the foaming reaction products were quite different for the various methods. When material prepared in the mortar and pestle was used, the foaming reaction was incomplete, as shown by low porosity and nonuniformity of the product. Fritsch-milled reagents reacted to give a higher-porosity uniform foam. Spex-milled powders gave the highest-porosity foams. Thorough grinding probably removes a thin layer of nonreactive oxides and hence activates the powder for subsequent reaction.

## Density and Porosity

The porosity and density of the LiH-$BeH_2$ foam can be controlled either by varying the initial stoichiometry or by expanding the foam into a confining volume. We found that mixtures containing 50 to 55 mole % LiH and 50 to 45 mole % $BeH_2$ gave the most uniform foaming reaction and the highest-porosity foams. Equimolar composition maximizes the effect of the foaming reaction. To produce foams with a density less than 95 percent, we heated and expanded an equimolar pellet in a chamber that limits the expansion. In this way, we made foams with a porosity as low as 28 percent.

Foam porosity and density are related by:

$$P_{total} = 1 - \rho_{bulk}/\rho_{skeletal} \quad , \qquad (1)$$

where $\rho_{bulk}$ = bulk density of the foam (kg/m$^3$), $\rho_{skeletal}$ = density of fully dense LiH-$BeH_2$ (kg/m$^3$), and $P_{total}$ = total porosity, or fraction of the volume occupied by pores.

The skeletal density is calculated from:

$$\rho_{skeletal} = 700X_{LiH} + 640X_{BeH_2}\ (kg/m^3) \quad , \qquad (2)$$

where $X_{LiH}$ and $X_{BeH_2}$ are the mole fractions in the mixture, the density of $^6$LiH is 700 kg/m$^3$, and the density of amorphous $BeH_2$ is 640 kg/m$^3$ (Ref. 3). From Eq. (2), the skeletal density of equimolar LiH-$BeH_2$ is 670 kg/m$^3$.

Some fraction of the pores is completely sealed and not accessible to intruding fluids. Closed porosity is less than 5 percent when the total porosity is above 70 percent, but increases sharply at 60 to 70 percent porosity.

We determined the pore-size distribution using mercury porosimetry for foams of 69, 77, 87, and 97 percent porosity. With 69 to 77 percent porosity, the pore-size distribution is narrow and centered on 400 nm, comparable to the pore size in other submicrocellular foams (e.g., silica aerogel). With foams whose porosity is 87 percent, the pore-size distribution broadens and centers on 600 nm. At 97 percent porosity, the pore-size distribution is bimodal, with one broad maximum at 4 μm, and about 20 percent of the pores are too big to be detected by mercury porosimetry (>130 μm). Scanning electron photomicrographs verify the mercury porosimetry results; the large pores (>130 μm) are visible in high-porosity foams and are not present in lower-porosity foams.

## Physical Characteristics

The LiH-$BeH_2$ foam is a rigid gray material. It is physically robust, for even with 95 percent porosity it can be easily handled and machined in a standard lathe. Deviations in density in foam disks having a density of 130 kg/m$^3$ (diameter 50–150 mm, length 25–50 mm) are less than ±10 percent as calculated from digitized radiographs.

LiH-$BeH_2$ foams are moisture-sensitive and are generally handled in a glove box with a dry inert atmosphere. In the presence of moisture, the components form $Be(OH)_2$ (Ref. 4) and $Li_2CO_3$ (which we identified using x-ray crystallography), but the hydrolysis reaction is slow in moist air and negligible in dry air (<10 ppm $H_2O$). The foam can be handled in moist air for a few minutes and in dry air for many days without significant degradation.

The LiH-$BeH_2$ foam is typically about 95 wt% pure. The major impurities are beryllium metal (1–3 wt%), and carbon and oxygen (1–2 wt% each).

## Analysis of the Foaming Reaction

During visual observation of a foaming pellet, we saw bubbles blowing out of the expanding fluid mass. From mass-spectrometric analysis, the evolved gas was found to be primarily hydrogen with a few percent of organic compounds, chiefly $C_2H_6$. The mass loss during foaming, 0.5–1.0 percent, reflects the gas evolution that provides the force needed to blow the plastic mixture into a foam.

The porosity/stoichiometry data shown in Fig. 1 suggest that the compound $LiBeH_3$ may be involved as an intermediate or final product, since the foaming is strongest near equimolar mixtures. Synthesis of $LiBeH_3$ has been attempted by Bell and Coates[5] and by Ashby and Prasad,[6] but neither study provided definitive evidence of its existence. The compound $Li_2BeH_4$ was synthesized by both groups. However, if $Li_2BeH_4$ were involved in the foaming reaction, we would expect vigorous reaction at 67 mole % LiH, whereas Fig. 1 shows that the foaming is nearly stopped at this composition.

We do not fully understand the foaming reaction and have not identified the products. Our efforts are continuing in this area with differential thermal analysis/thermogravimetric analysis and with x-ray crystallography.

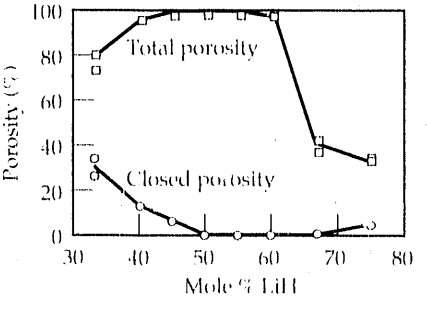


**Figure 1.**

**Stoichiometric dependence of porosity of freely expanded foams.**

## Summary

Foam is readily produced from LiH and $BeH_2$. The foam has a unique combination of low density, high porosity, low atomic number, and robust physical properties. We do not fully understand the mechanism of the foaming reaction, but it appears that the compound $LiBeH_3$ may be involved as an intermediate or final reaction product. We are continuing to develop this foam and are conducting basic studies into the foaming mechanism.

*This work was supported by the Weapons Program and by Weapons Supporting Research.*

## References

1. G. W. Fraser et al., "A Composite X-ray Polarimeter for XMM, Instrument Proposal in Response to ESA AO 5(C1 (88)1, June 1988. Part 1: Scientific and Technical Plan," University of Leicester, Leicester, England (January 1989).
2. R. W. Baker, G. J. Brendel, B. R. Lowrance, J. R. Mangham, E. M. Marlett, and L. H. Shepherd, Jr., *J. Organometallic Chem.* **159**, 123 (1978).
3. G. J. Brendel, E. M. Marlett, and L. M. Niebylski, *Inorg. Chem.* **17**, 3589 (1978).
4. J. C. Bailar, H. J. Emeleus, R. Nyholm, and A. F. Trotman-Dickenson, Eds., *Comprehensive Inorganic Chemistry* (Pergamon Press, Oxford, 1973).
5. N. A. Bell and G. E. Coates, *J. Chem. Soc. (A)*, 628 (1968).
6. E. C. Ashby and H. S. Prasad, *Inorg. Chem* **14**, 2869 (1975).

# Planar Stokes Flow Driven by Capillarity: Coalescence of Cylinders

R. W. Hopper

*This article describes a newly developed general theory of creeping viscous planar flow driven by surface tension on a free surface. The shape evolution is described in terms of a time-dependent mapping $z = \Omega(\zeta,t)$ of the unit circle, conformal on $|\zeta| \leq 1$. The time-dependent parameters of the mapping are determined by a general shape-evolution equation. The coalescence of two cylinders of arbitrary diameters is given as an example.*

## Introduction

We have been studying the evolution of microstructures of porous materials during sintering. These studies were done in connection with the precursors of certain low-density foams[1]. In the course of this work, a new mathematical theory of a special type of hydrodynamic problem was developed[2]: the shape evolution of a free simply-connected region undergoing planar Stokes flow (creeping viscous flow) driven solely by the surface tension. Such problems are fundamentally nonlinear because of the large changes in shape, and it is emphasized that no mathematical approximations are made. Besides providing insight into viscous sintering, the method has applications to the theory of glass strength[3] and to the technology of fiber-optic systems.

Physically, the region is regarded as the cross section of an infinitely long isothermal general cylinder of Newtonian viscous liquid having dynamic viscosity $\eta$, density $\rho$, and surface tension $\gamma$, in a gravitational field $\mathbf{g}$, all these being constants. The flow is planar; that is, the velocity vector is normal to, and independent of, the axial coordinate. A reduction to dimensionless form is chosen appropriate to a flow driven by surface tension. Let $R_0$ be a characteristic distance of the problem, and $\mathbf{x}_0$ and $t_0$ the position vector and time. Define dimensionless position $\mathbf{x}$ and time $t$ as $\mathbf{x} = \mathbf{x}_0/R_0$, $t = \gamma t_0/\eta R_0$. When the Suratman and Bond numbers ($\rho\gamma R_0/\eta^2$ and $\rho R_0^2 g/\gamma$) are small, inertial and gravitational effects are small in comparison with viscous and surface-tension forces, and the flow is governed by Stokes' equations: $\nabla^2\mathbf{u} = \nabla p$ (momentum), and $\nabla\cdot\mathbf{u} = 0$ (continuity). Ordinarily, the requirement of a small Bond number requires a small size, thereby assuring a small Suratman number. The planar-flow approximation holds for long cylinders constrained against flowing in the axial direction. If the ends of the cylinder are free, then capillarity induces, in addition to incidental flows near the ends, a general axial flow causing the body to shorten and its cross-sectional area to increase, but this is often unimportant[2,4].

## General Theory

The time-dependent shape of the region in the complex $z$ plane is described in terms of a time-dependent conformal mapping function in a parametric form, i.e., $z = \Omega(\zeta,t) = \Omega[\zeta; a_1(t), a_2(t), \ldots]$ on the fixed region $|\zeta| \leq 1$ of the complex $\zeta$ plane. In practice, the form of the mapping must first be guessed. The correctness of the map is verified, and the time dependence of the parameters determined, using a "shape-evolution equation." Its derivation proceeds along the following lines: The hydrodynamic problem is re-formulated in terms of the Kolosoff-Muskhelishvili equations of elasticity,[5] in which the stresses and velocities are determined by two analytic functions $\phi(\zeta)$ and $\psi(\zeta)$. A kinematic condition is obtained relating $\partial\Omega(\zeta,t)/\partial t$ to the surface velocities. This determines $\phi(\zeta)$ in terms of a Cauchy integral involving $\partial\Omega(\zeta,t)/\partial\zeta$. Simultaneously requiring that the surface stresses, which are implicit in $\Omega(\zeta,t)$, be correct then leads to a complicated nonlinear equation relating $\Omega(\sigma,t)$ to $\psi(\sigma,t)$ on $|\sigma| = 1$. This equation may be written:

$$\Omega'(\sigma,t)\,\psi(\sigma,t) = \frac{d}{d\sigma}\left[\sigma\Omega'(\sigma,t)\Omega(\sigma,t)^* I(\sigma,t)\right] - \frac{d}{dt}\left[\Omega'(\sigma,t)\Omega(\sigma,t)^*\right], \quad (1)$$

where an asterisk denotes the complex conjugate and $d/d\sigma$ denotes the directional derivative on $|\sigma| = 1$. The requirement is that $\psi(\sigma,t)$ be the boundary values of some function $\psi(\zeta,t)$ analytic on $|\zeta| \leq 1$; that is, that the function on the unit circle can be continued analytically onto the unit disk. The function $I(\zeta)$ is defined by the Cauchy integral:

$$I(\zeta) = \frac{1}{2\pi i}\int_{|\sigma|=1} \frac{1}{|\Omega'(\sigma,t)|}\,\frac{\sigma+\zeta}{\sigma(\sigma-\zeta)}\,d\sigma, \quad (2)$$

where the contour integral is taken around the unit circle, $|\sigma| = 1$. This formula defines a single function on $|\zeta| \le 1$, with the boundary values given by a Plemelj formula. Rather than solving Eq. (1) directly, the time dependence of $\Omega(\zeta,t)$ is adjusted to eliminate all singularities of $\psi(\zeta, t)$ on $|\zeta| \le 1$.

It has been inferred, but not proved, that the map describing any physically realizable flow of the type under consideration must be rational, and that if the initial shape is given by a mapping that is the ratio of an $M$th- to an $N$th-order polynomial, with $M \le N$ and having no common or repeated factors, then the shape at all subsequent times will be described by this same form.

## Coalescence of Cylinders

The shape evolution of two coalescing cylinders was determined. This example is a useful analogue of viscous sintering. The planar-flow approximation is excellent during the earlier stages of coalescence even if the ends of the cylinder are free.[2,4] Let the initial diameters of the cylinders be $D_1$ and $D_2$, with $D_1 \ge D_2$, and choose $D_2$ as the characteristic length ($R_0$). The dimensionless initial diameter of the smaller cylinder is now 1, and that of the larger one is $D = D_1/D_2$. The candidate map was constructed by applying a bilinear transformation to the family of inverse ellipse maps, which describe equal cylinders.[5] The degree of coalescence is specified by a time-dependent parameter $a$. Additional parameters, $b$ and $A$, are functions of $D$ and $a$. The map is given by:

$$\Omega(\zeta) = A\zeta\left(\frac{a}{1-a\zeta} + \frac{b}{1+b\zeta}\right) , \tag{3}$$

with

$$b = \left[1 + \left(\frac{1-a^2}{2aD}\right)^2\right]^{1/2} - \left(\frac{1-a^2}{2aD}\right) , \tag{4}$$

**Figure 1.** Coalescence of cylinders in planar flow driven by surface tension. Initial diameter ratio $D = D_1/D_2 = 2$; dimensionless times $t = \gamma t_0/\eta D_2 = 0.029$, 0.317, and 0.754.

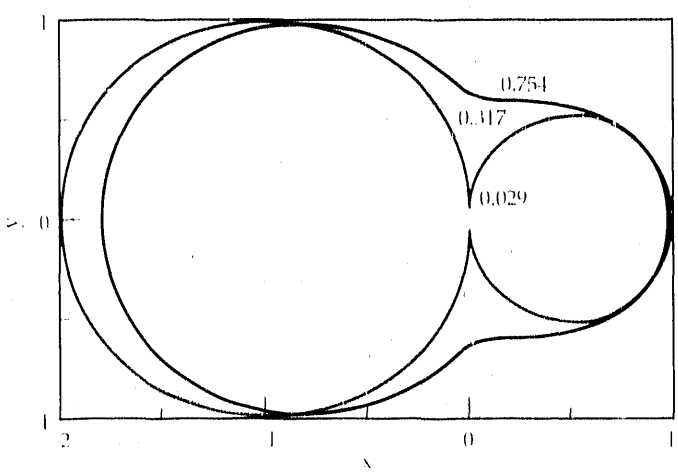


and

$$A = \frac{1}{2}\left[\left(\frac{a}{1-a^2}\right)^2 + \frac{2ab}{(1+D^2)(1+ab)^2}\right]^{1/2} , \tag{5}$$

The time is given by:

$$t(a_0) = \pi \int_{a_0}^{1} \frac{(a+b)A}{a(1-a^2)(1+b^2)K(ab)}\,da , \tag{6}$$

where $K(k)$ is the complete elliptic integral of the first kind defined by:

$$K(k) = \int_0^{\pi/2} (1 - k^2\sin^2\varphi)^{-1/2}\,d\varphi , \tag{7}$$

Thus $a(t = 0) = 1$ and $a(t = \infty) = 0$.

These equations give the shape evolution of coalescing cylinders. The result is mathematically exact, though subject to the physical approximations made. Their use requires no more than a programmable scientific calculator. Figure 1 shows the shapes at three values of time, when the initial diameter ratio is 2.

## Discussion

Exact solutions to moving free-boundary problems are rare in hydrodynamics, except for wave motions. That certain shapes should evolve so simply, when viewed as conformal maps, is suggestive of deep connections between geometry, mappings, and dynamics in this class of problems. The problems analyzed are rather restricted and special, in that the surface stresses are intrinsic in the geometry. It is desirable to extend the conformal mapping formalism to other capillarity-driven flows, such as doubly connected regions, extensional flows, and axisymmetric flows.

*This work was supported by Weapons Supporting Research and the Weapons Program.*

## References

1. R. W. Pekala and R. W. Hopper, "Low Density Microcellular Carbon Foams," *J. Mater. Sci.* **22**, 1840–1844 (1987).
2. R. W. Hopper, *Plane Stokes Flow Driven by Capillarity on a Free Surface*, Lawrence Livermore National Laboratory, Livermore, Calif., UCRL-101084 Rev. 1 (August 21, 1989). Submitted to *J. Fluid Mech.*
3. R. W. Hopper, "Crack Blunting by Viscous Flow," presented at the 90th Annual Meeting of the American Ceramic Society, Cincinnati, Ohio, May 1988.
4. L. G. Sills, Jr., *Coalescence of Glassy Fibers*, B.S. thesis, New York State College of Ceramics at Alfred University, Alfred, N.Y. (1986).
5. N. I. Muskhelishvili, *Some Basic Problems in the Mathematical Theory of Elasticity*, translated by J. R. M. Radok (P. Noordhoff, Gröningen, 1953).
6. R. W. Hopper, "Coalescence of Two Equal Cylinders—Exact Results for Creeping Viscous Plane Flow Driven by Capillarity," *J. Am. Ceram. Soc. (Comm.)* **67**, C262–264 (1984).

# Micromechanics of Fiber-Composite Materials

R. M. Christensen and
S. J. DeTeresa

*We have developed a new theoretical and experimental program to characterize the failure characteristics of high-performance fiber-composite materials. Through an examination of events occurring on the microscale, we have achieved a new understanding of the interaction of individual fibers with the surrounding matrix phase.*

## Introduction

The use of fiber-composite materials is expanding rapidly because of their extraordinary properties. For example, the usable strength of composites of Toray T1000 and Hitex 46-9A graphite fibers is in the neighborhood of 1.38 GPa, while bare filaments have tensile strengths of 6.9 GPa. Compare these values with that of high-performance aluminum (ALCAN 8090), which has an ultimate strength of about 0.517 GPa. Almost all high-technology applications place a premium on light weight. Dividing these strengths by the respective densities of the materials gives a specific strength of 0.86 $Mm^2/s^2$ for the composites and 0.19 $Mm^2/s^2$ for the high-performance aluminum. Other properties, such as specific modulus, show a similar advantage for composites. Comparisons with materials other than aluminum are even more favorable to the composites.

High-performance fibers for composite reinforcement are produced from all of the general classes of materials—metals, ceramics, glasses, and organics. Despite this diversity of materials, virtually all fibers are fabricated with a filament diameter of only 10 μm, about one-tenth the diameter of a human hair. For most materials, these tiny dimensions are required to achieve the mechanical properties required for composite applications.

Fiber selection is usually based on issues of performance and cost. Metal fibers are rarely used because they are too heavy. For high-temperature applications (>1000°C), fibers based on ceramics, such as silicon carbide, are invariably selected. Glass, normally considered a weak and brittle material, can be fabricated at relatively low cost into high-strength fibers. Organic fibers exhibiting tensile strengths greater than that of steel have been produced from both exotic liquid-crystalline polymers and more common plastics such as polyethylene.

By far, the fibers of choice for "high-technology" applications in the defense and aerospace industries are those based on graphite. More than 100 types of graphite fibers are now available, constituting a class of materials exhibiting some of the highest tensile strengths ($10^6$ psi) and the highest tensile moduli ($1.3 \times 10^8$ psi) ever measured for any structural material.

Composites are almost always used with a polymeric binder phase. If modern fibers in a polymeric matrix phase offer such desirable properties, would not the same fibers in a metallic or ceramic matrix phase be even better? Researchers are actively seeking to answer this question, but the answer appears to be no; polymer composites offer better performance except at temperatures above 300 to 400°C. The reasons are not completely understood, but they relate to the very complex microscale state of the interaction of the individual filament with its surrounding matrix and the different failure modes that are possible on this scale. A relatively compliant polymeric matrix phase provides a more harmonious balance of properties with those of the high-strength, high-stiffness fibers than do other candidate matrix materials. This observation introduces the area of research described here: the micromechanics of composite failure.

## Analysis and Experiments

Aligned fiber-matrix systems at the level of a lamina within a laminate have macroscopic properties characterized by a state of transversely isotropic symmetry, which corresponds to the hexagonal symmetry of crystallography. These laminates have five independent elastic properties, the moduli, whereas a completely isotropic material has two.

Our research program on micromechanics has concentrated on the microscale fiber-matrix interactions that contribute to the five macroscopic behavior properties. There are rigorous micromechanics analyses that predict macroscopic stiffness properties in terms of the properties of the individual fiber and the matrix phases themselves. The solutions for the five properties are quite complex except for the simplest one, which will

be given here to illustrate a fundamental effect. The axial or longitudinal shear modulus is that in the direction of the aligned fibers. The micromechanics solution for this property is given by:

$$\mu_l = \mu_m \left| \frac{\mu_f(1+c) + \mu_m(1-c)}{\mu_f(1-c) + \mu_m(1+c)} \right| , \qquad (1)$$

where $\mu_f$ and $\mu_m$ are the fiber and matrix shear moduli, respectively, and $c$ is the volume fraction of the fiber phase. Notice two limiting cases from this expression. As the matrix modulus vanishes ($\mu_m \to 0$), the composite modulus also vanishes ($\mu_l \to 0$). But as the fiber modulus becomes unbounded ($\mu_f \to \infty$), the composite modulus remains bounded ($\mu_l \to [(1+c)/(1-c)]\mu_m$). This composite behavior is obviously that of a matrix-dominated property. Of the five micromechanics properties, two are fiber dominated and three are matrix-dominated. This characteristic provides the key to a new methodology.

With the physical characteristic just described, we are able to derive the constitutive relation between stress, $\sigma_{ij}$, and strain, $\varepsilon_{ij}$:

$$\sigma_{ij} = \lambda\varepsilon_{kk}\delta_{ij} + 2\mu\varepsilon_{ij} + (E_{11} - E)\delta_{1i}\delta_{1j}\varepsilon_{11} , \qquad (2)$$

where $E_{11}$ is one of the fiber-dominated properties, with axis 1 in the fiber direction, and $\delta_{ij}$ is the Kronecker symbol. Properties $\lambda$, $\mu$, and $E$ are determined by the other fiber-dominated property and the matrix-dominated properties, but are most strongly determined by the matrix properties. This constitutive form provides the bridge to the derivation of the corresponding failure criteria, which forms are essential to all applications of composite materials.

The last term in the constitutive form represents the direct fiber contribution, while the other two terms are effectively matrix-dominated effects. The resulting failure criterion for the composite material retains the micromechanics-induced distinction between fiber- and matrix-dominated effects. In fact, the criterion degenerates into two criteria, one for fiber failure and one for matrix failure:

$$\varepsilon_1^{(-)} \le \varepsilon_{11} \le \varepsilon_1^{(+)} \qquad \text{(fiber failure)} , \qquad (3)$$

and

$$\alpha\varepsilon_{kk} + e_{ij}e_{ij} \le k^2 \qquad \text{(matrix failure)} , \qquad (4)$$

where $e_{ij}$ is the deviatoric strain tensor. The failure criteria are accessed with only the four failure parameters shown.

We compared our model description with experimental failure data for fiber-failure and matrix-failure conditions. The agreement is very satisfactory. From a materials perspective, however, it would be desirable to go one step further in our predictive capability to try to bridge the gap between constituent (fiber and matrix) properties and composite properties. Predicting ultimate strengths of composite structures on the basis of fiber and matrix properties is presently beyond our reach.

We are studying failure at the level of single fibers in order to further our understanding of the relation between micromechanics and macromechanics. In one approach, we are determining the properties of fibers that most strongly influence the ultimate strains for fiber-dominated composite failure. When a composite is stretched in the fiber direction, it fails when the fiber's tensile strength is exceeded. Failure by compression of the composite in the fiber direction is a much more complex process, involving several failure modes, including fiber-matrix debonding, fiber microbuckling, and fiber compressive failure. Clearly, the optimum composite compressive strength is achieved when fibers fail in compression rather than buckle or debond from the matrix.

To determine the inherent compressive strength of graphite fibers and thereby set the limit of compressive performance of a composite, we have recently developed a technique for monitoring compression of a single filament. We bond a single graphite fiber to the

**Figure 1.**

Morphology of axial compressive failure in a single Magnamite IM7 graphite fiber.

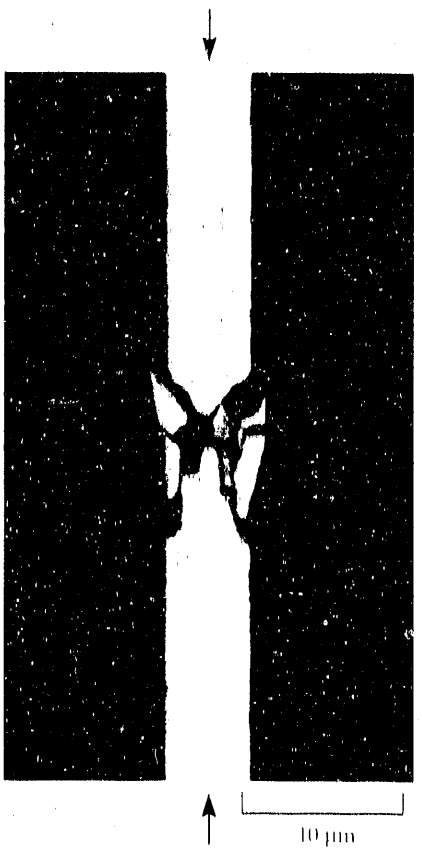

surface of a polymer compression specimen and use the fiber as a resistance strain gage. We can measure fiber compression up to failure. Fiber failure strains and failure morphologies vary among the different types of graphite fibers; an example of compressive failure in a high-strength fiber is shown in Fig. 1.

We are using this technique to study compressive failure in composites with many types of fibers. We are looking at fiber-fiber interaction and at such imperfections as voids and fiber waviness. Our preliminary results show that graphite-fiber compressive failure does not occur in real composites, and that imperfections and matrix properties play major roles in determining composite compressive strength.

## Summary

The demands placed on the performance of advanced polymer composites require a more fundamental level of understanding of material behavior than our current level. Technology has followed the natural progression of materials research down to finer levels of scale. The combined theoretical and experimental approach to the micromechanics of failure described here is only part of a comprehensive LLNL program that covers all aspects of composites technology, from synthesis and processing to field testing.

*This work was supported by the Department of Defense.*

## Overview

The C&MS Department provides research and development services in materials science and technology to meet the demands of all the major LLNL programs. In particular, we design and develop advanced materials for special—and frequently extremely harsh—operating conditions. We also test and characterize such materials to obtain the necessary parameters for weapons design codes. To meet these commitments, we maintain laboratory facilities that fulfill nearly all of the requirements of modern metallurgical and ceramic applied research and development. These capabilities include arc, induction, and resistance furnaces for melting and heat treating in a variety of atmospheres, and facilities for hot pressing, sintering, grinding and milling, and sputtering and vapor deposition. We also perform mechanical testing of specimens in a variety of ways and environments.

Research and development is carried out primarily in the following general areas: physical metallurgy, joining, forming and processing, metallography, ceramics and glass technology, cermets, polymer composites, coatings and surface modification, and corrosion and compatibility. We also perform analytical and materials characterization functions. In addition, C&MS administers and operates a facility devoted exclusively to research on plutonium and uranium. Future capabilities will include a 4-MeV ion accelerator, which will be on-line in the coming year and used for materials-modification studies.

The study of phase transformations is a very important aspect of physical metallurgy. Tailoring alloys to specific applications usually requires an understanding of the effects of impurities, microstructure, and heat treatment on the transformations leading to the desired product. We have shown that the premartensitic tweed structure results from small inhomogeneous strain fields and is a precursor to the actual nucleation sites for martensite. The premartensitic structure is correlated with a change in the vibrational spectrum as established by neutron diffraction. It is worth noting that the diffusionless martenistic transformation is the basis for our most important alloy, steel.

During the past year, mechanical-properties experiments included the investigation of ultrahigh strain rates in both copper and tantalum. We used a relatively new technique in which a freely expanding ring of the substance under investigation is the secondary winding of a transformer. The primary solenoid is pulsed by a capacitor bank to initiate the expansion. This technique was used to determine fracture behavior including strength, ductility, and fragmentation at ultrahigh strain rates with controlled heating.

In other research, we investigated the extended ductility of pure aluminum deformed to ultralarge strains. These strains are far greater than those accounted for by superplasticity, and a new mechanism, geometric-dynamic recrystallization, is proposed to explain this extreme ductility. According to this scheme, small crystallites form during the deformation as a consequence of the large increase in high-angle boundary area, and they account for the enhanced ductility.

Theoretical studies are pursued on a variety of topics, and our theoretical and computational program has been selected by the C&MS Department for enhanced future growth. Here we report results of phase-stability calculations of ordered vs disordered states using several theoretical approaches.

In other work, the superplastic properties of ultrahigh-carbon steels were studied and improved. Compositional modifications were discovered that slow the rate of carbon precipitation during cooling, and subsequent warm rolling establishes the superplastic microstructure.

As the fabrication of most metal objects begins with the metal in the molten state, we find it important to study the process of solidification. Rapid solidification of stainless steels of varying composition was studied by electron-beam melting of the surface, leading to very rapid cooling. Precipitate compositions and microstructures were recorded as a function of cooling rate.

A computational model combining mass, momentum, and heat transfer has revealed a way of possibly improving an electron-beam vaporizer. This research serves to illustrate the application of modern mathematical analysis to current engineering processes, a widespread service rendered by the C&MS Department.

Modeling the complex fracture mode of fiber-wound polymer composites aided in designing unique structures. The successful application of this technology for a compressively loaded component was predicted by the model and confirmed by tests. In addition, improved modeling of the molecular processes that occur during curing of the composite matrix material led to a better understanding of the influence of processing on the resultant properties.

Advancements in ceramic processing and fabrication continue to find applications, particularly for $B_4C$ structures. Defense and commercial industrial applications are being developed.

The use of physical vapor deposition (PVD) technology in creating engineered nanometer-scale structures has led to improved resolution and advances in the efficiency of x-ray optics.

Section 3

# Metallurgical Science and Technology

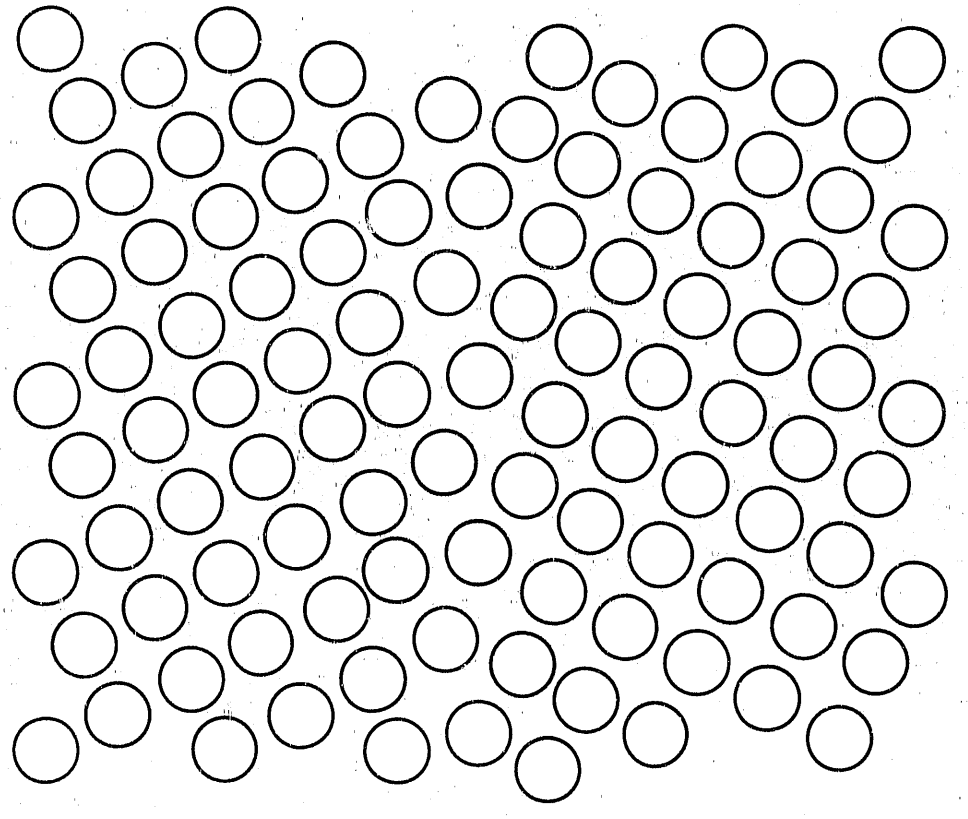

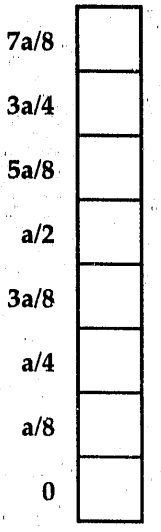


Simulation of the atomic arrangement of a grain boundary

# Studies of Premartensitic Behavior in the Nickel-Aluminum Beta Phase

L. E. Tanner

*Our high-resolution electron microscopy and neutron-scattering studies have shown, for the first time, a direct relationship between the evolution of premartensitic microstructures and the anomalous lattice dynamics of the ordered nickel-aluminum beta phase. These studies have also shown that martensite nucleation is a localized heterogeneous process at special defect sites within this premartensitically modulated lattice.*

## Introduction

Phase transformations are of great interest to materials technologists because they are a remarkably effective means of controlling structure-sensitive properties of metallic alloys and ceramics.[1] We understand diffusional transformations, where material "moves" as atoms rearrange themselves on sites throughout the crystal lattice, but not diffusionless displacive transformation behavior, in which a solid undergoes cooperative atomic shifts without lattice site interchange. We must gain an understanding of displacive transformations in order to better optimize material properties.

The most common displacive structural changes are the martensitic shear transformations that occur in steels and in a wide variety of other metallic alloys and ceramics. It is now well established that the crystalline phases that undergo first-order martensitic transformations upon cooling show unusual changes as they approach their transformation temperature, $M_s$.[2] We are examining these precursor effects within the parent phases for the light they shed on the crystal symmetry-lowering transformation process itself. Prominent among these effects are tweed-like striations in transmission electron microscopy (TEM) images[3]; these striations are derived from local lattice distortions that develop well above the transformation temperature and become more pronounced with cooling. In addition, there is an anomalous anisotropic "softening" of the parent lattice[2]; that is, certain elastic constants and lattice vibrational modes are unusually low and decrease further with falling temperature.

**Figure 1.**

Images of premartensitic nickel-aluminum alloy. (a) CTEM image, and (b) electron diffraction pattern.

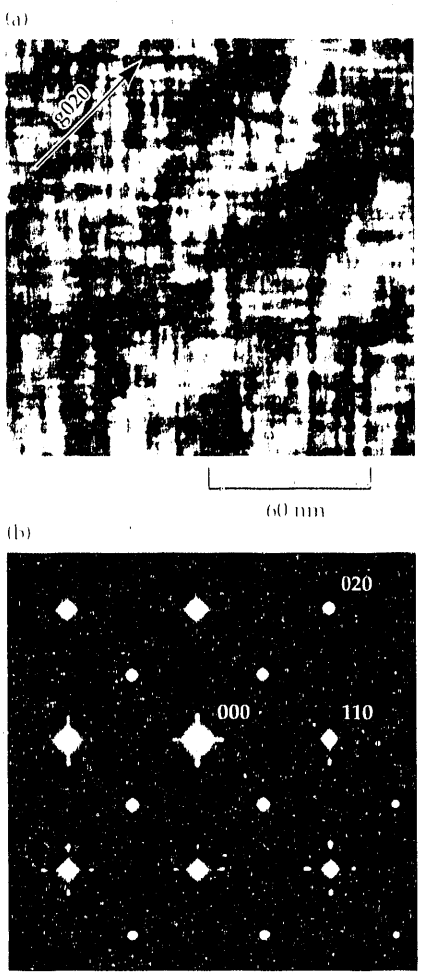


## Experimental Procedure

We have been studying the metallic alloys $Ni_xAl_{100-x}$ ($50 < x < 65$), some of which display the premartensitic effects rather prominently.[4–6] Examination of samples from high-purity single crystals using conventional contrast TEM (CTEM), high-resolution TEM (HREM), and electron diffraction in conjunction with elastic and inelastic neutron scattering reveal microstructural evolution and lattice dynamical variations over a range of temperatures down to $M_s$, which is usually below room temperature. The HREM studies were carried out at the

National Center for Electron Microscopy at the Lawrence Berkeley Laboratory. Neutron-scattering experiments were carried out at Brookhaven National Laboratory in collaboration with S. M. Shapiro and co-workers.

## Results and Discussion

The CTEM images display the quasi-periodic tweed strain contrast [Fig. 1(a)]; electron diffraction reveals a related diffuse scattering—both streaks and satellites—in the vicinity of parent-phase Bragg reflections [Fig. 1(b)]. Contrast amplitude increases and striations become more sharply defined as $M_s$ is approached. The diffuse scattering intensities also increase.

Using HREM, we can see the distorted atomic configurations that underlie the tweed contrast. The microstructure is a fine-scale mosaic assembly of variously distorted and modulated domains of fractional nanometer-scale atomic displacements [Fig. 2(a)]. Images of the unstrained lattice of this ordered cubic parent phase must be calculated [since the unstrained lattice cannot be retained from elevated temperatures; see Fig. 2(c)]. With proper choice of imaging conditions for the crystal orientation of interest, we simulate a square pattern of repeating white dots that is directly related to the projected columns of atoms of either all-nickel or the mixed nickel-aluminum sublattices of this body-centered structure [see Fig. 2(c)].

Comparison of the observed and ideal unstrained patterns provides insight into the local atomic movements.[6] Within the contiguous domains 4 to 6 nm in extent, we find an inhomogeneous micromodulated substructure. Each three-dimensional domain should contain one of six possible variations of the micromodulation, where only two, roughly parallel to the traces of $(\bar{1}10)$ and $(1\bar{1}0)$ lattice planes, would be visible in this (001) viewing plane. The modulation involves 6 to 7 lattice planes with a wavelength of about 1.3 nm and is derived from a sinusoidal displacement wave ("shuffle") superimposed on a homogeneous lattice shear of the form $\{110\}\langle\bar{1}10\rangle$, as shown schematically in Fig. 2(d). A simulation of this distortional pattern can also be made [Fig. 2(b)], and it is in quite good agreement with our observed images.

Shapiro et al.[4,6] used elastic neutron scattering to investigate the functional characteristics of this quasi-static microstructural assembly, and inelastic scattering to probe the lattice vibrational or phonon spectra associated with its development. The latter reveals remarkably anomalous behavior for the $\Sigma_4[\zeta\zeta 0]$ transverse acoustic mode corresponding to displacements of the $\{110\}\langle\bar{1}10\rangle$ type mentioned above. The entire phonon branch is of extremely low energy and exhibits an unusual dip in frequency at the wave vector $\zeta \approx 0.16$, which deepens further with cooling as $M_s$ is approached. The position $\zeta \approx 0.16$ along the $\langle 110\rangle$ direction in reciprocal space corresponds to the location of the diffuse satellites that we observe in the diffraction patterns. Satellites flanking Bragg reflections are the signature of a structural modulation and, indeed, their distance from the Bragg peaks is inversely proportional to the micromodulation wavelength in the real-space HREM images.[6]

The evolution of the premartensitic microstructure and its role in the martensitic transformation are understood as follows. As the alloy cools, distortional fluctuations related to the softened phonon modes "freeze out" in the strain fields of lattice defects having appropriate transformation geometry. The most numerous of these are associated with centers of low strain amplitude arising from atomic size differences, point defects, impurities, etc., and result in the tweed domain substructure. The remaining defect sites (e.g., structural interfaces and dislocation tangles) have significantly higher associated strain amplitudes, and the distortions in these regions approach the critical strain required for

**Figure 2.** Images of premartensitic nickel-aluminum alloy. (a) HREM image, (b) computed strained or micromodulated pattern, (c) relation of the sublattices and computed unstrained pattern, and (d) model of the premartensitic micromodulation.

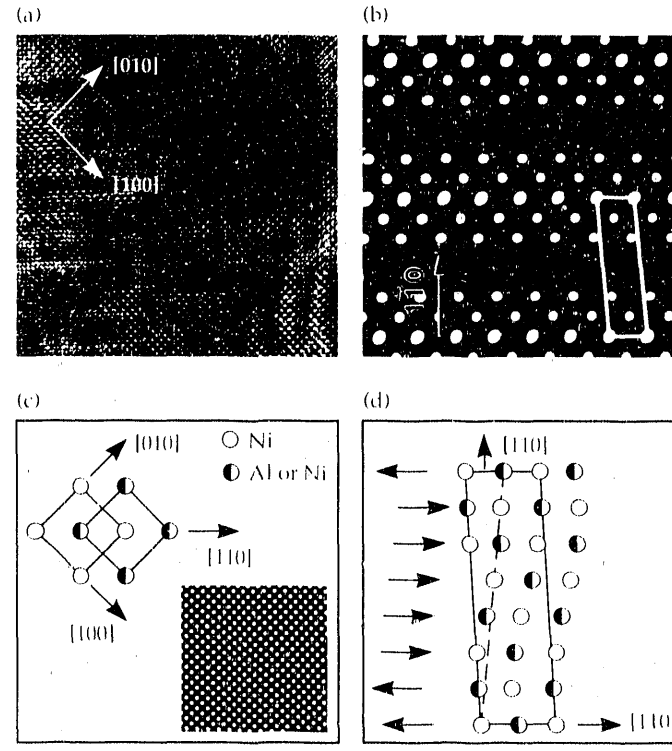

transformation. Consequently, these become favored sites (the strain embryos) for heterogeneous nucleation of the martensitic product phase at $M_s$. In the nickel-aluminum alloy $\beta_2$ phase, we find that the amplitudes of the $\{110\}\langle 1\bar{1}0\rangle$ shears and shuffles are increased at the heterogeneous sites to form nuclei of the 7-lattice plane, 1.4-nm-periodicity orthorhombic martensite.[6]

## Conclusions

With these experimental observations, we have established for the first time a direct relationship between the evolution of the premartensitic microstructure and the anomalous lattice dynamical behavior of the parent phase. Furthermore, we have shown that martensite nucleation is a localized heterogeneous process at special defect sites within this premartensitically modulated lattice. On the basis of these unique observations, we are now developing theoretical models of the mechanism for martensitic nucleation.

*This work was supported by the Division of Materials Science of the DOE Office of Basic Energy Sciences.*

## References

1. J. W. Christian, *The Theory of Phase Transformations in Metals and Alloys* (Pergamon Press, Oxford, 1965).
2. V. V. Kondrat'yev and V. G. Pushin, *Phys. Met. Metall.* **60**(4), 629 (1985).
3. L. E. Tanner, A. R. Pelton, and R. Gronsky, *J. de Phys.* **43**, Colloq. C4, C4-169 (1982).
4. S. M. Shapiro, J. Z. Larese, Y. Noda, S. C. Moss, and L. E. Tanner, *Phys. Rev. Lett.* **57**, 3199 (1986)
5. S. M. Shapiro, B. X. Yang, G. Shirane, Y. Noda, and L. E. Tanner, *Phys. Rev. Lett.* **62**, 1298 (1989).
6. D. Schryvers, L. E. Tanner, and S. M. Shapiro, in *International Meetings on Advanced Materials*, K. Otsuka and K. Shimizu, Eds. (Materials Research Society, Pittsburgh, Pa., 1989), Vol. 9, "Shape Memory Materials," p. 35.

# Constitutive Properties of Copper and Tantalum at High Rates of Tensile Strain: Expanding-Ring Results

W. H. Gourdin

***We have used the electromagnetic launch technique to study the properties of oxygen-free electronic (OFE) copper and 99.9% tantalum rings of various grain sizes expanded at peak strain rates of $10^4$ $s^{-1}$. The advantages of this technique are that it places the specimen in an unambiguous state of uniaxial tension without wave effects, heats the specimen quickly, and can be used to study fragmentation under well-controlled conditions. The results obtained for OFE copper indicate an increasing flow stress as grain size decreases. Tantalum specimens likewise show an increase in the flow stress as grain size decreases, but they display virtually no apparent work hardening at high strain rates. Our data suggest some modifications to constitutive models in the literature.***

## Introduction

A freely expanding ring provides a means of studying the properties of materials at high rates of tensile strain. It is free of the nonuniformities in deformation that can appear in tensile split Hopkinson pressure bar[1] and related[2] experiments. The electromagnetic launch technique[3–5] avoids such effects by making use of the body force produced between two uniform counter-rotating currents. We have applied this technique to well characterized tantalum and OFE copper (Alloy 101) of various grain sizes.

## Experimental Method

The specimen ring[5,6] is a moving secondary winding of a transformer in which the primary is a six-turn solenoid of magnet wire wound on a polycarbonate mandrel. The solenoid is pulsed with a capacitor bank charged to 3 to 6 kV, depending upon the strain rate desired. The pulse induces counter-rotating currents in the solenoid and the specimen. The current in the specimen interacts with its own field and that of the solenoid to produce a large outward force that expands the ring rapidly and uniformly. Although most of the expansion occurs when magnetic forces are small, the current induced during acceleration in a low-resistivity specimen such as copper (1.7 μΩ·cm) is several tens of kiloamperes, and resistive heating can be substantial, limiting the strain rates that can be achieved.[5] For high-resistivity metals such as tantalum (12.45 μΩ·cm), a low-resistivity pusher of aluminum is used to launch the specimen. The pusher is stripped away shortly after maximum expansion speed is reached, allowing the specimen to continue unimpeded.[5,6] The expansion speed is measured with a velocity interferometer system for any reflector (VISAR), and the flow stress of the specimen is calculated from the measured deceleration of the ring during free expansion using the equation of motion for a thin ring[5,7].

The hot-rolled OFE copper used in these experiments was processed to introduce substantial internal strain without also producing a strong texture. Rings 3.2 cm in mean diameter with a square cross section of 0.01 $cm^2$ were heat-treated to yield grain sizes between 10 and 200 μm. The electron-beam-melted and rolled tantalum sheet ("Ta6") was tested in the as-received condition and had a uniform equiaxed grain size of about 65 μm. Powder metallurgy material ("Ta5"), also tested in the as-received condition, had significantly smaller 25-μm equiaxed grains.

## Results

Figure 1 gives the stress-strain data for OFE copper specimens for strains larger than 12 to 13% expanded at peak strain rates of about $10^4$ $s^{-1}$. At smaller strains, magnetic forces are much larger than the flow stress, making it difficult to extract the flow stress accurately. Although the sample-to-sample variations overlap

between adjacent grain sizes, the increase in the flow stress at a given strain as the grain size decreases from 150–200 μm to 10 μm is unmistakable. The variation from specimen to specimen can be reduced by 30 to 50% with more uniform working of the material prior to heat treatment. When the higher temperature of the ring experiments[5] is taken into account, agreement with the data of Follansbee[8] appears to be excellent. Figure 1 also indicates the average of the observed strains at failure for each grain size, obtained from the measured radius at which the first break in the ring occurs; these values decrease with increasing grain size.

**Figure 1.** Stress-strain results for OFE copper rings.

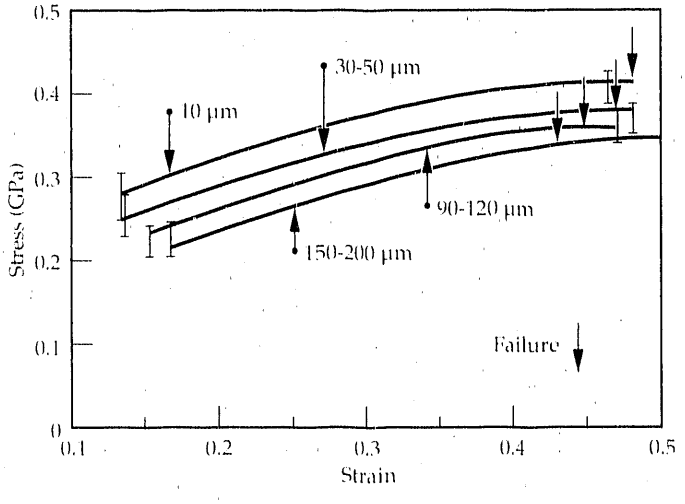


**Figure 2.** Stress-strain results for tantalum rings. The dashed line was computed using the model of Hoge and Mukherjee.[9] The dotted curve is the quasi-static stress-strain behavior of a tantalum similar to Ta6.

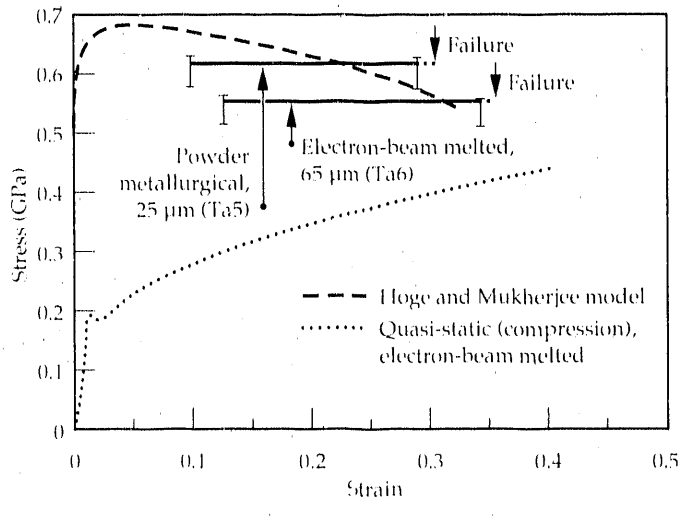


Figure 2 summarizes results for tantalum at peak strain rates of 7000 $s^{-1}$. The powder-metallurgy material, Ta5, has a slightly higher flow stress than the electron-beam-melted material, Ta6. A striking feature of the data is the apparent absence of any hardening as the strain increases. The flow stress for Ta5 is in excellent accord with the lower yield stress data of Hoge and Mukherjee.[9] Average strains at failure are 30 to 35%.

## Discussion

Follansbee and Kocks[10] developed a detailed constitutive model based on thermally activated glide (the mechanical threshold stress [MTS] model) and applied it to OFE copper with a 40-μm grain size. The stress is given by

$$\sigma = \hat{\sigma}_a + (\hat{\sigma} - \hat{\sigma}_a)\left(1 - \frac{kT}{G_0} \ln \frac{\dot{\varepsilon}_0}{\dot{\varepsilon}}\right)^{3/2} \quad (1)$$

where the flow stress at 0 K ("mechanical threshold stress"), $\hat{\sigma}$, is partitioned into athermal $\sigma_a$ and thermal $\hat{\sigma}_t = \hat{\sigma} - \hat{\sigma}_a$ components, $G_0$ and $\dot{\varepsilon}_0$ are constants, and $\dot{\varepsilon}$ is the strain rate. The evolution of the material structure, in particular its strain-hardening behavior, is specified in differential form as

$$d\hat{\sigma}/d\varepsilon = \theta_0[1 - F(\hat{\sigma})] \quad , \quad (2)$$

where $F$ is an empirical function of the hyperbolic tangent of the mechanical threshold. Application to the expanding ring, using measured strain-rate and temperature histories for 30- to 50-μm material, yields acceptable agreement (Fig. 3), although the calculated curve generally falls above the ring data. It is important to note that the general shape of the stress-strain curve is described reasonably well. While the MTS model has no explicit provision for the effects of grain size, if the athermal component of the mechanical threshold is increased from 40 to 70 MPa, an excellent fit to data for 10-μm material is obtained (Fig. 4). However, agreement is poor even when $\hat{\sigma}_a$ is reduced to 0 for the

**Figure 3.**

Comparison of the MTS model with results for 30- to 50-μm OFE copper.

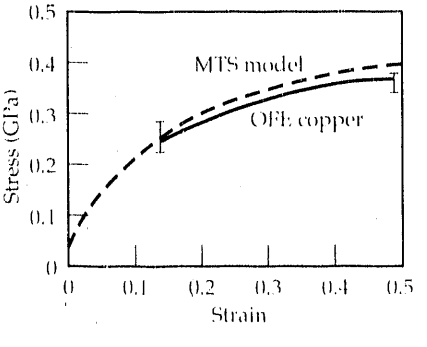

specimens with a 150- to 200-μm grain size. These observations suggest that, although the description of the structure evolution embodied in the function $f$ and the initial hardening rate $\theta_0$ is adequate for material of grain size comparable to that used in the original fitting, it may require modification for material that is substantially different.

Hoge and Mukherjee[9] applied thermally activated glide in their analysis of the flow stress of tantalum, and they specifically identified the Peirels mechanism with the thermal component. They also invoked dislocation drag and neglected any hardening or structural evolution. The thermal component of the stress is obtained from the solution of

$$\dot{\varepsilon} = \{C_0 \exp[(G_0/kT)(1 - \sigma_t/\sigma_p)^2] + D_0/\sigma_t\}^{-1} , \qquad (3)$$

where $\sigma_p$ is the Peirels stress, $D_0$ is a drag coefficient, and $C_0$ and $G_0$ are constants. As in the MTS model, the flow stress is assumed to be the sum of $\sigma_t$ and an athermal component, $\sigma_a$.

The stress-strain behavior obtained using measured strain-rate and thermal histories in Eq. (3) is compared in Fig. 2 with the ring-expansion results. Although the model successfully predicts the general magnitude of the flow stress, the decreasing strain rate and rising temperature as the ring expands produce a downward trend in the calculated results that is not in accord with the observed behavior. This suggests that some hardening must occur to counter the effects of strain rate and thermal softening. Tantalum can certainly show such hardening at quasi-static rates, as illustrated in Fig. 2 for an electron-beam-melted and forged material unrelated but similar to Ta6.

## Conclusions

We have demonstrated that electromagnetically launched expanding rings can be used to obtain reliable constitutive information at tensile strain rates of $10^3$ to $10^4$ $s^{-1}$, and have applied the technique to copper and tantalum. Preliminary comparisons indicate that the MTS model provides a good description of the stress-strain behavior of copper rings as long as the initial microstructure does not deviate substantially from that of the material used to derive the model parameters. For microstructures that are substantially different, the athermal stress and the phenomenological description of the structure evolution must be modified. A similar thermally activated approach provides better than order-of-magnitude estimates of the flow stress of tantalum, but fails to describe the apparent lack of hardening at strain rates of 7000 $s^{-1}$.

*This work was supported by Weapons Supporting Research and the DoD Office of Munitions.*

## References


1. G. Regazzoni, J. N. Johnson, and P. S. Follansbee, *ASME J. Appl. Mech.* **53**(6), 519 (1986).
2. R. Dormeval and M. Stelly, *Inst. Phys. Conf. Ser.* **47**, 154 (1979).
3. H. C. Walling and M. J. Forrestal, *AIAA J.* **11**, 1196 (1973).
4. D. E. Grady and D. A. Benson, *Exp. Mech.* **23**, 393 (1983).
5. W. H. Gourdin, *J. Appl. Phys.* **65**(2), 411 (1989).
6. W. H. Gourdin, S. L. Weinland, and R. M. Boling, *Rev. Sci. Instrum.* **60**(3), 427 (1989).
7. R. H. Warnes, T. A. Duffey, R. R. Karpp, and A. E. Carden, *Shock Waves and High-Strain-Rate Phenomena in Metals: Concepts and Applications*, M. A. Meyers and L. E. Murr, Eds. (Plenum Press, New York, 1981), pp. 23–36.
8. P. S. Follansbee, *Metallurgical Application of Shock-Wave and High-Strain-Rate Phenomena*, L. E. Murr, K. P. Staudhammer, and M. A. Meyers, Eds. (Marcel Dekker, New York, 1986), pp. 451–479.
9. K. G. Hoge and A. K. Mukherjee, *J. Mater. Sci.* **12**, 1666 (1977).
10. P. S. Follansbee and U. F. Kocks, *Acta Metall.* **36**, 81 (1988).


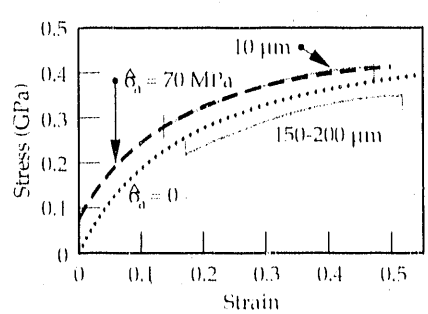


**Figure 4.**

**Comparison of the MTS model (broken lines) with ring data for 10-μm and 150- to 200-μm OFE copper.**

# Deformation of Metals to Ultralarge Strains

M. E. Kassner

***Many metals and alloys can be plastically deformed to ultralarge strains under certain conditions. We have investigated the fundamental basis of this extended ductility. Our new understanding of this phenomenon allows for more efficient metal-forming processes and offers new insight into dynamic restoration processes and the mechanism of elevated-temperature plasticity.***

## Introduction

It has recently been discovered that some metals and alloys can be plastically deformed to incredibly large strains under certain conditions of deformation rate, temperature, and stress state (tension, compression, or torsion). Soviet workers[1] found that at roughly $0.75T_m$ ($T_m$ is the absolute melting temperature) and at relatively high strain rates, there are dramatic ductilities with pure shear or torsion in metals such as relatively pure aluminum. For example, a solid cylinder 25 mm long and 5 mm in diameter can be twisted at a rate of about 2 twists/min at roughly $0.75T_m$ for more than 500 revolutions without failure. This unusually high level of plastic deformation is equivalent to the uniaxial extension of a 10-mm-long specimen to a new length of over $10^{65}$ mm!

This phenomenon is not the one that has more recently been described as "superplasticity." Superplasticity usually refers to a modest enhancement of tensile ductility in terms of an increase in gage length by a factor of 5 or so. We refer to the dramatic shear or torsional ductility as *extended ductility*.[2]

**Figure 1.**

The variation of the torsional strain-to-failure (ductility) of pure aluminum at three strain rates.

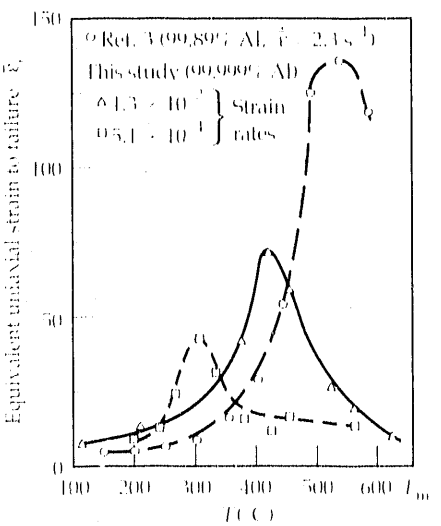


Our investigation had two separate aspects. First, a better understanding of extended ductility would allow this phenomenon to be used for more efficient metal-forming operations. Achieving such an understanding requires (1) determining the effect of strain rate and temperature on ductility at elevated temperatures, and (2) an applicable theoretical analysis. The second aspect of the investigation consisted of carefully examining the deformed microstructure as a function of strain, using polarized light and transmission electron microscopy. This endeavor eventually revealed very unusual microstructural developments that provided substantial new insight into the rate-controlling process for elevated-temperature plasticity. Superpure aluminum was chosen as the metal to be investigated.

## Extended Plasticity

The torsional or shear ductility of the aluminum as a function of temperature and strain rate is illustrated in Fig. 1. At each strain rate, the ductility first increases with temperature to a "peak ductility." Further increases in temperature beyond the "peak-ductility temperature" result in decreases in ductility. Dramatic ductilities—of over 70 (over 200 twists) in some cases—are observed in the vicinity of the peaks. The peak ductility appears to increase with strain rate, and the temperature at which peak ductility is observed increases with increasing strain rate. These trends are rationalized by the expectation that, at lower temperatures, increasing temperature is associated with increasing dynamic recovery, which effectively mitigates internal stresses and retards crack nucleation to produce increased ductility. At high temperatures, diffusive pore formation reduces the ductility. The dramatic ductility in this case is due to effective dynamic recovery, where the defect annihilation rate is very high. Figure 2 illustrates a torsion specimen twisted to 50 revolutions without failure.

## A New Recrystallization Mechanism

Metals are, typically, a polycrystalline aggregate. The individual grains or crystals are separated at boundaries across which there is a misorientation of about 10 to 60 deg. We discovered that substantial deformation causes a dramatic increase of several orders of magnitude in the high-angle boundary area. Such an observation would be explained classically as the result of forming new grains by a "recrystallization" process. However, it was determined that the traditional recrystallization processes, discontinuous-dynamic or continuous-dynamic, were not operating. Rather, we developed a new concept of geometric-dynamic recrystallization.[4,5] According to this model, the grains spiral about the torsion axis with deformation; as a consequence, the high-angle boundary area dramatically increases so that very small "crystallites" form. This phenomenon is shown in Fig. 3. It may be possible to utilize it commercially to produce refined substructures that could improve formability, strength, and fracture properties.

This mechanism provides significant new insight into the rate-controlling process for elevated-temperature plasticity. Specifically, its discovery demonstrates that the microstructural feature associated with power-law creep cannot be the low-energy dislocation features, called subgrain boundaries, as the scientific community previously believed[5]. This is because the flow stress during geometric-dynamic recrystallization is essentially constant despite the increase in high-angle boundary area. This observation suggests that such heterogeneities as boundaries, e.g., low-energy dislocation configurations, are not important in the rate-controlling processes for elevated-temperature plasticity.

## Summary

We observed extremely large ductilities at certain combinations of temperature and strain rate when aluminum was deformed in pure shear. The extended ductility of aluminum is provided by effective dynamic recovery. We discovered a new recrystallization mechanism, geometric-dynamic recrystallization, which provides insight into the fundamental mechanism of elevated-temperature plasticity.

*This work was supported by Weapons Supporting Research.*

## References

1. M. E. Kassner, H. J. McQueen, and M. M. Myshlyaev, "Large-Strain Torsional Deformation of Aluminum at Elevated Temperature," *Mater. Sci. Eng.* **108**, 45–61 (1989).
2. H. J. McQueen and M. E. Kassner, "Extended Ductility in α-Iron and Aluminum Alloys," *Superplasticity in Aerospace*, H. C. Heikkenen and T. R. McNelley, Eds. (AIME, Warrendale, Pa., 1988), pp. 77–96.
3. J. R. Cotner and W. J. McG. Tegart, *J. Inst. Met.* **97**, 73 (1969).
4. M. E. Kassner, "Large-Strain Deformation of Aluminum Single Crystals at Elevated Temperature: A Critical Test for Geometric-Dynamic-Recrystallization," *Metall. Trans.* **20A**, 2182–2185 (1989).
5. M. E. Kassner and M. E. McMahon, "The Dislocation Microstructure of Aluminum Deformed to Very Large Steady-State Creep Strains," *Metall. Trans.* **18A**, 835–846 (1987).

**Figure 2.**

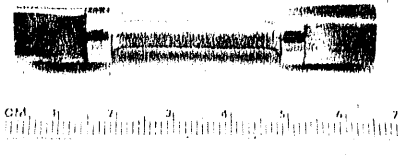

Pure aluminum deformed to a strain of about 16 (roughly 50 twists) at 371°C and a strain rate of about $5 \times 10^{-4}\ s^{-1}$.

**Figure 3.**

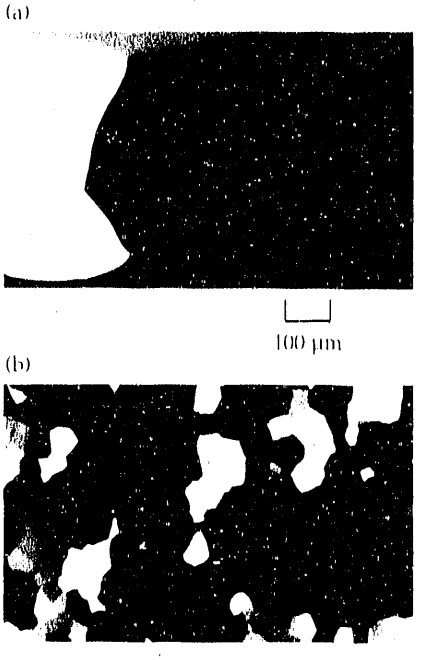


Polarized-light micrographs of (a) undeformed aluminum, and (b) aluminum deformed to a large strain at an elevated temperature (see Fig. 2). Numerous high-angle boundaries are observed in the deformed specimen.

# Interplay Between Crystalline Structure, Electronic Properties, and Configurational Order in Substitutional Alloys

P. E. A. Turchi

***We review our recently developed advanced theoretical methods of studying alloy phase stability. To illustrate these methods, we describe the effect of a tetragonal distortion in the body-centered cubic (bcc) crystalline structure on the thermodynamic properties of transition-metal alloys. We also discuss our predictions of the existence of new ordered states based upon the A15 crystalline structure.***

## Introduction and Methodology

The study of ordering processes in binary substitutional alloys is of great interest in both the theory and technology of alloy phase stability. Most of the physical properties of the alloys depend on the occurrence of ordered phases or intermetallic compounds. Alloys based upon simple underlying crystalline structures, such as face-centered cubic (fcc), bcc, and hexagonal close-packed (hcp), for which a large variety of ordered states can exist, have therefore received much attention in recent years.[1-3] Unfortunately, few fundamental studies have been undertaken to investigate the interplay between crystalline structure, electronic properties, and configurational order in substitutional alloys. Of special interest are alloys that depart from ideal simple crystalline structure or have a complex crystallographic arrangement, as in the case of the Frank-Kasper phases.[4]

When dealing with a microscopic description of phase stability, one has to combine electronic-structure calculations with statistical studies, each having a high degree of accuracy. One way to achieve such a goal is to design a reference medium that is as close as possible to any ordered state of an alloy based upon a given crystalline structure. Such a suitable medium is given by the totally configurationally disordered state, as calculated by the coherent potential approximation (CPA).

When a perturbation technique, the so-called generalized perturbation method (GPM), is applied to this reference medium in order to take into account local fluctuations of concentration from site to site, a proper description of the configurational contribution to the internal energy is obtained in terms of a rapidly convergent expansion. The expansion coefficients, also called effective cluster interactions (ECIs), formally justify the validity of a three-dimensional generalized Ising model, which in turn can be used to study the ground-state properties of a given alloy (at $T = 0$ K) as well as to solve the statistical part of the problem. These ECIs, as calculated in the GPM context, depend on the geometrical characteristics of the clusters (i.e., topology and metric) as well as on the alloy parameters: the total number of electrons or the number of valence electrons of each species and their concentrations. Hence, the ordering energy, i.e., the difference in energy between the totally ordered and disordered states, takes the following form:

$$\Delta E_{ord}(\{p_n\}) = \frac{1}{2N} \sum V_{nm}(p_n - c)(p_m - c) + \frac{1}{3N} \sum V_{nml}(p_n - c)(p_m - c)(p_l - c) + \ldots \quad (1)$$

for any particular configuration specified by a set of occupation numbers $p_n$ ($p_n = 0$ or 1 depending on whether or not site n is occupied by a B species). The potentials $V$ refer to the ECIs; in particular, $V_{nm}$ is a pair interaction between sites n and m and is given by:

$$V_{nm} = V_{nm}^{AA} + V_{nm}^{BB} - 2V_{nm}^{AB} \quad . \quad (2)$$

The electronic structure of the reference medium can be obtained either in a first-principles framework such as the Korringa Kohn Rostoker–CPA, based on multiple scattering theory, or by using the semiphenomenological tight binding method (TB-CPA). Either approach represents a pertinent route for the study of relative phase stability at $T = 0$ K (Ref. 5). Moreover, computing phase diagrams through the use of TB-CPA-GPM ECIs to describe the ordering energy on one hand, and a statistical model such as the cluster variation method (CVM) or Monte-Carlo simulations to calculate the equilibrium configurational part of the total free energy on the other, showed that the main features of coherent and noncoherent phase diagrams can be obtained.[1-3] As an illustration, we consider two examples.

## Applications

At low temperature, a wide variety of binary substitutional alloys undergo a structural transformation that has the characteristics of a martensitic transformation. Associated with these transformations are unusual properties such as pseudoelasticity and shape memory. As a first step toward obtaining a fundamental understanding of the structural transformation with respect to the underlying electronic structure, we studied the structural transition from a B2 ordered state, built on the bcc crystalline structure, to an $L1_0$ configuration, a tetragonal version of the B2 superstructure, when $T$ decreases. Starting from a long-range ordered B2 phase, the close-packed face-centered martensite can be obtained by a homogeneous Bain strain that consists of an expansion parallel to the $[001]_{bcc}$ axis and a compression normal to it (see Fig. 1). If we assume that the transformation occurs at constant volume, a unique parameter $\alpha$ can be defined to describe the tetragonal distortion of the lattice:

$$\alpha = 1 - \frac{c/a - 1}{\sqrt{2} - 1} \quad . \tag{3}$$

Therefore $\alpha$ takes the value 0 (1) for an ideal fcc (bcc) crystalline structure.

Electronic structure calculations based on the TB-CPA-GPM allowed us to examine the properties of the ECIs as a function of the alloy parameters and of the Bain strain $\alpha$. As an example, Fig. 2(a) shows the effective pair interactions $V_l$ up to the fourth-neighbor shell [of the body-centered tetragonal (bct) structure] normalized to $V_1^{fcc}$, the first pair interaction in the fcc structure, for an alloy specified by the number of valence d-electrons (7.80 and 4.27 for the two species) and a concentration $c = 1/2$. From a ground-state analysis of the Ising model, the set of ECIs so derived proves that the generic B2 ordered configuration is the only probable state at $T = 0$ K. Fig. 2(b) shows the energetic properties at $T = 0$ K, namely the energies of the totally ordered and disordered states (from which a concentration-averaged energy associated with both species was subtracted) as a function of the Bain strain. For this particular alloy, the ground state is therefore a generic B2 built on a bct structure with $\alpha = 0.30$.

For $T \neq 0$ K, we performed statistical calculations with an updated version of the CVM in order to estimate the configurational entropy and finally to obtain the equilibrium free energy. Figure 3 presents the configurational part of the free energy as a function of a reduced temperature $T^* = kT/V_1^{fcc}$ for various values of $\alpha$. It is found that the B2 (bcc case) disorders at higher-temperature $T_c^*$ than any other tetragonally distorted version of it. This effect is mainly responsible for the occurrence of a structural transition at $T_m^*$ and is supported by a careful analysis of the two major components of the free energy, i.e., the internal energy

**Figure 1.** Structural description of the $L1_0$ (fcc)-B2 (bcc) phase transformation.

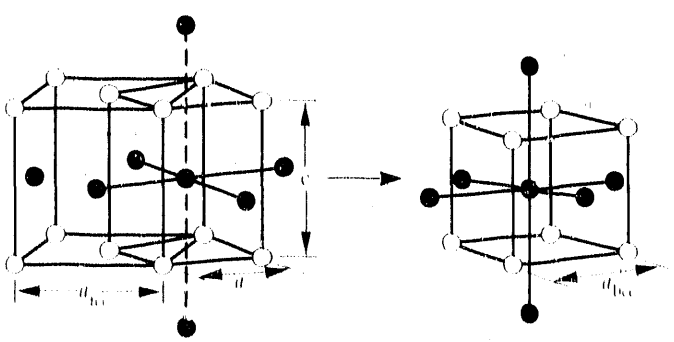


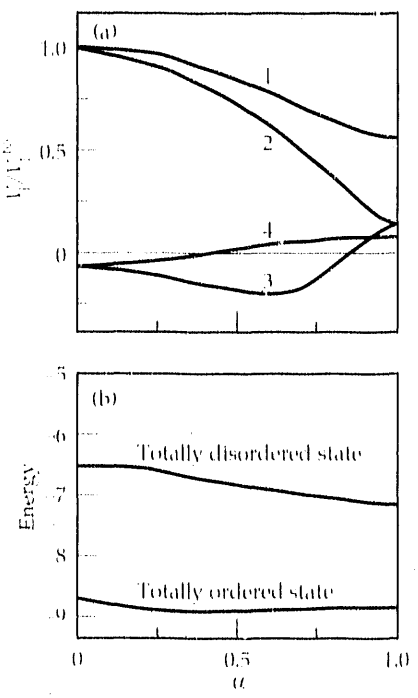


**Figure 2.** (a) $V_l/V_1^{fcc}$ ($l$ = 1, 4), and (b) energetic properties at $T$ = 0 K as a function of the tetragonal distortion, $\alpha$. In (a) and (b), $c$ = 1/2.

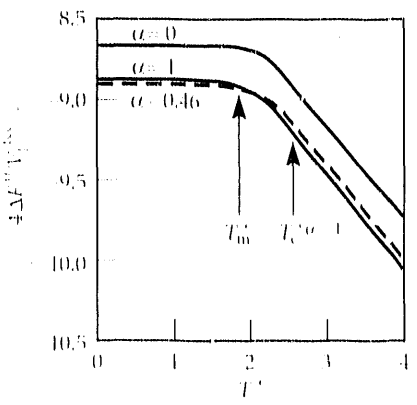


**Figure 3.** Configurational free energy as a function of reduced temperature, $T^*$.

and the entropy. Hence, we have shown that the tendency toward a metastability of an ordered phase, at very low temperature, can be the signature of a structural transformation.[6] The B2 (bcc case, $\alpha = 0.3$) is the ground state (at $T = 0$ K) and as $T$ increases, a transformation to bcc B2 occurs before the alloy disorders. The lack of frustration in the bcc structure gives rise to an excess configurational entropy and therefore favors the bcc B2 at high temperature. This effect reinforces, in the case of the alloy, the well-known excess residual vibrational entropy, of the order of $0.3k$, when comparing fcc with bcc.

We have recently shown[7] that the scheme discussed in the first section is also applicable to the A15-based alloys. Ordering processes can be described by a three-dimensional generalized Ising model for simple alloys. By performing a ground-state analysis of the Ising model on the A15 lattice with first-, second-, and weak third- and seventh-neighbor effective-pair interactions,[8] we obtained, besides the pure metal configuration (F),

**Figure 4.**

Ordered structures based upon the A15 crystalline structure.

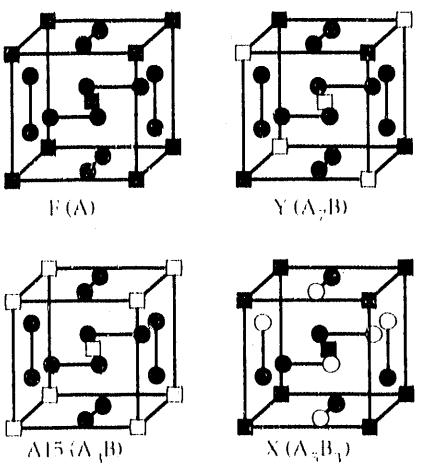


**Figure 5.**

Prototype A15-based order-disorder phase diagram: temperature vs concentration in A species.

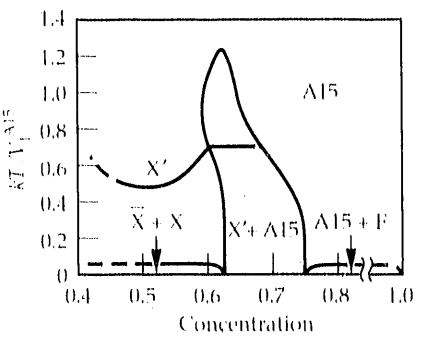


and the well known A15 configuration at the composition $A_3B$, two new ordered states at the compositions $A_5B_3$ (X) and $A_7B$ (Y) (see Fig. 4). These four configurations represent the most probable states for the most common sets of ECIs that can be calculated from the TB-CPA-GPM.

We investigated stability properties as a function of temperature and concentration by means of the CVM and also by Monte Carlo simulations. Typical prototype A15-based order-disorder phase diagrams show remarkable features associated with the intrinsic nonsymmorphicity of the lattice (see Fig. 5). At the stoichiometric composition $A_3B$, there is no real order-disorder transition as $T$ increases, and below this composition, a two-phase region involving the X and A15 phases can exist in a specific regime of ECIs. Finally, the X phase is found stable below the stoichiometric composition $A_5B_3$. Short-range diffuse scattering with x rays or neutrons, above the domain of existence of the X phase, should show maxima of diffuse intensity specifically assignable to this predicted ordered state. A few alloy candidates that exhibit an A15 phase over a broad range of concentrations hold the possibility of validating such expectations.

## Conclusion

Although some formal problems remain to be solved if we are to provide a quantitative ab initio solution to the general problem of alloy phase stability, we have shown that new concepts and predictions can support experimental work. This development holds promise for achieving better control over the design and processing of high-performance, high-temperature materials.

*This work was supported by Weapons Supporting Research.*

## References

1. P. E. A. Turchi, M. Sluiter, and D. de Fontaine, *Phys. Rev.* **B36**, 3161 (1987).
2. M. Sluiter, P. E. A. Turchi, F. Zezhong, and D. de Fontaine, *Phys. Rev. Lett.* **60**, 716 (1988).
3. N. C. Tso, M. Kosugi, and J. M. Sanchez, *Acta Metall.* **37**, 121 (1989).
4. W. B. Pearson, in *Crystal Chemistry and Physics of Metals and Alloys* (Wiley-Interscience, N.Y., 1972).
5. P. E. A. Turchi, G. M. Stocks, W. M. Butler, D. M. Nicholson, and A. Gonis, *Phys. Rev. B* **37**, 5982 (1988).
6. P. E. A. Turchi, *J. Mater. Sci. Tech.* (in press).
7. P. E. A. Turchi, G. Treglia, and F. Ducastelle, *J. Phys. F* **13**, 2543 (1983).
8. P. E. A. Turchi and A. Finel, Lawrence Livermore National Laboratory, Livermore, Calif., UCRL-101962 (1989); submitted to *Europhys. Lett.*

# Fine-Structure Development for Improved Superplastic Formability in Ultrahigh-Carbon Steels

M. J. Strum,
A. Goldberg,*
O. D. Sherby,†
R. P. Kershaw,
R. J. Gross,* and
E. M. Sedillo

*We have improved the superplastic properties of heavy-section ultrahigh-carbon steels (UHCSs) through microstructural refinement. The microstructure has been refined by adjustments in alloy composition and by improved thermomechanical processing. The compositional modifications slow carbide precipitation kinetics enough to prevent deleterious carbide-network formation at grain boundaries. The conversion of thick-section material into fine superplastic microstructures was achieved by combining an isothermal transformation process, which controls carbide morphology, with optimized warm-working temperatures for grain-size refinement.*

## Introduction

The fabrication of engineering components by superplastic forming to near-net shape is attractive in comparison with conventional processing because it can greatly reduce the need for costly machining and joining operations. Commercial applications of superplasticity in metals utilize what is termed fine-structure (or fine-grained) superplasticity. This deformation mechanism causes the flow stress to be highly sensitive to the rate of deformation and is the basis for achieving high tensile elongations. The mechanism of superplastic deformation in fine-structure superplasticity is generally understood as a grain-boundary sliding phenomenon; that is, individual grains slide past each other along their common boundary to produce macroscopic deformation. The grain size required for fine-structure superplasticity is generally 10 μm or less. Superplasticity is achieved when these highly refined microstructures are deformed within a specific window of temperature and strain rate.

The economics of superplastic forming as a substitute for conventional forming, machining, and joining operations are dictated by the maximum achievable superplastic strain or forming rate. Existing analytical expressions for fine-structure superplasticity predict that maximum superplastic strain rates increase as the cube of the reciprocal grain size, and also increase with temperature because of greater atomic diffusivities. Forming rates are improved both by adjusting alloy composition and by developing thermomechanical processing to produce fine-grained materials that are resistant to coarsening at high forming temperatures.

The most promising steels for commercial applications are hypereutectoid alloys containing 1 to 1.8 wt% carbon (15 to 30 vol% carbide particles).[1] In spheroidized form, the carbides function as grain-boundary pinning sites and assist in the stabilization of a fine ferrite grain size.

## Experimental

Superplastic formability in these alloys is being demonstrated at both the laboratory and commercial level.[2] Laboratory experiments establish the window of superplastic behavior from measurements of the tensile response of the material over a wide range of strain rates. Superplastic forming of UHCS alloys using commercial forming equipment is also in progress. Figure 1 shows a superplastically formed demonstration part from our modified UHCS material. This part was formed by closed-die forging at 750°C at a strain rate of 0.1 %/s from an originally round cylinder 76 mm in diameter and 40 mm long.

Modifications of composition to a base alloy of Fe-1.5Cr-0.5Mn-1.25C were evaluated using 500-lb (225-kg) experimental ingot castings. The castings were hot-rolled from a soaking temperature of 1210°C, hot-sheared, and air-cooled. Warm-processing studies by rolling were performed using 20-mm-thick coupons. The rolls were preheated to 300°C. Warm forging was performed on samples up to 75 mm thick using a 300-ton press with platens preheated to the forging temperature. Heat treatments were performed in air furnaces.

## Results

The following are our three principal achievements in fine-structure development for improved superplastic formability in UHCS alloys:

- Prevention of carbide-network formation at grain boundaries during cooling through the two-phase austenite-plus-carbide range.
- Efficient transformation of plate-like carbides into fine spherical carbides.
- Production of high-angle-boundary ferrite grains with grains near 1 μm in diameter.

A minimum of two processing stages were used to develop the required microstructure in the UHCS alloys. The first creates a homogeneous pearlitic state. Continuous networks of carbides tend to form during the cooling of high-carbon (hypereutectoid) steels such as the UHCS alloys. These carbide networks are undesirable because their presence in the final product decreases the total amount of carbide available as grain-boundary-pinning sites and contributes to poor mechanical properties at ambient temperatures by creating brittle crack paths. Figure 2(a) shows an example of network carbides in as-cooled hypereutectoid pearlite.

In the past, these grain-boundary carbide networks were avoided through incorporation of special processing procedures, such as semicontinuous hot and warm working, while cooling through the temperature range in which networks can develop. These procedures are both costly and difficult to apply in thick sections, however. Our studies have shown that the extent of grain-boundary carbide networks in the air-cooled pearlitic microstructures can be controlled through compositional modifications. Figure 2(b) shows typical network-free pearlitic microstructures in modified UHCS alloys.

Conversion of the network-free pearlitic steel microstructure into a superplastic microstructure is accomplished by the completion of two events: spheroidization of the plate-like carbides, and refinement of the iron matrix (ferrite). The driving force for spheroidization of the lamellar carbides is the reduction in carbide-ferrite surface area and associated surface energy. The process of spheroidization is time-dependent, being controlled by the diffusion of atoms.

We have refined a process in which the carbide dissolves and reprecipitates under conditions favorable to spheroidization of UHCS alloys. We call this process a divorced-eutectoid transformation (DET). Processing consists first of raising the temperature of the material just above the pearlite-stability range, where most of the carbides rapidly dissolve in iron. The remaining undissolved carbides are finely dispersed at this stage in spheroidized form instead of existing as network carbides. The undissolved carbides, as well as regions

**Figure 1.** This rotor hub was superplastically formed from a UHCS alloy at 750 °C at a strain rate of 0.1 %/s. The originally round billet was 76 mm in diameter and 40 mm tall. The fine die-flashing on the upper rim of the part is indicative of good die-filling properties.

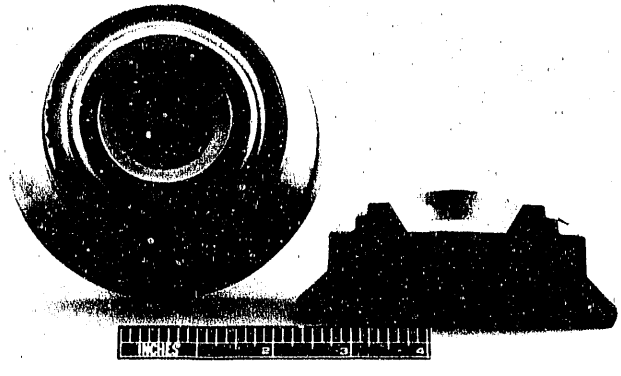


**Figure 2.** (a) Significant networks of grain carbides form along the grain boundaries during cooling in the base UHCS. (b) Compositional modifications prevent carbide-network formation and produce a fine and uniform pearlite structure (alternating layers of carbide and iron matrix phase). (c) Special processing techniques convert the pearlitic structure into a superplastic structure consisting of fine ferrite grains with fine spherical carbides at the grain boundaries.

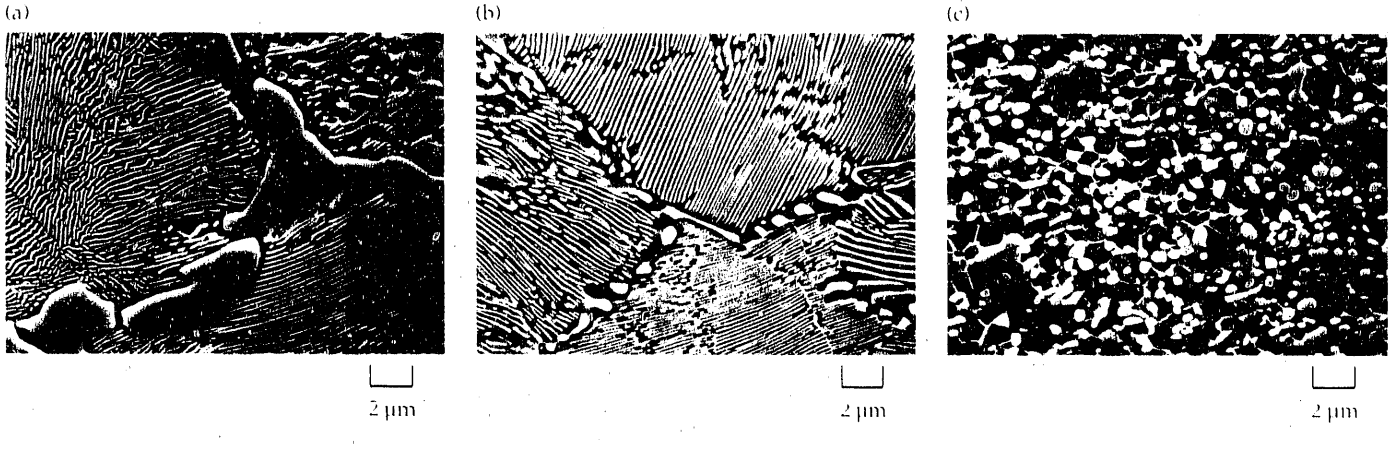

where partitioning of carbon and/or other alloying elements has occurred, can serve as sites for nucleation and growth of carbides. The large number of intragranular nucleation sites for the eutectoid carbides causes a fine, uniform carbide dispersion. DET processing for carbide spheroidization significantly reduces processing times, and much finer carbide distributions are achieved than by pearlite-coarsening treatments.

To obtain a successful DET microstructure of fully spheroidized carbides, the sluggishness of the transformation kinetics in the modified UHCS alloys required special consideration. While air-cooled structures are fully spheroidized in the basic UHCS alloy, desirable compositional modifications dramatically reduce the fraction of spheroidized carbides. Isothermal-transformation studies have characterized the transformation kinetics of these alloys, and for each alloy variation of UHCS, it has been possible to define a critical cooling rate below which complete spheroidization results. These cooling rates are based on the transformation rates and the morphological sensitivity to transformation temperature.

The rate of spheroidization can be increased by the introduction of concurrent deformation. This process has been termed DETWAD (divorced-eutectoid transformation with associated deformation). In addition to assisting the process of spheroidization, the concurrent deformation effectively produces fine ferrite grain sizes of about 1 μm (mean intercept length method), as shown in Fig. 2(c).

Investigation of the relative importance of deformation both above and below the dissolution temperature has led to an improved understanding of the DETWAD process. The degree of warm working required for successful conversion processing has been reduced through the use of discrete vs semicontinuous deformation. These developments have resulted in an optimized processing sequence consisting of an isothermal DET step to produce a fine distribution of spherical carbides, followed by warm working at temperatures most suitable for ferrite-grain refinement. This process has successfully produced superplastic microstructures and improved superplastic formability in thick sections.

## Conclusions

We have improved the superplastic properties of UHCS through microstructural refinement. Compositional modifications to UHCS alloys slow the carbide precipitation kinetics enough to prevent deleterious carbide-network formation at grain boundaries. An isothermal DET process controls carbide morphology, efficiently transforming plate-like carbides into fine, spherical carbides in thick sections. The production of a high-angle-boundary ferrite grain size near 1 μm in diameter was achieved through subsequent warm-deformation processing at controlled temperatures.

Continued efforts to improve superplastic formability will focus on alloy compositional modifications that increase the high-temperature stability of the fine microstructures.

*This work was supported by Weapons Supporting Research; by the DOE Office of Conservation and Renewable Energy; and by the DOE Steel Initiative Program with contributions from three industrial partners: Caterpillar, Inc., Ladish Company, Inc., and North Star Steel Company.*

*Mechanical Engineering Department.
†Stanford University, Stanford, Calif.

## References

1. O. D. Sherby, T. Oyama, D. W. Kum, B. Walser, and J. Wadsworth, "Ultrahigh Carbon Steels," *J. Metals* **37**(6), 50–56 (1985).
2. *Steel Initiative Management Plan*, Office of Industrial Programs, Office of Conservation and Renewable Energy, U.S. Department of Energy, Washington, D.C. (April 1, 1987).

# Microstructural Evolution During Rapid Resolidification of Stainless Steel Alloys

J. W. Elmer, S. M. Allen,* and T. W. Eagar*

*We analyzed high-purity iron-nickel-chromium alloys that were rapidly resolidified by electron-beam (EB) surface glazing. Twelve microstructural morphologies were identified in the resolidified melts and were shown to develop from the two primary phases, austenite and ferrite. Microstructural evolution was studied by determining the effect of cooling rate on the primary solidification mode (PSM), solute redistribution during solidification, and solid-state transformation of ferrite during cooling. The results enable us to predict the primary mode of solidification, the residual ferrite content, and the complex microstructural morphologies that form in resolidified stainless steel alloys.*

## Introduction

The fabrication of stainless steel alloy components often involves fusion welding under precisely controlled conditions. Welds of this nature are generally performed using laser beams or EBs, which produce fusion zones that cool significantly faster than those produced by conventional processes. Under these conditions, dramatic changes in the microstructure occur, and these can influence the integrity of the final component.

In this investigation, we studied the effect that cooling rate has on the microstructure of stainless steel alloys to gain a better understanding of the link between processing conditions and microstructure. An example of the dramatic influence of cooling rate on the microstructure of stainless steel alloys is shown in Fig. 1, which compares the responses of two alloys of similar composition. The low-cooling-rate microstructures are present in the substrate ($2 \times 10^3$ K/s), and the high-cooling-rate microstructures are present in the EB-resolidified zone ($2 \times 10^6$ K/s).

In each of the iron-nickel-chromium ternary alloys, the substrate contains a mixture of ferrite and austenite phases. When rapidly resolidified, however, Alloy 4 (25.5 percent chromium, 15.8 percent nickel) becomes fully austenitic, and Alloy 5 (28.1 percent chromium, 12.7 percent nickel) becomes fully ferritic. Thus, the residual ferrite content of Alloy 4 decreases, and that of Alloy 5 increases with increasing cooling rate. In both alloys, the formation of second phases is suppressed at high cooling rates, leading to single phase solidification conditions.

This comparison illustrates the low- and high-cooling-rate extremes for alloys that lie on opposite sides of the

**Figure 1.**

Comparison of the rapidly resolidified zones in Alloys 4 and 5. (a) Alloy 4 contains 9.6 percent ferrite in the substrate and 0 percent ferrite in the resolidified zone. (b) Alloy 5 contains 36.3 percent ferrite in the substrate and 100 percent ferrite in the resolidified zone.

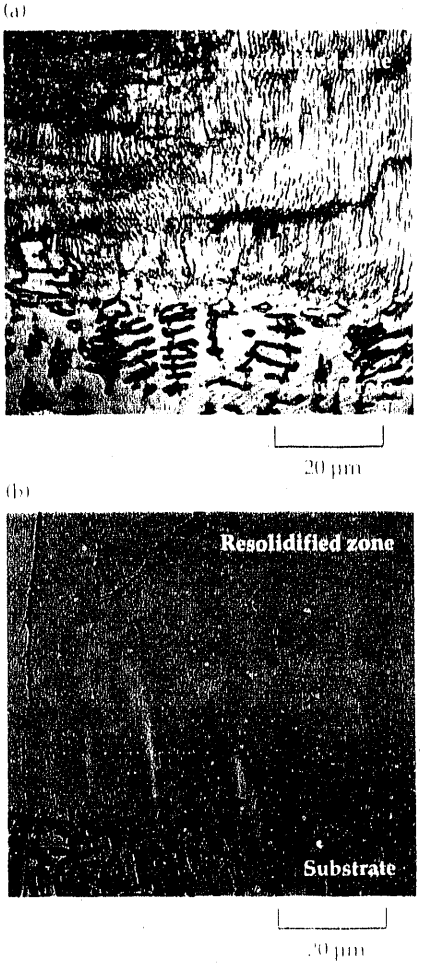

line of two-fold saturation. In addition to these microstructures, many other microstructures can develop as a result of the influence of cooling rate on solidification and the solid-state transformation of ferrite during cooling. Our objective was to develop a means of identifying and explaining each of the microstructural morphologies that develops during the solidification of stainless steel alloys.

## Approach

Experiments were performed on a series of high-purity iron-nickel-chromium alloys that spanned the line of two-fold saturation along the 59-wt% iron isopleth of the ternary alloy system. The chromium/nickel ratios of these alloys ranged from 1.1 to 2.2. These ratios were selected such that Alloys 1–3 solidify through the liquid-plus-austenite two-phase field and Alloys 4–7 solidify through the liquid-plus-ferrite two-phase field under equilibrium conditions. Each of these alloys was solidified using a high-speed EB surface-glazing technique at scan speeds up to 5 m/s. The microstructures that were formed under these conditions were analyzed using optical metallography, electron microprobe analysis, scanning electron microscopy, and a vibrating sample magnetometer. The high-speed EB surface-glazed microstructures were shown to have dendrite arm spacings that ranged from 42 to 4.3 μm, which correspond to cooling rates ranging from $7 \times 10^0$ to $7.5 \times 10^6$ K/s, respectively. Reference 1 contains a complete description of the experimental procedures, alloy compositions, and cooling-rate calculations.

## Results and Discussion

**Residual Ferrite Content.** The residual ferrite content of each of the rapidly solidified alloys was measured using a technique that was developed as part of this investigation.[2] These results are summarized in Fig. 2, which shows three different trends in the residual ferrite content with scan speed: (1) The residual ferrite content of Alloys 1, 2, and 3, which have a low chromium/nickel ratio, decreases with increasing cooling rate, and these alloys eventually become fully austenitic. (2) The residual ferrite content of Alloys 4 and 5, which are close to the line of two-fold saturation, passes through a relative maximum at intermediate cooling rates. (3) The residual ferrite content of Alloys 6 and 7, which have a high chromium/nickel ratio, increases with increasing cooling rate, and these alloys eventually become fully ferritic.

These different behaviors of the residual ferrite content with EB scan speed can be explained by the influence that the cooling rate has on the PSM, solute redistribution during solidification, and solid-state transformation of ferrite during cooling.[3]

**Primary Solidification Mode.** Stainless steel alloys solidify in one of five primary solidification modes: single-phase austenite (A), primary austenite with second-phase ferrite (AF), eutectic ferrite-plus-austenite (E), primary ferrite with second-phase austenite (FA), and single-phase ferrite (F). Detailed descriptions of these PSMs are discussed in Ref. 4.

Figure 3 summarizes the influence of cooling rate on the PSM. Two important effects are seen. First, at low scan speeds (<100 mm/s), four modes of solidification are present, whereas at high scan speeds (>500 mm/s), only the single-phase solidification modes are present. Second, alloys that are close to the line of two-fold saturation can change their solidification mode from primary ferrite to primary austenite as the scan speed is increased.

Microstructural analysis of the resolidified alloys shows that the initial growth of all phases occurs from the melt periphery by an epitaxial mechanism.[4] At low cooling rates, epitaxial growth results in the more thermodynamically stable solidification mode becoming the PSM. However, at high cooling rates, changes in the low-cooling-rate PSM can occur because of the more favorable growth conditions for metastable austenite at the melt periphery. These effects were most notable in Alloy 4, which lies close to the line of two-fold saturation, solidifying in the FA mode at low cooling rates and in the AF mode at high cooling rates.

**Microstructural Morphology.** Twelve microstructural morphologies were observed during the resolidification of the high-purity iron-nickel-chromium alloys.[4] These microstructural features are summarized in Table 1 along with the solidification and solid-state transformation events responsible for their development. In this table, F, A, and L refer to the ferrite, austenite, and liquid phases, respectively, and the subscripts P and E refer to the primary and secondary phases, respectively.

**Figure 2.** Residual ferrite content of the seven alloys plotted as a function of EB scan speed.

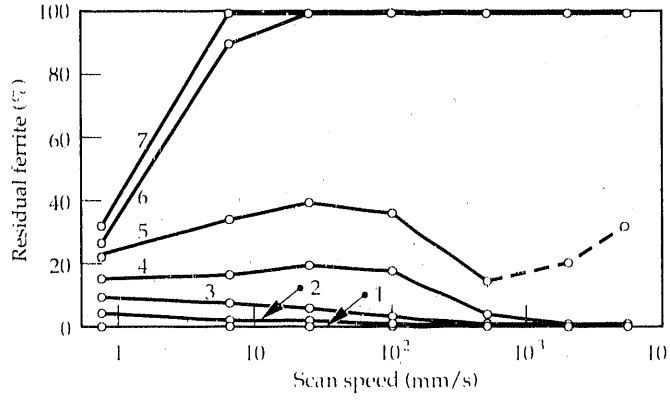

These effects are graphically summarized in Fig. 3, where each microstructure is associated with a range of scan speeds and alloy compositions.

## Summary

The evolution of microstructures during the rapid resolidification of stainless steel alloys can be described by the influence that cooling rate has on the PSM, solute redistribution during solidification, and solid-state transformation of ferrite during cooling. The results of this study show that the PSM can be altered at high cooling rates by (1) the preferred growth of metastable austenite from the melt periphery, or (2) the elimination of secondary phases, leading to single-phase solidification. Furthermore, solute redistribution during solidification is influenced by the cooling rate; the amount of secondary phase that solidifies from the melt decreases with increasing cooling rate. Finally, the cooling rate further modifies the microstructure through its influence on the nucleation-and-growth characteristics of austenite during the solid-state transformation of ferrite.

*This project was funded principally by Weapons Supporting Research. Some work was performed at the Massachusetts Institute of Technology under partial funding by the Office of Naval Research under contract N00014-80-C-0384.*

*Massachusetts Institute of Technology, Cambridge, Mass.

**Figure 3.** Scan-speed/composition map of the microstructural morphologies that result from the combined effects of solidification and solid-state transformation. The solid lines indicate the four PSM regions, while the dashed lines represent the different morphologies that result from the solid-state transformation of ferrite.

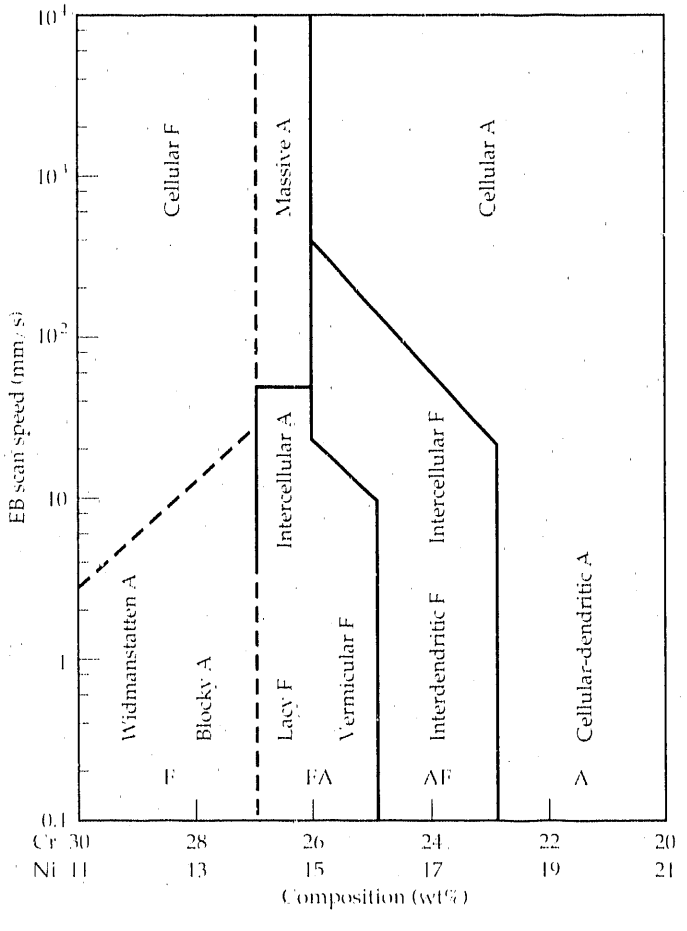


## References

1. J. W. Elmer, Sc.D. thesis, Department of Materials Science and Engineering, Massachusetts Institute of Technology, Cambridge, Mass. (September 1988).
2. J. W. Elmer and T. W. Eagar, "Measuring the Ferrite Content of Rapidly Solidified Stainless Steel Alloys," *Welding J.* (in press).
3. J. W. Elmer, S. M. Allen, and T. W. Eagar, "The Influence of Cooling Rate on the Ferrite Content of Stainless Steel Alloys," *2nd Int. Conf. Trends in Welding Research, Gatlinburg, Tenn., May 1989.*
4. J. W. Elmer, S. M. Allen, and T. W. Eagar, "Microstructural Development During Solidification of Stainless Steel Alloys," *Metall. Trans. A* **20A**, 2117–2131 (1989).

**Table 1.** Development of the twelve microstructural morphologies.

| Mode | Solidification sequence | Solid-state transformation | Morphology |
|---|---|---|---|
| A | $L \rightarrow (L + A_P) \rightarrow A$ | None | Cellular-dendritic A |
| | | None | Cellular A |
| AF | $L \rightarrow (L + A_P) \rightarrow (L + A_P + F_E)$ $\rightarrow (A_P + F_E)$ | $F_E \rightarrow A_T$ | Interdendritic F |
| | | $F_E \rightarrow A_T$ | Intercellular F |
| E | $L \rightarrow (L + F_E + A_E)$ $\rightarrow (F_E + A_E)$ | $F_E \rightarrow A_T$ | Eutectic |
| FA | $L \rightarrow (L + F_P) \rightarrow (L + F_P + A_E)$ $\rightarrow (F_P + A_E)$ | $F_P \rightarrow A_T$ | Intercellular A |
| | | $F_P \rightarrow A_T$ | Vermicular F |
| | | $F_P \rightarrow A_T$ | Lacy F |
| | | $F_P \rightarrow A_T$ | Blocky A |
| F | $L \rightarrow (L + F_P)$ | $F_P \rightarrow A_W$ | Widmanstatten A |
| | | $F_P \rightarrow A_M$ | Massive A |
| | | None | Cellular F |

# Time-Dependent Free Convection in Liquid Metals

M. A. McClelland and
P. J. Meyer

*A numerical analysis is given for the time-dependent free convection of highly conductive liquids in a rectangular cavity. The results of this analysis are relevant to the electron-beam vaporization of metals. The spatial problem is solved with the Galerkin finite-element method, and the time integration is performed with a backward Euler method incorporating step-size control. Streamwise dispersion is introduced for cases involving large convection and numerical instabilities. Results are given for flows in the transition region between laminar and turbulent.*

## Introduction

Electron-beam vaporizers are commonly used to generate metal vapor at high rates. Typically, the metal is confined in a crucible with cooled walls and is heated with an electron beam under vacuum (see Fig. 1). A portion of the energy is used to vaporize the metal, and the balance skips to a beam dump, conducts to the crucible walls, and thermally radiates to the surroundings. A pool forms in the region where the beam strikes the metal. The liquid circulates primarily as a result of buoyancy forces that are generated by temperature-induced gradients in density.

In order to improve performance, we are modeling the mass, momentum, and heat transfer in the vaporizer. Challenges are provided by the need to model vapor and liquid flow coupled with moving phase boundaries and thermal radiation. Our attention is currently concentrated on the liquid pool. At the operating conditions of interest, circulation rates are high and the flow is in the transition region between laminar and turbulent. Numerical analysis is difficult because the flow is time-dependent and dominated by convection.

We are presently investigating buoyancy-driven flow in a two-dimensional rectangular cavity (see Fig. 2). A liquid metal circulates in a counterclockwise direction as it is heated on the right vertical wall ($x = 4$) and cooled on the left vertical wall ($x = 0$). The selection of this geometrically simple system allows us to focus on the numerical problems. However, this flow does share features with the vaporizer pool flow. Both types of free-convection flow take place in shallow cavities and have shear-free upper boundaries.

The flow is laminar and steady at low circulation rates. As the circulation rate is increased, a critical point is reached at which the flow becomes unstable and oscillatory. With further increases in circulation rate, the flow moves through the transition region until it becomes fully turbulent. In previous investigations of the flow system in Fig. 2, calculations were performed for steady

**Figure 1.**

System for vaporizing metal by means of energy from an electron beam.

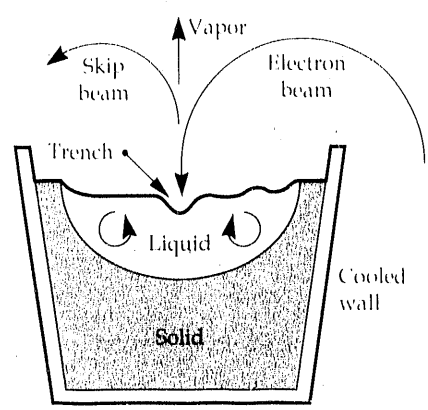


**Figure 2.**

Coordinates, boundary conditions, and 12 · 32 finite-element mesh for free convection in a rectangular cavity. $v_x$ and $v_y$ are dimensionless velocity components in coordinate directions, and $T$ is the dimensionless temperature.

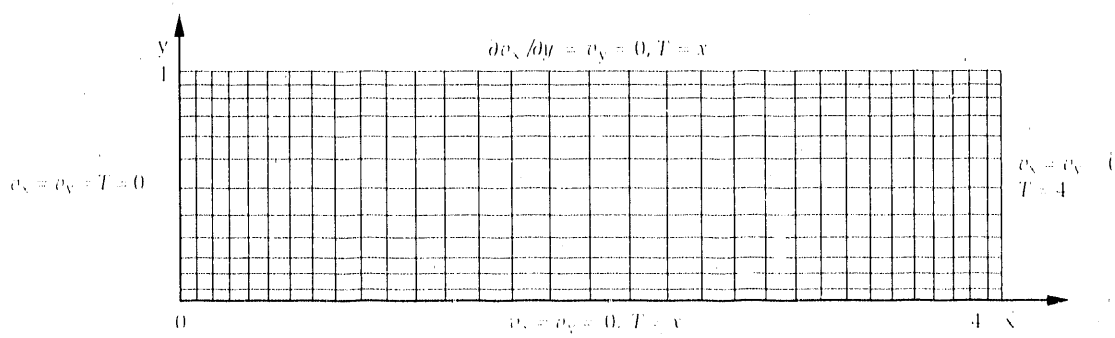

and periodic flows.[1-3] Here, we present results for higher circulation rates in the transition region.

## Theory

The differential conservation equations for mass, momentum, and energy[4] are solved to obtain velocity, pressure, and temperature profiles. In these expressions, all physical properties are assumed to be constant except for the density, which decreases linearly with temperature. Writing the equations of change in terms of scaled variables, we obtain the Grashof and Prandtl numbers as dimensionless groups that characterize the flow:

$$\mathrm{Gr} = \frac{\beta \Delta T g H^4}{L \nu^2}, \quad \mathrm{Pr} = \frac{\nu}{\alpha} \quad . \tag{1}$$

Here $H$ and $L$ are the height and length of the cavity, $\Delta T$ is the temperature difference over the length of the cavity, and $\beta$, $\nu$, and $\alpha$ are the volumetric expansion coefficient, kinematic viscosity, and thermal diffusivity, respectively. The Grashof number is a characteristic ratio of buoyancy forces that drive the flow to viscous forces; the latter resist flow. The Prandtl number is a representative ratio of momentum diffusion to thermal diffusion. For liquid metals, values of Pr are low; we use Pr = 0.015.

The problem statement is complete with the specification of boundary conditions (see Fig. 2). The vertical boundaries are maintained at different temperatures, while linearly interpolated temperatures are used on the horizontal boundaries. The liquid sticks to all of the boundaries except the top one, which is taken to have perfect slip.

## Numerical Method

At the large circulation rates of interest, high spatial and temporal resolution is required for accurate solutions. Unfortunately, this resolution generally requires excessive amounts of computing time, while lesser resolution leads to solutions with spurious oscillations. In the latter case, these oscillations can propagate and overwhelm a solution. In addition, a great deal of computation time may be required to track these oscillations. To treat this problem, we use an approach based in part on the "splitting-up" Taylor-Galerkin method developed by Donea et al.[5] In our approach, dispersion is applied in the local direction of flow, where it is needed most. Spurious oscillations can be reduced while smoothing solutions to a minimum extent. For liquid metals, the convection of momentum is much larger than the convection of energy, and we introduce dispersion in the momentum equation alone. The results given below are characterized in terms of the Grashof number that is defined above and a smaller streamwise Grashof number, $\mathrm{Gr}_{sw}$, which accounts for the additional momentum dispersion (viscosity) in the flow direction.

The Galerkin finite method is used to solve the equations of change with the streamwise dispersion terms.[6] Within a given element, nine-node biquadratic functions are used to represent the velocity and temperature, while four-node bilinear functions are used to represent the pressure. A fully implicit backward Euler method with automatic step-size control is used to perform the time integration.[7] The algebraic equations are solved using the Newton-Raphson method in which the final matrix problem is handled using a Frontal solver.

**Figure 3.**

Streamlines and temperature contours at four times, with $\mathrm{Gr} = 1 \times 10^6$ and the $18 \times 48$ mesh. Contours for the stream function are plotted in 12 equal increments that span the range of values. Temperature contours are plotted in 10 increments, from $T = 0$ at $x = 0$ to $T = 4$ at $x = 4$ (see Fig. 2).

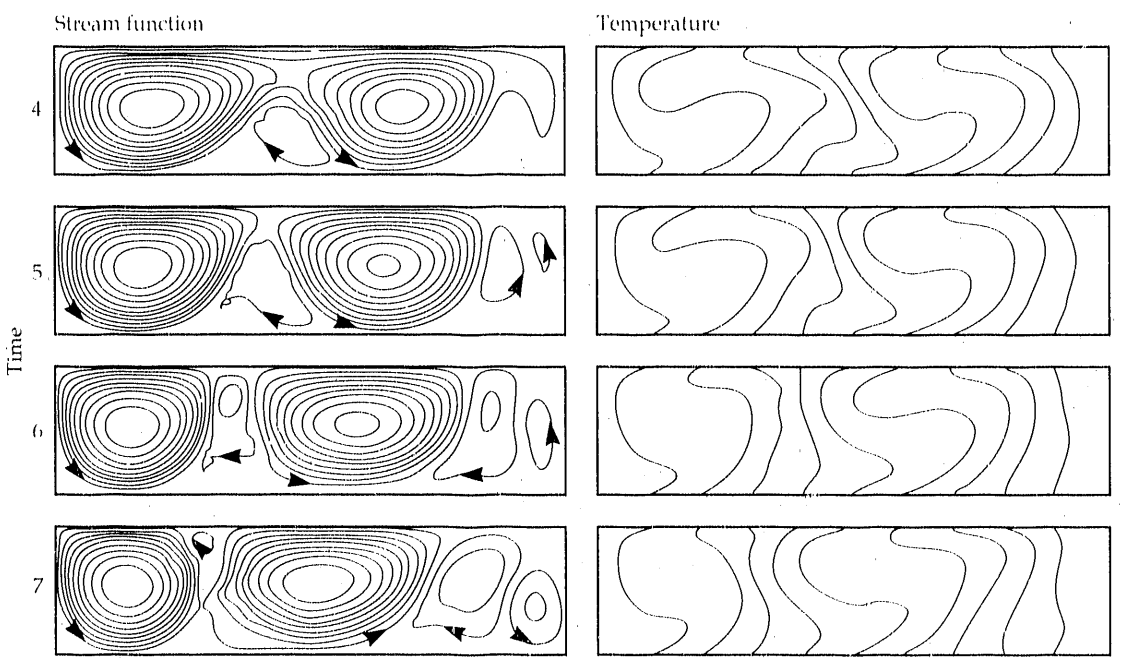

Two graded meshes of differing refinement are used in this investigation. The $12 \times 32$ mesh shown in Fig. 2 has 5259 unknowns, while a finer $18 \times 48$ mesh has 11,631 unknowns. On a VAX 8650, approximately 70 and 200 h of CPU time are required to perform typical calculations for the coarse and fine meshes, respectively.

## Results

Figure 3 shows streamlines and temperature contours for a Grashof number of $1 \times 10^6$, which corresponds to a moderately difficult case in the transition-flow region. Although the flow primarily circulates in the counterclockwise direction, there is considerable variation in time as vortices form, move, and disappear. The smooth contours suggest that adequate resolution is achieved with the fine mesh. Figure 4 shows the center-point temperature plotted vs time. In the absence of streamwise dispersion ($Gr_{sw} = 1 \times 10^6$), use of the coarse mesh yields spurious oscillations. The introduction of a large amount of dispersion ($Gr_{sw} = 2.5 \times 10^5$) eliminates these oscillations but is detrimental to the solution. For an intermediate case, with $Gr_{sw} = 5.63 \times 10^5$, the oscillations are reduced without compromising the solution. For flows with higher circulation rates, the introduction of streamwise dispersion will be essential for obtaining good solutions.

*This work was supported by the Isotope Separation and Materials Processing Program.*

## References

1. M. J. Crochet, F. T. Geyling, and J. J. Van Schaftingen, *Int. J. Num. Methods Fluids* **7**, 29–47 (1987).
2. K. H. Winters, *Proc. 5th Int. Conf. on Numerical Methods in Thermal Problems, Montreal, June 1987*, R. W. Lewis, K. Morgan, and W. G. Habashi, Eds. (Pineridge Press, Swansea, 1987), pp. 299–310.
3. B. Roux (Ed.), *Proc. Conf. Numerical Simulation of Oscillatory Convection in Low Pr Fluids, Marseille, France, October 12–14, 1988* (Vieweg, 1989).
4. R. B. Bird, W. E. Stewart, and E. N. Lightfoot, *Transport Phenomena* (Wiley, 1960), p. 320.
5. J. Donea, S. Giuliani, H. Laval, and L. Quartapelle, *Comp. Methods Appl. Mech. Engr.* **45**, 123–145 (1984).
6. B. A. Finlayson and M. A. McClelland, *Numerical Methods in Heat Transfer, III*, R. W. Lewis and K. Morgan, Eds. (Wiley, Chichester, England, 1985), pp. 269–287.
7. S. L. Josse and B. A. Finlayson, *J. Non-Newt. Fluid Mech.* **16**, 13–36 (1984).

**Figure 4.** Dimensionless center-point temperature for $Gr = 1 \times 10^6$ and two meshes. $Gr_{sw}$ decreases as additional viscosity is introduced in the local flow direction.

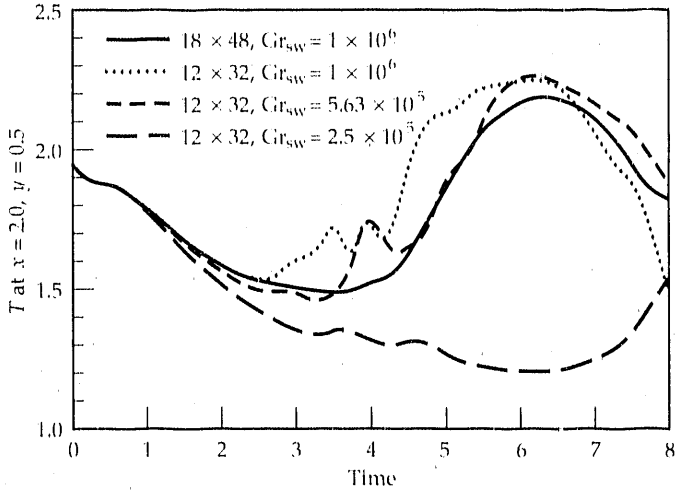

# Overview

The suitability of a material for a specific application often depends as much upon its surface as it does upon its bulk properties. In fact, in many instances it is the former that is the major consideration. The C&MS Department conducts research on a wide variety of phenomena and fabrication processes in which surfaces play an important role, including the joining of different materials by welding or diffusion bonding; the resistance of substances to degradation by corrosion; the reactions occurring at internal interfaces, such as grain boundaries, which can profoundly alter bulk mechanical properties; and catalysis and sintering. Because the C&MS Department has programmatic responsibilities in these areas, it supports substantial research on the chemical, physical, and metallurgical behavior of surfaces and interfaces. These activities are further encouraged by the lack of information about new materials, whose response to even conventional usage is perforce unknown.

The joining of more or less exotic materials to one another has become a standard request made of the C&MS Department. Silver interlayers are frequently used to weld metals and alloys such as uranium, beryllium, aluminum, and steel. A recent investigation has disclosed that plastic strain in the silver weld is the primary cause of failure. Additional research has demonstrated the synergistic effect of stressing the specimens in a humid atmosphere. Tests led to catastrophic stress corrosion cracking, although water vapor in the absence of stress produced no noticeable effect.

Grain boundaries and dislocations are frequently attractive locations for the accumulation of impurities and are often preferred nucleation sites for unwanted phases. The mechanical properties of a solid can be seriously degraded by such phenomena, in particular the latter. As a result, we are performing fundamental theoretical work to calculate the electronic structure of interfaces and extended defects.

We have devised experimental methods for the direct measurement of the bond strength between layers of metal and ceramic materials. The free-surface velocity produced by shock-induced spalling is measured by laser interferometry. An important initial conclusion is that the interfacial bonds break simultaneously, as the measured times for debonding are too short to allow for crack propagation. The bonding of metals to ceramics is often used in LLNL's emerging technologies. This new technique should greatly assist our effort at improving the strength of such joins.

The atomic mismatch at the interface of multilayer metallic systems produces strain. We have measured the strains in a gold-nickel multilayer system. Our theoretical interpretation relates the strain to the atomic displacements and can explain both the stiffening and softening of the biaxial elastic modulus. The model is also applicable to strained superlattice structures.

An experimental and theoretical investigation is under way that leads to a method of uniformly depositing reflecting coatings on mirrors. Such coatings will protect the beam-turning mirrors of the Nova laser from the current undesirably high levels of radiation damage. Using naphthalene as a trial substance, we have designed a plasma-initiated chemical vapor deposition apparatus that will produce radially uniform layers of $SiO_2$.

Withstanding higher temperatures and increasingly harsh chemical environments is a frequent requirement of materials in a world of advancing technology. One response to these stringent specifications is the use of protective coatings, which allow the mechanical advantages of the otherwise reactive base material to be retained. We have been developing corrosion-resistant coatings for a variety of high-melting metals and alloys, and we report our findings on several types of coatings that protect against high-temperature oxidation or attack by molten metals.

Section 4

# Surfaces and Interfaces

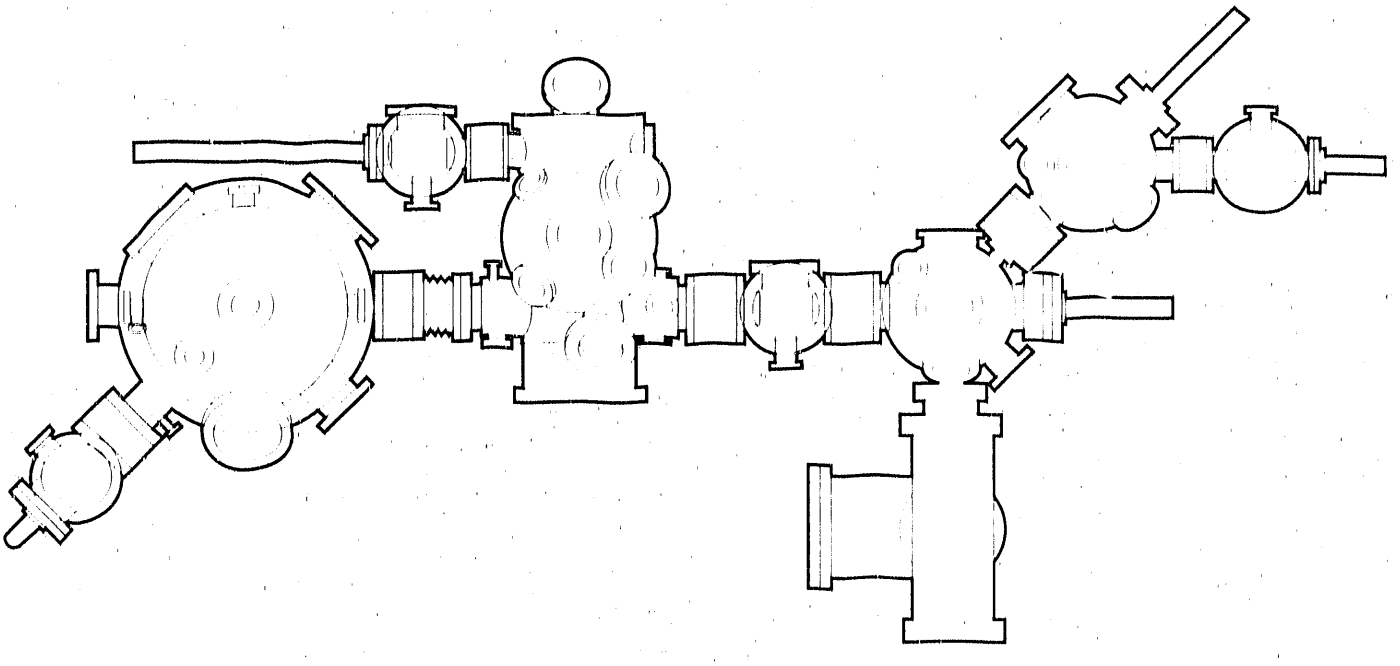

Diffusion-bonding machine

# Delayed Failure of Thin Interlayer Diffusion Welds

R. S. Rosen and
M. E. Kassner

*We have studied the mechanical behavior of diffusion-welded silver joints and identified three classes of delayed failure. For the case of an applied stress that does not produce plastic deformation in the base metals, failure appears to be controlled by time-dependent plasticity within the silver interlayer. In the second case, base metals that deform plastically accelerate failure within the interlayer. For the case of "reactive" base metals such as uranium, failure may be further accelerated by stress-corrosion cracking (SCC) at the silver/base-metal interface.*

## Introduction

The use of metal interlayers for low-temperature diffusion welding may be appropriate under some conditions. This technique may be employed when excessive stresses from differential thermal contraction during cooling or from persistent oxides preclude the use of conventional methods of joining the base metals, such as fusion welding or brazing. High-strength joints can be fabricated at relatively low temperatures and pressures using silver. Silver interlayers are usually applied to the base metals by physical vapor deposition in vacuum. To achieve adequate adhesion of the silver, the surface oxide must be removed from the base metal by sputter-etching before deposition.

Materials that have been joined by this method include uranium, beryllium, aluminum, and steel. Figure 1 shows a typical silver-silver diffusion weld with a 150-μm-thick interlayer deposited by planar-magnetron sputtering. The details of fabrication are discussed in Ref. 1. The high tensile strength of joints formed in this way is due to the mechanical constraint provided by the nondeforming base metals, which restricts transverse contraction of the interlayer. The constraint produces a triaxial state of stress and reduces the effective stress, thus reducing the tendency of the joint to plastically deform. The reduction in plasticity inhibits ductile failure.

Our study had two objectives. The first was to determine whether mechanical delayed failure occurs under conditions of constant tensile stress in specimens fabricated using elastic base metals (which do not show evidence of time-dependent plasticity) and plastic base metals (for which there is some plasticity). Common structural materials frequently exhibit some time-dependent plasticity or creep. Very-high-strength metals, ceramics, and ordinary metals at low stresses show only elastic deflections under stress. For the case in which delayed failure is observed, our goal was to formulate detailed mechanisms. The second objective of this study concerned SCC, which is known to occur in metals such as uranium in humid air. We wanted to determine whether SCC also occurs at the uranium-silver interfaces under tensile and shear loading.

**Figure 1.**

Diffusion-welded silver interlayer between steel base metals. Joint thickness is 150 μm.

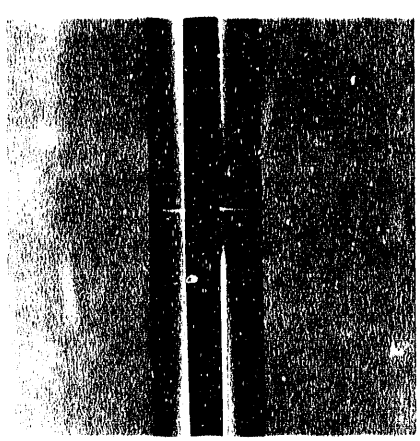

## Delayed Mechanical Failure

Our study confirmed the occurrence of delayed failure in silver joints between both elastic and plastic base metals. Figure 2 shows the creep rupture time as a function of applied stress for diffusion-welded silver joints between maraging steel and between the relatively soft annealed Type 304 stainless steel. The figure shows that as the applied stress decreases, the rupture time substantially increases. Delayed tensile failure was observed at stresses as low as 20% of the ultimate tensile strength. Fracture in either type of specimen occurred principally at the silver-silver interface and exhibited classic microvoid coalescence.

The silver-silver interface in specimens loaded to various fractions (1, 10, 25, and 99%) of the expected rupture time at a given stress was examined by transmission and scanning electron microscopy. These results suggest that failure is most likely controlled by the nucleation, growth, and interlinking of cavities resulting from plastic deformation (creep) of the silver. This explanation of failure is also supported by an analysis of the temperature dependence of failure and by finite-element-method analysis of the plastic strain in the interlayer.

For the same applied stress, the rupture times for diffusion-welded silver joints between maraging steels are higher than bonds between plastically deforming (creeping) annealed stainless steels. We determined plastic strain vs time in both the silver interlayer and the stainless steel base metals by direct measurements. These results confirm that creep plasticity in the stainless steel base metal near the interlayer, which is controlled by the effective (von Mises) stress in this region, induces concomitant plastic strain within the interlayer, thereby accelerating delayed failure.

In summary, for the case of elastic base materials, plasticity within the interlayer occurs under the action of the effective stresses within the interlayer; and cavities are nucleated. Cavity concentration increases with plastic strain, and failure occurs by ductile microvoid coalescence. Significant plasticity of the base metal accelerates shear within the interlayer, and cavity nucleation again occurs at or very near one or more of the three interfaces. Catastrophic ductile failure by microvoid coalescence occurs when the concentration is sufficient for interlinkage. The faster of the above two creep rates determines the failure time. A detailed explanation of the mechanical failure mechanism is given in Refs. 2 and 3. It should be emphasized that these findings are applicable to joints in which the interlayers are prepared by processes other than physical vapor deposition (brazing, electroplating, solid foils, etc.).

## Environmentally Induced Failure

We also fabricated silver-interlayer diffusion welds between uranium and stainless steel. These joints were machined into a bend-test configuration for environmental testing under tensile stress (the bend test induces tensile stress). Bend-test specimens were loaded to 1/2, 1/3, or 1/6 of the ultimate strength and placed in laboratory air [40% relative humidity (RH)] or saturated water vapor for various periods of time or until specimen fracture. Bend-test results indicate that air of 100% RH causes catastrophic SCC at uranium-silver interfaces when the joints are simultaneously subjected to applied or residual stresses. The results also suggest a trend of increasing time-to-fracture with decreasing applied tensile stress. Specimens subjected to the same 100% RH in an unstressed state exhibited no loss in strength even after lengthy exposure. Somewhat lower humidities (≈100% RH) are also expected to induce delayed failure by SCC. A detailed explanation of this phenomenon is given in Ref. 4.

## Conclusions

Although high-strength joints can be fabricated using diffusion-welded silver interlayers, these joints may be susceptible to delayed failure at stresses well below the ultimate strength. The following conclusions regarding the failure mechanisms are based on our delayed-failure experiments. For diffusion welds utilizing essentially elastic base materials, the time-to-failure is controlled by the creep rate of silver in the interlayer, which is determined by the effective stress within the interlayer. For diffusion welds between essentially plastic base materials, the interlayer creep rate may be accelerated by base-material creep resulting from the effective stress in the base material. For the case of "reactive" base metals such as uranium, failure may be further accelerated by SCC at the silver/base-metal interface.

*This work was supported by Weapons Supporting Research.*

## References

1. R. S. Rosen and M. E. Kassner, *J. Vac. Sci. Technol. A* (in press).
2. J. W. Elmer, M. E. Kassner, and R. S. Rosen, *Weld. J.* **67**, 157s–162s (1988).
3. M. E. Kassner, R. S. Rosen, G. A. Henshall, and W. E. King, *Brazing, High Temperature Brazing, and Diffusion Welding* (DVS-Verlag, Düsseldorf, FRG, 1989), pp. 47–52.
4. R. S. Rosen, S. Beitscher, and M. E. Kassner, *Proc. Int. Conf. Environment-Induced Cracking of Metals, Kohler, Wis.* Also, Lawrence Livermore National Laboratory, Livermore, Calif., UCRL-97917 (1988).

**Figure 2.** **Rupture time vs applied stress for diffusion-welded silver joints between maraging steel and for joints between annealed stainless steel, at ambient temperature. The maraging steel only strains elastically, whereas the stainless steel creeps at these stresses.**

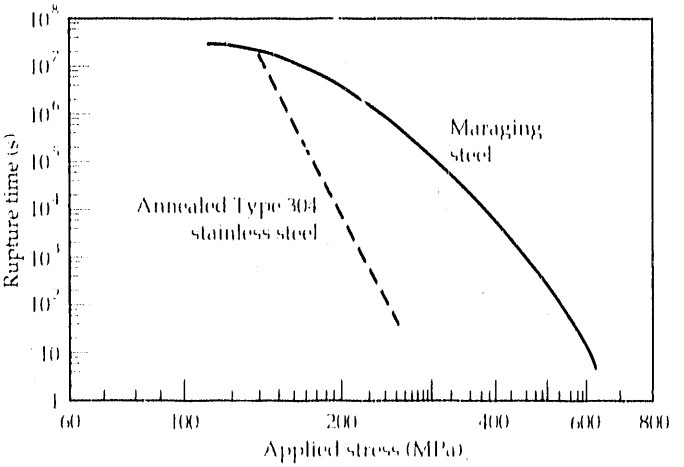

# Real-Space Calculation of the Electronic Structure of Systems with Reduced Symmetry: Application to Grain Boundaries

E. C. Sowa, A. Gonis, X.-G. Zhang,* and S. M. Foiles†

*We report the first application of the recently developed real-space multiple-scattering theory to the calculation of the local density-of-states (DOS) at metallic grain boundaries. Our method treats properly the semi-infinite nature of the material on either side of the boundary. We compare local DOSs at selected sites for both unrelaxed and relaxed Σ5 (100) 36.9°-twist grain boundaries in copper. The atomic coordinates of the relaxed configurations were obtained with the embedded atom method (EAM). This article briefly discusses the main features of our method.*

## Introduction

In determining the electronic structure and the associated physical and mechanical properties of condensed matter, it is convenient to distinguish three types of materials according to the arrangement of their atoms in space. These three types are (1) materials possessing translational invariance, (2) materials in which translational symmetry is broken along one or more directions, and (3) materials with no recognizable periodic structure.

Materials of the first type can be thought of as being generated by the translation of a spatially finite unit cell through basis vectors along a prescribed set of axes; this group includes fully periodic, bulk elemental solids and two-dimensional periodic films of finite thickness. The second class contains materials characterized by the presence of regions through which translational symmetry is broken, such as surfaces and internal interfaces. Amorphous materials, e.g., glasses and liquids, may serve as representatives of the third type. The ability to calculate electronic structures relies on a knowledge of the atomic structure of a material and on methods, both formal and computational, for treating the structure at hand.

In the case of materials with full translational periodicity, the atomic structure can often be determined experimentally, through, for example, x-ray crystallography. Once this structure is known, the electronic structure can be obtained through the use of Bloch's theorem and the associated lattice Fourier transforms, which allow the exact diagonalization of the Hamiltonian in reciprocal space (k-space).

In the case of systems with reduced symmetry, e.g., surfaces and grain boundaries, and in the case of amorphous materials, determining both the atomic and the electronic structure becomes much more problematic. The experimental determination of surface atomic structure through, for example, low-energy electron diffraction[1] is often limited to surfaces with a low Miller index. Recently, the technique of scanning tunneling microscopy (STM)[2,3] has successfully produced direct space images of atomic positions on surfaces as well as of organic molecules adsorbed on selected substrates. On the other hand, none of these techniques can be used to image atomic positions at internal interfaces. In this case, partial information may be obtained experimentally through electron microscopy, but one must usually rely on computer simulation studies such as those afforded by the EAM.[4,5]

Finally, the description of amorphous materials and liquids often consists of experimentally or numerically determined pair-distribution functions. There is at present no fully satisfactory first-principles method for calculating the electronic properties of structurally disordered materials.

Unlike materials with regular lattice structures, for the second class of systems discussed above, knowledge of atomic coordinates does not necessarily allow the calculation of electronic structure through conventional methods. Nearly all existing, fully first-principles formalisms for performing such calculations require translational invariance and the use of Bloch's theorem. Consequently, it has often been found necessary to invoke rather severe approximations with respect to the structure of a system,

such as the use of slabs of finite thickness to treat surfaces, or of repeating slabs or supercells to study internal interfaces. Such approximations are highly undesirable for several reasons. First, they are "uncontrolled," yielding results which should be checked for dependence on slab thickness on a case-by-case basis. Second, they are conceptually unattractive, involving rather severe approximations to the underlying geometry of the system. Third, the extent to which they may yield accurate results may lull one into a false sense of accomplishment, obscuring the existence of a still-unsolved problem.

This problem, stated briefly, consists of finding the solution of the one-particle Schrödinger equation, within the Born-Oppenheimer approximation (fixed nuclei) and the local-density approximation to density functional theory, that satisfies the proper boundary conditions imposed by the structure of a particular semi-infinite material.

## Methodology

In a recent publication,[6] a first-principles multiple-scattering formalism was introduced that allows the exact treatment of the problem just stated. This formalism provides a unified treatment of the electronic properties of a broad spectrum of systems that includes, but is not limited to, pure elemental solids, compounds, ordered alloys, surfaces and interfaces, and other low-symmetry systems. As the formal aspects of this real-space multiple-scattering theory (RSMST) method have been reviewed in previous work,[6,7] we forgo a description of the method here.

## Computational Results

In the calculations reported here, we used the self-consistent potentials for bulk copper given by Moruzzi et al.[8] The atomic coordinates of the unrelaxed grain boundaries are easily found through an appropriate twisting or tilting of one-half of the underlying lattice. These appear to be the first ab initio electronic DOS calculations of a twist grain boundary. We used the EAM to obtain the atomic coordinates of relaxed twist and tilt grain boundaries in copper.

Figure 1 displays the electronic local DOSs corresponding to a coincidence site (a site that is common to the lattices on both sides of an interface) at both an unrelaxed and a relaxed Σ5 (100) 36.9°-twist grain boundary in copper compared with the DOS for bulk copper. The unrelaxed DOS exhibits considerable smearing of structure compared with the bulk DOS because of the loss of periodicity and the associated destruction of the Van Hove singularities. The grain-boundary DOS is slightly broader than that of the bulk material because of the decreased distance between some of the copper atoms across the interface. (In fact, simply twisting one-half of the crystal with respect to the other results in some of the atoms overlapping across the boundary.)

The results of the EAM calculations indicate that the interplanar spacing increases by about 20 percent across the interface from its bulk value, decreases by 2 percent in the next set of layers, and remains essentially unchanged in layers deeper inside the material. In these first calculations, we included only the 20 percent expansion at the boundary layer, which is the dominant effect. It is seen in Fig. 1(b) that the DOS at the grain boundary is indeed narrower than that of bulk copper. It is also seen that the DOS for the relaxed grain boundary is shifted slightly toward lower energies compared both with that of bulk copper and that of the unrelaxed configuration, and that it possesses somewhat sharper structure than the DOS at an unrelaxed grain boundary [solid curve in Fig. 1(a)].

## Discussion

As these calculations illustrate, the RSMST method allows one to obtain the electronic structure of materials with extended defects, such as surfaces and interfaces, on an atom-by-atom basis. Although our code is

**Figure 1.** Electronic DOS associated with a coincidence site at a Σ5 (100) 36.9° -twist grain boundary in copper. (a) Unrelaxed configuation. (b) Relaxed configuration.

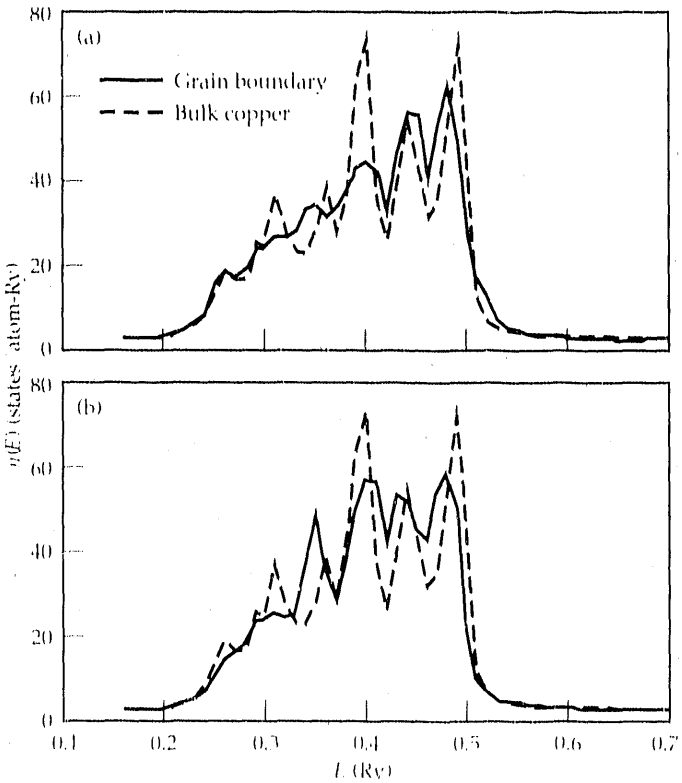

presently slower than those based on conventional methods when applied to systems of high symmetry, it holds the distinct advantage of being applicable to low-symmetry structures that are not otherwise amenable to treatment. We are currently attempting to increase the efficiency of our codes as well as to incorporate charge self-consistency and total-energy capabilities into them.

*This work was supported by Institutional Research & Development and by the Division of Materials Science of the DOE Office of Basic Energy Sciences.*

*Northwestern University, Evanston, Ill.
†Sandia National Laboratories, Livermore, Calif.

## References

1. M. A. Van Hove, W. H. Weinberg, and C.-M. Chan, *Low-Energy Electron Diffraction* (Springer Verlag, N.Y., 1986).
2. G. Binnig, H. Rohrer, C. Gerber, and E. Weibel, *Phys. Rev. Lett.* **49**, 57 (1982).
3. T. P. Beebe, Jr., T. E. Wilson, D. F. Ogletree, J. E. Katz, R. Balhorn, M. B. Salmeron, and W. J. Siekhaus, *Science* **243**, 370 (1989).
4. M. S. Daw and M. I. Baskes, *Phys. Rev. B* **29**, 6443 (1984).
5. S. M. Foiles, "Calculation of the Structure of Gold Grain Boundaries Using the Embedded Atom Method," in *Proc. Fall 1988 Meeting of the Materials Research Society* (in press).
6. X.-G. Zhang and A. Gonis, *Phys. Rev. Lett.* **62**, 1161 (1989).
7. X.-G. Zhang, A. Gonis, and J. MacLaren, *Phys. Rev. B* (in press).
8. V. L. Moruzzi, J. F. Janak, and A. R. Williams, *Calculated Electronic Properties of Metals* (Pergamon Press, N.Y., 1978).

# Direct Measurement of Interface Bond Strength

G. L. Nutt, W. Lai, K. E. Froeschner,* and W. E. King

*We have demonstrated a novel method of measuring the bond strength of metal/ceramic interfaces. A short planar shock pulse is launched into a target composed of a ceramic substrate and a vapor-deposited metal overlayer. If the shape and amplitude of the wave are properly controlled, the interface will spontaneously debond. The free-surface velocity of the metal film, which is related to the bond strength, is monitored during spall by laser interferometry. Debonding occurs in less than 1.0 ns, a time too short for crack propagation along existing flaws. We conclude that simultaneous breaking of atomic bonds, rather than propagation and coalescence of cracks, is the way in which the film and substrate are separated.*

## Introduction

The cohesive strength of homogeneous materials is commonly tested by spalling them with triangular-shaped shock waves.[1-3] Bond strengths have also been investigated using laser-induced spallation.[4]

We have constructed a "magnetic hammer" for a series of experiments intended to measure the bond strength of metal/ceramic interfaces. As shown schematically in Fig. 1, a metal flyer and a ceramic substrate with a metal overlayer are the basic experimental components. Upon impact, a shock wave is generated that propagates through the substrate and film. At the free surface, the compressive wave is reflected as a tensile wave that is subsequently incident on the bonded interface, as indicated in Fig. 2. If the tensile stress at the bond surface, $\sigma_z$, exceeds the strength of the bond, $\sigma_s$, the interface will spall.

Novikov and Chernov[2] have discussed a method of determining spall stress by measuring the free-surface velocity of the spall. The spall stress is related to the velocity measurements through the relation

$$\sigma_s = \frac{\rho_0 C}{2}(u_0 - u_k) \quad , \tag{1}$$

where $\sigma_s$ is the stress on the interface at the instant of rupture, $\rho_0$ is the density of the film, $C$ is the velocity of propagation of the stress wave of the free surface of the scab, $u_0$ is the initial jump-off velocity, and $u_k$ is the

**Figure 1.**

Flyer impacting a specimen that has a laser-illuminated free metal surface.

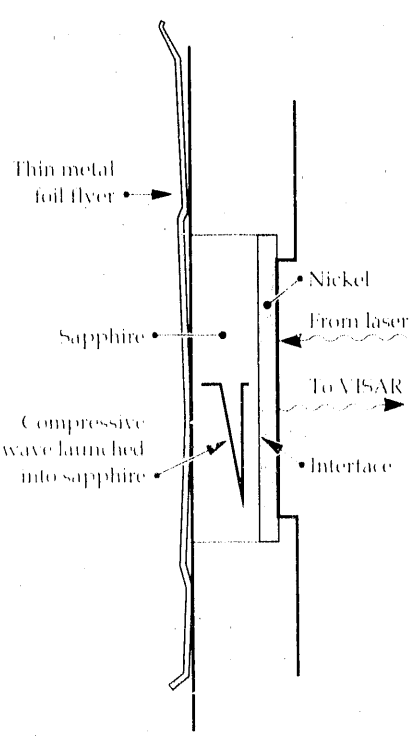


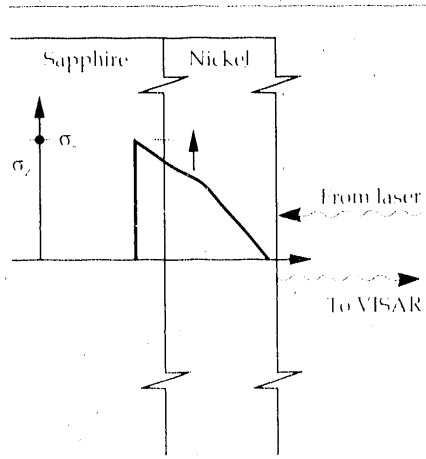


**Figure 2.**

Reflected tensile wave interacting with the bond interface. Stress at the bond rises toward a critical value. The bond is ruptured and a free surface is created at the interface.

velocity at the first pull-back. The relationships among the parameters in Eq. (1) and the signal from a laser interferometer are shown in Fig. 3. We measure the bond strength directly by monitoring the velocity of the free surface of the spalled film using a laser interferometer.

The time-position plot in Fig. 3 correlates the wave and particle motions in the specimen with the velocity of the film surface. The time of arrival of the shock at the surface is $t_0$, and $t_k$ is the time at which the signal from the newly created surface at the spall plane arrives at the film surface. Velocities $u_0$ and $u_k$ correspond to times $t_0$ and $t_k$, respectively.

This interpretation of the measured velocity history in terms of bond strength is valid if the amplitude of the stress wave is not great enough to cause the material to deform plastically, i.e., the axial stress does not exceed the Hugoniot elastic limit (HEL) of the material. In this case, $C$ is the elastic sound speed of the metal film. Eq. (1) applies to interfacial bonds between strong materials. If the stress wave is great enough to introduce some plasticity into the film, the appropriate value of $C$ is the harmonic mean of the elastic and plastic sound speeds.[3]

Attachments to the specimen can affect the bond by introducing residual stress. The measurement of bond strength requires that the bond be ruptured rapidly so that separation does not occur through growth of cracks, which focuses stress concentrations at the edge of the crack. Needless to say, the critical stress for separation by crack growth is not simply related to the molecular forces of attachment across the interface. In ductile materials, the stress depends on the plastic deformation in the neighborhood of the crack tip. Consequently, two of the most important features of our method are that no fixtures are attached to the specimen and that rapid rise times are possible in the application of the tensile stress.

The time required for debonding by crack growth can be estimated from Young's modulus $E$ and the surface tension of the crack, $T$ (Ref. 5):

$$\dot{l}^2 = \frac{2\pi E}{k\rho}\left(1 - \frac{l_0}{l}\right)\left(1 + \frac{l_0}{l} - \frac{4TE}{\pi\sigma^2 l}\right), \qquad (2)$$

where $\sigma$ is the tensile stress, $l$ is the instantaneous crack length, $l_0$ is the initial crack length, and $k$ is a dimensionless constant. For typical values ($T = 2$ J/m$^2$ and $E = 7 \times 10^4$ J/cm$^3$), and a stress of 0.1 GPa, the cracks that propagate are greater than 1 μm in size. At slightly above the threshold stress, a 1-μm crack doubles in size on a time scale of 100 ns, while free-surface velocity measurements show that the rise time of the stress pulse is less than 1 ns. Hence, with sufficient care in sample preparation, it is expected that bond rupture will be the mechanism of separation in this experiment rather than propagation and merging of cracks.

**Figure 3.** Characteristics and corresponding velocity history of the free surface.

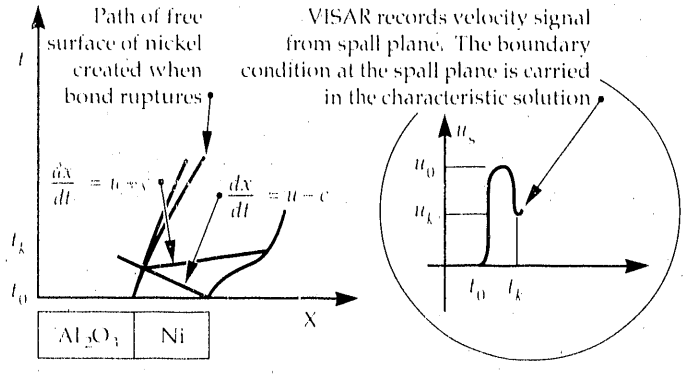


## Experiment

A power supply is used to charge two 14-μF capacitors as high as 20 kV. A trigger generator causes the stored charge to flow through an armature via a spark-gap switch, as shown in Fig. 4. The current flowing through the foil and back through the return creates an electromagnetic force, causing the foil to shear along the rails and to accelerate until it impacts the specimen.

Laser light reflected from the surface of the film is split into two portions, one of which is sent through a delay.

**Figure 4.**

The armature and specimen holder assembly of the magnetic hammer.

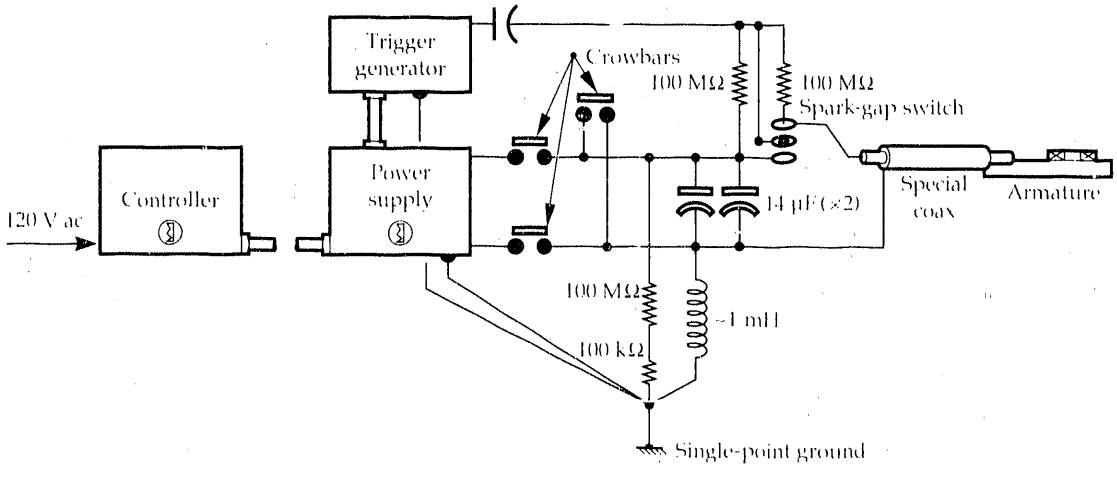

The two portions of the reflected light are then mixed to give the velocity change in the surface during the delay. Interference fringes are recorded on photomultipliers, and a five-point running average is made of the raw digital data to smooth the photon noise. The velocity history of the free surface is calculated using the length of the delay section of the interferometer, the index of refraction of the etalon block, and the laser frequency.

Samples were prepared by sputter deposition of 20 μm of nickel on a sapphire substrate at room temperature. The sapphire was 1.27 cm in diameter and 0.32 cm thick. The substrate was impacted with a copper flyer 0.0064 cm thick at velocities in the range of 0.020 to 0.029 cm/μs. This method produced a peak axial stress in the nickel film in the range of 2.4 to 3.5 GPa near the interface, with a pulse 32 ns long. The yield strength $Y$ of nickel is nominally 1.2 GPa, and the HEL of sapphire is 14 GPa. The relation between HEL and dynamic yield strength is

$$\sigma_{HEL} = \frac{1-\nu}{1-2\nu} Y \quad , \tag{3}$$

where $\nu$ is Poisson's ratio.

## Results and Conclusions

Figure 5 shows a typical measured free-surface velocity. The rise time of the incident shock is too short to record, even with 3-ns resolution. The ringing period of the metal film, estimated from an elastic sound speed of 0.587 cm/μs for nickel, is about 6.8 ns and is clearly evident. Upon recovery of the test specimens, we found the nickel film attached around the edge, but the foil was detached in the center, with a "dog ear" occasionally standing as evidence of film separation. Thus, after initial separation, the foil near the center would return to contact with the substrate. The source of the other oscillations appearing in the velocity data is thought to be ringing of the flyer. For example, the 21.0-ns ringing period of the copper flyer appears for at least two cycles. Any two-dimensional effects in the form of relief waves from the lateral surfaces are estimated to appear around 0.24 μs after jump-off.

Table 1 shows four determinations of the cohesive strength of the sapphire-nickel bond. If we take the HEL of nickel as 2.1 GPa from Eq. (3), using $\nu = 0.3$, the data fall in a limited region where the transition from elastic to plastic behavior of the metal film occurs. Limiting the stress to less than 1.0 GPa would have ensured that the nickel remained in the elastic region. However, our main objective in these exploratory measurements was to demonstrate that spall occurred.

Except for shot 16, the elastic sound speed is used for calculation of the bond strength. Since the stress wave in shot 16 exceeded the HEL of nickel, the harmonic mean of the plastic and elastic sound speeds is used, as recommended by Romanchenko and Stepanov.[3] The tabulated data give the mean value of 0.177 ± 0.024 GPa for the spall strength of the bond.

Lower flyer velocities will improve the signal-to-noise ratio of the measured velocities and avoid a plastic condition in the metal overlayer. Time resolution on the order of 1 ns is possible using a VISAR laser interferometer. We expect to improve on the accuracy of these promising results.

*This work was supported by Weapons Supporting Research.*

*Martin, Froeschner & Associates, Livermore, Calif.

## References


1. K. E. Froeschner, D. Maiden, and H. Chou, "Spall due to Short High-Intensity Impulses," *J. Appl. Phys.* **65**(8), 2964–2973 (1989).
2. S. A. Novikov and A. V. Chernov, "Determination of the Spall Strength from Measured Values of the Specimen Free-Surface Velocity," *J. Appl. Mech. Tech. Phys.* **5**, 703–705 (1982).
3. V. I. Romanchenko and G. V. Stepanov, *J. Appl. Mech. Tech. Phys.* **21**, 555 (1980).
4. J. L. Vossen, "Measurements of Film-Substrate Bond Strength by Laser Spallation," *Proc. Symp. Adhesion Measurement of Thin Films, Thick Films, and Bulk Coatings, Philadelphia, Pa., Nov. 2–4, 1976* (ASTM, Philadelphia, Pa., 1976), ASTM Special Technical Publication No. 640, pp. 122–133.
5. D. K. Roberts and A. A. Wells, "Velocity of Brittle Fracture," *Engineering* **178**, 820–821 (1954).


**Figure 5.**

A sample velocity history of the free surface of the metal.

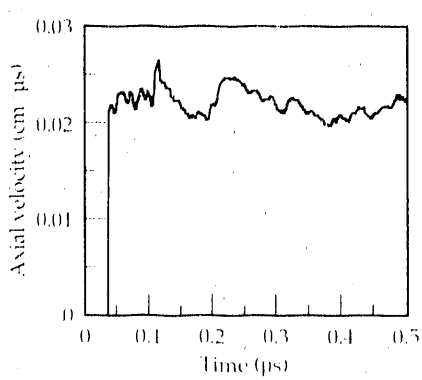


**Table 1.** Measurements of the strength of the nickel/sapphire bond.

| Shot No. | Flyer velocity (cm/μs) | Time resolution (ns) | $u_0$ (cm/μs) | $u_k$ (cm/μs) | σ (GPa) |
|---|---|---|---|---|---|
| 14 | 0.0206 | 9 | 0.0118 | 0.0111 | 0.183 |
| 16 | 0.0288 | 3 | 0.0218 | 0.0209 | 0.208 |
| 18 | 0.0202 | 5 | 0.0125 | 0.0119 | 0.156 |
| 21 | 0.0211 | 3 | 0.0114 | 0.0107 | 0.162 |

# Elastic Behavior of Multilayers

A. F. Jankowski

***The elastic moduli of alloy systems can be changed by two orders of magnitude using multilayer structures. Both increases and decreases have been measured in a variety of metal superlattice systems. We are using thin-film synthesis and a coherency strain model (CSM) to investigate the origin of such changes, which are unattainable by means of conventional bulk processing techniques.***

## Introduction

Multilayers are thin-film structures in which the composition is modulated in one dimension. When multilayers consist of metal-layer pairs, their elastic properties have values different from those obtained by bulk averaging of the components, as in the cases of semiconductor superlattices or amorphous-layer pairs.

Two techniques are predominantly used to evaluate the elastic moduli. The "bulge test"[1] measures the in-plane biaxial modulus $Y$, and "Brillouin scattering"[2] determines the shear modulus $C_{44}$ normal to the modulation planes. In general, a stiffening of the biaxial modulus by several hundred percent is observed in (111) fcc strained-layer superlattices of binary noble-transition metal systems; and a softening of the shear modulus by tens of percent is observed in (111) fcc/(110) bcc metal superlattices, as compared with those expected from a rule-of-mixtures value.

While the experimental results are reproducible, obtaining them is almost always tedious. New measurement techniques for exploring the elastic behavior may be facilitated through the use of microindentation/deflection instrumentation.[3,4]

The apparently anomalous elastic behavior of softening and stiffening is believed to result from the metastable configuration of atoms that is due to the artificial ordering created during material synthesis. This description is referred to as the CSM.[5-8]

**Figure 1.**

A gold/nickel multilayer shown in bright field, produced by transmission electron microscopy of a sample prepared in cross section. The multilayer is a result of artificial ordering produced by the sequential deposition of gold and nickel by magnetron sputtering.[12]

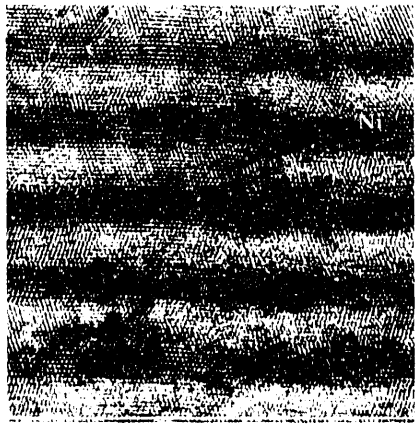


## Experiment

A strained-layer superlattice is a result of artificially ordering a crystalline system (Fig. 1). The effects of lattice distortions on the physical behavior of the alloy system are accentuated when the atomic displacements are magnified, for example, in symmetrically similar crystal systems with a large lattice misfit. The layered system chosen for our study was gold/nickel with a misfit of 15 percent. When measured by the bulge test, the biaxial elastic modulus increased more than 200 percent in micrometer-thick films of $Au_{0.5}$-$Ni_{0.5}$ layer pairs in which the repeat period was less than 3 nm.[1] Microindentation with a pyramid-shaped stylus provides a direct measurement of physical properties without the substrate removal needed for the bulge test. Table 1 shows an initial determination of the mechanical properties of 0.4-μm-thick, magnetron sputter-deposited (111) gold/nickel multilayers, where $d$ is the thickness of an individual gold/nickel layer pair, and $H$ is the hardness.[9] A maximum at $d = 2$ nm is consistent with predicted trends in modulus enhancement.[5] Elastic moduli are being determined from a separation of the elastic and plastic components of indenter load-displacement curves.

**Table 1.** Hardness ($H$) of magnetron sputter-deposited (111) gold/nickel multilayers, where $d$ is the thickness of an individual gold/nickel layer pair.[9]

| $d$ (nm) | $H$ (GPa) |
|---|---|
| 0.82 | 6.75 |
| 1.24 | 6.25 |
| 1.77 | 8.50 |
| 2.51 | 6.30 |
| 4.41 | 5.90 |

The microstructure of the gold/nickel multilayers is characterized by coherently strained interfaces. Kinematic modeling of the x-ray diffraction θ/2θ profiles indicates maximum strain at the gold-nickel interface (compressive for gold and tensile for nickel), with relaxation into the intralayer region[10] (Fig. 2). The magnitude of the strain in the growth direction decreases with longer repeat periods. A "single-phase" highly strained lattice exists for multilayers with repeat periods of less than about 3 nm. These short-period structures are therefore interface-dominated. Electron diffraction in cross-section and plan view confirms the single- to multiple-phase transition with increasing repeat period.[11] For long periods, relaxation of the lattice from the interface into the intraface results in the presence of the "bulk" lattice parameters in addition to the short-period "single phase."

## Theory

A model for modulus enhancement or softening in metallic multilayers requires structural considerations. Interaction between atoms (across the layer interfaces and within the layers) needs to be accounted for to describe the way in which atoms locally rearrange, thereby accommodating forces originating from like- or unlike-pair potentials. The influence of both the long- and short-range order for each multilayer repeat period and composition profile results in a change in the equilibrium lattice spacings from one structure having a short repeat period to the next. This idea was confirmed in the x-ray and electron microscopy examinations.

The periodic repetition in the displaced atomic positions of the distorted lattice in the modulation direction can be described in terms of a strain wave.[6] The strain wave can then be incorporated into a system-energy formulation of the elastic constants and moduli with respect to a high-order differentiation of the lattice deformation.[5] This approach comprises the CSM, in which relaxation from coherently strained interfaces is considered in modeling the metallic superlattice structure.

Results of the computations for the variation of the biaxial modulus $Y$ (100) with repeat period reproduce the modulus-enhancement, i.e., stiffening, trends observed for fcc/fcc noble-transition metals[5] [Fig. 3(a)]. The noble-metal layers are in compression, whereas the transition-metal layers are under tension. The softening in shear modulus $C_{44}$ is also reproduced using the

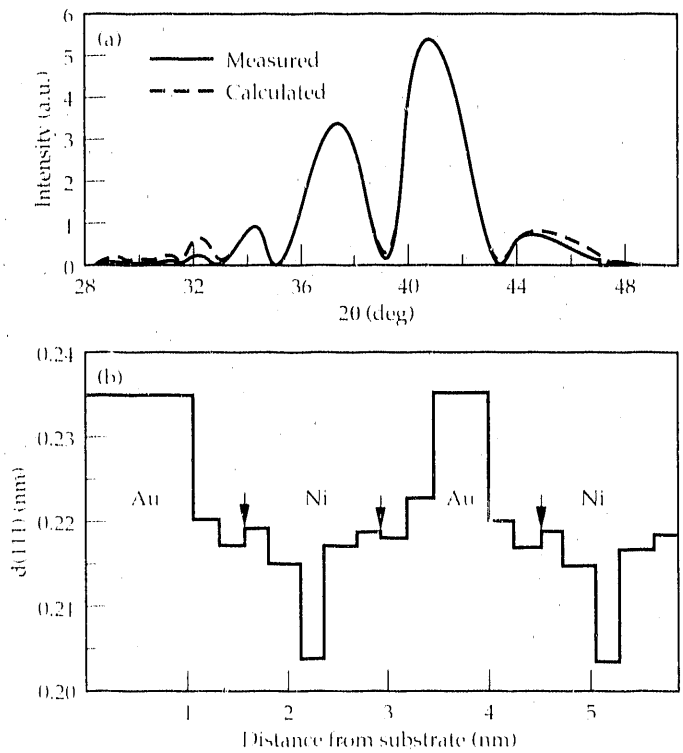


**Figure 2.** (a) Measured and calculated Cu $K_\alpha$ x-ray diffraction scans of a gold/nickel superlattice with a 2.92-nm repeat period. (b) The lattice spacing in the modulation direction, as it varies with distance from the substrate, is shown as determined from the iterative fitting of the calculated and measured diffraction curves of (a). The gold/nickel interfaces are marked by arrows.[10]

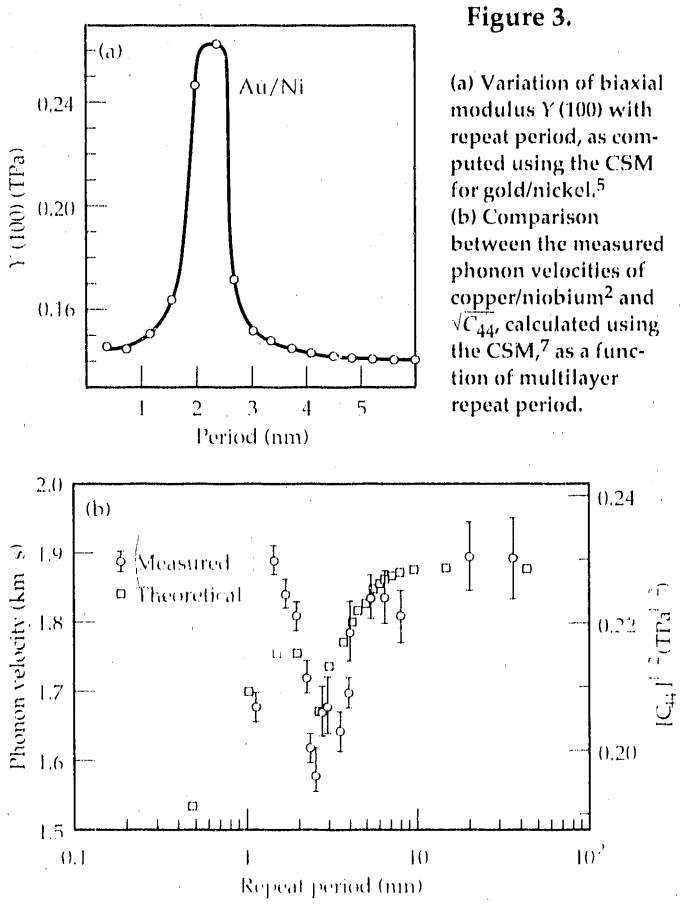


**Figure 3.** (a) Variation of biaxial modulus $Y$ (100) with repeat period, as computed using the CSM for gold/nickel.[5] (b) Comparison between the measured phonon velocities of copper/niobium[2] and $\sqrt{C_{44}}$, calculated using the CSM,[7] as a function of multilayer repeat period.

CSM. Figure 3(b) shows both experimental and calculated results for (111) Cu/(110) Nb multilayers, in which a shear component is superimposed on the fcc metal in tension and the bcc metal in compression.

## Summary

An understanding of atomic displacements in the strained-layer superlattice structures of metal systems proves essential to explaining measured elastic moduli. X-ray diffraction and electron microscopy confirm the notion of a structural strain wave in the modulation direction. We have modeled this structural feature within the coherency strain approach to simulate both stiffening and softening of the metal superlattice. New techniques, such as microindentation/deflection, are being pursued to facilitate the experimental measurement of elastic-plastic properties in multilayer systems.

*This work was supported by Institutional Research & Development.*

## References

1. W. M. C. Yang, T. Tsakalakos, and J. E. Hilliard, *J. Appl. Phys.* **48**, 876 (1977).
2. A. Kueny, M. Grimsditch, K. Miyano, I. Banerjee, C. M. Falco, and I. K. Schuller, *Phys. Rev. Lett.* **48**, 166 (1982).
3. M. F. Doerner and W. D. Nix, *J. Mater. Res.* **1**, 601 (1986).
4. T. P. Weihs, S. Hong, J. C. Bravman, and W. D. Nix, *J. Mater. Res.* **3**, 931 (1988).
5. A. F. Jankowski, *J. Phys. F* **18**, 413 (1988).
6. A. F. Jankowski, *J. Phys. Chem. Solids* **50**, 641 (1989).
7. A. F. Jankowski, *Mater. Res. Soc. Symp. Proc.* **141**, 147 (1989).
8. A. F. Jankowski, *Mater. Sci. Eng. Lett.* **A114**, L17 (1989).
9. This work was performed at Stanford University in collaboration with S. P. Baker and W. D. Nix.
10. J. Chaudhuri, S. Shah, and A. F. Jankowski, *Mater. Res. Soc. Symp. Proc.* **132**, 231 (1989).
11. S. R. Nutt, K. A. Green, W. D. Nix, S. P. Baker, and A. F. Jankowski, *Mater. Res. Soc. Symp. Proc.* **130**, 129 (1989).
12. M. A. Wall and A. F. Jankowski, *Thin Solid Films* **181**, 313 (1989).

# Fluid Dynamics and Mass-Transfer Characteristics in Radial-Flow, Multijet PICVD Reactors

J. A. Britten

***We are investigating the deposition of reflective coatings on optical substrates by plasma-initiated chemical vapor deposition (PICVD) as a process for creating mirrors with a high damage threshold for the Nova laser. Radial uniformity of deposition on the substrate is largely controlled by the fluid dynamics in the reactor. We have studied the fluid dynamics and mass-transfer characteristics of a PICVD reactor experimentally and theoretically to determine conditions under which uniform deposition on the substrate can be expected.***

## Introduction

Damage to beam-turning mirrors at high fluences is a critical limiting factor to increased power output on the Nova laser. Currently, several processes for manufacturing damage-resistant reflecting optics are being investigated by the Advanced Drivers group of the Inertial Confinement Fusion (ICF) Program, with support from the Chemistry & Materials Science Department. The aim of using these processes is to deposit alternating layers of material of differing refractive index [e.g., layers of pure silica ($SiO_2$) alternating with layers of silica doped with germania ($GeO_2$) or fluorine] on a flat optical-quality silica substrate. The layer thickness, on the order of 100 nm, is to be precisely controlled, and the number of layers should be sufficient, on the order of several hundred, to create a multilayer reflector capable of greater than 99 percent reflection of the 1.06-μm light produced by the Nova laser. The goal of the present effort is to produce a mirror with a damage fluence threshold of more than 40 J/cm$^2$, with damage and reflective properties uniform over a 15-cm scale.

One process under development involves the use of a radio-frequency- (RF-) generated plasma to initiate free-radical chemical reactions in a PICVD reactor. These reactions lead to $SiO_2$ formation in a reaction volume continuously swept by $SiCl_4$ and $O_2$ at a relatively low pressure (0.1–1 kPa). In this process, $SiO_2$ forms from reaction and deposits on the substrate, which is one surface of the reaction volume confining the plasma. Periodic incorporation of dopant material into the deposited layer provides the refractive-index variation. The substrate surface must be hot enough to ensure fully-dense, fully-oxidized, defect-free layers, yet surface temperatures and/or deposition times must be sufficiently small that diffusion of dopant material does not smear the refractive-index profile.

Our group is presently taking delivery of a PICVD test reactor to test this technology. Figure 1 shows a schematic of the reactor and its flow characteristics. Reactant gas is introduced into the reactor through about 150 equally spaced small holes drilled into the gas distribution plate, and it flows radially out through holes drilled into the cylinder defining the reactor side-wall. The number and size of the injection holes are determined such that the pressure drop through the holes is very much larger than the radial pressure drop in the reactor, ensuring equal flow of gas through each hole.

Regardless of the complexities of plasma-gas coupling and reaction chemistry, radially uniform deposition on the substrate is not possible without uniform mass transfer, which is governed solely by the reactor's fluid dynamics. We have studied the mass-transfer

**Figure 1.** Schematic of a PICVD reactor.

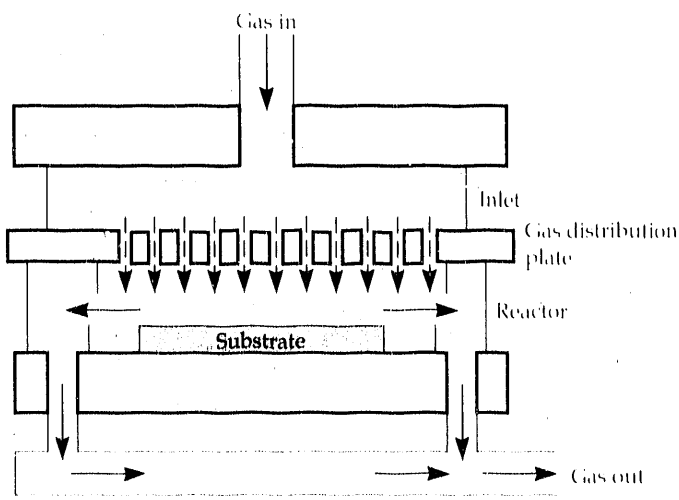

characteristics of a similar flow system both experimentally and theoretically in order to determine conditions under which radially uniform mass transfer can be expected in the real reactor.

## Experimental Method

We constructed a flow system identical to that in Fig. 1 and studied mass transfer at the substrate surface by sublimation of naphthalene into an air stream at ambient temperatures. Flow and pressure conditions were similar to those that will be used in the actual PICVD reactor. The naphthalene substrates were made by hot-pressing crystals into disks. Overall sublimation rates and radial uniformity were quantified by weighing and profiling the surface before and after an experiment.

## Results and Comparison with Model Studies

The experiments have shown that for relatively low gas flow rates, radially uniform sublimation of the naphthalene substrate occurs. We conclude from this result that uniform deposition of $SiO_2$ will occur under similar conditions in the PICVD reactor. A stagnation flow model, which assumes uniform injection of gas over the entire upper reactor surface and neglects edge effects, predicts mass-transfer rates that agree very well with the experimental values for these low flow rates, as shown in Fig. 2. Given reaction kinetics and other data applicable to the PICVD reaction system, this model is also capable of predicting silica deposition rates in the real system. Figure 2 shows, however, that as the flow rate becomes larger, experimental mass-loss rates begin to deviate significantly from predicted values. This deviation is due to locally enhanced mass transfer, which is a result of jet impingement on the substrate. Figure 3 shows a naphthalene disk after a high-mass-loss experiment. The dimpling pattern on the surface reflects the spacing of the injection holes above; troughs are directly under the holes, and ridges are formed between adjacent holes. In the actual coater, since deposition to the surface and not removal from the surface occurs, this pattern would be reversed, with troughs formed between adjacent holes.

We have developed a model for jet impingement in order to quantify the operating conditions that would eliminate these localized mass-transfer nonuniformities. In the interest of tractability, a single jet in an axisymmetric geometry is analyzed; the influence of adjacent jets is implicitly accounted for by imposing a zero radial-flow boundary at a distance $s/2$ midway between the jets. Also, the upper confining surface has been removed in our computational geometry to allow gas to escape. Figure 4 depicts this idealized flow field.

**Figure 2.**

Experimentally determined naphthalene mass-loss rates compared with predictions of the stagnation flow model. (Stagnation flow Reynolds number Re = $Q_t H/A\mu$, where $Q_t$ is the total gas flow rate, $H$ is the plate-to-substrate spacing, $A$ is the injector surface area, and $\mu$ is the gas viscosity.)

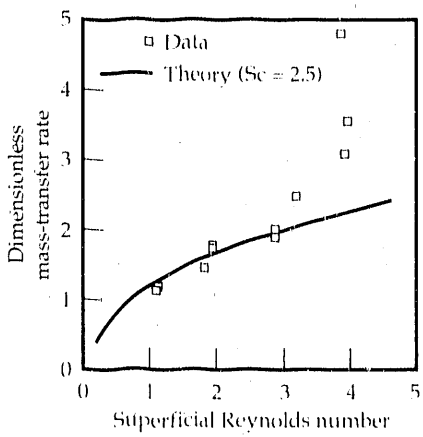


**Figure 3.**

Effect of jet-impingement-enhanced mass transfer on naphthalene sublimation.

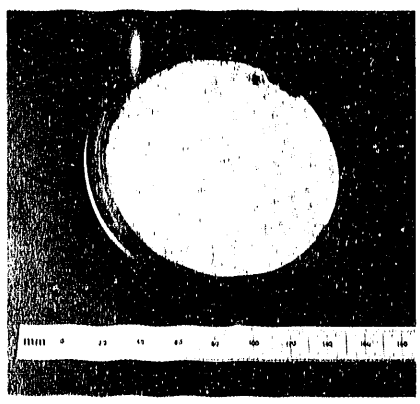

**Figure 4.**

Idealized computational flow field for studying nonuniformities in jet-impingement mass transfer. Point A is the stagnation point, and Point B is the flow-separation point. $Y$ is a dimensionless mass fraction, and $u_r$ and $u_z$ are radial and axial velocities, respectively.

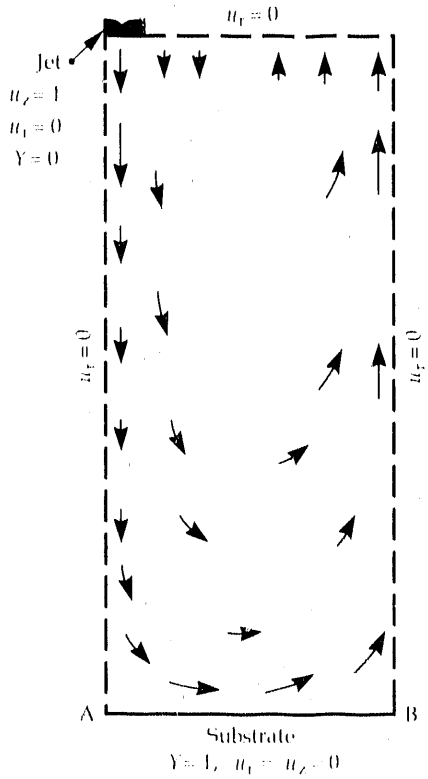

We use a commercially available finite-element flow code to (1) solve the Navier-Stokes equations for steady laminar flow along with the advection-diffusion (mass-transfer) equations, and (2) quantify the radial variation of the mass-transfer rate at the substrate from the jet-stagnation point to the flow-separation point at $s/2$. Parameters are (1) the jet Reynolds number $Re_j = 4Q/\pi d_j \mu$, where $Q$ is the gas flow rate through the jet, $d_j$ is the jet diameter, and $\mu$ is the gas viscosity, (2) the jet-to-substrate spacing $H$, and (3) the jet-to-jet spacing $s$.

Figure 5 shows representative model results. The model as well as the experiments show that mass-transfer nonuniformities are very sensitive to $Re_j$ for conditions of interest in the PICVD reactor. Furthermore, predicted values of $Re_j$ for which the onset of significant jet-enhanced mass transfer occurs agree quite well with the experimental data. This study has aided in sizing the gas-injection holes and in determining suitable operating flow rates for the reactor.

## Conclusions

Experimental and modeling studies of fluid dynamics and mass transfer in a flow system simulating a PICVD reactor have led to a greater understanding of the process and have defined operating conditions that will optimize radial uniformity of deposition rates.

*This work was supported by the ICF Program.*

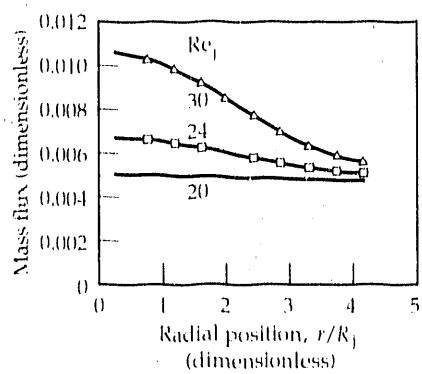


**Figure 5.**

**Model predictions of variation in the jet-induced mass-transfer rate from stagnation point to flow-separation point for various $Re_j$, with $H$ = 2 cm, $s$ = 1 cm, and the Schmidt number Sc = 2.5 for diffusion of naphthalene in air. $R_j$ is the jet radius.**

# Corrosion-Resistant Coatings for High-Temperature Applications

O. H. Krikorian and
P. G. Curtis

*We have been developing corrosion-resistant coatings for metals such as stainless steel, vanadium, niobium, and tantalum. We have shown that aluminide and silicide coatings provide oxidation protection in burning-fuel environments. We have also shown that CeS and $Ce_2O_2S$ coatings are capable of containing molten metals such as uranium and plutonium.*

## Introduction

For the past two years, we have been developing improved coatings to provide metals with corrosion protection at high temperatures. The coatings are of two types: one for resistance to oxidation in air and flames, and the other for molten-metal containment. Substrate metals being coated are vanadium, niobium, tantalum, and a stainless steel (21-6-9). Corrosion-resistant coatings have applications in fire safety of nuclear weapons, jet-engine components, liquid-metal cooling in advanced fission and fusion reactors, and the foundry casting of reactive molten metals such as uranium and plutonium.

The aerospace industry has developed aluminide and silicide coatings for oxidation protection in jet-engine components fabricated from refractory metals.[1,2] We have found that aluminide coatings are useful up to a temperature of about 1500 K for hundreds of hours, and silicide coatings up to 1800 K for several hours or as high as 2200 K for several minutes. Little is known about the use of coatings for molten-metal containment.

## Application of Oxidation-Resistant Coatings

Our development of aluminide coatings has concentrated on $NbAl_3$ coatings on niobium. Adherence and thermal-expansion match for these coatings are very good. We use aluminum powder in a slurry-melt technique at 1373 K to form $NbAl_3$ coatings about 30 μm thick. The main problem in achieving a successful coating is to stabilize the growth of a continuous and protective surface scale of $Al_2O_3$ in preference to $NbAlO_4$ or $Nb_2O_5$, which do not form protective scales. Suitable chemical additives (e.g., chromium, silicon, boron, and yttrium) are known to overcome this problem.

Our main improvements to the aluminide-coating process are (1) adding a fluoride flux to the coating reactants to clean metal surfaces, thus giving a more reliable and reproducible process, and (2) developing a technique for patching bare regions in the coating, such as at weld joints, by applying slurry coatings and sealing them in place by laser welding. These coatings maintain good oxidation resistance after coated parts have been severely bent or deformed. We believe that this is a breakthrough in ceramic-coating performance.

Silicide coatings work well at high temperatures because they form a highly viscous glass of nearly pure silica as an oxidation barrier. Our work has concentrated on the development of coatings of $NbSi_2$ on niobium and $TaSi_2$ on tantalum that will survive for a few minutes either in air or in solid-propellant rocket fuel flames at temperatures of about 2100 K (Ref. 3). We used a pack-cementation process to apply coatings about 40 μm thick. Chromium additions to these coatings greatly improve their performance. During oxidation, the chromium converts to a $Cr_2O_3$ layer above the $SiO_2$ glass. The $Cr_2O_3$ serves two functions. It provides a physical barrier that shields the $SiO_2$ from reacting with impurities that would lower its viscosity, and it also provides radiative cooling to the surface because of its high emissivity.

## Application of Coatings for Molten-Metal Containment

We have applied coatings to substrates of stainless steel, vanadium, and niobium that are not wetted by molten metals. Stainless steel is especially difficult to coat because its thermal expansion is much higher than that of commonly used coating materials such as oxides. We found that a relatively unexplored class of materials, the rare earth sulfides, gives a much better thermal-expansion match than do oxides, while having the lowest known solubilities for most molten metals.[4]

We used physical vapor deposition (PVD) to apply coatings about 10 μm thick to CeS and NdS. Direct coating with CeS still presented thermal-expansion mismatch

problems, but these were overcome by using a thin bonding layer of chromium (4 μm) between the stainless steel and the CeS; this thin layer resulted in very tenacious bonding. NdS has a closer thermal-expansion match, and the NdS coatings survived without the need for a bonding layer. Above about 1450 K, CeS and NdS undergo a change from nonwetting to wetting by molten uranium. The oxysulfide, $Ce_2O_2S$, however, remains unwetted by uranium up to at least 1700 K. Good-quality $Ce_2O_2S$ coatings about 10 μm thick were deposited on vanadium and niobium by PVD.

## Results of Corrosion Tests

**Oxidation Resistance.** Table 1 summarizes the most successful performances achieved to date. We find that $NbAl_3$-coated niobium can be protected for at least 100 h at 1473 K in air, although use times drop off quickly at higher temperatures. The continued oxidation protection of a $NbAl_3$-coated sheet at 1473 K, even after two bendings, is especially noteworthy. A post-mortem metallographic examination of this sheet showed that the aluminide coating had developed transverse microcracks spaced about every 50 μm apart, but that these had healed by a filling of protective oxide during the oxidation exposures. Similar results were obtained on a 20-cm-diam $NbAl_3$-coated niobium plate that had been rapidly deformed with an air-gun apparatus (see Fig. 1). Specimens containing exposed areas such as weld joints were protected by an $NbAl_3$ coating using the laser-melt technique described above.

Silicide coatings protected both niobium and tantalum for at least 15 min at 2100 K in air. However, in rocket-flame tests,[3] we encountered the additional complication of the presence of molten steel originating from support fixtures in the apparatus. The silicide-coated tantalum survived this dual attack of rocket-propellant flame and molten steel for 100 s at about 2100 K, but silicide-coated niobium did not, and was melted.

**Figure 1.** Appearance of a $NbAl_3$-coated niobium plate after deformation into a dish shape in an air-gun apparatus, followed by exposure to air at 1473 K for 30 min. Remarkably, the plate survived with only minor oxidation effects (see the yellow-colored oxide near the edge), in spite of the microfractures that developed in the coating during deformation. The plate is 20 cm in diameter and 1.5 mm thick.

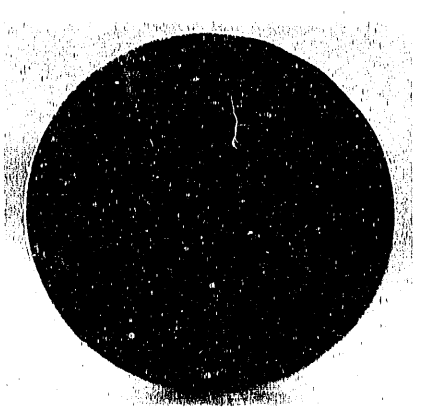

**Molten-metal containment.** Cr/CeS coatings gave consistently good protection to stainless steel for either molten uranium or plutonium at about 1400 K. NdS coatings, although adherent, occasionally developed pinholes and localized attack. The $Ce_2O_2S$ coatings on vanadium and niobium proved to be adherent and provided containment without wetting for both uranium and plutonium. A test on a pellet of $Ce_2O_2S$ showed it to be unwetted by uranium to above 1700 K.

**Table 1.** Summary of successful performances achieved for various coatings and substrates under a variety of use conditions.

| Substrate | Coating | Demonstrated use | | | |
|---|---|---|---|---|---|
| | | T (K) | Atmosphere | Time (h) | Comment |
| Niobium coupon | $NbAl_3$ | 1473 | Air | 100 | — |
| | | 1573 | Air | 2 | |
| Niobium sheet | $NbAl_3$ | 1473 | Air | 3 | Three 1-h cycles, bending between cycles |
| Niobium plate | $NbAl_3$ | 1473 | Air | 0.5 | Coated plate, deformed with air gun prior to test |
| Niobium cylinder, with weld joint | $NbAl_3$ | 1433 | Air | 1 | Weld joint, $NbAl_3$-coated by laser melting |
| Niobium coupons | $NbSi_2$ | 2100 | Air | 0.25 | |
| Tantalum coupons | $TaSi_2$ | 2100 | Air | 0.25 | |
| Tantalum crucible | $TaSi_2$ | 2100 | Solid-propellant flame | 0.03 | Molten steel present |
| Stainless steel (21-6-9) | Cr/CeS | 1453 | Molten uranium | 1 | — |
| | | 1373 | Molten plutonium | 2 | |
| Vanadium dish | $Ce_2O_2S$ | 1523 | Molten uranium | 2 | 5% Cr in uranium |
| | | 1373 | Molten plutonium | 2 | |
| Niobium dish | $Ce_2O_2S$ | 1700 | Molten uranium | 1 | |

## Conclusions

We can provide coatings that give reliable protection against oxidation to metals such as vanadium, niobium, and tantalum. We can also provide coatings that protect from attack by molten metals. Especially significant is an oxidation-resistant aluminide coating for niobium. This coating continues to protect even after the coated part is bent or deformed. Microscopic examination shows that the coating has microfractures which develop and then heal by filling in with oxide, thus continuing the protection. Stainless steel can be protected from molten-metal attack up to 1450 K by using a CeS coating.

*This work was supported by Weapons Supporting Research and B Division Technical Base.*

## References

1. *Coatings of High-Temperature Materials*, H. H. Hausner, Ed. (Plenum Press, New York, 1966).
2. *Oxidation of High-Temperature Intermetallics*, T. Grobstein and J. Doychak, Eds. (The Minerals, Metals, and Materials Society, Warrendale, Pa., 1988).
3. P. G. Curtis, O. H. Krikorian, and E. H. Helm, *Rocket-Propellant Burn Tests of Silicide-Coated Niobium and Tantalum*, Lawrence Livermore National Laboratory, Livermore, Calif., UCID-21395 (1988).
4. O. H. Krikorian and P. G. Curtis, *High Temp.–High Press.* **20**, 9 (1988).

## Overview

Almost from its inception, LLNL has fostered a vigorous research program on energetic materials. Although this activity is clearly a natural adjunct to nuclear weapons research, explosive substances do have a variety of nonmilitary uses. For this reason, the generic term "energetic materials" is deemed a more appropriate name. Nontraditional applications of energetic materials include (1) use as rocket propellents, (2) use in special welding processes, explosive forming, generation of seismic signals, and dynamic equation of state measurements, and (3) use in the production of ultrahigh pulses of electric current—up to $10^6$ A. As a class, energetic materials are by far the most efficient energy reservoirs known in terms of available energy content per unit weight. Because of this high energy content, they will undoubtedly find further uses after the fundamental physics and chemistry of initiation and detonation are better understood.

Our research capabilities were significantly increased in 1989 when C&MS Department personnel occupied Building 191, the High Explosives Applications Facility (HEAF). Dedicated exclusively to the study of energetic materials, HEAF is regarded as the best facility of its kind in the world.

Broadly speaking, our research goals are to invent explosive formulations that can be handled with greater safety than those used at present. At the same time, these formulations must satisfy the seemingly paradoxical objective of possessing higher energy densities. Although sensitivity to accidental detonation generally rises with energy density, there are noteworthy exceptions that encourage us in this pursuit.

Our research effort has several distinguishable yet highly interactive components. There are the theorists, who use computer modeling to study the equations of state, hydrodynamics, and chemical kinetics of energetic materials and reactions. Experimentalists synthesize new energetic compounds. Others formulate mixtures of these original compounds with various binders and nonexplosive additives that modify the explosive behavior. Each explosive mixture is characterized by a variety of measurements that specify the final performance parameters of the new product. Because of the inherently short times involved in explosive detonations, ingenious methods unique to this field must be employed for such investigations; detonation velocities attain values approaching 10 km/s and generate local pressures in excess of $5 \times 10^5$ atm within nanoseconds. The data from the performance characterization is supplied to the theorists to use as input for further modeling.

Most of our research is unclassified. Consequently, those engaged in this work have the customary associations with colleagues in other laboratories, both in the U.S. and abroad. In this field, technology transfer from LLNL to industry is nearly automatic. Once a new formulation has been tested and approved, it is turned over to industry for further development and, when appropriate, commercial exploitation.

In addition to our research into energetic materials, an effort which dominates this section, we report on the discovery of a synthesis capable of producing transition-metal trifluoromethyl complexes. An account is also given of the combustion synthesis of a Ti-C-Ni-Al composite. This novel one-step process holds promise for the reduction of the porosity generally associated with the manufacture of such materials by conventional methods.

Section 5

# Energetic Materials and Chemical Synthesis

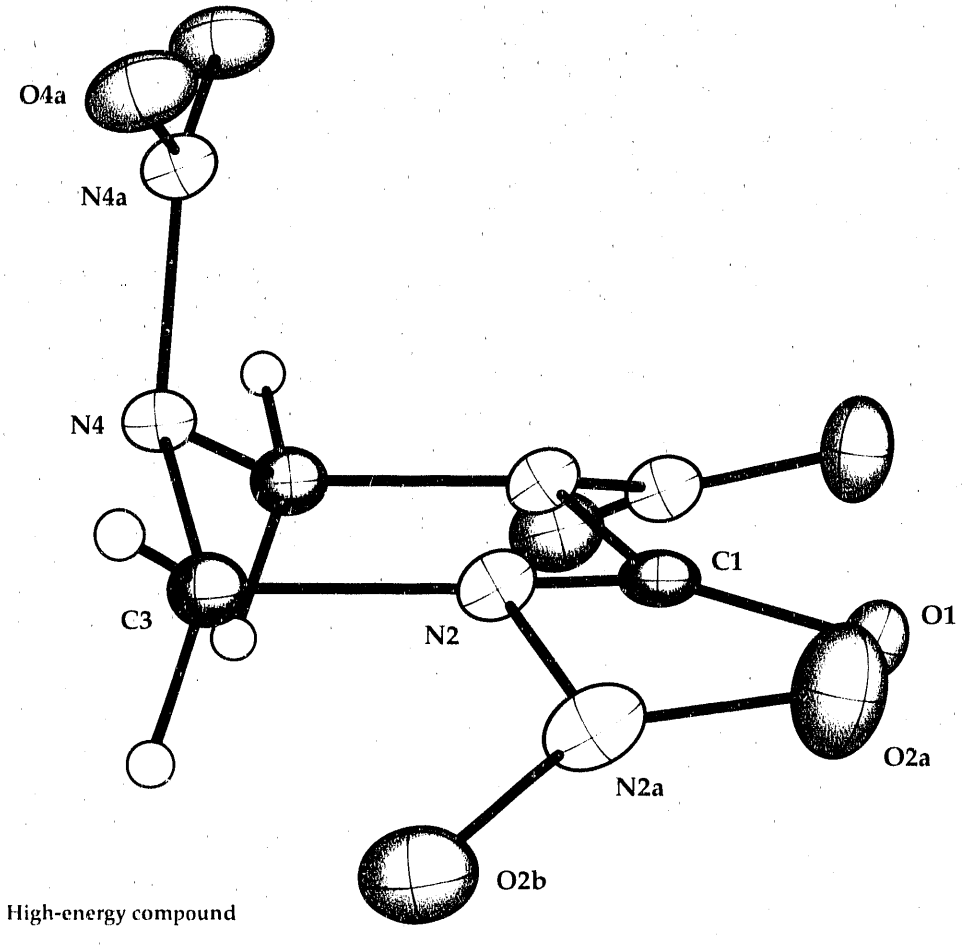


High-energy compound

# Modeling Phase Separations

D. F. Calef and
E. A. Chandler*

***The characteristic structures formed by a fluid mixture separating into two phases are important for modeling a wide variety of applications, such as phase separations in the product gases of explosives and diffusion of porous media. The rate at which these structures form is also important. We have developed a method for modeling such applications.***

## Introduction

Modeling of phase separations of binary mixtures has a wide variety of applications. Perhaps the most familiar example of a binary fluid-phase separation is oil and water. The dynamic process that we are interested in occurs when an initially well-mixed fluid is suddenly made thermodynamically unstable and driven toward physical separation into two fluids.

Attempts at accurate calculations of explosive properties of HMX†-based explosives have led theorists to postulate the presence of a phase separation in the products into a $N_2$-rich phase and a $N_2$-poor phase.[1] The importance of such a phase separation, however, depends on how rapidly it can occur. If the process is too slow, the energy released will not influence the shock front and hence will not affect detonation properties.

Similarly, models that can represent the rate of phase separation will be useful in understanding the rate at which materials diffuse together. Such mixing is important in attempting to develop composite explosive materials.

The structures that form during the separation process are also of general interest. As we shall see, the domains of a single phase tend to form a complicated interpenetrating pattern. These patterns can be used to model other materials. As an example, the interface between the two phases can be used to model a very porous foam.

## Theory

The important length scales for phase separations fall between the molecular and macroscopic. The process that we are interested in involves so many molecules that molecular dynamics is too time consuming as a modeling approach, yet a degree of detail is required that is difficult to achieve with traditional macroscopic flow equations. For practical applications, we need fast methods for very large systems. In addition, we need to develop tools to visualize, interpret, and use the results. We are implementing and experimenting with simplified cellular models for the dynamics of phase separations.

The form of lattice model we are using was originated by Oono and Puri in 1988.[2] Each site on the lattice is

**Figure 1.** A phase-separating mixture at three times: (a) $\tau = 10$, (b) $\tau = 100$, and (c) $\tau = 1000$. To relate the dimensionless time, $\tau$, to a physical time, it is necessary to specify a diffusion coefficient and lattice spacing.

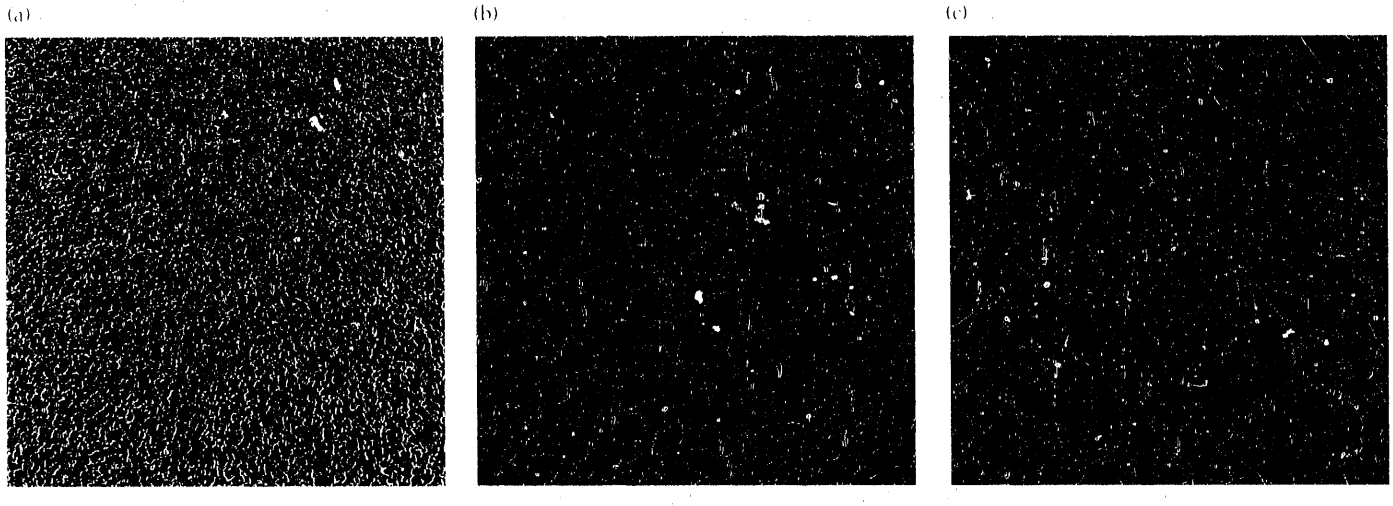

described by a concentration variable that specifies how far it is from the average concentration. We then specify how much free energy it costs to maintain this, usually nonequilibrium, concentration. Minimizing the free energy will then drive the system either toward or away from phase separation, as the case may be. Conservation of mass, however, requires that a nonequilibrium concentration can relax only by exchanging material with neighboring cells. The dynamics for this process are treated using a discretized version of the diffusion equation.

These models "grow" spatially inhomogeneous structures called spinodal structures that can be used to represent, for example, carbon foams[3] as well as partially separated mixed-phase fluid systems.

The practical use of such a model lies in the ability to map its behavior onto that of observed systems. In other words, the constants that go into the model calculations are very hard to estimate from first principles, so a more empirical approach relying on comparison of results with real systems must be employed.

## Examples and Discussion

Visualization plays an important role in this type of modeling. Although complex structures are often categorized using a few numbers, such as pore size or volume, a much greater understanding can be gained from visual inspection. Most of our effort has been directed toward creating large three-dimensional models; however, for purposes of visualization, we show two-dimensional systems here.

Figure 1 shows a phase-separating mixture at three sequential times. The color gradient from red to blue corresponds to the concentration gradient from one pure phase to the other. This figure clearly shows that after a very short initial period, most of the material is in one phase or the other, with very sharp boundaries. Growth of macroscopic domains is then slow.

Figure 2 shows use of a structure grown using the method that produced Fig. 1. Here, a phase-separating mixture was frozen at a certain degree of separation; then the boundary between the two phases was used as a model for a porous material. We used this replica of the porous media to model tracer diffusion into the material. The pictures show a tracer originally localized in the outer regions of the matrix slowly diffusing into the center. The color gradient now corresponds to the gradient in tracer concentration. Clearly, diffusion is a slow process in this system. As the tracer diffuses, much of it becomes localized in regions of varying size, resulting in large variations in the concentration. It is also evident that large interior domains can only be reached through very narrow passages, greatly slowing the diffusion.

The development of this level of modeling gives us a new tool to explore a wide variety of diffusional processes on a scale previously difficult to obtain.

*This work was supported by Weapons Supporting Research and the Weapons Program.*

*A Division, R Program.
†HMX is octahydro-1,3,5,7-tetranitro-1,3,5,7-tetrazocine.

## References

1. F. H. Ree, *J. Chem. Phys.* **84**, 5845 (1986).
2. T. Oono and S. Puri, *Phys. Rev. A* **78**, 434 (1988).
3. R. W. Hopper, *J. Non-Cryst. Solids* **70**, 111 (1985).

**Figure 2.** A tracer diffusing into a porous material, as a function of time from left to right. The red regions have the highest concentration, the blue the lowest. The walls of the porous material are shown in light blue.

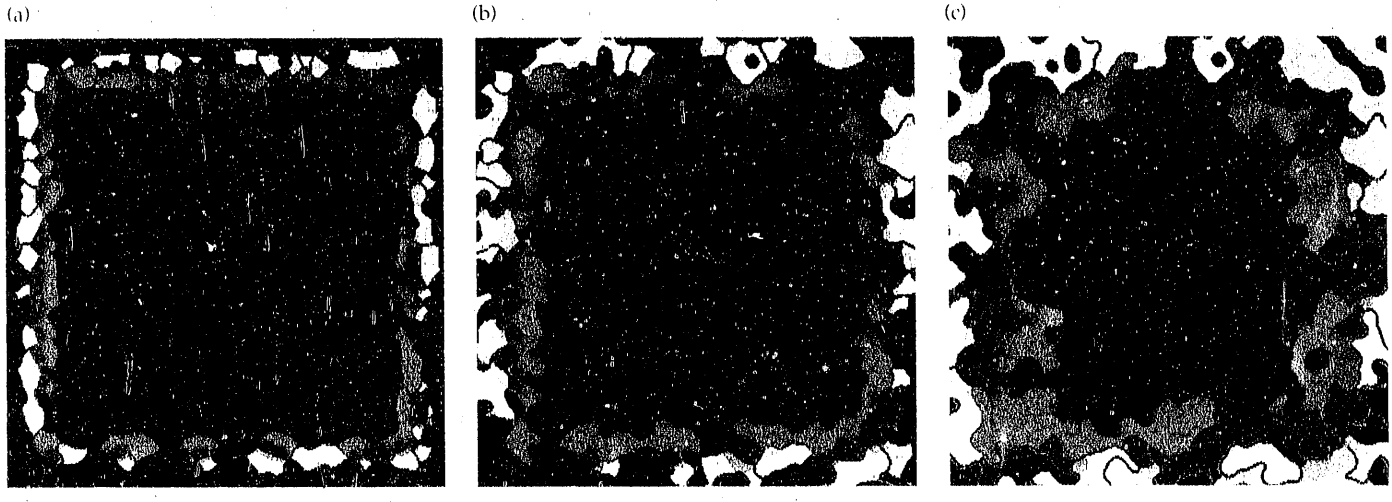

# A Comparison of Shock Sensitivity of HMX Formulations

R. L. Simpson,
P. A. Urtiew, and
F. H. Helm

*We have determined the shock sensitivity of HMX* formulations using precise one-dimensional experiments in which time-varying properties are measured. The mean HMX particle size was varied from 5 to 1700 μm. Formulations with inert and reactive continuous-fluid phases were examined. Both the HMX particle size and the nature of the continuous phase were found to affect the shock sensitivity.*

## Introduction

Initiation of a condensed-phase energetic material and its transition to detonation results from a complex interaction between mechanics and chemistry. Once a detonation is formed, a supersonic wave propagates through an explosive at velocities approaching 10 km/s.

At the shock front, pressures can reach 60 GPa (600,000 atm, or approximately $9 \times 10^6$ lb/in$^2$). These pressures are sufficiently high to shock-compress unreacted material to nearly half its original volume, resulting in a temperature rise of 1500 to 2500 K. At these high temperatures, the explosive will rapidly decompose, releasing large amounts of energy. This energy, in the form of high-pressure product gases, supports advancement of the shock front, thereby producing a steady-state detonation wave complex. The time scale of the energy release ranges from less than 10 to 150 ns. High-density explosives are capable of releasing over $10^{10}$ W/cm$^2$ at the detonation front.

Although the process of detonation is not yet fully understood, the science is sufficiently advanced for many modeling applications. However, this is not true for the process of initiating the detonation. In the initiation process, a relatively low-amplitude shock wave moves through the reactive medium at a much slower rate than at detonation (microseconds vs nanoseconds), and the shock front cannot be treated as a uniform, one-dimensional plane.

Experimentally and theoretically, it has been shown that the temperature rise resulting from such shock-loading is insufficient for chemical reactions to occur at fast enough rates to support the detonation process. Instead, energy is localized across the shock front in regions commonly referred to as "hot spots." These locally heated regions can be produced by a number of different processes, such as viscous pore collapse, intergranular friction, shear band dislocations, microjetting, and shock-wave interactions due to the difference in shock impedance between separate components of the high explosive.

Typically, a high-density explosive consists of a polycrystalline powder and a binder. For reasons outlined above, the sensitivity to detonation can be a dramatic function of the crystalline defect structure, the particle size of the binder as well as the type of binder, and the void volume of the material. As an example, one of our most powerful explosives, HMX, will not detonate as a single crystal. Another explosive, TATB,[1] is unable to sustain a detonation if the particle size is reduced below 1 μm.

Because the means exist to significantly modify the sensitivity of an energetic material through changes in its physical characteristics, and because LLNL is committed to developing powerful high explosives that are also insensitive, we have an ongoing program to investigate these phenomena. These investigations are performed by shock-loading reactive materials and observing their behavior under well-controlled conditions. We have emphasized measuring time-varying properties in the hydrodynamic flow to elucidate the behavior of energetic material during the initiation process.

**Figure 1.** Shock-front velocity histories of 5-, 60-, 120-, and 1700-μm HMX particles surrounded by a continuous phase of water. Shock loading was accomplished under one-dimensional conditions by the impact of a high-velocity flyer. The differences in the initial and final velocities between samples are due to variations in the initial packing density of HMX.

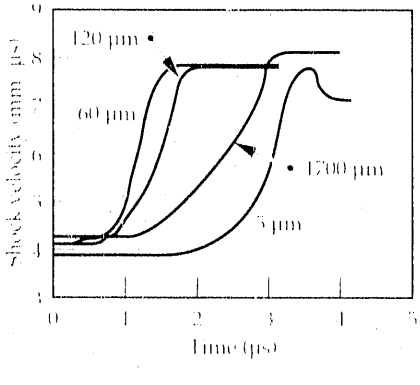


## Experimental Methods and Results

Figure 1 shows the shock-velocity histories in samples composed of 5-, 60-, 120-, and 1700-μm HMX in water.

The samples were shock-loaded to 5.0 GPa. At early times the velocity is an approximation to the inert Hugoniot[1] (locus of end states reached by a shock wave). Later the reaction-supported shock front increases in velocity, eventually reaching the value of a fully developed detonation wave. The variations in initial and final velocities are due to slight differences in the packing densities of the HMX.

The information shown in Fig. 1 illustrates the effect of particle size on the process of initiation. In the 60- and 120-μm cases, the processes are very similar. It appears that the 5- and 1700-μm cases are less sensitive in terms of the time required to attain transition to detonation, i.e., the shock wave must travel greater distances. However, close examination of the 1700-μm velocity history shows that acceleration of the shock begins at times (distances) similar to those of the 60- and 120-μm cases, but builds up much more slowly.

Hydrodynamic differences are also indicated in Fig. 1. Unlike the other formulations, the 5-μm HMX mixture shows a slight overshoot in the velocity profile before it levels off to the final steady-state value. This overshoot occurs because detonation conditions are first reached behind the shock front, where the unreacted material has already been compressed by the shock wave, and the detonation front moves through this region at a higher velocity than it would move through a medium at rest. When the detonation front catches up with the shock front, the observed velocity immediately decreases to its steady-state detonation velocity value.

To examine the decrease in sensitivity of materials with less than a 60-μm particle size, shock-ignition studies were done on 200-mg samples of 10-μm-wide HMX sieve cuts ranging from less than 10 μm to 60–70 μm. Figure 2 shows the experimental configuration used in this study. An electric gun is used to accelerate flat polycarbonate projectiles into the sample. Pressures can be sustained for about 0.45 μs before a rarefaction wave relieves the stress at the flyer/sample interface. A multichannel radiometer is used to measure the spectral radiance of the shocked samples. For the materials at these high pressures, the radiance signal is principally that of a graybody.

Figure 3 illustrates the radiant-emittance traces obtained at a wavelength of 490 nm when the samples were shocked to a pressure of 8.0 GPa. It can be seen that the signal intensities are similar for all samples with particle sizes greater than 20 μm. A formulation having a 10- to 20-μm particle-size distribution showed a dramatic decrease in the signal intensity. The radiance signal is even further reduced in the sample containing HMX particles that are smaller than 10 μm.

This thermal-radiance technique can also be used to determine the shock pressures that are necessary to produce ignition sites for a given composition. Figure 4 shows the 490-nm radiance traces from a 5-μm HMX sample shocked to pressures of 4.0, 6.0, and 8.0 GPa. At pressures of 4.0 GPa or below, ignition is minimal. In a large sample, a supported shock wave would require 20 mm or more distance to run before transition to detonation could occur.[2] At 6.0 GPa, the radiance shows evidence of earlier reactions, whereas at 8.0 GPa, a prompt detonation would be realized. It is possible to relate these small-scale results to larger-scale experiments where detonations are attained.

In an effort to develop explosives with greater energy but low vulnerability, we have examined the

**Figure 2.** Electrically driven flyer experiment with radiometric measurements.

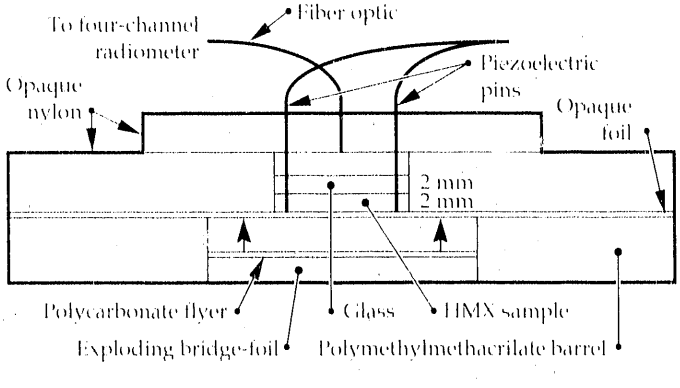


**Figure 3.** Radiance traces at a wavelength of 490 nm from seven samples shocked to 8.0 GPa.

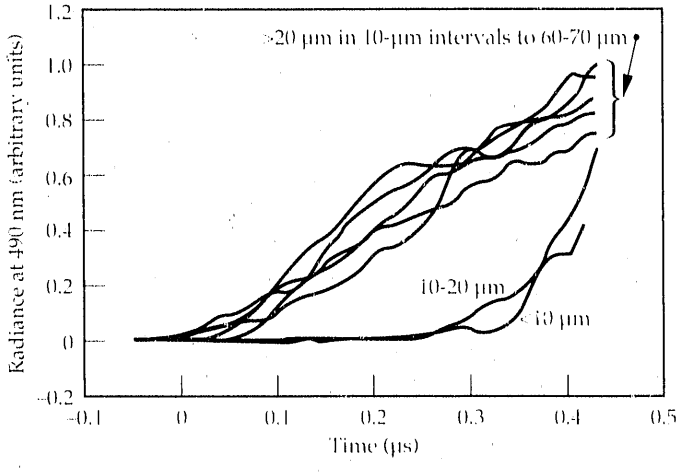


**Figure 4.**

Radiance traces of 5-μm HMX in water shocked to 4.0, 6.0, and 8.0 GPa.

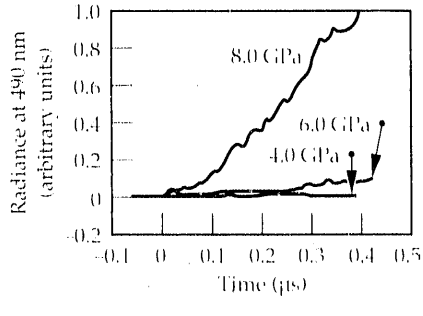

initiation properties of a void-free mixture of HMX surrounded by the highly energetic liquid FEFO.‡ For the purpose of this and similar studies, a new gauge technique was developed[3,4] to measure in situ pressures in shock-loaded samples.

The gauges consist of several transducer elements placed at an angle to the oncoming flow so that each element is not only at a different depth within the sample, but is also probing the original shock wave and the reactive flow behind it without disturbances from the preceding gauge elements. The flow is generated by the impact of the flyer plate at the front surface of the shock assembly. As the shock traverses the energetic sample, the material begins to react.

The different reaction rates of HMX and FEFO are shown in Fig 5. At 3 mm into the hydrodynamic flow, the pressure increases for almost 3 μs before starting to decrease. As the wave moves through the sample, the reaction-supported shock-front pressure begins to increase. At 4.5 mm, the reaction behind the shock front proceeds at a faster rate, lasting about 2.4 μs before falling. However, 0.2 μs after the fall there is a second rapid buildup in pressure. This buildup is due to the later time reaction of FEFO.

Although the chemical kinetic rates of FEFO at these pressures are slower than those of HMX, the two pressure peaks can mainly be attributed to the initiation mechanism. The shock-loading process ignites the HMX crystals intragranularly. By the time FEFO begins to react significantly, HMX decomposition has gone to completion.

**Figure 5.** Pressure vs time measurements on 1700-μm HMX in FEFO shocked to 5.0 GPa. The first and second pressure peaks are the result of HMX and FEFO decomposition, respectively.

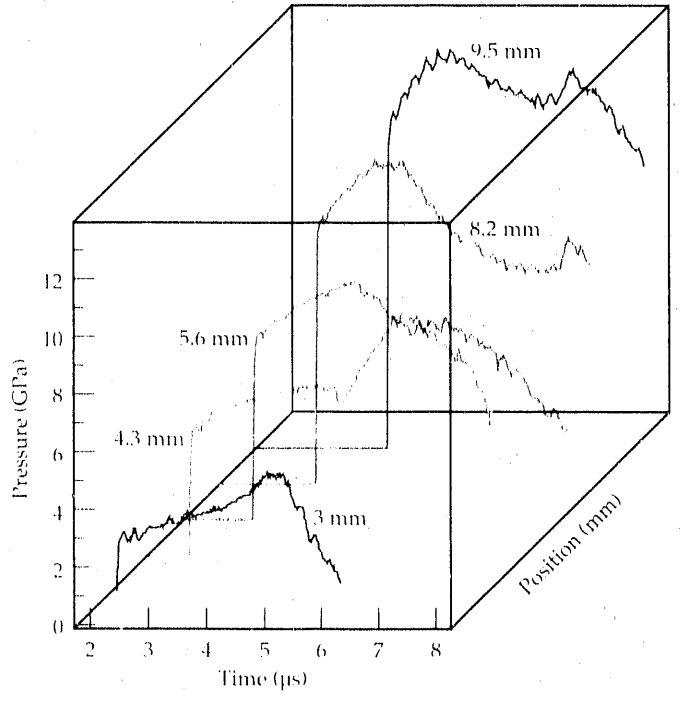


When an inert liquid such as water is substituted for FEFO, the early-time buildup behavior remains the same, which, in part, supports this conclusion. Although the presence of an energetic liquid does decrease the run-distance to detonation, it does not do so in a dramatic way. Hence, high-energy materials may be formulated without a significant increase in sensitivity.

When the shock reaches 5.6 mm, as shown in Fig. 5, the two peaks are beginning to coalesce. At 8.2 mm, there is a strong shock front and only one pressure maximum. By 9.5 mm, the sample is nearly detonating, as can be seen by the high pressure at the shock front and the rapid rise to the maximum pressure level. In the case of full detonation, the peak pressure would be at the shock front and would be followed by an isentropic expansion of the detonation products, which reduces the pressure.

## Conclusions

Quantitative one-dimensional information can be obtained during the initiation process of condensed-phase explosives. To significantly reduce shock sensitivity in HMX-based explosives, particle sizes less than 20 μm are required. The addition of a high-energy liquid to a system may provide additional energy without increasing sensitivity to an unacceptable level. In fact, the extensibility added by a fluid phase can dramatically decrease sensitivity in other initiation configurations.[5]

*This work was supported by Weapons Supporting Research and the Weapons Program.*

*HMX is octahydro-1,3,5,7-tetranitro-1,3,5,7-tetrazocine.
†TATB is 2,4,6-trinitro-1,3,5-triaminobenzene.
‡FEFO is 1,1'-[methylenebis(oxy)]bis[2-fluoro-2,2'-dinitroethane].

## References

1. R. L. Simpson, F. H. Helm, and J. W. Kury, "Non-Reactive HMX Shock Hugoniot Data," *J. Propellants Explosives Pyrotech.* (in press).
2. R. L. Simpson, F. H. Helm, P. C. Crawferd, and J. W. Kurt, "Particle Size Effects in the Initiation of Explosives Containing Reactive and Non-Reactive Continuous Phases," *Ninth Int. Symp. Detonation, Portland, Ore., August 28–September 1, 1989.*
3. P. A. Urtiew and L. M. Erickson, *Multiple Gauges for In Situ Measurements of Pressure and Particle Velocity in Condensed Materials*, Lawrence Livermore National Laboratory, Livermore, Calif., UCRL-100106 (1989)
4. P. A. Urtiew and L. M. Erickson, "Multiple Gauges for In Situ Measurements of Pressure and Particle Velocity in Condensed Materials," *Progress in Astronautics and Aeronautics* (in press).
5. K. Scribner, E. von Holtz, and R. L. Simpson, *High Performance Extrusion Cast Explosives with Low Sensitivity*, Lawrence Livermore National Laboratory, Livermore, Calif., UCRL-53890 (1989).

# Composite Explosive Energetics: I. The Role of Metallic Additives

W. C. Tao, C. M. Tarver, D. R. Breithaupt, and D. L. Ornellas

***Composite explosives have found major applications in air-blasting, cratering, fragmentation, underwater energetics, and other commercial and military systems in which prompt delivery of the available energy is not a primary requirement. In metal acceleration, such as in nuclear implosion, composite explosives generally have not been effective because their potential energy is transformed to work energy over time periods extending to tens of microseconds. We are interested in defining the rate-determining steps and understanding the chemical interactions between different components in the composite explosive formulation in order to partition the delivery of the available work energy.***

## Introduction

A typical composite explosive formulation consists of a fuel (HMX*), an oxidizer (ammonium perchlorate), metallic additives (aluminum), and a binder/plasticizer (Viton/Estane). These multicomponent systems almost always deviate in their detonation behavior from most homogeneous (or "ideal") high explosives because the zone in which the energetic reactions take place is generally much larger than that for ideal explosives. The large reaction zones are indicative of the complex interactions taking place between the initial components toward the formation of the final detonation products.

Consider the above mixture of fuel and oxidizer components. A physical model describing the chemical conversion of unreacted material to work energy might involve the following events. As a unit volume of unreacted heterogeneous mixture passes through the reaction zone, the HMX and ammonium perchlorate undergo thermal decomposition and combustion. Simultaneously, the aluminum is converted from solid particulates to superheated vapor. Mass and thermal transport limitations then determine the rates of reaction between the aluminum, intermediate oxidizing species, and detonation-product species.

The formation of $Al_2O_3$, an extremely exothermic reaction, directly affects distribution of the equilibrium product along the isentropic expansion. As the product gas expands, the available thermal energy is partitioned between the rotational and vibrational states of the detonation products. This stored energy is recovered from deactivation of the excited states and transformed into translational kinetic energy in the expansion push at later times. The respective rates are dependent on detonation temperature, particle size, and degree of mixing of the composite explosive.[1–3]

In this article, we report on the ongoing fundamental investigation of the energetics of composite explosives, emphasizing the role of metallic additives. The specific objective of this study is to understand the rate of reaction between aluminum and the detonation intermediate and product species. Of interest is the partition of energy from the exothermic formation of $Al_2O_3$ into the product gas. Toward this end we will discuss the effect of aluminum loading in the formulation on the initial energy delivery.

## Experimental Methods

We have chosen a bicomponent composite explosive consisting of PETN[4] and 5-μm spherical aluminum particles, with PETN serving as a combined fuel and oxidizer matrix for different weight percents (5–40 wt%) of aluminum additive. The reaction zone of PETN is so short (i.e., the conversion to detonation products takes place almost immediately) that we are monitoring the heat-up and subsequent reaction of aluminum with the detonation product gas itself.

To measure the effect of the additive on performance, we use a simple metal acceleration test called the tantalum plate-push, which involves measuring with laser interferometry the free-surface velocity of a 5-mil tantalum plate adhered to an explosive pellet.

The pellet is solvent-pressed to greater than 95% of the theoretical maximum density of the specific PETN/aluminum formulation.

A similar setup is used to measure the particle velocity at the surface of the pellet as the reaction zone passes. In this case, the tantalum reflective surface is replaced by a thin layer of aluminum fluorosilicate paint, and a lithium fluoride crystal is used as an impedance-matching barrier to hold the surface of the pellet intact long enough for velocity measurements. Figure 1 illustrates the experimental setup.

## Results

Figure 2 shows a typical profile of tantalum free-surface velocity for various PETN/aluminum formulations. The nomenclature RX40AA to RX40AE denotes formulations with 5-, 10-, 20-, 30-, and 40-wt% aluminum additives, respectively. Ringing of the velocity trace in the first microsecond is due to rarefaction waves traversing within the tantalum foil between free surfaces (impedance discontinuities).

In contrast to using large-copper-cylinder expansion techniques, we are probing the initial energy release of the explosive and, thus, the extent of aluminum reaction and contribution to the energy push. The velocity profile from a pure PETN pellet, pressed to similar density and physical dimension pushing a 5-mil tantalum foil, is included in Fig. 2. In this case, the data are calculated from an experimentally determined equation of state for PETN.

Within the initial 1.5 μs, increasing the aluminum content in the formulation above 20 wt% dilutes the available energy. We assume that not all of the aluminum is heated up for the 30- and 40-wt% formulations within this time and that reaction with oxygenated product species is mass- and thermal-transport-limited. However, we note that within the first 0.5 μs, the 5- and 10-wt% aluminum formulations actually outperform pure PETN. A large amount of aluminum in these formulations reacted with the detonation products and provided additional energy from the exothermic reaction. As shown in Fig. 2, replacing 22 wt% of PETN with 5-μm spherical aluminum yields the same amount of available energy.

## Discussion

The run distance of the charge associated with the results in Fig. 2 is 5 mm. For longer run distances or larger charge diameters, the increase of tamping in the system provides more confinement for the reaction. This results in further consumption of unreacted aluminum in the formulations with higher aluminum content and is reflected in the increasing velocity. After 2 μs, the surface velocity of the tantalum foil for a formulation with a 10-mm run distance and 10 wt% aluminum surpasses that of the 5-wt% formulation.

Extending this effect to cases in which there is a sustained shock via a piston driver or an overdriven reaction with a booster charge, we can effectively enhance the reaction of aluminum with the detonation products. One would expect the extent of reaction to increase as the confinement and duration of sustained pressure increase. Subsequently, the extent of the reaction will

**Figure 1.** **Configuration of the tantalum plate-push test for characterization of early-time performance of energetic materials. This test is relatively simple to perform and is commonly used to evaluate new explosive formulations for equation-of-state calculations. The addition of a lithium fluoride crystal allows us to measure particle velocity.**

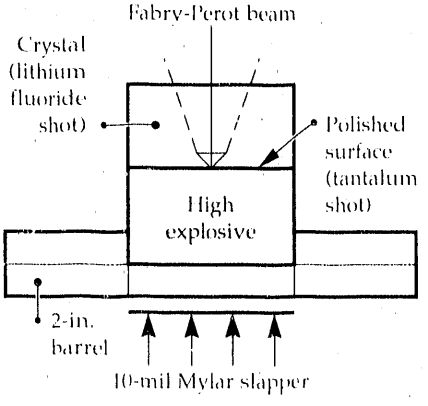


**Figure 2.** **Free-surface velocities of a 5-mil tantalum foil accelerated by different formulations of PETN/aluminum. For both the 5- and 10-wt% aluminum loading, the metal acceleration performance is better than that of pure PETN. In fact, about 22 wt% of PETN can be replaced by 5-μm spherical aluminum without any detriment to performance.**

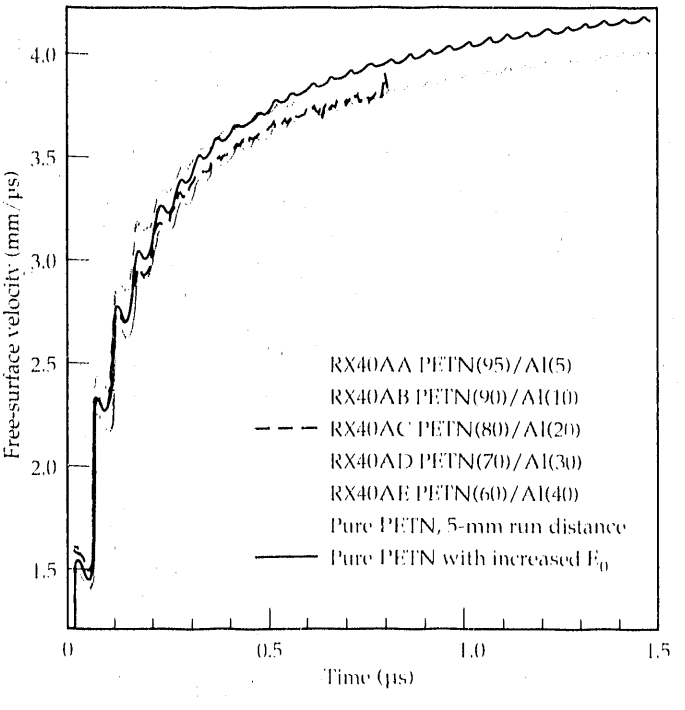

peak and start to diminish as the increase in confinement reaches a point at which diffusion and transport limitations again dominate. These experiments are currently being investigated.

At this stage, the information obtained from the velocity measurements of the different PETN/aluminum formulations allows us to estimate the extent and rate of the aluminum reaction. Starting with pure PETN, we increase the amount of initial chemical energy, $E_0$, in the reactive flow code so that we match the velocity data of the 5- and 10-wt% formulations. We then calculate, using a thermodynamic-hydrodynamic code such as TIGER, the amount of aluminum reaction required to account for the increase in chemical energy. The calculations indicate that approximately 100 percent and 85 percent of the aluminum reacted within 1.5 μs in the formulations containing 5 wt% and 10 wt% aluminum, respectively.

## Summary

It is our goal to understand the different physical, chemical, and thermal mechanisms influencing the complex kinetics associated with composite explosive systems, in the hope that we can tailor the rate of energy delivered by the explosive. We have briefly described experimental methods for probing one of these mechanisms: the role of metal additives and their rate of reaction with the detonation product and oxidizing medium. In the future, we will extend our understanding concerning the effects of mass diffusion, temperature effects, and energy coupling on the expansion gas.

*This work was supported by Weapons Supporting Research and the DoD Office of Munitions.*

*HMX is octahydro-1,3,5,7-tetranitro-1,3,5,7-tetrazocine.
†PETN is 2,2-bis[(nitroxy)methyl]-1,3-propanediol,dinitrate.

## References

1. M. Finger, H. C. Hornig, E. L. Lee, and J. W. Kury, "Metal Acceleration by Composite Explosives," *Proc.Fifth Detonation Symp.* (Pasadena, Calif., 1970), p. 137.
2. R. R. McGuire, D. L. Ornellas, and I. B. Akst, "Detonation Chemistry, Diffusion Control in Non-Ideal Explosives," *Propellants and Explosives* 4(2), 23–26 (1979).
3. R. R. McGuire and M. Finger, "Composite Explosives for Metal Acceleration: The Effect of Detonation Temperature," *Proc. Eighth Detonation Symp.* (Silver Spring, Md., 1985), p. 1018.

# Composite Explosive Energetics II: Fundamentals of Reactive Metal Combustion

W. C. Tao, A. M. Frank, J. E. Shepherd, R. R. McGuire, and R. E. Clements

*We have used high-speed and high-resolution microphotography to examine the ignition and combustion of small aluminum wires (25–76 μm in diameter, 23 mm long) in water that have been rapidly heated by a capacitor-discharge system. Streak photographs were obtained over periods of 30 to 500 μs with a spatial resolution of 2 μm. The temperature of the wire was determined as a function of time by integrating the circuit equation with the energy equation for an adiabatic wire and known aluminum electrical resistivity and temperature functions of energy density. We discovered a transition in the ignition and combustion of the aluminum from mildly to rapidly sustained chemical reaction with the water when the wire was heated above a critical temperature within 1 μs. The triggering mechanism for this rapid reaction appears to be the collapse of a vapor blanket during its first oscillation.*

## Introduction

The combustion of metals, such as aluminum, in the presence of gaseous and liquid oxidizers is relevant to many disciplines.[1–3] These range from nuclear reactor safety and industrial manufacturing to propellant and composite-explosives applications. In the first two areas of interest, the temperature encountered by the metal is not much higher than the melting point, and the interaction with water results in the explosive production of steam because of rapid heat transfer from the molten metal to the water.

In explosive applications, such as airblasting, cratering, and fragmentation, metallic additives react chemically with the oxidizer and are used to tailor the rate of energy delivered by the expansion gas. Mass and thermal-transport limitations determine the reaction rates between the aluminum, intermediate oxidizing species, and detonation products. The formation of aluminum oxide, which is an extremely exothermic reaction ($\Delta H_{f,298} = -1675.7$ kJ/mol), increases the temperature of the expansion gas and directly influences distribution of the equilibrium product.

As the product gas expands, the increase in thermal energy is partitioned between the rotational and vibrational states of the detonation products. This stored energy is recovered from the deactivation of the excited states and transformed into translational kinetic energy in the expansion push at later times (tens of microseconds). For example, for underwater applications in which prompt delivery of the available energy to the bubble expansion is not required, the aluminum content in typical explosive formulations can be as high as 30 to 35 wt%.[4]

In all applications, the major issues are the coupled processes of chemical reaction between the aluminum and the oxidizing medium; the role of energy (i.e., heat) transfer; and fluid dynamics. Although the specific mechanism for sustained chemical reactions remains in question, it is generally accepted that fragmentation of the molten particle and disruption of the oxide layer are necessary. It has been shown that physical mixing or even steam explosion does not trigger any appreciable chemical reaction unless the combustion temperature is above the melting point of its oxide.[5,6] The two are obviously related in the sequence of events from boiling to explosion.

The objectives of this study are to probe the initial reaction of molten aluminum with water, without a preexisting vapor blanket, and to monitor the subsequent heat transfer and chemical reaction between the two fluids. The mode of interaction between the molten mass and water is of special interest.

## Experimental Methods

To study combustion of an aluminum particle with an oxidizer medium, we used a unique combination of an ultrafast laser microphotography facility[7] and a modified aluminum exploding bridge-wire arrangement. The experimental setup, shown in Fig. 1, is modular in design for flexibility. A Nd:YAG laser and an argon continuous-wave (CW) laser provide both pulse and diffuse illumination for front-lit, back-lit, and Schlieren photography. The same illumination sources serve as probe beams for spectral measurements.

The shot module consists of a metallic chamber with four-way optical access and is capable of withstanding a confined detonation of up to 5 g of explosives. We used a conventional capacitor-discharge fire-set to provide the thermal energy for heating up the aluminum. The combustion event is then imaged by intensified framing and streak cameras, with or without including a spectrograph. This unique facility allows imaging to be performed with spatial and temporal resolutions up to 1 μm and 1 ns, respectively.

The combustion experiment consists of time-resolved imaging of a cross section of a pure aluminum wire immersed in water. A known thermal profile is discharged into the wire, and the reaction between the aluminum and water is "streaked out" in time. From the current and voltage profiles, we determine the resistivity of the wire and thus the temperature of the aluminum as a function of time.

Streak images of the combustion of a 51-μm-diameter aluminum wire in water are illustrated in Fig. 2. The triggers for the camera and timing fiducials are initiated at 5 and 2 μs, respectively, prior to the discharge from the fire-set into the wire. We dump the energy content stored in the 0.49-μF capacitor into the wire within 1 μs and shunt the fire-gap in the circuit to prevent restriking. This sequence of events, in effect, mimics the instantaneous placement of an inertially confined, superheated, aluminum molten particle into a mean field of water and the subsequent monitoring of the reaction between the aluminum and the surrounding oxidizing medium.

## Results and Discussion

At 900 V, with an equivalent energy density of 0.74 MJ/kg and a wire temperature of 933 K, a vapor blanket consisting of hydrogen and steam forms around the wire 1 μs after energy discharge. The instability of this vapor blanket is evident in the oscillation shown in Fig. 2. The emission from within the opaque region at a later time is not self-lighting, but rather it is refraction of the laser illumination through a cylindrical lens formed by the vapor blanket. As the charging voltage is increased to 1.75 kV, with an equivalent energy density of 4.45 MJ/kg and a wire temperature of 2793 K, the amplitude and period of the vapor oscillations increase, which results in a transition to rapidly sustained combustion.

The most significant result of our experiment was the discovery of a transition in the ignition and combustion behavior of the system when the wire was heated above a critical temperature. Below a threshold temperature of about 2000 K, very little appears to happen in the water surrounding the wire. Between 2000 and 2500 K, a slow chemical reaction apparently occurs, resulting in an asymmetric vapor blanket (or bubble), which oscillates and slowly grows. At 2600 to 2793 K (the boiling point of aluminum), an initial vapor blanket is formed, and when it collapses, a vigorous ignition and combustion event occurs. At still higher temperatures, ignition and combustion begin promptly without any vapor blanket being created. Triggering of the chemical reaction by the collapse of the vapor blanket is a new observation that has great potential significance in helping us understand interactions of metal and water in both deliberate and accidental explosions.

For combustion of aluminum particles in water, we are interested in extending the results obtained under ambient conditions to more realistic combustion environments, such as a hot, dense detonation-product medium. Close examination of the early streak records (1–5 μs) indicates that there is a luminous sheath within the expanding vapor blanket that has the same dimensions as the wire. Unlike refraction of the laser illumination, this emission is uniform, indicating self-lighting within the aluminum. The temperature within this region, as calculated from the change in resistivity, is well above that of the vapor point. It is reasonable to

**Figure 1.** Schematic of the modular high-speed laser microphotography apparatus.

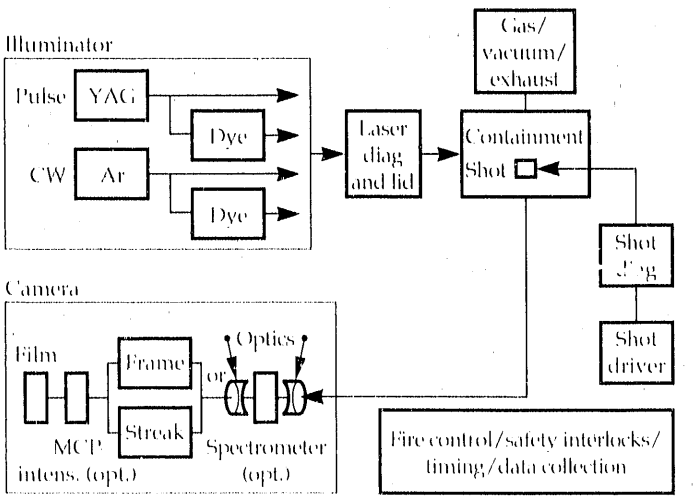

assume that this light originates from superheated aluminum vapor that is inertially confined by the water during the first few microseconds after heat-up.

The surface of this superheated vapor reacts with the surrounding water to generate an expanding vapor blanket consisting of steam, hydrogen, and aluminum oxides. Later, hydrodynamic instability disperses the superheated mixture, rapidly exposing new surface areas for reaction. This is reflected by the sudden increase in the expansion rate of the vapor blanket. Interestingly, there is an absence of shock waves in the water.

The amount of energy dumped into the wire is not enough for the wire to burst promptly, such as is the case for a bridge-wire detonator. Therefore, the expansion rate of the vapor blanket, estimated using the tangential velocity, is approximately 10 m/s, which corresponds more to combustion and deflagration velocities. Experiments directed toward measuring the generation rates of hydrogen and aluminum oxide are planned.

## Future Work

The present results will be extended to higher initial pressures and temperatures as well as to other oxidizing atmospheres, such as carbon monoxide and carbon dioxide. Another goal is the direct observation of chemical species by emission and Raman spectroscopy. Heat transfer by conduction, fluid motion, evaporation,

**Figure 2.**

Streak images (100-μs sweep) of the combustion of 51-μm-diameter aluminum wire in water. The fireset charging voltages are (a) 0.90 kV, (b) 1.05 kV, (c) 1.20 kV, (d) 1.35 kV, (e) 1.50 kV, (f) 1.75 kV, (g) 2.00 kV, and (h) 2.50 kV.

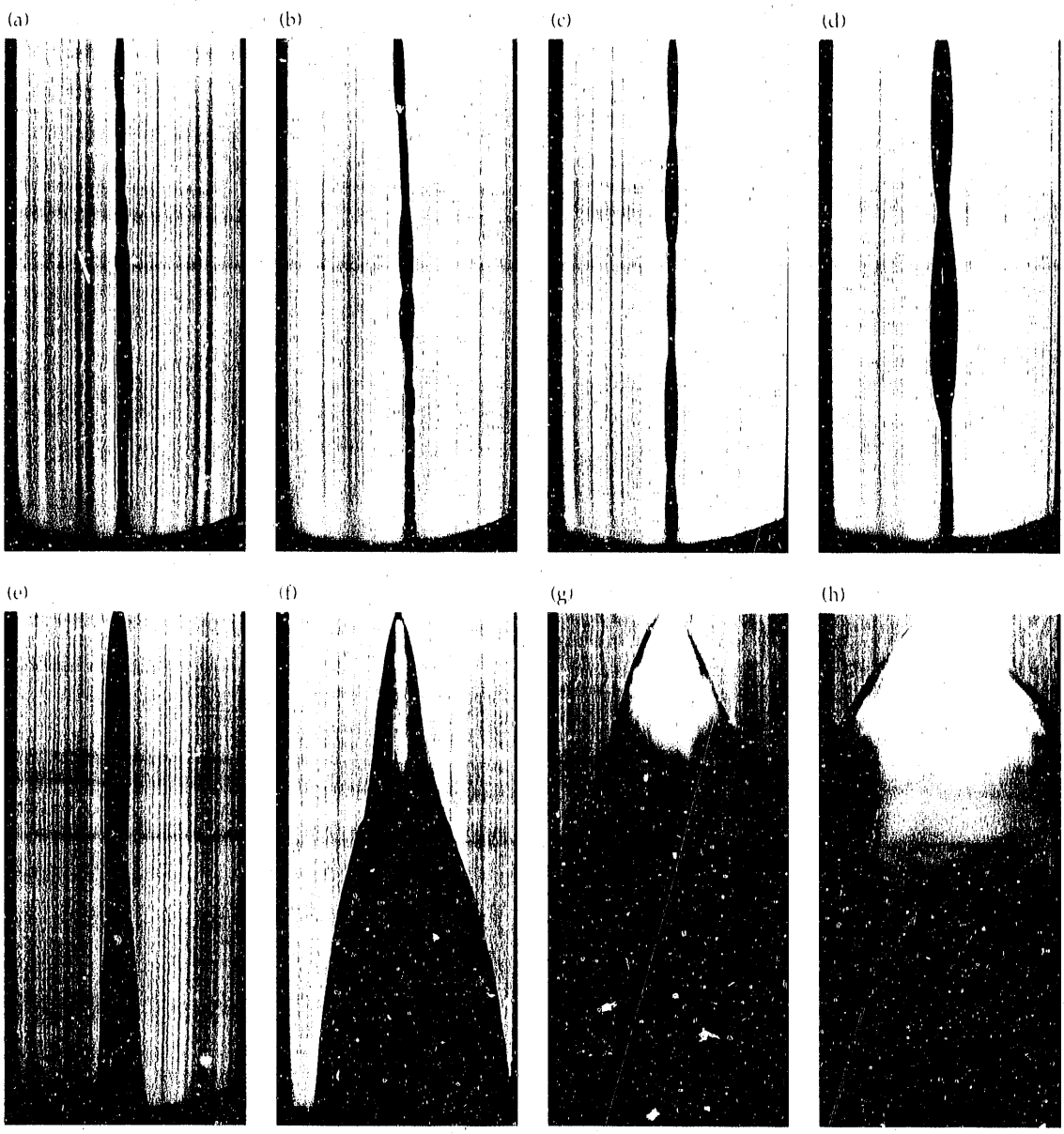

and chemical reaction are all being added to the existing adiabatic computations in the wire-heating model. Our ultimate goals are to obtain measurements of reaction rates and evidence of reaction mechanisms at high temperatures and pressures. These measurements will eventually be used to develop numerical models for the reaction zones in detonating composite explosives.

*This work was supported by Weapons Supporting Research and the DoD Office of Munitions.*

## References

1. L. Baker, Jr., R. Warchal, R. Vogel, and M. Kilpatrick, *Studies of Metal-Water Reactions at High Temperatures (I)*, Argonne National Laboratory, Chicago, Ill., AEC R&D Report ANL-6257 (1961).
2. L. Baker, Jr., and L. Just, *Studies of Metal-Water Reactions at High Temperatures (III)*, Argonne National Laboratory, Chicago, Ill., AEC R&D Report ANL-6548 (1962).
3. L. Baker, Jr., and R. Liimatainen, "Chemical Reactions," *The Technology of Nuclear Reactor Safety*, T. Thompson and J. Beckerley, Eds. (The MIT Press, Boston, Mass.), vol. 2, chap. 17.
4. M. Finger, E. Helm, E. Lee, R. Boat, and H. Cheung, "Characterization of Commercial Composite Explosives," *Sixth Detonation Symp., Silver Spring, Md., 1976*, p. 729.
5. Y. Frolov, P. Pokhil, and V. Logachev, "Ignition and Combustion of Powdered Aluminum in High Temperature Gaseous Media," *Fiz. Goreniya I Vzryva* **8**(2), 212–235 (1972).
6. A. Belyayev, Y. Frolov, and A. Korotkov, "Combustion and Ignition of Particles of Finely Dispersed Aluminum," *Fiz. Goreniya I Vzryva* **4**(3), 323–329 (1968).
7. A. M. Frank, "High-Speed Microphotographic Laboratory," *18th Int. Congress High-Speed Photography and Photonics, Xian, China, August 28–September 2, 1988.*

# Optical Studies of High-Pressure Reaction Chemistry within a Diamond Anvil Cell

S. F. Rice

***Coherent anti-Stokes Raman scattering has been used to probe the reaction chemistry of rapidly reacting nitromethane within a high-pressure environment provided by a diamond anvil cell. Time-resolved, streak-camera records of pulsed laser-ignited reactions show that different pressure regions up to 37.0 GPa have a different reaction chemistry. Deuterium kinetic isotope effects suggest that this chemistry is very different from the simple gas-phase reactivity exhibited by this molecule at low pressure.***

## Introduction

The study of the fundamental reaction chemistry associated with high explosives and the relationship of these details to the macroscopic thermodynamic and mechanical properties involved in a detonation is a rapidly developing field at LLNL and other laboratories throughout the world.[1,2] This chemistry occurs at temperatures of several thousand kelvin and at pressures greater than 10 GPa over a few microseconds. It is anticipated that these studies will ultimately yield the experimental data needed to develop an improved model of the performance of new energetic materials and to predict properties related to sensitivity and safety.

There are, however, many difficulties with the experimental environment implicit in attempts to study these chemical systems directly. Explosions and detonations are essentially single events, typically destroying nearby

**Figure 1.**

Schematic of the experimental layout for single-shot, broadband CARS within a diamond anvil cell. Approximate pulse energies are indicated where relevant. Neutral-density filters in both beams attenuate them to avoid damage to the diamonds. Nd:YAG is neodymium:yttrium-aluminum-garnet.

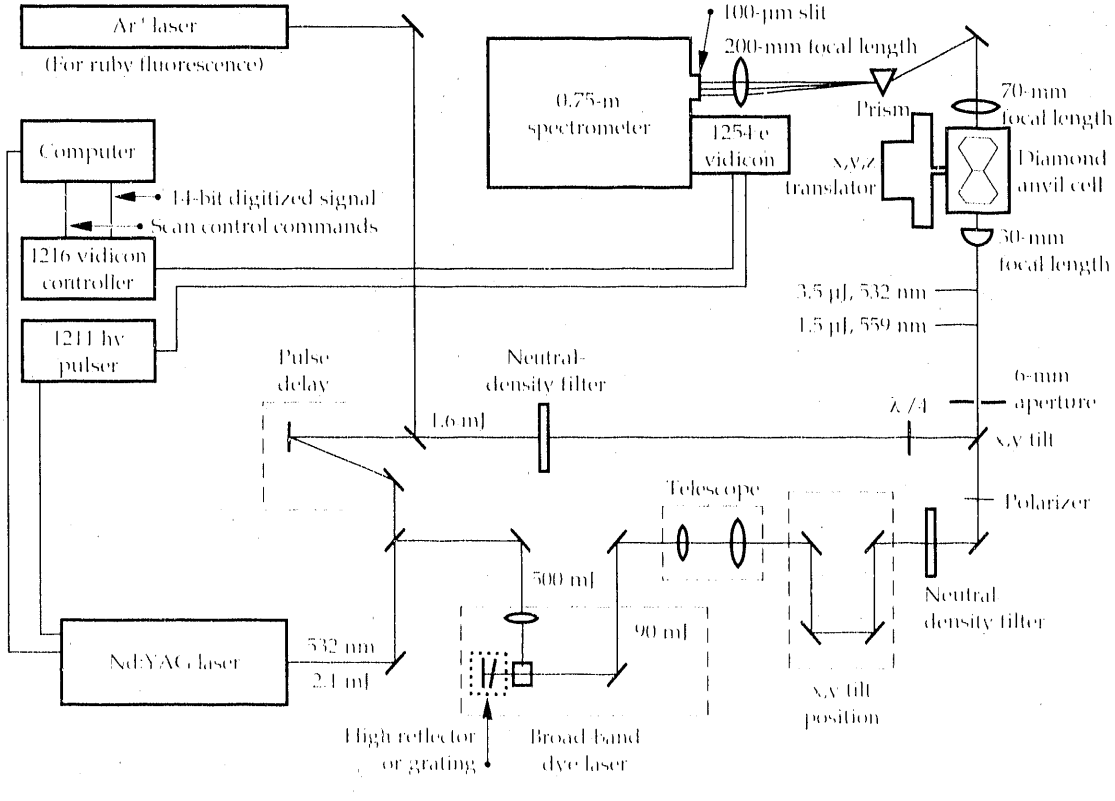

diagnostics or probes embedded in samples. Also, there is no stable sample lending itself to the conveniences of signal-averaging techniques. In addition, at any point in the sample, state variables such as temperature, pressure, and density are evolving rapidly under conditions in which an equation of state relating these variables is not known.

The time scale of the chemical events suggests that laser spectroscopic probes may provide a way to gain the desired information despite these difficulties. Although many sensitive spectroscopic techniques can be overwhelmed by the bright flash emitted directly from the reacting sample, the development of nonlinear Raman techniques and improvements in pulsed laser systems combine to offer an optical diagnostic, coherent anti-Stokes Raman scattering (CARS)[3] that can overcome many of these complications.[4]

## Experimental Method

Our approach to sorting the important reaction chemistry from the experimental complications uses CARS to study tiny controlled "microexplosions" caused by pulsed-laser ignition of nitromethane within the confines of a diamond anvil cell. By combining this very sensitive spectroscopic probe with a sampling method that can statically generate very high densities, we can study the reactivity of energetic materials under conditions that mimic many of those present in a true detonation without most of the technical difficulties.

CARS probes the frequencies of the molecular vibrations that are characteristic of individual or groups of bonds. As a consequence, the intensity of the CARS signal at a specific frequency reflects the concentration of a particular molecular species, be it initial reactive energetic material, intermediate, or final product. CARS has special advantages for our purposes that are related to its applicability as a single-shot probe—without the need for signal averaging—and to its established capabilities in dense and turbulent sample environments.[5]

The diamond anvil cell offers a unique environment for the study of high explosives. Within the small sample area located between the faces of two gem-quality diamonds, pressures as high as 200 GPa have been generated on the laboratory bench.[6] The pressures present in the reaction region in a detonating explosive (10–40 GPa) are, therefore, easily accessible with these cells. The diamond anvil cell adds the particular advantage of affording a clear optical path to the sample from two sides of the cell.

Chemical reactions, phase transitions, and mixing phenomena can be studied directly using optical spectroscopic and microscopic techniques. The optical arrangement used to generate a CARS signal from nitromethane is shown in Fig. 1.[7] The foundation of the system is a frequency-doubled Nd:YAG laser that serves as a 10-ns-long, pulsed light source for the 532-nm CARS pump beam and as the optical pump source for the broad-band dye laser.

These two beams are combined and focused to a 6.4-μm-diameter spot within the diamond anvil cell. The CARS signal, representative of the carbon–nitrogen bond in nitromethane in this case, is spectrally dispersed and recorded on a vidicon two-dimensional detector. Figure 2 shows the results obtained from a single 10-ns pulse. The signal-to-noise ratio near 50 indicates that this technique is sufficiently sensitive to monitor nitromethane reaction kinetics.

We now require some method of igniting the sample whose reactivity is to be studied. Further, the spatial characteristics of this ignition process and the subsequent flame-front propagation behavior must be well characterized. We have designed a pulsed-laser ignition scheme, which, when observed with a streak camera, provides this information.

**Figure 2.** Single-pulse CARS spectrum of (a) nitromethane in a diamond anvil cell at 0.75 GPa, and (b) the diamond in the diamond anvil cell, depicting the nonresonant background scattering that shows the spectral profile of the dye-laser pulse used to produce curve (a). Pulse energies are the same as those indicated in Fig. 1.

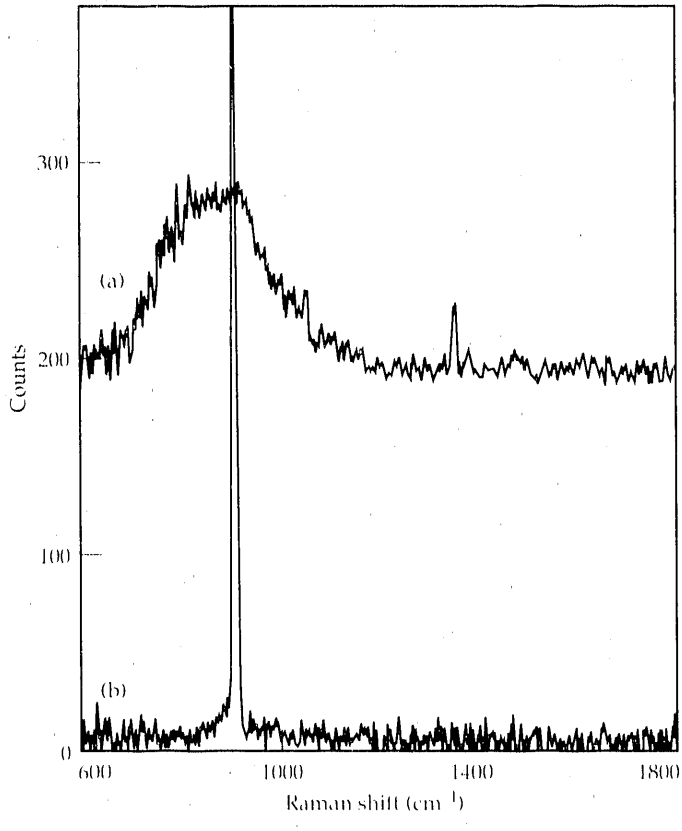

Two typical streak-camera records, at 5.3 GPa and 34.2 GPa, are presented in Fig. 3; these records show the time evolution of the optical transmission properties of nitromethane following ignition by a 10-ns laser pulse. A reaction front that propagates symmetrically and at constant velocity from the ignition point in the center of the sample is a strong function of the sample pressure.

## Results and Discussion

The reaction-front propagation velocities of nitromethane and nitromethane-$d_3$ are plotted in Fig. 4 as a function of initial sample pressure. Two general pressure regimes can be identified. At less than 20 GPa, the pressure dependence of the burn front is essentially a linear function increasing with pressure. The reaction products are gases that vent the sample confinement, destroying the steel sealing gasket. Above 20 GPa, the burn front velocity increases rapidly, and above 30 GPa, it begins to decrease. The reaction products do not vent the sample area, and they appear as a transparent fluid when observed through a microscope in the region greater than 20 GPa.

These results suggest that the overall reaction mechanism switches from one that produces usual combustion product gases at lower pressures, such as $N_2$, $H_2O$, and CO, to one that in some way is prevented from producing these energetically preferred small molecules. The validity of these arguments can be ascertained using the spectroscopic CARS probe described above.

The reaction-front propagation rate for nitromethane-$d_3$ is almost a factor of 2 slower than that for ordinary nitromethane. Kinetic isotope effects such as this are common in a variety of organic reaction mechanisms and have been identified in the thermolysis of other explosives.[8]

This effect can be used to help interpret the nature of the rate-limiting step in a complicated series of reactions. For example, a reaction whose rate-limiting step consists of breaking a carbon–hydrogen bond will exhibit, theoretically, a hydrogen/deuterium reaction-rate ratio that is greater than 1.41 (primary deuterium isotope effect).[9] For a reaction step that is not as easily described as simple bond breaking, ratios somewhat less than 1.41 are typically observed.

The large hydrogen/deuterium ratio exhibited here suggests that, in this case, breaking the carbon–nitrogen bond is indeed crucial to the overall energy-releasing rate exhibited by nitromethane over a wide pressure regime.

## Summary

The initial decomposition step of an energized, single nitromethane molecule in the gas phase is along a pathway that involves homolysis of the carbon–nitrogen bond to form $CH_3$ and $NO_2$ radicals. In the condensed

**Figure 3.**

(a) Streak-camera record of laser-ignited deflagration of nitromethane at 5.3 GPa. The reaction front can be seen as a disturbance on the vertical lines caused by a laser speckle pattern illuminating the sample from behind. The y axis is 4.8 μs for the full length; the x axis is 0.11 mm. (b) Streak record at 34.2 GPa; the y axis is 1.0 μs full scale.

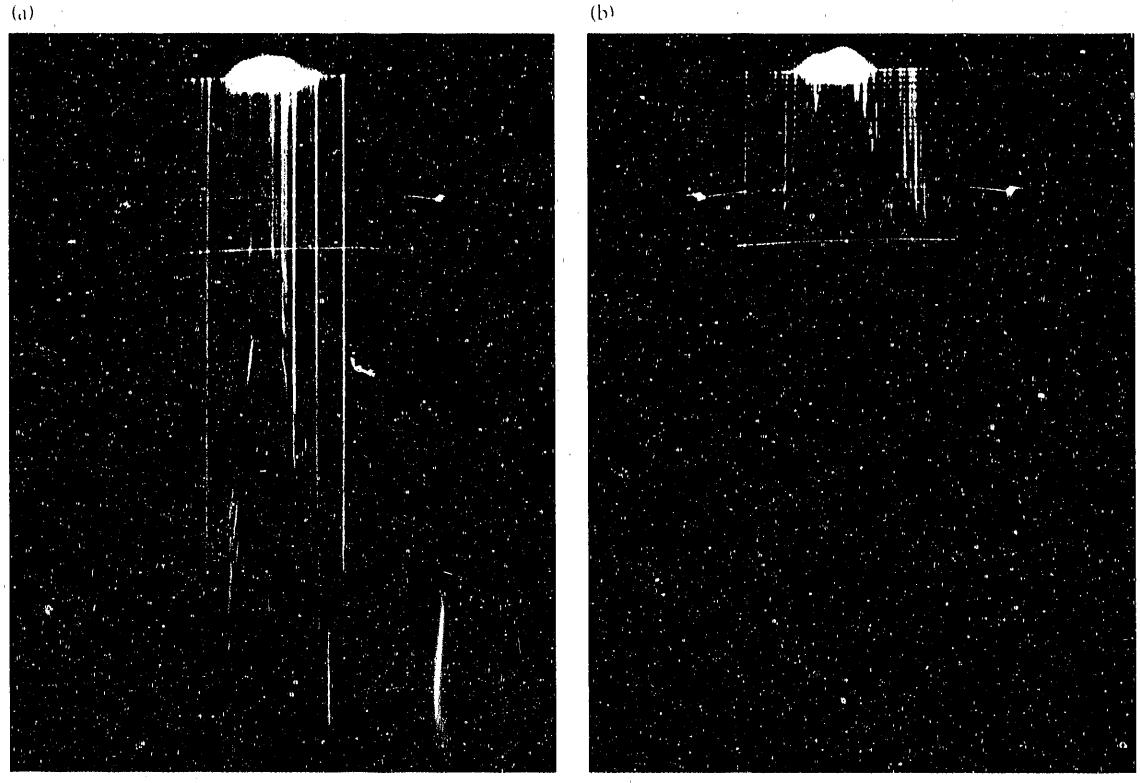

phase, the situation is much more complicated. Bimolecular reaction pathways that involve breaking carbon–hydrogen bonds must be considered. Our research has shown that these more complicated reaction mechanisms do play an important role and must be understood before chemical reaction kinetics can be incorporated effectively into future performance and sensitivity models for high explosives.

*This work was supported by Weapons Supporting Research.*

## References


1. W. M. Trott and A. M. Renlund, *Appl. Opt.* **24**, 1520 (1985).
2. R. Behrens, Jr., *Rev. Sci. Instrum.* **58**, 451 (1987).
3. S. A. Druet and J.-P. E. Taran, *Prog. Quantum Electron.* **7**, 1 (1981).
4. D. S. Moore, S. C. Schmidt, M. S. Shaw, and J. D. Johnson, *J. Chem. Phys.* **90**, 1368 (1989).
5. A. C. Eckbreth, G. M. Dobbs, J. H. Stufflebeam, and P. A. Tellex, *Appl. Opt.* **23**, 1328 (1984).
6. R. J. Hemley, P. M. Bellm, and H. K. Mao, *Science* **237**, 605 (1987).
7. S. F. Rice and M. S. Costantino, *J. Phys. Chem.* **93**, 536 (1989).
8. S. A. Shackleford, M. B. Coolidge, B. B. Goshgarian, B. A. Loving, R. N. Rogers, J. L. Janney, and M. H. Ebinger, *J. Phys. Chem.* **89**, 3118 (1984).
9. J. Bigeleisen and M. Wolfberg, *Advances in Chemical Physics 1*, I. Prigogine, Ed. (Interscience Publishers, New York, 1958), pp. 15–31.


**Figure 4.** Plot of the reaction-front propagation rate as a function of pressure for nitromethane and nitromethane-$d_3$. Errors in the pressure measurement are from slight inhomogeneities within the diamond anvil cell. Errors in the propagation rate are due to the overall quality of the streak-camera record.

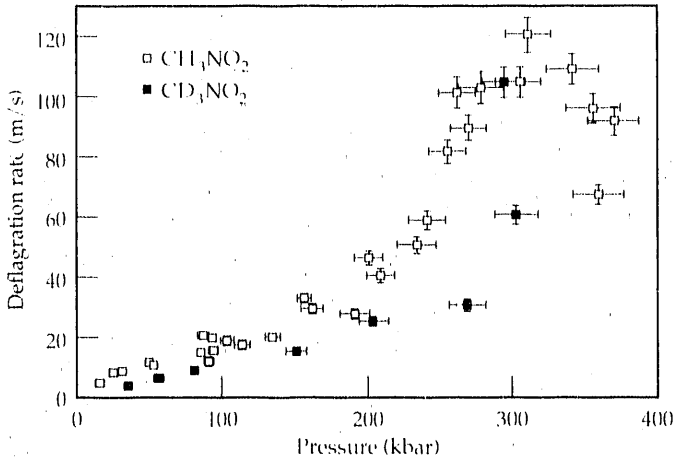

# New Methods for the Synthesis of High-Energy Materials

C. L. Coon, P. F. Pagoria, and W. C. Tao

*The synthesis of new energetic materials often involves the development of new synthetic procedures. In preparing several important target materials, three new reagents for incorporating nitro groups into organic molecules were discovered. These new reagents include the use of dinitrogen pentoxide ($N_2O_5$) in 100% nitric acid, in trifluoroacetic anhydride, and in trifluoromethanesulfonic acid anhydride. These new procedures broaden our general knowledge of nitramine chemistry and will be especially useful in the synthesis of many energetic molecules that had previously been difficult to synthesize.*

## Introduction

The two primary objectives of this project are to develop (1) a new high-energy material to replace HMX[*], and (2) a new insensitive explosive to replace TATB[†]. We are aiming for higher energy content while maintaining good thermal and sensitivity properties. Toward this end, new molecules for synthesis are selected on the basis of predicted densities, heats of formation, stability, and initiation properties; and synthetic paths are then devised and studied. Uncertainties in estimated density and heat of formation can affect predicted performance parameters, such as detonation velocity and pressure, by as much as 10 to 15%. The synthetic routes to these new molecules

**Figure 1.**

New energetic target materials for synthesis research.

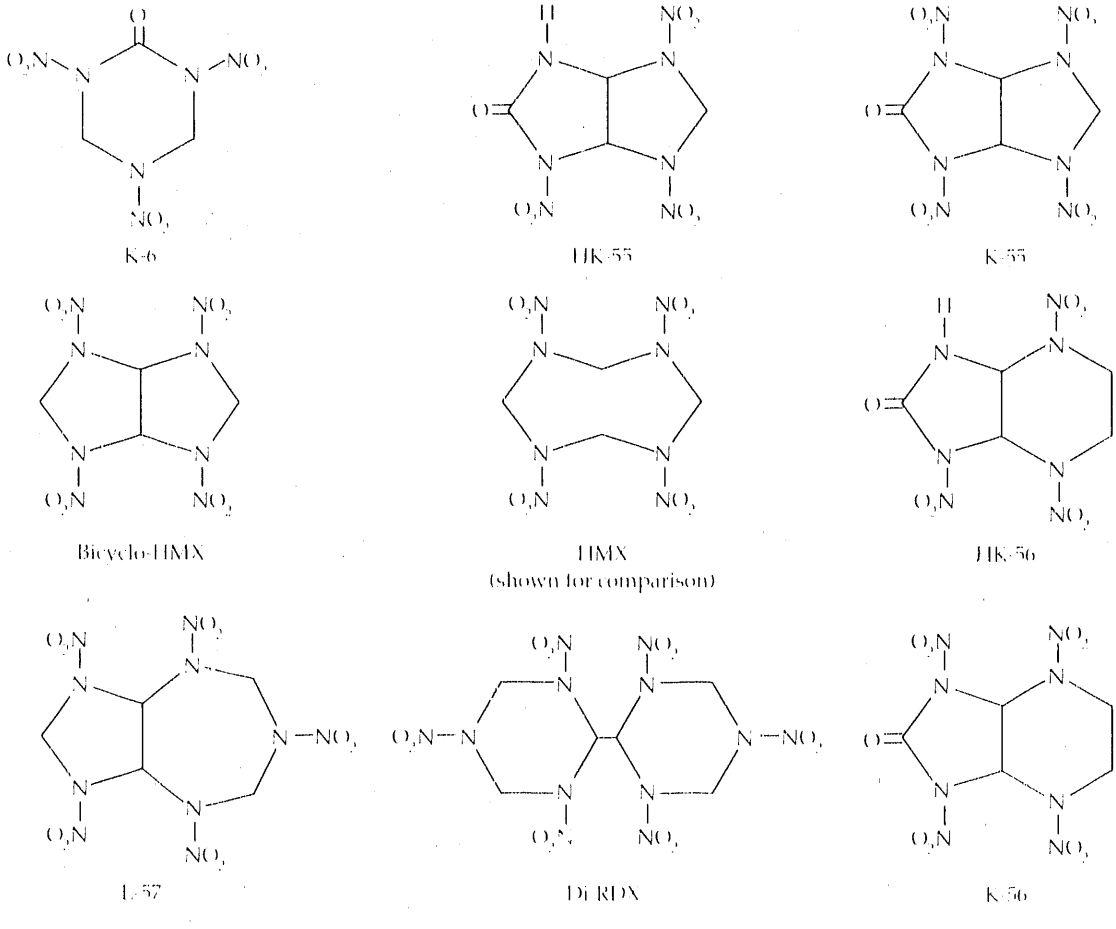

often involve the development of new synthetic procedures. Three such procedures are described here.

## Results

In the area of new high-energy materials, we sought molecules that are similar to HMX in molecular structure but contain smaller heterocyclic and fused heterocyclic rings. Examples of the new target materials whose syntheses are complete or nearly complete (along with the structure of HMX) are shown in Fig. 1.

A synthesis problem arose in our work on dimethyl di-RDX[‡] when no conventional reagent was found to convert the diacetyl derivative to its dinitro analog (Fig. 2, Eq. 1). The conventional procedures either gave no reaction or resulted in decomposition of the substrate. The conversion proceeded successfully with the use of a new nitrolyzing medium composed of dinitrogen pentoxide ($N_2O_5$), 100% nitric acid, and trifluoroacetic anhydride (TFAA[§]). This reagent produced an 85% yield of a nearly pure product that separated from the reaction mixture as an easily isolated white powder.

A second synthesis problem was encountered during research on the synthesis of bicyclo-HMX. The new nitrolysis reagent $N_2O_5$/100% nitric acid/TFAA could be used to convert the dinitrodiacetyl intermediate to the trinitromonoacetyl derivative, but yields were never greater than 10% (Fig. 3, Eq. 2). The use of propionyl derivatives in place of acetyl derivatives produced a remarkable increase in yield (>90%) with the same nitrolysis reagent (Fig. 3, Eq. 3). The development of this key step eventually led to the synthesis of the important target material bicyclo-HMX.

A third nitrolysis reagent was developed for the final step in the synthesis of K-56 (Fig. 4, Eq. 4). Conventional nitrolysis reagents were either ineffective or destroyed the bicyclic ring system. However, the use of a mixture of $N_2O_5$ and 100% nitric acid in trifluoromethanesulfonic acid anhydride (TFMSAA) successfully accomplished the desired nitrolysis in about 40% yield, giving the target material K-56.

**Figure 2.** **Effect of a new nitrolysis reagent, $N_2O_5$/$HNO_3$/TFAA, on the yield of the di-RDX intermediate.**

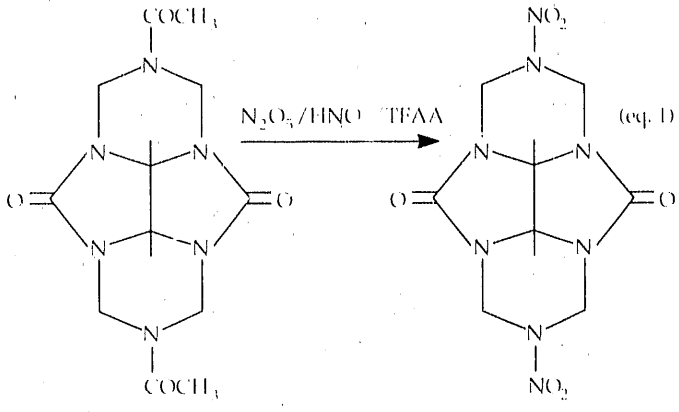


| Reagent | Yield |
|---|---|
| $HNO_3$ | Decomposition |
| $N_2O_5$/$HNO_3$ | Decomposition |
| $HNO_3$/$Ac_2O$ | No reaction |
| $HNO_3$/TFAA | Decomposition |
| $N_2O_5$/$Ac_2O$ | <10% yield |
| $NO_2BF_4$ | No reaction |
| $N_2O_5$/$HNO_3$/TFAA | >85% yield |

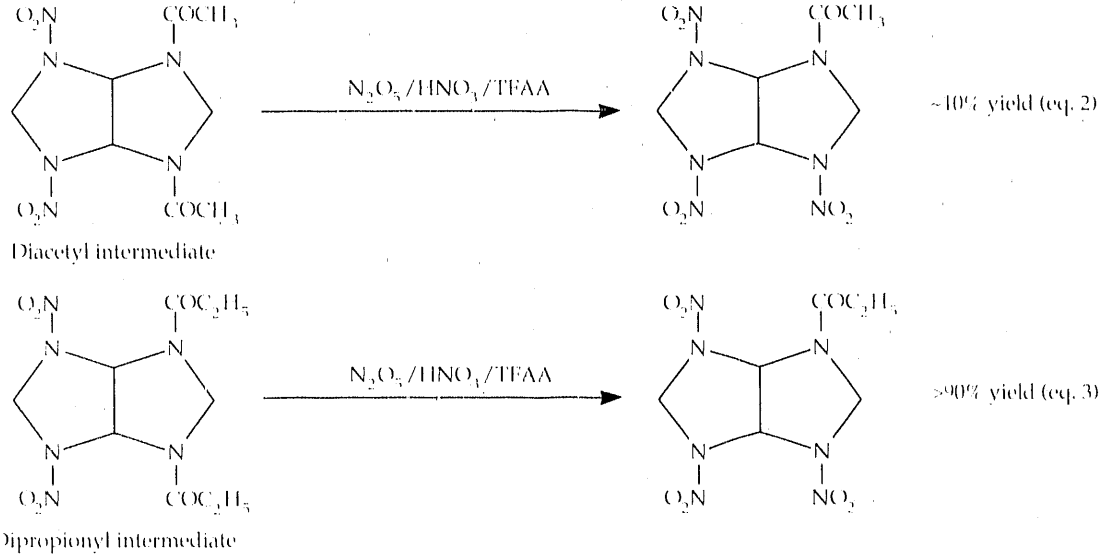


**Figure 3.**

**An increase in nitrolysis yield was achieved using propionyl substitution instead of the usual acetyl substitution.**

In summary, we have developed three new techniques for the synthesis of the nitramino group, opening the way to a family of new energetic materials that are otherwise unavailable. These new synthetic procedures should be useful not only in preparing additional explosive target materials, but also as convenient tools in general organic synthesis.

**Figure 4.** Effect of a new nitrolysis reagent on the yield of K-56.

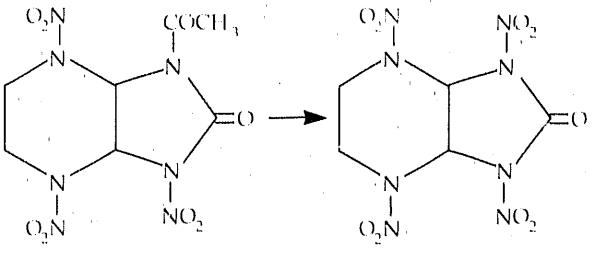


(eq. 4)

K-56

| Reagent | Yield |
|---|---|
| $HNO_3/Ac_2O$ | No reaction |
| $N_2O_5/HNO_3$ | Decomposition |
| $NOBF_4$ | No reaction |
| $HNO_3$/TFAA | No reaction |
| $HNO_3$/TFMSAA | ~40% yield |

*This research was supported by Weapons Supporting Research and the Weapons Program; and by the DoD Office of Naval Research and Office of Munitions.*

*HMX is octahydro-1,3,5,7-tetranitro-1,3,5,7-tetrazocine.
†TATB is 2,4,6-trinitro-1,3,5-benzenetriamine.
‡RDX is hexahydro-1,3,5-trinitro-1,3,5-triazine.
§While the use of $N_2O_5$/100% nitric acid/TFAA for the nitrolysis of this diamide to the dinitramine is very effective, it should be used with caution only by chemists with experience in handling explosives. There were two explosions during our experiment because of the buildup of trifluoroacetyl nitrate, an explosive liquid. Safe handling procedures can be obtained from the authors.

# Synthesis and Characterization of (Trifluoromethyl)gold Complexes

R. D. Sanner

***We have prepared 20 new gold compounds that use the trifluoromethyl ($CF_3$) group as a ligand. This article describes synthesis of $(CF_3)AuL$ (L = $PMe_3$, $PEt_3$, $PPh_3$) from LAuCl and $(CF_3)_2Cd•DME$*. These linear gold(I) compounds readily add excess halogen to form the predominantly* trans*, square-planar gold(III) dihalides $(CF_3)AuX_2(L)$ (X = Br, I), while addition of $CF_3I$ leads to $(CF_3)_2AuI(L)$. Treatment of $(CF_3)_2AuI(PMe_3)$ with $(CF_3)_2Cd•DME$ in the presence of excess $CF_3I$ leads to the fully trifluoromethylated species, $(CF_3)_3AuPMe_3$. These new complexes have been completely characterized by $^{19}F$ and $^1H$ nuclear magnetic resonance (NMR) spectroscopy.***

## Introduction

Fluorocarbon-metal sigma bonds are generally more robust than the analogous hydrocarbon-metal sigma bonds; thus, we anticipate that metal complexes containing fluorocarbon ligands will exhibit enhanced thermal stability compared with their hydrocarbon-ligated analogs, which would expand their useful temperature range. Although the first trifluoromethyl ($CF_3$) derivative of a transition metal was reported over 30 years ago,[1] synthesis and study of such complexes have been limited.[2] This may be due, in part, to the paucity of trifluoromethylating reagents available.

While the synthetic chemist may choose among Grignard reagents, methyllithium, dimethylzinc, or other common alkylating agents, trifluoromethyl analogs of these standard reagents are either unknown or ineffective in the preparation of transition-metal compounds. As part of our studies on gold alkyl compounds, we set out to synthesize the mono-, bis-, and tris(trifluoromethyl)gold phosphine complexes, $(CF_3)AuL$, $(CF_3)Au(L)X_2$, $(CF_3)_2Au(L)X$, and $(CF_3)_3AuL$, and investigate their physical and chemical properties vis-à-vis their methyl analogs.[3] We have utilized a variety of phosphine (L) and halide (X) ligands in this work to examine the effect of the ligand on the reaction products.

## Results and Discussion

**Synthesis of $(CF_3)AuL$.** We have found that a general procedure[4] for preparation of $(CF_3)AuL$ compounds involves treatment of the phosphine halide complex with $(CF_3)_2Cd•DME$ in methylene chloride [Eq. (1)].

$$2ClAuL + (CF_3)_2Cd•DME \rightarrow 2(CF_3)AuL + CdCl_2 \quad (1)$$

In contrast to their methyl analogs, $(CF_3)AuL$ cleanly adds excess halogen ($X_2$= $Br_2$, $I_2$) to form $(CF_3)AuX_2(L)$ [Eq. (2)]. Comparisons of the new $(CF_3)AuX_2L$ with their methyl analogs are not possible; indeed, simple monoalkylgold(III) complexes are unknown. The square-planar stereochemistry of the dihalides is predominantly *trans*, with phosphorus–fluorine coupling constants in the 75- to 90-Hz range in the $^{19}F$ NMR spectra.

$$(CF_3)AuL + X_2(excess) \rightarrow (CF_3)AuX_2(L) \quad (2)$$

**Synthesis of $(CF_3)_2AuX(L)$.** Our first attempts to prepare a bis(trifluoromethyl)gold complex utilized the cadmium reagent and gold(III) precursors, but resulted in reduction to $(CF_3)AuL$. Puddephatt[5] reported the (irreproducible) preparation of $(CF_3)MeAuI(PMe_3)$ from the *cis* oxidative addition of $CF_3I$ to $MeAuPMe_3$. We have extended this approach and find that methylene chloride solutions of $(CF_3)AuL$ (L = $PMe_3$, $PEt_3$) react with $CF_3I$ at 50°C to generate $(CF_3)_2AuI(L)$ [Eq. (3)].

$$CF_3AuL + CF_3I \rightarrow (CF_3)_2AuI(L) \quad (3)$$

The rate of addition is strongly dependent on the nature of the phosphine ligand. Thus, the ratio of the disappearance half-lives for $(CF_3)AuL$, $t_{1/2}(PMe_3)/t_{1/2}(PEt_3)$,

The $^{19}F$ NMR spectra of these compounds are quite characteristic: all three complexes exhibit doublets 30 ppm upfield of $CFCl_3$ with phosphorus–fluorine coupling constants of about 45 Hz.

was found to be 600. No reaction at all was observed with L = $PPh_3$. These results suggest that the steric bulk of the phosphine ligand is an important factor in determining the rate of the oxidative addition reaction shown in Eq. (3). Thus, the smallest of the three ligands examined, $PMe_3$, exhibits the fastest rate, while the largest ligand, $PPh_3$, completely inhibits the addition of $CF_3I$. Attempts to prepare bromide analogs of $(CF_3)_2AuI(L)$ by using $CF_3Br$ in place of $CF_3I$ were unsuccessful, presumably because of the greater bond strength of carbon–bromine compared with carbon–iodine.

The $^{19}F$ NMR spectrum of $(CF_3)_2AuI(PMe_3)$ is shown in Fig. 1. Although the *cis* isomer predominates (~95%), the presence of both *cis* and *trans* isomers is in contrast to the analogous $Me_2AuI(L)$ complexes, in which only the *cis* isomer is found. The formation of $Me_2AuI(L)$ was shown by earlier workers[6,7] to proceed via oxidative addition followed by methyl-for-iodine exchange to produce $Me_3AuL$ as an intermediate. We believe simple *cis* oxidative addition forms our trifluoromethyl complexes and see no evidence of $CF_3/I$ exchange.

The isomers of $(CF_3)_2AuI(L)$ are easily distinguished on the basis of their splitting patterns. Figure 1 shows the expected doublet ($^3J_{P-F}$ = 11 Hz) at –19.3 ppm for the equivalent trifluoromethyl ligands in the *trans* isomer. The small value of $^3J_{P-F}$ is in accord with both trifluoromethyl ligands oriented *cis* to the trimethylphosphine. Each trifluoromethyl group in the *cis* isomer should, to first order, appear as a doublet ($^3J_{P-F}$) of quartets ($^4J_{F-F}$) with a substantially larger phosphorus–fluorine coupling for the trifluoromethyl group *trans* to the phosphine. [Recall $^3J_{P-F}$ = 75–90 Hz for *trans*-$(CF_3)AuX_2(L)$ and 10–20 Hz for *cis*-$(CF_3)AuX_2(L)$.]

Figure 1 shows a well-separated doublet of quartets at –22 ppm with $^3J_{P-F}$ = 79 Hz and $^4J_{F-F}$ = 8.1 Hz that we assign to the trifluoromethyl ligand *trans* to the trimethylphosphine group. Figure 1 also shows a complex pattern that may be fit to an (exactly) overlapping doublet of quartets with $^3J_{P-F}$ = 16 Hz and $^4J_{F-F}$ = 8.1 Hz at a chemical shift of –26.3 ppm. We assign this spectral feature to the trifluoromethyl group *cis* to $PMe_3$ on the basis of the small phosphorus–fluorine coupling. This exact overlap of quartets is due to the fortuitous relationship of the coupling constants in the complex, $^3J_{P-F} = 2(^4J_{F-F})$.

**Synthesis of $(CF_3)_3AuPMe_3$.** The synthesis of the fully trifluoromethylated gold(III) complex initially utilized cadmium reagent. As shown in Eq. (4), this reaction produced the target molecule but was plagued by the reductive elimination of $CF_3I$ with concomitant formation of $CF_3AuPMe_3$. We found it possible to inhibit this elimination reaction by carrying out the synthesis under a $CF_3I$ atmosphere. This led to an 80-percent yield of the fully trifluoromethylated product [Eq. (5)].

$$3(CF_3)_2AuI(PMe_3) + (CF_3)_2Cd \bullet DME \rightarrow 2(CF_3)_3AuPMe + CF_3AuPMe_3 + CF_3I + CdI_2 \quad (4)$$

$$2(CF_3)_2AuI(PMe_3) + (CF_3)_2Cd \bullet DME \rightarrow 2(CF_3)_3AuPMe_3 + CdI_2 \quad (5)$$

The $^{19}F$ spectrum of this compound (Fig. 2) is entirely in accord with a square-planar structure having two inequivalent sets of trifluoromethyl ligands in a 2:1 intensity ratio. The trifluoromethyl group *trans* to the

**Figure 1.** $^{19}F$ NMR spectrum ($CH_2Cl_2$, 188.25 MHz, $CFCl_3$ reference) of $(CF_3)_2AuI(PMe_3)$.

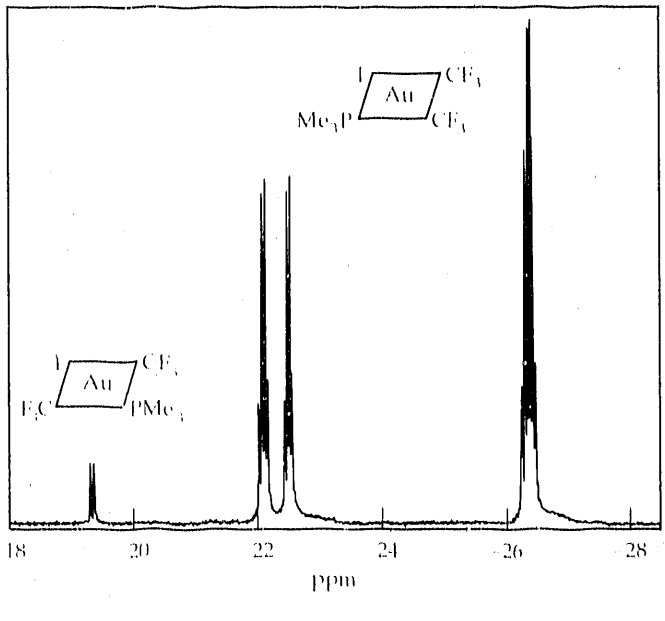


**Figure 2.** $^{19}F$ NMR spectrum ($CH_2Cl_2$, 188.25 MHz, $CFCl_3$ reference) of $(CF_3)_3Au(PMe_3)$.

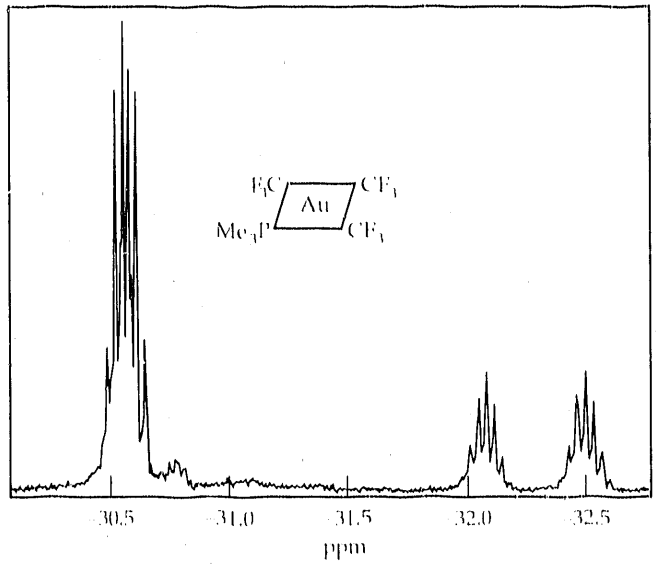

phosphine should, to first order, appear as a well separated doublet ($^3J_{P-P}$) of septets ($^4J_{F-P}$). Figure 2 exhibits just such a pattern (the intensity ratio within the septet is 1:6:15:20:15:6:1), with $^3J_{P-P}$ = 79 Hz and $^4J_{F-P}$ = 6.4 Hz at a chemical shift of –32.3 ppm. The two equivalent trifluoromethyl groups *cis* to the phosphine should appear as a doublet of quartets that might be expected to overlap severely. Figure 2 shows this predicted pattern with $^3J_{P-P}$ = 10.5 Hz and $^4J_{F-P}$ = 6.4 Hz at –30.6 ppm.

The upfield chemical shifts displayed by $(CF_3)_3AuPMe_3$ are the largest we measured for the (trifluoromethyl)gold complexes. There is a clear trend of increased shielding with increased trifluoromethyl coordination. This trend is also reflected in the $^1H$ NMR spectra of the trimethylphosphine ligand, wherein $I_3AuPMe_3$ (2.30 ppm) and $(CF_3)_3AuPMe_3$ (1.78 ppm) represent the two extremes of this gold(III) series.

## Conclusions

We have prepared the (trifluoromethyl)gold(I) phosphine compounds $(CF_3)AuL$ and the entire series of gold(III) complexes $(CF_3)_nAuX_{3-n}(L)$ ($n$ = 1–3). An overview of these reactions is presented in Fig. 3. The cadmium reagent $(CF_3)_2Cd$•DME, while sometimes suitable, does not have the general applicability of a Grignard or lithium reagent. In particular, it promotes the reduction of gold(III) in cases in which methyllithium is known to act as a suitable substitution reagent. However, its use as a trifluoromethylating reagent for gold(I) and, under certain conditions, for gold(III) extends its scope beyond the previous confines of the group VIII metals and suggests its inclusion in the short list of procedures available to synthesize transition-metal trifluoromethyl complexes.

*This work was supported by Weapons Supporting Research and the Weapons Program.*

*DME is 1,2-dimethoxyethane.

## References


1. T. H. Coffield, J. Kozikowski, and R. D. Closson, *Abstr. 5th Int. Conf. Coord. Chem.* 1959, p. 126.
2. J. A. Morrison, *Adv. Inorg. Chem. Radiochem.* **27**, 293 (1983).
3. R. D. Sanner, J. H. Satcher, Jr., and M. W. Droege, *Organometallics* **8**, 1498 (1989).
4. C. D. Ontiveros and J. A. Morrison, *Inorg. Synth.* **24**, 35 (1986).
5. A. Johnson and R. J. Puddephatt, *J. Chem Soc., Dalton Trans.*, 1360 (1976).
6. A. Johnson and R. J. Puddephatt, *J. Organomet. Chem.* **85**, 115 (1975).
7. A. Tamaki and J. K. Kochi, *J. Organomet. Chem.* **64**, 411 (1974).


**Figure 3.** Summary of synthetic pathways.

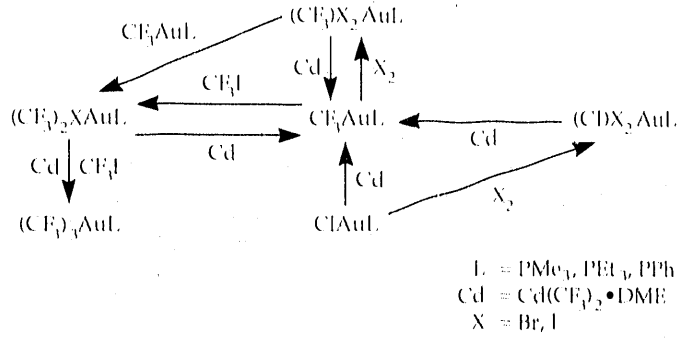

# Combustion Synthesis of the Composite Ti–C–Ni–Al

J. B. Holt and
S. D. Dunmead

*We used the process of combustion synthesis to produce a ceramic-metal composite consisting of titanium carbide and an intermetallic alloy of the nickel–aluminum system. The samples were produced by rapidly heating a mixture of elemental titanium, carbon, nickel, and aluminum powders in a graphite die up to the ignition temperature. By applying mechanical pressure during or immediately following the combustion reaction, products with greater than 99 percent of theoretical density were obtained. By varying the combustion-synthesis parameters, the properties of the product can be tailored to meet specific applications needs. Possible applications of such composites include cutting tools, wear parts, structural components, and armor.*

## Introduction

One of the major drawbacks in combustion synthesis of refractory materials is the highly porous nature of the products. This porosity is caused by three basic factors: (1) the change in the molar volume that is inherent in the reaction, (2) the porosity of the unreacted sample, and (3) the adsorbed gases present on the reactant powders. For example, in the reaction between titanium and carbon to form titanium carbide (TiC), the product is approximately 23 percent more dense than the reactants. Furthermore, the unreacted powders are generally cold-pressed to 50 to 70 percent density. Thus, without densification occurring, one could not expect to obtain a product with a density greater than about 50 percent.

Maksimov et al.[1] and Holt and Munir[2] have also found that adsorbed gases greatly contribute to the porosity of the final product. This effect is due to the specimen expansion (5–50%) that takes place as these gases are rapidly heated from the ambient temperature up to the combustion temperature. Because of the porosity, the majority of the materials produced are used in powder form. If dense parts are desired for a specific application, the powders must undergo some type of densification process, such as sintering or hot pressing. The ideal production process would combine synthesis and densification into a one-step operation.

In this article, the use of a low-pressure, hot-pressing technique to produce dense ceramic-metal composites will be demonstrated by results from work on the Ti–C–Ni–Al system. This system was selected because strongly exothermic reactions occur in both the TiC and nickel–aluminum (Ni–Al) systems and because of interest in composite materials consisting of TiC and an intermetallic alloy of the Ni–Al system for various structural, cutting tool, and armor applications.

**Table 1.** X-ray diffraction results for reactions of the form 50 wt% (Ti + C) + 50 wt% ($x$Ni + $y$Al).

| | Product | | | | | | | | |
|---|---|---|---|---|---|---|---|---|---|
| Binder | TiC | Ni | $Ni_3Al$ | $Ni_5Al_3$ | NiAl | $Ni_2Al_3$ | $NiAl_3$ | Al | $TiAl_3$ |
| Ni | M | M | — | — | — | — | — | — | — |
| 3Ni + Al | M | — | S | — | — | — | — | — | — |
| 5Ni + 3Al | M | — | S | — | S | — | — | — | — |
| Ni + Al | M | — | — | — | S | — | — | — | — |
| 2Ni + 3Al | S | — | — | — | — | M | — | — | — |
| Ni + 3Al | S | — | — | — | — | M | m | — | m |
| Al | m | — | — | — | — | — | — | m | M |

M, major phase; S, secondary phase; m, minor phase.

## Experimental Procedures

Reagent powder mixtures were prepared for the following three basic reactions:

$$Ti + C + x(Ni + Al) \quad , \tag{1}$$

$$Ti + C + x(3Ni + Al) \quad , \tag{2}$$

$$50\ wt\%(Ti + C) + 50\ wt\%(yNi + zAl) \quad , \tag{3}$$

where $x$ ranged from 12.5 to 75 wt%, while $y$ and $z$ were such that the proper stoichiometry existed in the mixture to form each of the Ni–Al compounds known to exist. The Ni–Al part of both the reagents and products is referred to as the "binder."

The powder mixture was cold-pressed at a pressure of 20.7 MPa (3000 psi) and achieved about 50 percent of theoretical density. The die assembly was then inserted into the hot-pressing apparatus and resistively heated at about 1500 K/min. A thermocouple was inserted into a hole in the side of the die so that the approximate temperature of the die at ignition could be monitored. When ignition occurred, the hydraulic rams were compressed to the desired pressure; this pressure was held for about 1 to 2 min (until the die was no longer red hot).

## Results and Discussion

**X-Ray Diffraction.** Table 1 shows the results of x-ray diffraction measurements for the detection of combustion products of the mixtures shown in Eq. (3). It is seen that binder compositions of Ni, (3Ni + Al), and (2Ni + 3Al) gave products containing only TiC and a Ni–Al phase with the same stoichiometry as in the reactants. However, when the binder composition was (5Ni + 3Al), the product consisted of TiC, NiAl, and $Ni_3Al$. This result can be explained by noting that $Ni_5Al_3$ decomposes on heating at approximately 973 K (700°C) into NiAl and $Ni_3Al$. As the compact cools, the kinetics of the peritectoid reaction between solids NiAl and $Ni_3Al$ to form $Ni_5Al_3$ are slow enough so that the phases present in the higher-temperature, two-phase field are quenched in. It is also apparent from Table 1 that the compositions with high aluminum content, (Ni + 3Al) and Al, result in complex phase relationships, including the formation of $TiAl_3$.

**Binder Content.** The effect of the amount of binder in the compact on the residual porosity of the final product was studied. Figure 1 shows that for two sets of samples in which the product was either a TiC–NiAl or TiC–$Ni_3Al$ composite, there is a slight decrease in porosity with increasing binder content. This result is probably caused by an increase in the quantity of liquid phase present during the reaction.

It is also evident in Fig. 1 that at low binder contents, the identity of the binder has little effect on the residual porosity in the product. Higher binder contents of NiAl result in compacts that have consistently lower levels of porosity than those which contain $Ni_3Al$. This result is likely due to the difference in the heat of formation between NiAl (–71,650 J•mol$^{-1}$) and $Ni_3Al$ (–37,550 J•mol$^{-1}$). The compacts that contain NiAl have higher combustion temperatures, which promote the formation of liquid and, thus, favor densification.

**Microstructure.** Figure 2 contains an optical photomicrograph of the combustion product of 50 wt%(Ti + C) and 50 wt%(Ni + Al). This product has a residual porosity of 0.3 percent. The spherical TiC grains (55 vol%) in this sample were found to average 1.2 mm, and the microhardness was measured to be 930 kg/mm$^2$. It is interesting to note that the TiC grains in this sample appear as if they were precipitated from a melt. The postulated mechanism of reaction is solution precipitation rather than diffusion through a solid product layer of TiC. Titanium and carbon dissolve in molten nickel, and the TiC spherical grains precipitate as spherical grains.

The sample with 50 wt%(Ti + C) and 50 wt%(3Ni + Al) was combusted under the same conditions as the one shown in Fig. 2. Here, the product was found to have a residual porosity of 3.0 percent, an average grain size of 1.1 mm, and a microhardness of 1111 kg/mm$^2$. The product of combustion of 75 wt%(Ti + C) and 25 wt%(Ni + Al), under the same conditions as the previous two samples, resulted in a residual porosity of 5.7 percent. The average grain size of the TiC was 5.9 mm, and the microhardness was 1916 kg/mm$^2$. These TiC grains are much larger than those seen in Fig. 2, because as the TiC content is increased, the combustion temperature increases, thus enhancing the grain growth.

**Applied Pressure.** Figure 3 shows the effect of the amount of applied pressure on the level of porosity in the product for samples that contain 50 wt% of either (Ni + Al) or (3Ni + Al) as the binder. Here, it can be seen that the application of pressures as low as 6.98 MPa (1000 psi) has dramatic effects on the level of porosity. It

**Figure 1.**

Residual porosity of samples containing varying amounts of (Ni + Al) or (3Ni + Al) as the binder, combusted under 20.7 MPa (3000 psi).

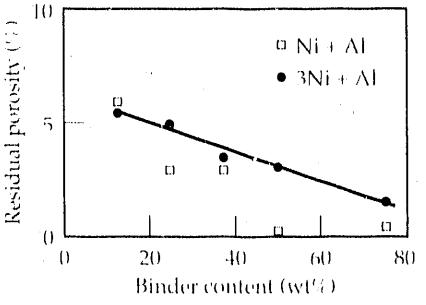


**Figure 2.**

Optical photomicrograph (at 1000× magnification) of the product of combustion of 50 wt% (Ti + C) + 50 wt% (Ni + Al) under 20.7 MPa (3000 psi).

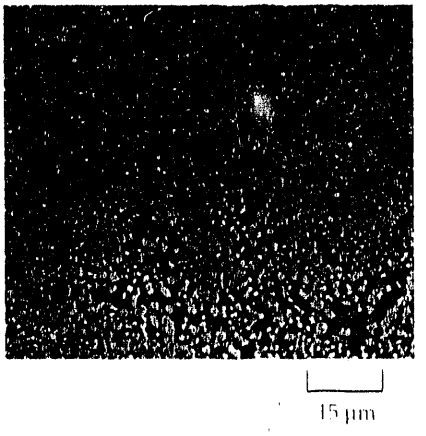

also shows that, as expected, an increase in the amount of applied pressure results in a decrease in the residual porosity of both binders.

## Summary

By using a simple hot-pressing apparatus, certain refractory materials may be synthesized and densified in a one-step combustion process. Specifically, composite materials consisting of TiC–Ni, TiC–NiAl, and TiC–$Ni_3Al$ can be produced at near theoretical density using combustion synthesis under relatively low mechanical pressures. We have shown that very fine-grained materials can be produced in this way and that the grain size can be controlled by changing the amount of binder. By adjusting the synthesis conditions, it is possible to tailor the properties of the product further and to develop a viable materials production process.

*This work was supported by Weapons Supporting Research and the Weapons Program.*

**Figure 3.**

Residual porosity for samples containing either (Ni + Al) or (3Ni + Al) as the binder, combusted under various pressures.

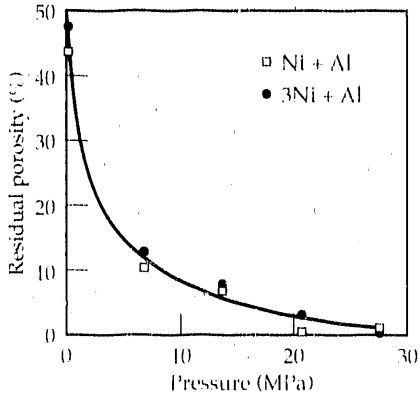


## References

1. Y. M. Maksimov, A. G. Merzhanov, A. T. Pak, A. G. Raskolenko, and B. S. Braveman, "High-Temperature Synthesis in the System Ti-B-Fe," *Metally* **2**, 219–223 (1985).
2. J. B. Holt and Z. A. Munir, "Combustion Synthesis of Titanium Carbide: Theory and Experiment," *J. Mat. Sci.* **21**, 1 (1986).

Thus far we have reported on research on a variety of topics in pure and applied science. In this section, we record the interests and capabilities of the C&MS Department in engineering research.

Transportation fuels are a critical energy commodity, and nearly all are derived from crude oil. While coal and nuclear power have the potential for meeting the global demand for electricity for many years, assuming a stable world population, petroleum shortages are predicted to occur early in the 21st century. Our energy-related research therefore emphasizes the critical area of transportation fuels.

Because there are large proven reserves of natural gas, we are developing catalysts to convert it to higher-molecular-weight hydrocarbons. This research makes use of our expertise in the manufacture of low-density gels and in the application of synchrotron radiation for the characterization of catalytic substances.

In the field of oil exploration, we are modeling when and where oil forms, migrates, and accumulates. The thermal history of an oil-generating region is revealed in the reflectance of an accompanying, complex high-molecular-weight mixture of organic compounds called vitrinite. We are performing laboratory studies on vitrinite to obtain a better correlation between reflectance and thermal history.

The pyrolysis of coal under reducing conditions produces a liquid hydrocarbon that can be converted into a liquid fuel. We are conducting research on an externally heated screw pyrolyzer to determine the optimum operating parameters, such as temperature and feed rate. Improvements in design features are also under consideration. Technology transfer is an active and important aspect of this program.

We have designed and are testing a continuous-loop pilot plant system for the retorting of oil shale. This second-generation apparatus operates at the level of several tons/day and allows studies to be performed that are required for the design of the next-generation pilot plant. The latter will have a capacity of 100 to 1000 t/day and will be installed at a mine site in Colorado. In addition, we have analyzed the composition of the pyrolysis products to assist in mathematical modeling of the retorting process.

LLNL supports major programs in controlled thermonuclear fusion. The C&MS Department lends its assistance to both inertial confinement and magnetic confinement research. We also work on the problem of disposal of nuclear waste generated by conventional nuclear reactors.

In support of research in inertial confinement fusion (ICF), we have designed and built equipment for producing coated microspheres of polystyrene. When filled with DT, these spheres are used for direct-drive implosion in ICF investigations. Also in support of fusion research, we have had an ongoing program whose aim is to polarize liquid D-T. Theory suggests that the polarized state might possess a 50 percent larger cross section for fusion than the random one. This larger cross section would also likely be of significant benefit to the magnetic fusion effort. We mention here that the C&MS Department administers and operates the tritium facility, which houses essentially all the tritium research and technology at LLNL.

The major stumbling block to the growth of nuclear power is widely perceived to be the safe disposal of nuclear waste. The currently favored procedure calls for disposal in metal canisters that are to be placed in a geologic repository. We are evaluating candidate alloys for the disposal canisters to determine which will best maintain its integrity under mildly hostile chemical conditions.

Section 6

# Energy-Related Research and Development

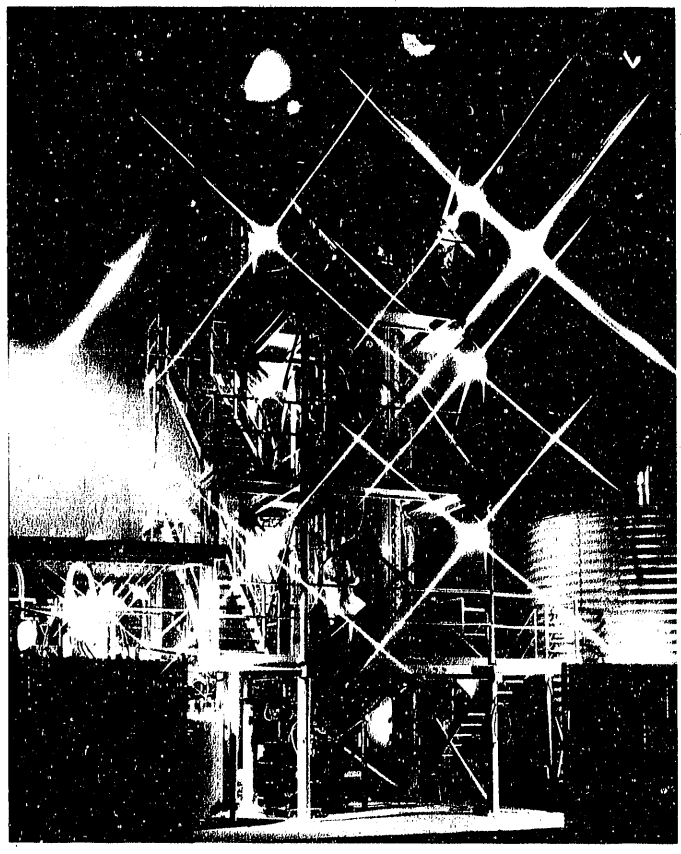

Pilot oil shale retorting system

# The Development of Catalysts for the Conversion of Methane to Liquid Fuels

M. W. Droege

***The effective utilization of remote natural gas requires the development of catalyzed reactions for the conversion of methane to liquid fuel. Reactions of interest include the partial oxidation and oxidative coupling of methane, using oxygen. Our efforts have focused on the synthesis, characterization, and reactions of new catalysts that perform these oxidative processes with methane. Successful materials will serve as the basis of new processes that directly convert natural gas to liquid hydrocarbons.***

## Introduction

Transportation fuels are a critical energy commodity, accounting for 27 percent of the total energy consumption in the U.S. Nearly all transportation fuels are derived from crude oil, and they account for 63 percent of all U.S. oil use. The transportation sector will continue to use more oil than the nation produces, and a strong need for transportation fuels is projected well into the next century. Consequently, there is a major emphasis on the economical conversion of domestic fossil energy resources other than crude oil to hydrocarbon liquids for use as transportation fuels.

Natural gas is a readily available resource with large known and anticipated reserves. The U.S. has large reserves of remote natural gas such as that present in Alaska, for which there is no ready market and no cost-effective means of transportation to a market. Worldwide, there are about 3500 trillion cubic feet of proven natural gas reserves. If these reserves could be processed to a liquid hydrocarbon, they would yield an estimated 100-yr worldwide supply of transportation fuels.

The future of methane conversion and natural gas processing depends on the development of catalyzed routes that directly convert methane to liquid hydrocarbons. The thermodynamically allowed, general reaction that transforms methane ($CH_4$) to higher hydrocarbons is

$$nCH_4 + (y/2)O_2 \rightarrow C_nH_{4n-2y} + yH_2O \quad , \qquad (1)$$

which is an oxidative process that is facilitated by the use of a catalyst. Uncatalyzed, simple thermal reactions of methane and oxygen require very high operating temperatures (700–800°C). At such temperatures, the product yield of hydrocarbons is unacceptably low because of the uncontrolled over-oxidation of methane to carbon monoxide and carbon dioxide. The key to upgrading methane to liquid fuels is the controlled catalytic activation of the C–H bond of methane to prevent over-oxidation.

The major emphasis of this project is the development of new materials that might catalyze reactions for conversion of methane to liquid fuel. Reactions of interest include the partial oxidation of methane (forming methanol and formaldehyde) and oxidative coupling (forming ethane and ethylene), using oxygen. One part of our current effort is focused on the synthesis, characterization, and reactions of new catalysts that select and accelerate the partial oxidation or coupling reactions.

The catalysts typically consist of an inorganic oxide matrix such as $SiO_2$, into whose oxide coordination environment early transition-metal and lanthanide ions are incorporated. We have performed characterization studies including elemental analysis, surface-area evaluations, and structural investigations, the latter by x-ray absorption near edge structure (XANES) to elucidate the bulk properties of the catalysts and the details of the metal-ion coordination environment. Reactor studies are in progress to test the catalysts for partial-oxidation reactions.

## Experimental Method

**Preparation of Catalyst Materials.** Mixed metal-silica gels are prepared by hydrolysis of a metal alkoxide with either a silica pre-gel or a silicon alkoxide. Metal loading is determined by the ratio of metal alkoxide to silica pre-gel or silicon alkoxide prior to hydrolysis.

The silica pre-gel is formed by the substoichiometric hydrolysis of a silicon alkoxide. A solution of distilled water and 0.25 g concentrated sulfuric acid is slowly

added to a solution of silicon tetraethoxide (TEOS) in ethanol. The resulting clear solution is brought to reflux under a nitrogen atmosphere. After refluxing and removal of ethanol solvent by distillation, the system is cooled and the resultant thick oil is anaerobically transferred to a glove box and maintained under a dry oxygen-free atmosphere.

Examples of the two synthetic approaches to preparing metal-silica gels follow.

**Titanium-Silica Gel: Direct Hydrolysis.** A methanol solution of concentrated $NH_4OH$ is prepared. Silicon tetramethoxide (TMOS) is added to this solution in a dry inert atmosphere. This solution is then added to titanium tetraisopropoxide and stirred. The addition of water produces a gel. After aging, the gel is dried in a critical-point drying apparatus with liquid carbon dioxide. The final product is a monolithic cylinder of metal-silica aerogel that is colorless and transparent to translucent.

**Lanthanum-Silica Gel: Indirect Hydrolysis.** An ethanol solution of lanthanum isopropoxide is prepared by dissolving it in anhydrous oxygen-free ethanol. A stock solution is prepared containing distilled water and 48 to 50 percent tetrafluoroboric acid (in water). The stock solution is added dropwise to the metal-silica-ethanol solution, and the remaining processing is performed as described above for the titanium-solution gel.

**Characterization of Catalyst Materials.** We determined elemental compositions by inductively coupled plasma–atomic emission spectroscopy, and evaluated surface areas by gas-adsorption measurements. XANES studies were performed at the National Synchrotron Light Source (Brookhaven National Laboratory, Upton, N.Y.), at an electron energy of 2.5 GeV and a storage ring current of about 100 mA. A monochromatic synchrotron x-ray beam was obtained using a Si (111) crystal with a resolution of about 0.4 eV at the titanium K edge of 4966 eV. XANES data were obtained using the fluorescence technique.

## Results and Discussion

The basic synthetic approach is the hydrolysis of a metal alkoxide in the presence of a silicon alkoxide (direct hydrolysis) or a partially hydrolyzed silica pre-gel (indirect hydrolysis). The resulting mixed metal-silica gel is then dried either by critical-point extraction, which results in a metal-silica aerogel, or by controlled evaporation, which results in a metal-silica xerogel. The reactivity of the metal alkoxide to hydrolysis determines whether a direct or indirect hydrolysis route is appropriate. In general, metal alkoxides that undergo hydrolysis at a rate comparable to that of silicon alkoxides will form suitable materials by direct hydrolysis. Those metal alkoxides that undergo hydrolysis at much faster rates than silicon alkoxides tend to yield suitable materials by the indirect hydrolysis procedures. However, our experience is that the optimum synthetic procedure can vary greatly, and it is a complex function of metal alkoxide, silicon alkoxide, temperature, concentration, order of reagent addition, gelation catalyst, and solvent.

Nevertheless, we have successfully prepared a variety of metal-silica catalysts as transparent, homogeneous, monolithic solid materials. These materials contain primarily the early transition metals yttrium, titanium, zirconium, vanadium, niobium, tantalum, and tungsten, along with the lanthanide metals lanthanum and samarium. Bulk properties include densities of 100 to 200 mg/cm$^3$ and typical surface areas of 700 to 800 m$^2$/g. Elemental analysis indicates that the metal ions introduced during synthesis are incorporated into the silica matrix and are not lost during processing. Table 1 shows some typical results.

In addition to studies of the bulk properties of the new catalyst materials, studies of the structural environment of the metal ions in the silica matrix are in progress. Since these materials are inherently amorphous, we have turned to using synchrotron radiation methods [XANES and extended x-ray absorption fine structure (EXAFS)] to investigate their structure. The XANES data allow us to identify the metal ion, its oxidation state, and the coordination number, and give an indication of the coordination geometry about the metal ion. This information, when coupled with EXAFS data that identify the atomic type and distance of first and possibly second coordination neighbors, will allow us to develop a comprehensive picture of the structural environment.

Figure 1 shows preliminary XANES data for several model Ti-$SiO_2$ compounds. Tetrahedrally coordinated Ti(IV) oxide complexes are represented by titanium tetraisopropoxide [$Ti(OiPr)_4$] and titanium tetra (trimethylsiloxane) [$Ti(OSi(CH_3)_3)_4$]. Six-coordinate, pseudo-octahedral Ti(IV) oxide complexes are represented by the two forms of $TiO_2$ (rutile and anatase) and by Tyzor, a commercial titanate. The tetrahedral

**Table 1.** Elemental compositions of the catalysts.

| Catalyst | Percent found | | Percent calculated | |
|---|---|---|---|---|
| | $SiO_2$ | Metal oxide | $SiO_2$ | Metal oxide |
| Zr-$SiO_2$ | 60.7 | 19.9 | 58.6 | 22.9 |
| Nb-$SiO_2$ | 72.9 | 15.0 | 73.5 | 14.4 |
| Ta-$SiO_2$ | 72.2 | 16.1 | 73.4 | 14.9 |

four-coordinate complexes exhibit two main features: an intense, sharp pre-edge line at about 4 eV, followed by a broad, indistinct edge structure at 20 to 60 eV. On the other hand, the six-coordinate, pseudo-octahedral complexes are characterized by a weak pre-edge line split into a triplet, and a sharp, complex edge structure. In general, the tetrahedral Ti(IV) ions are easily distinguished from the pseudo-octahedral case.

Figure 2 shows the XANES data obtained for the Ti-$SiO_2$ catalyst materials, both in the as-prepared condition and after various processing conditions. The Ti-$SiO_2$ processed at room temperature exhibits a low-intensity triplet pre-edge line (see inset) centered at 4.6 eV, and distinct, sharp edge features. As the Ti-$SiO_2$ is processed, first by heating to 500°C and then to 800°C, a transformation is observed in the XANES spectra. The low-intensity triplet pre-edge line collapses to a single line that grows in intensity with increasing thermal processing. In addition, the distinct edge features observed at room temperature are less prominent, and the edge becomes broad and indistinct with further thermal treatment.

A consistent explanation of these results is summarized in Fig. 3. As prepared, the Ti-$SiO_2$ materials contain six-coordinate pseudo-octahedral Ti(IV) ions, where the metal ligands are derived from the silicon oxide matrix, along with coordinated water and/or alkoxide ligands. With thermal treatment, the labile ligands (water and alkoxide) are lost and the $d^0$-Ti(IV) ion converts to its desired tetrahedral form. Our preliminary results indicate that titanium is uniformly distributed through the bulk of the matrix as a four-coordinate ion, with no evidence for the appearance of $TiO_2$. Surface areas measured after thermal treatment were 200 to 300 $m^2/g$, while before thermal treatment the areas were 700 to 800 $m^2/g$.

## Summary and Conclusions

We have developed synthetic methods of preparing a variety of metal-containing silica-based catalysts. Both bulk properties and preliminary structural studies (XANES) indicate a uniform dispersion of the metal ions in the silica matrix. In the case of Ti-$SiO_2$ materials, structural transformations about the metal ion are observed during simple thermal treatments, which result in a tetrahedral form of the Ti(IV) ion dispersed throughout the bulk with no formation of separate $TiO_2$ and $SiO_2$ phases. Although four-coordinate titanium in $SiO_2$ is known to occur in high-density, low-surface-area glasses prepared by the high-temperature melting of titanium and silicon oxides, the materials described

**Figure 1.**

Preliminary XANES data for model Ti-$SiO_2$ compounds and for Ti(IV) oxide complexes. The latter are the two forms of $TiO_2$ (rutile and anatase) and the commercial titanate Tyzor.

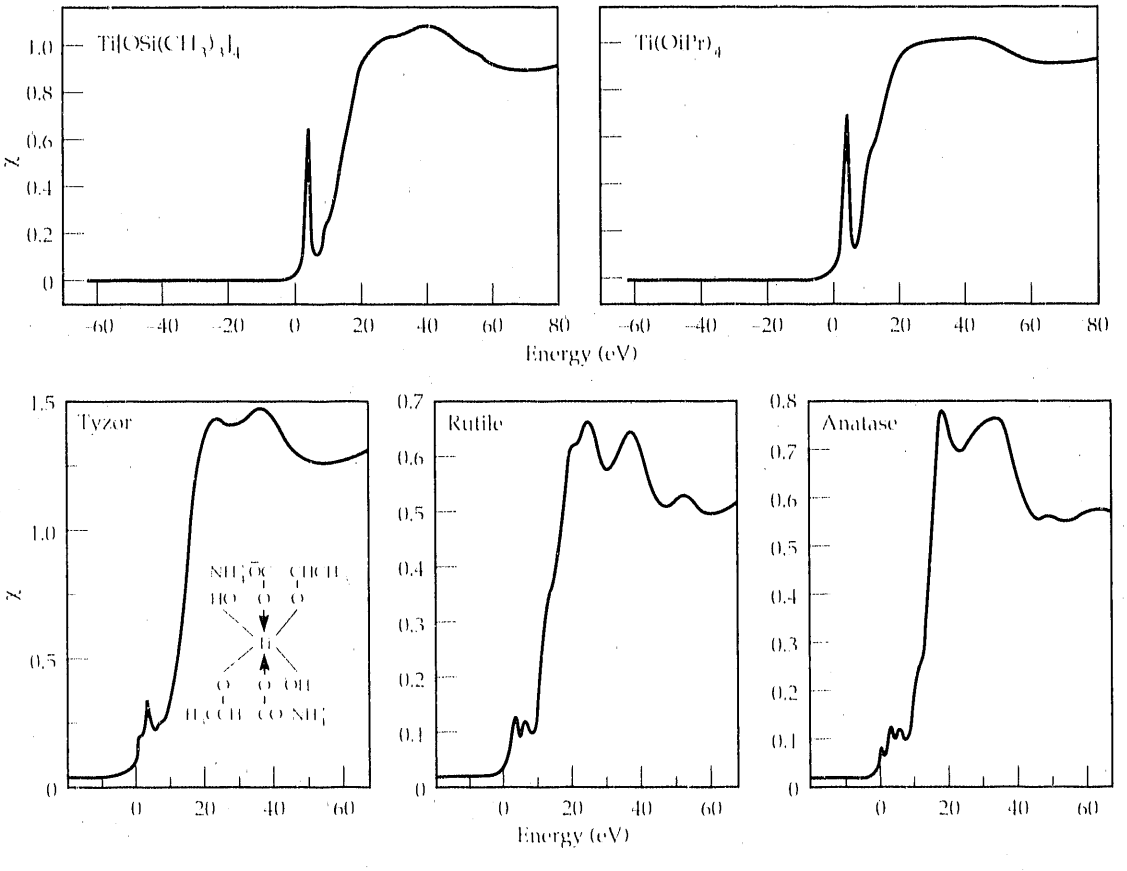

above have low density and high surface areas, possess a regular tetrahedral coordination environment about the titanium ions, and can be obtained by relatively low-temperature processing.

This new class of metal-silica materials may find a wider array of applications as catalytic, thermal, acoustical, and optical materials than traditional high-density glasses. Titanium and other metal-containing silica catalysts are currently being evaluated to determine their potential for selective catalytic methane oxidation.

**Figure 2.**

XANES data for the Ti-$SiO_2$ catalyst materials (a) at room temperature; and after being heated first to (b) 500°C, and then (c) to 800°C. The inset in (a) shows an expansion of the triplet pre-edge line centered at 4.6 eV.

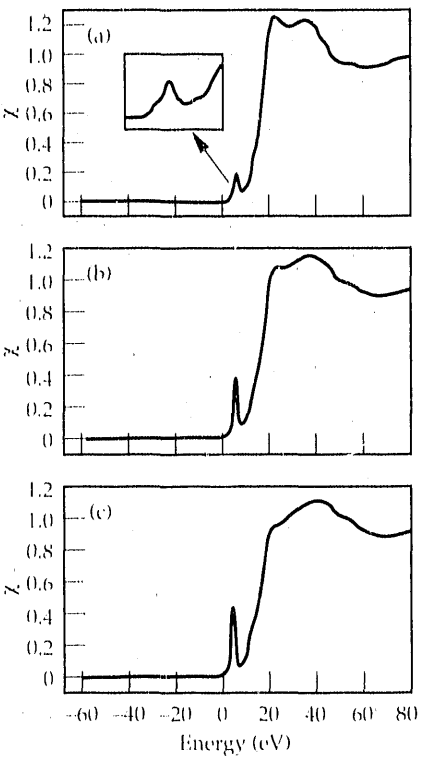


*This work was supported by the Morgantown Energy Technology Center of the DOE Office of Fossil Energy, and by the Gas Research Institute. The synchrotron studies were supported by Institutional Research & Development.*

**Figure 3.**

Conversion of the $d^0$-Ti(IV) ion to its desired tetrahedral form during heat treatment.

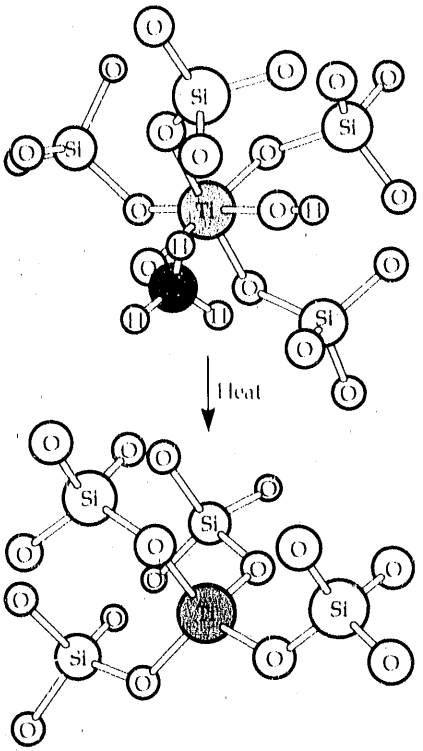

# Modeling Petroleum Generation and Expulsion

A. K. Burnham,
J. J. Sweeney, and
R. L. Braun

*We have developed new chemical-kinetic models of vitrinite reflectance and petroleum generation and expulsion. The vitrinite-reflectance model will help in developing and testing thermal histories of potential petroleum-generating sediments. The petroleum generation and expulsion model uses these thermal histories to predict the timing and efficiency of petroleum generation and its expulsion from the source rock. These models will aid in evaluating which traps located by geophysical techniques are likely to contain oil.*

## Introduction

Traditional petroleum exploration uses geophysical techniques to locate traps (reservoirs) where oil and gas may have accumulated. We are trying to improve the predictions obtained from these techniques. Oil is generated from organic matter (principally phytoplankton) that is deposited in an oxygen-poor environment and subsequently heated to 80 to 160°C by burial at depths of 3 to 6 km over tens of millions of years.[1] Once formed, oil may either be expelled from the source rock to accumulate in a trap or be converted to gas as it undergoes further burial.

**Figure 1.** A multiple parallel reaction model for the carbonization of vitrinite. The extent of each reaction is combined with the elemental balance constraints in Eq. (1) to calculate the composition of the remaining solid. Reflectance is then calculated by correlation with residual-solid composition.

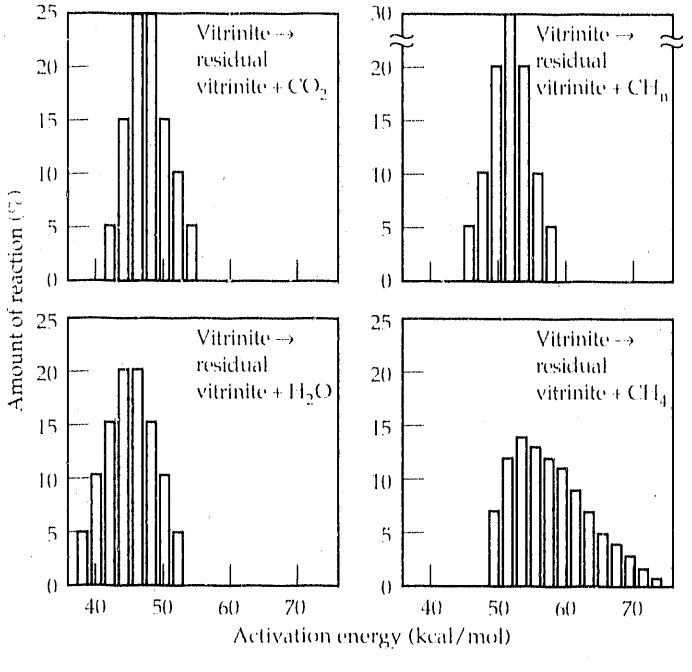


We are working to improve the reliability of a technique called integrated basin analysis, which incorporates many aspects of geochemistry, geology, geophysics, and hydrology in an attempt to model, in a deterministic fashion, when and where oil is generated, migrates, and accumulates. This technique involves (1) calculating the thermal history of the basin, (2) combining that thermal history with chemical-kinetic expressions to predict when and where oil and gas are generated, and then (3) estimating from various physical parameters when and to where the oil moves. We need to know not only whether oil and gas were formed but also whether expulsion from the source rock occurred at the right time and geometry to fill a trap. A trap may be formed before, after, or during expulsion by crustal folding, faulting, or erosion and redeposition.

This year, we made significant advances in two aspects of integrated basin analysis. First, we developed an improved chemical-kinetic model of vitrinite maturation and reflectance that will better constrain thermal-history models of sedimentary basins.[2] Second, we incorporated fluid equations of state, a simple mechanical model of source-rock compaction, and a pseudo-one-dimensional calculation of mass transport into our detailed chemical-kinetic model of oil and gas generation and destruction. We then made the most detailed nonproprietary calculation to date of oil expulsion from a generating source rock.[3]

## Vitrinite-Reflectance Model

A crucial requirement for an integrated basin analysis is a knowledge of the thermal history of all sedimentary layers at several locations throughout the basin. This information is obtained from steady-state heat-flow calculations at all historical times, using inferred sedimentary thicknesses. Many approximations are required, so there are many possible sources of error. It is therefore necessary to have some independent means of checking the calculated thermal history. The reflectance of light

by vitrinite, a major constituent of coal and a minor constituent in many other sediments, is the most common indicator used to constrain geothermal histories. However, there is a long-standing disagreement in the literature on how vitrinite reflectance depends on time and temperature.

We have developed an improved method of calculating vitrinite reflectance from thermal histories. Our model builds on the historical correlation between vitrinite reflectance and its composition, particularly its hydrogen/carbon ratio. As vitrinite becomes more graphitic, its reflectance increases. We derived a simple chemical-kinetic model that reproduces changes in vitrinite composition, and hence in reflectance, for both geological and laboratory maturation. Maturation is assumed to proceed by the following mechanism:

$$CH_xO_y \rightarrow C_{1-b-c-d}H_{x-2a-nc-4d}O_{y-2b-a} + aH_2O + bCO_2 + cCH_n + dCH_4 \quad , \qquad (1)$$

where $CH_n$ represents organic gases and liquids with molecular weights greater than that of methane. Each reaction is described by a distribution of activation energies, as shown in Fig. 1. Together, the stoichiometric coefficients and the calculated extent of each reaction define the composition of the residual material. We also derived improved correlations between composition and reflectance from literature data.[4,5] Combining these two improvements allows us to calculate reflectance for maturation at time scales ranging from hours to millions of years. A comparison of measured and calculated reflectance values for three different time scales is given in Fig. 2. No previous model has the capability of predicting reflectance over such a wide range of thermal histories.

## Modeling Oil Expulsion

Once a thermal history has been calculated and verified for each sedimentary layer, it can be used to calculate when oil generation commenced and over what time period it was generated in various parts of the basin. Our calculations for the Uinta Basin in Utah have been described previously.[1] However, the most crucial issue is not when oil is generated, but when it is expelled from the source rock for migration to a trap. While in the source rock, oil is continually cracked to lower-molecular-weight oil and gas, so the delay between generation and expulsion dictates the oil/gas ratio expected in a given trap.

To model this process, we must understand (1) the temperature and pressure dependence of the chemical kinetics of oil cracking, (2) how the decrease in rock porosity (compaction) depends on overburden (lithostatic) pressure, (3) how expulsion depends on porosity and pore-fluid pressure, and (4) how compaction is inhibited by pore pressure. The volumes and compositions of the oil and gas phases are calculated using corrected Redlich-Kwong-Soave equations of state[6] in our chemical-kinetic model.[7] The source rock can be an open, closed, or leaky system. For the leaky system, we adopted the mechanical model shown in Fig. 3. Equilibrium porosity is assumed to decrease exponentially with the difference between the lithostatic pressure and the excess pore pressure (pore pressure in excess of hydrostatic). It is further assumed that the rate of expulsion is proportional to the effective hydraulic conductivity estimated from the Kozeny-Carman equation.[8] Finally, a pressure relief valve is added so that the pore pressure cannot exceed lithostatic pressure. Activation of this valve simulates the process of natural hydrofracturing.

Figure 4 shows a calculation of generation, expulsion, pressure, and compaction curves for an idealized segment of rich source rock that is buried at 3°C/My in

**Figure 2.** Comparison of measured and calculated values of vitrinite reflectance for three drastically different time-temperature regimes: (a) sealed bomb pyrolysis experiments for samples heated at 1°C/wk, (b) temperatures of 200 to 450°C experienced over 50,000 to 500,000 years as heat dissipates from a volcanic intrusion (assuming 1143°C magma) near Walsen Dike, Wyo., and (c) normal sedimentary heating to 180°C over 80 million years caused by deposition and subsidence (geothermal gradient of 24°C/km) near Wagon Wheel Well, Wyo.

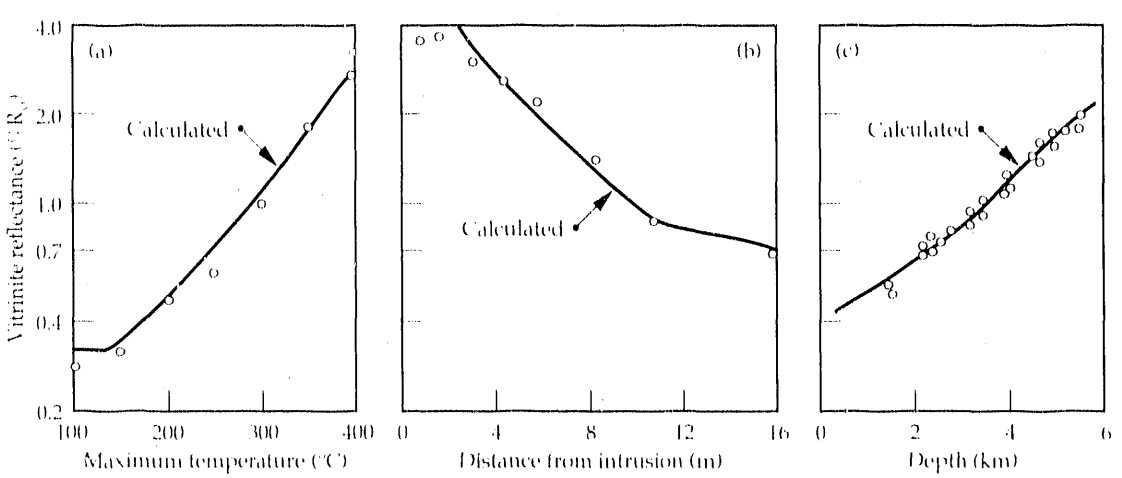

a geothermal gradient of 25°C/km. The proportionality constant for leakage was chosen so that the excess pore pressures were similar to those observed in the oil window of the Uinta Basin. We see that oil expulsion is delayed from generation by about 10°C, or three million years, during which time about 30 percent of the oil is cracked to gas. Other calculations indicate that the amount of oil cracking prior to expulsion is much larger for a source rock with less organic matter. These predictions are qualitatively consistent with general observations. Quantitative testing by comparison with field observations will be a part of our further work. We will also use this model to test simpler models under development that could be used more routinely.

## Summary

We have developed a kinetic model that can account for chemical changes in vitrinite over ranges of time and temperature covering laboratory experiments and geological maturation. It will be very useful in estimating thermal histories of petroleum-generating sediments, and it has already been incorporated into commercial software used by the oil industry. We have also developed a detailed model of oil generation and expulsion. This model confirms that oil-expulsion efficiency is a very strong function of the organic content of the rock, and rocks with only 1 or 2 wt% carbon are more significant sources of gas than oil.

**Figure 3.** **Simple mechanical model of source-rock compaction and petroleum expulsion. In the absence of pore pressures in excess of hydrostatic, rock porosity decreases exponentially with depth. Pore fluids can escape by leaking through matrix porosity or through fractures developed when the excess pore pressure exceeds the lithostatic load.**

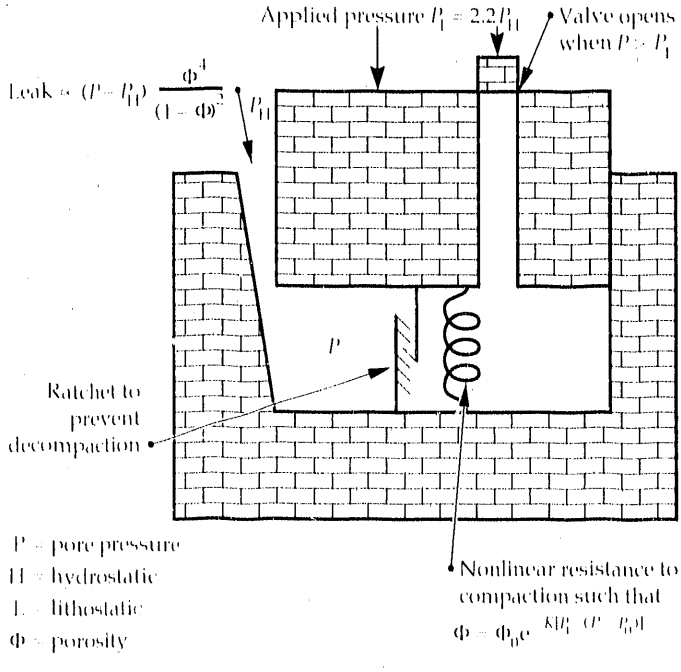


*This work was funded by the DOE Office of Basic Energy Sciences, the DOE Office of Fossil Energy, and a group of eight oil companies.*

## References

1. B. P. Tissot and D. H. Welte, *Petroleum Formation and Occurrence* (Springer-Verlag; Berlin, New York; 1984).
2. A. K. Burnham and J. J. Sweeney, *Geochim. Cosmochim. Acta* **53**, 2649 (1989).
3. R. L. Braun and A. K. Burnham, *Energy & Fuels* (in press).
4. J. T. McCartney and M. Teichmuller, *Fuel* **51**, 64 (1972).
5. A. Davis, In *Scientific Problems of Coal Utilization*, B. R. Cooper, Ed. (Technical Information Center, U.S. Department of Energy, Springfield, Va., 1978), pp. 13–45.
6. A. Peneloux, E. Rauzy, and R. Freze, *Fluid Phase Equilibria* **8**, 7 (1980).
7. A. K. Burnham and R. L. Braun, *In Situ* **9**, 1 (1985).
8. R. A. Freeze and J. A. Cherry, *Groundwater* (Prentice Hall, Englewood Cliffs, N.J., 1979), p. 351.

**Figure 4.** **Simulation of compaction, pressures, oil generation and degradation, and oil and water expulsion for Green River Shale. The shale initially contained 10 percent organic carbon and was heated at a rate of 3°C per million years. The effective geothermal gradient was 25°C/km.**

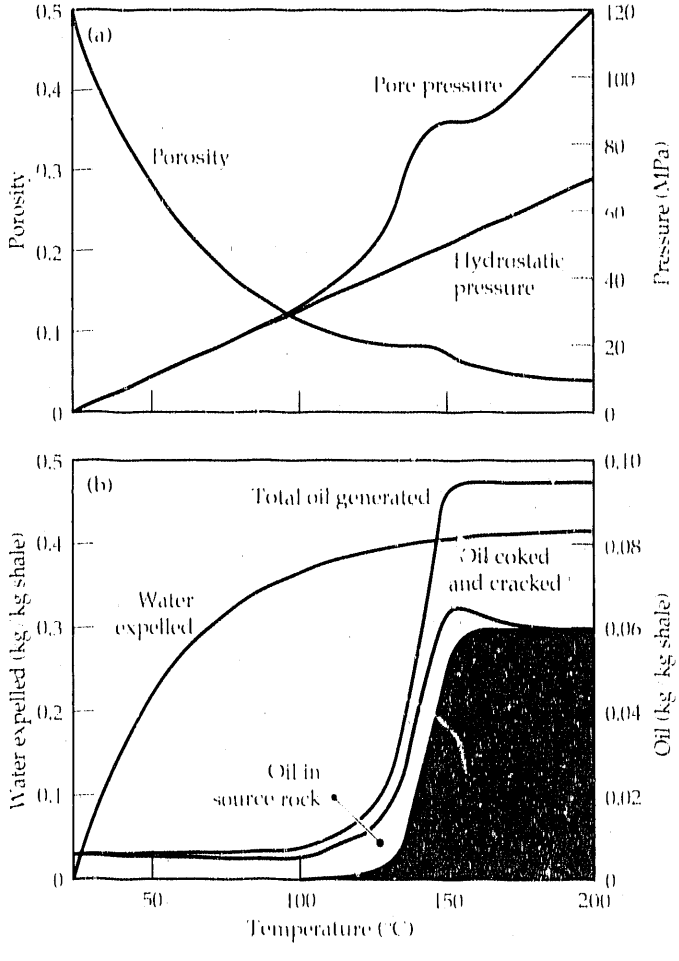

# Pyrolysis of Caking Coal in a Heated Screw

D. W. Camp and
R. G. Mallon*

*We have demonstrated the feasibility of using a heated screw to continuously pyrolyze sticky caking coal to produce hydrocarbon liquids, gas, and char. Although operation of a small single screw was usually steady, we could not achieve high throughput, and the torque required to turn the screw was undesirably high. We suspect that the reacting plastic coal adheres to the screw and then cross-links (thermosets) to form a stagnant char deposit. On the basis of this model, we expect that an intermeshing twin screw will show improved performance. The DOE is funding an American company to test this recommendation at large scale.*

## Introduction

Coal, heated in the absence of oxygen, pyrolyzes to yield a liquid product that can be upgraded to liquid fuel. The other products obtained from this process, sometimes called mild gasification, are char and medium-Btu gas. Yields are approximately 20 percent liquid, 70 percent char, and 10 percent gas. The gas could be burned on-site for process heat and sold in the local Btu market, and the char could replace coal in power plants.

The DOE, through the Morgantown Energy Technology Center, has a program to develop mild-gasification technology using a combination of industrial and scientific contractors. LLNL has been part of this program since March 1987. Our primary objectives are to identify, develop, and operate a reliable and inexpensive process at small pilot scale. Technology transfer to American industry is emphasized, and we actively share our results, experience, and recommendations with other government and industrial organizations.

High-volatile bituminous coals are targeted for mild gasification because they produce higher liquid yields than other rank coals. Further, the well-developed infrastructure for mining and transporting these coals, and their geographical location (primarily in Appalachia and the Midwest) would allow quick development when alternative liquid fuels are needed. A disadvantage of bituminous-rank coals, often called caking or agglomerating coals, is that during pyrolysis they soften, become sticky, swell, devolatilize, and then cross-link to form solid char. This behavior causes severe problems with most processes developed for oil shale or coal of other ranks.

We reviewed a number of proposed processes and identified an externally heated screw pyrolyzer as being one of the very few that could work well for caking coals (see Fig. 1). Both single-screw and twin-screw forms are possible. Coal is fed to the screw(s), which conveys it through a surrounding pipe called the barrel. External heat is supplied to the barrel and screw, which in turn heat the coal.

Our approach to developing and improving the screw pyrolyzer is mainly one of process experimentation that is aimed at understanding why the screw performs as it does. The experiments are guided and interpreted, where appropriate, by simple laboratory experiments and model calculations.

## Experimental System

We assembled and operated a small single-screw pyrolyzer and associated feed and product-collection systems. This pyrolyzer is a small-scale version of the system shown in Fig. 1. The screw has an outer diameter of 38 mm, a channel depth of 9.2 mm, and a pitch of 38 mm. The screw and barrel are 89 cm long. The barrel and screw are heated, typically to 650 °C, by electrical resistance heaters.

Preheated coal (high-volatile A bituminous), ground to −3 mm, is metered into the screw. The screw feed throat can be operated full or starved (metered rate equal to or less than the screw throughput capacity). Char discharged from the screw falls into a receiver heated to

520°C. The vapors disengage from the char at the screw exit and flow through a 520°C pipe to a ~40°C condenser. The system pressure is 2 psig.

## Results

Nine successful runs were made between July 1988 and August 1989, totaling 51 h of operation, in which 186 kg of coal was pyrolyzed. We investigated a wide range of operating conditions: screw speed of 5 to 37 rpm, coal feed rate of 30 to 127 g/min, maximum barrel temperature of 350 to 650°C, and barrel temperature gradient of 5 to 38°C/cm. The primary operating conditions were chosen on the basis of laboratory measurements and modeling calculations of heat transfer, pyrolysis kinetics, and the time-temperature-dependencies of coal viscosity and swelling.

A material balance was completed for one run. The yields were 73 percent char, 15 percent $C_5^+$ liquids, 10 percent $C_4^-$ gas, and 2 percent water. The liquid yield was below the 20 percent obtainable under favorable process conditions. This low yield was due to the low screw temperature needed to better understand the conveyance mechanism.

Under full-inlet feeding conditions, we measured the coal throughput over a range of screw speeds and temperatures. Figure 2 shows the results. As expected, in ambient tests the conveyance rate was proportional to the screw speed. Under pyrolysis conditions, however, the throughput curves unexpectedly reach an asymptotic limit. Lower barrel temperatures reduced the throughput even further. Screw C, which outperformed screw A, was nearly identical to it but had a smoother surface finish.

Under ambient conditions, the mechanical power (and hence the torque) required to turn the screw and convey the coal was very small (< 10 J/g). Under pyrolysis conditions, however, the power was erratic and high, far exceeding any predictions based on viscous-shear models. High torque and power are undesirable because they mean heavy construction, large motors, and high electrical costs. During starved-inlet operation, which required less power than full-inlet operation, the specific power increased with screw speed and feed rate with no clear trend apparent with temperature gradient.

## Discussion

Much of our experimentation was directed at quantifying and understanding the reasons for the limitations on throughput and the high and erratic power requirements. On the basis of all evidence available to us, we propose the following description, illustrated in Fig. 3, of how reacting caking coal is moved through the screw.

**Figure 1.**

Schematic of a proposed commercial-scale externally heated screw pyrolyzer.

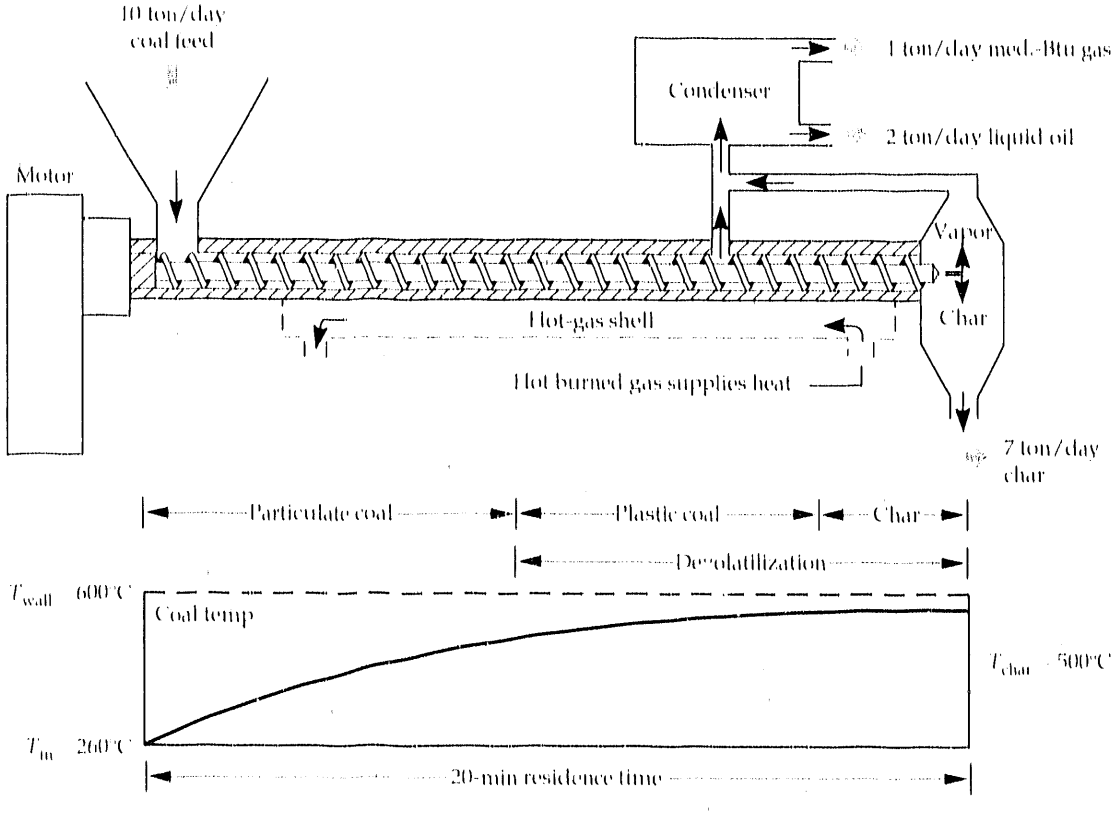

Near the inlet, loose particulate coal is simply conveyed forward. As the coal is heated, it becomes fluid and sticky. When the fluid, adhesive coal nears 500°C, cross-linking turns it to solid char that is adhered to the screw channel. This char tends to rotate with the screw without moving forward. Coal backs up behind this non-moving zone and is crushed and compacted. Driven by the powerful screw, this packed material pushes harder and harder against the adhered char until the char shears off from the screw. The sheared char pieces are easily conveyed out the end of the screw. The process repeats itself as new fluid coal adheres and cross-links on the screw.

This model suggests two approaches to improving performance. One is to reduce adhesion of the coal/char on the screw. Recent experiments with a chrome-plated screw showed no significant improvement, however. The second and more promising approach is to use two adjacent screws with intermeshing flights, which should help disrupt any adhesive char deposits. On the basis of our recommending the second approach to DOE and industry, DOE is funding an American company, Coal Technology Corporation, to build and operate a twin-screw pyrolyzer designed for 500 kg/h.

## Conclusions

Mild gasification produces liquid fuels from coal, with gas and char as valuable coproducts. Experiments at the 5-kg/h scale show that an externally heated screw pyrolyzer works with a difficult caking coal; it currently suffers, however, from low throughput and high torque requirements. Transport of reacting coal in the screw may occur by periodic shearing of char deposits that have adhered to the screw. Reducing coal-screw adhesion and using a twin screw may improve transport.

*This work was supported by the Morgantown Energy Technology Center of the DOE Office of Fossil Energy.*

*Earth Sciences Department.

**Figure 2.** Coal throughput of our small single-screw pyrolyzer. Throughput cannot be increased much by turning the screw faster.

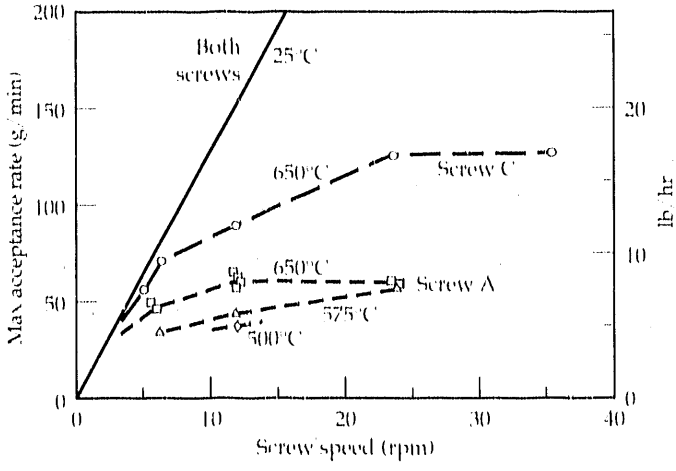


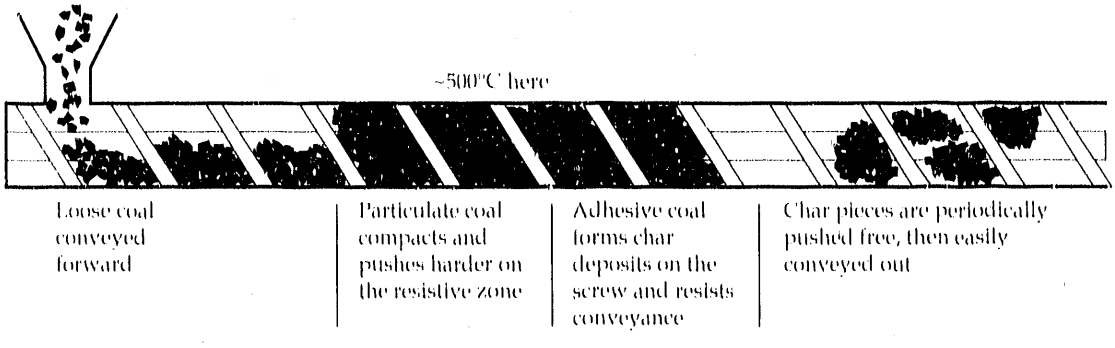


**Figure 3.**

Proposed description of how coal moves through the screw. We suspect that throughput is limited by periodic adhesion and shearing of char deposits.

# The Oil Shale Project

R. J. Cena

*We are studying aboveground oil shale retorting. Our 1-t/day continuous-loop pilot retorting system is being upgraded to process 4 t/day of commercially sized shale. The new system, like the 1-t/day system, is based on the LLNL hot recycled solid (HRS) process, a generic second-generation retorting system for rapid pyrolysis of oil shale. Operation of the upgraded retort will contribute to our understanding of pyrolysis and combustion over the full particle-size range, and begin to answer the many questions about bulk-solid handling in the scale-up of the HRS process. We have completed the conceptual design of two pilot tests of the HRS process, at the 100- and 1000-t/day scales, to be fielded at a mine site in western Colorado.*

## Introduction

We are studying oil shale retorting using recirculating hot solids in the laboratory and a continuous-loop pilot retorting facility. Much progress has been made in understanding the basic chemistry of hot-solid retorting processes. Using a triple quadrupole mass spectrometer (TQMS), we have measured the evolution of individual species during pyrolysis and combustion, including hydrocarbons, water, sulfur, and nitrogen compounds.

**Figure 1.**

Schematic of the new 4-t/day HRS retorting system.

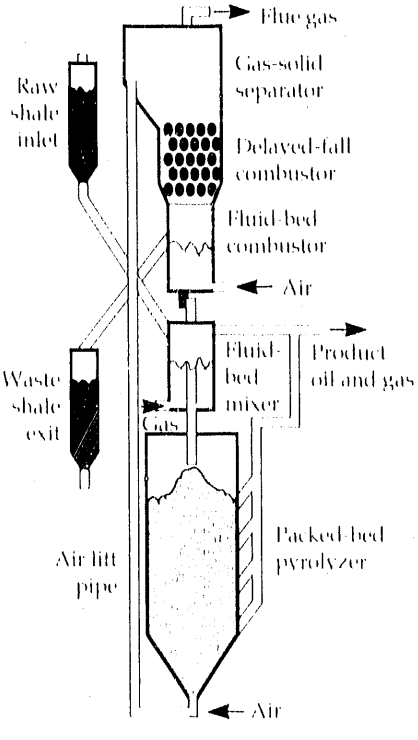


A fluidized bed and combustor system allows us to accurately determine the rate of oil production during isothermal pyrolysis and quantitatively measure the extent of oil degradation during pyrolysis under a variety of conditions.

We have developed the HRS process as a generic second-generation retorting system for rapid pyrolysis of oil shale. The system has been tested at a 1-t/day scale and will be upgraded to a 4-t/day plant using commercially sized shale in FY90. The new retorting system contains several new components, which will be tested for commercial viability. We have also completed a conceptual design of pilot tests of the HRS process at the 100- and 1000-t/day scales, to be fielded at a mine site in western Colorado.

## Laboratory Studies

The laboratory studies are designed to elucidate the chemical reactions and rates of oil shale processing as a guide in designing and operating more efficient and environmentally sound retorting systems. An on-line TQMS is used to determine (1) the kinetics and stoichiometry of retorting by tracking the evolution of oil and gas, and (2) the concentrations of trace sulfur and nitrogen species of environmental concern. In the past year, we have achieved increased specificity, better temperature uniformity, and the ability to determine quantities of gases with great accuracy. For example, we can measure CO in the presence of hydrocarbons by charge exchange with a krypton collision gas. The retort and furnaces have been redesigned to give a temperature uniformity of ±2°C throughout the sample, with heating rates as high as 10°C/min.

A laboratory fluidized bed is being used to determine isothermal kinetics for oil shale pyrolysis. Developed at LLNL, this unique instrument uses a combustion tube downstream of the fluidized bed to burn all evolved products to $CO_2$, $H_2O$, and $SO_2$, with on-line mass spectrometric detection. The technique provides accurate determination of the carbon and hydrogen released during pyrolysis, and, with subsequent combustion, the amount of the residual char left in the bed. The material balance obtained for carbon is routinely within 98 percent. The rate constants measured with this apparatus are faster than those previously published by as much as an order of magnitude. In the past, the cold transfer lines (<450°C) and the dust accumulating on the filters, which are typical for this type of experiment, delayed detection of products, causing significant errors in determinations of rate constants.

The fluidized-bed research has revealed the deleterious effect of oxidized shale on oil yield. We have measured up to a 15 percent decrease in oil yield when oxidized shale at a 4:1 ratio to raw shale is left in the bed. We are investigating what impact this would have under pilot retorting conditions and are also testing means of reducing yield loss using solid and gaseous additives.

## HRS Retort System

We have operated a 1-t/day continuous-loop HRS retorting system at LLNL since 1984 to study the retorting chemistry in an actual recirculating loop. This year, we are upgrading the retort to process 4 t/day of commercially sized shale to study pyrolysis and combustion kinetics in more detail and to answer the many questions on bulk-solid handling pertinent to the scale-up of the HRS process. The new facility, shown schematically in Fig. 1, contains a number of important components, including a rapid-throughput fluid-bed mixer and moving packed-bed pyrolyzer, an air pneumatic lift and delayed-fall combustor, and a fluid-bed combustor designed to separate and discharge fines while recycling coarse shale.

In this process, raw shale is rapidly heated in a gravity-bed pyrolyzer to produce oil vapor and gas. Residual carbon (char), which remains on the spent shale after oil extraction, is burned in a delayed-fall combustor, providing heat for the entire process. The heat is transferred from the combustion process to the retorting process by recycling the hot solid. A small fluid bed provides rapid mixing of the raw and recycled shale prior to introduction into the moving packed-bed pyrolyzer, where the shale resides for 1 to 2 min at 500°C, providing the residence time necessary to extract the oil. Leaving the retort, the solid is pneumatically lifted to the top of a cascading-bed combustor, where the char is burned during impeded-gravity fall, which raises the temperature to nearly 650°C. Below the burner, a small fluid bed separates and discharges fines and recycles the coarse shale.

Potential process improvements include rapid throughput, high oil recovery, complete fines utilization, and reduced environmental impact.

Unlike most processes in the chemical and petroleum industries, oil shale processing requires handling large volumes of solids. Understanding the unit operations of key solid-handling components and their interaction is a major focus of our current research. Our program plan encompasses the three scales of operation shown in Table 1.

Successful testing at these three scales would provide the technical know-how to private industry to build a full commercial-scale module (12,000 t/day). Scale-up from the large pilot test would involve a factor-of-3 change in vessel diameter, which is not unreasonable for solid-handling systems.

## Conclusions

The results of our laboratory and pilot plant studies are condensed into mathematical models describing the retorting process. These models are then used to scale-up the process and explore improved retorting methods. This interaction between experimental studies and modeling has been the key to our success in advancing the state of the art.

We are upgrading our HRS pilot retorting system to handle 4 t/day, and we have completed the conceptual design of two pilot tests of the HRS process, at the 100- and 1000-t/day scales. Pending DOE approval, detailed design of the 100-t/day pilot test could begin as early as October 1991.

*This work was supported by the Morgantown Energy Technology Center of the DOE Office of Fossil Energy.*

**Table 1.** Size of operations in the Oil Shale Project.

| Scale | Tonne/day | Pyrolyzer diameter |
|---|---|---|
| Laboratory | 1 | 8 in |
| Small pilot | 100 | 1.5 ft |
| Large pilot | 1000 | 4.5 ft |

# A Review of Fabrication Technology for ICF Target Shells

R. S. Upadhye

***Plastic microshells filled with $D_2$ are routinely used for direct-drive implosions in the Inertial Confinement Fusion (ICF) Program. The technology used to make these shells has been developed at LLNL during the last five years. This article summarizes the present technology of microshell fabrication.***

## Introduction

The technology of making microshells is based on the collective efforts of many researchers.[1–5] The shells are made of three layers (Fig. 1). The inner layer (often referred to as the mandrel) is made of polystyrene, which provides support for the middle layer, made of polyvinyl alcohol (PVA). The purpose of the PVA layer is to provide an adequate permeation barrier for the fuel and diagnostic gases. The tensile strength of PVA, however, is not sufficient to hold the high pressures of the fill gases, thus necessitating the outer layer, made of cross-linked plasma-polymerized material. This outer layer (often called the CH layer) also serves as the ablator in implosion experiments. This article describes how the polystyrene shells are made, how they are coated with the PVA and CH layers, and how they are characterized and filled.

## Polystyrene Shells

The process of making polystyrene mandrels, shown schematically in Fig. 2, is conceptually simple.[3] A solution of polystyrene in an organic solvent is introduced at the top of a drop tower through a double nozzle system, shown in the inset of Fig. 2. The solution flows through the inner nozzle, and the stripping gas flows through the outer nozzle. The column consists of three sections, referred to here as the top, middle, and bottom sections. The top section holds the nozzle assembly. The middle section is heated by a series of electrical heaters, and heated nitrogen gas is introduced at the bottom of the middle section, whence it flows upward against the falling droplet. Cold nitrogen gas is introduced at the bottom of the bottom section and flows upward, mixing with the hot gas at the bottom of the middle section and leaving the column at the top. The bottom of the bottom section is fitted with a collector for the product microshells.

The exact mechanism of how the shells are formed has not been completely established; the phenomenon can be explained qualitatively, however.[5] The falling drop goes through four stages: drying, skin formation, expansion, and stabilization. In the drying stage, the solvent evaporates from the droplet because of the heat transfer from the surrounding hot gas. At some point, when the polymer concentration at the outer surface exceeds a certain limit, a skin begins to form on the outside. This phenomenon greatly reduces the permeability of the outer layer to the evaporating solvent. As a result, the droplet begins to expand, as the solvent continues to boil off because of heat transfer from the counterflowing hot gas. Once all the solvent evaporates, the shell begins to shrink, as the solvent continues to permeate the shell skin. Finally, as the shell enters the bottom zone and contacts the cold gas, the soft skin cools and hardens, completing the stabilization process.

**Figure 1.**

Layers of an ICF microshell target.

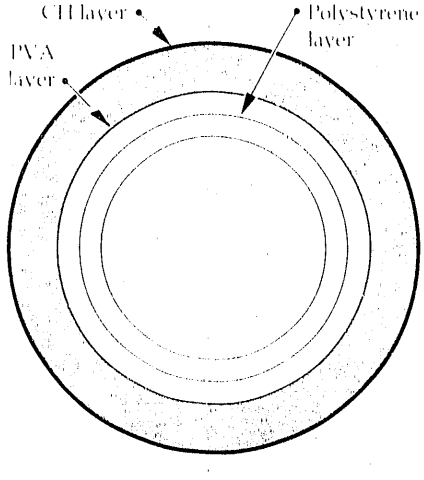


## PVA Coating Process

The polystyrene mandrels that are produced as described above have a very high permeability to the fuel gases, necessitating the PVA layer, which is added by a dip-coating process. The first step in this process

is to introduce the sorted polystyrene shells of acceptable surface quality into a capillary tube by suction. The shells are then placed inside a chamber, which is evacuated.[6] If the experiment for which the shells are being made calls for a certain diagnostic gas (such as argon in many implosion experiments), it is introduced into the chamber at this time, and the shells are allowed to equilibrate with the gas. An aqueous solution of PVA is then sucked into the capillary tube; this solution surrounds the shells, trapping the diagnostic gas inside.

The next step is to make the PVA layer uniform and to stabilize it by drying. Both are accomplished in the PVA drop tower, shown in Fig. 3.[6] The capillary tube filled with the mandrels and the PVA solution is attached to a hypodermic syringe filled with PVA solution, and the whole assembly is placed on top of the PVA column (see the inset of Fig. 3). The PVA column is equipped with a set of electrical heaters, which heat the nitrogen gas flowing up the column. The shells coated with the PVA solution are injected into the column at a uniform rate. The PVA solution layer becomes uniform in free fall because of surface tension. The hot nitrogen gas flowing past the falling wet shells helps dry them during their fall, and the dried shells, coated with a uniform PVA layer, are collected at the bottom of the column. Depending on the experiments for which they were made, shells of the right surface finish and dimensions are selected and sent to the CH coater.

## CH Coating Process

The PVA layer described above has a low permeability to the isotopes of hydrogen and the diagnostic gases such as argon, but it lacks the necessary tensile strength to hold high pressures. Therefore, a third layer with the necessary strength characteristics is needed. This layer should be relatively thick in order to also serve as an ablator. Plasma-polymerized films appear to possess the needed properties. The present method of forming a uniform CH layer on implosion targets, described briefly in the following paragraphs, is essentially a summary of work reported by Johnson et al.[7] and Letts et al.[8]

As shown in Fig. 4, the plasma polymerization apparatus consists of a vibrating bouncer pan and a helical resonator. The vibrating pan, driven piezoelectrically, ensures that each sphere receives a uniform coating during exposure in the active plasma field. The pan is constructed by fastening a thin stainless steel plate, previously hydroformed into the shape of a saucer, to a piezoelectric crystal. The crystal is driven by a white noise source.

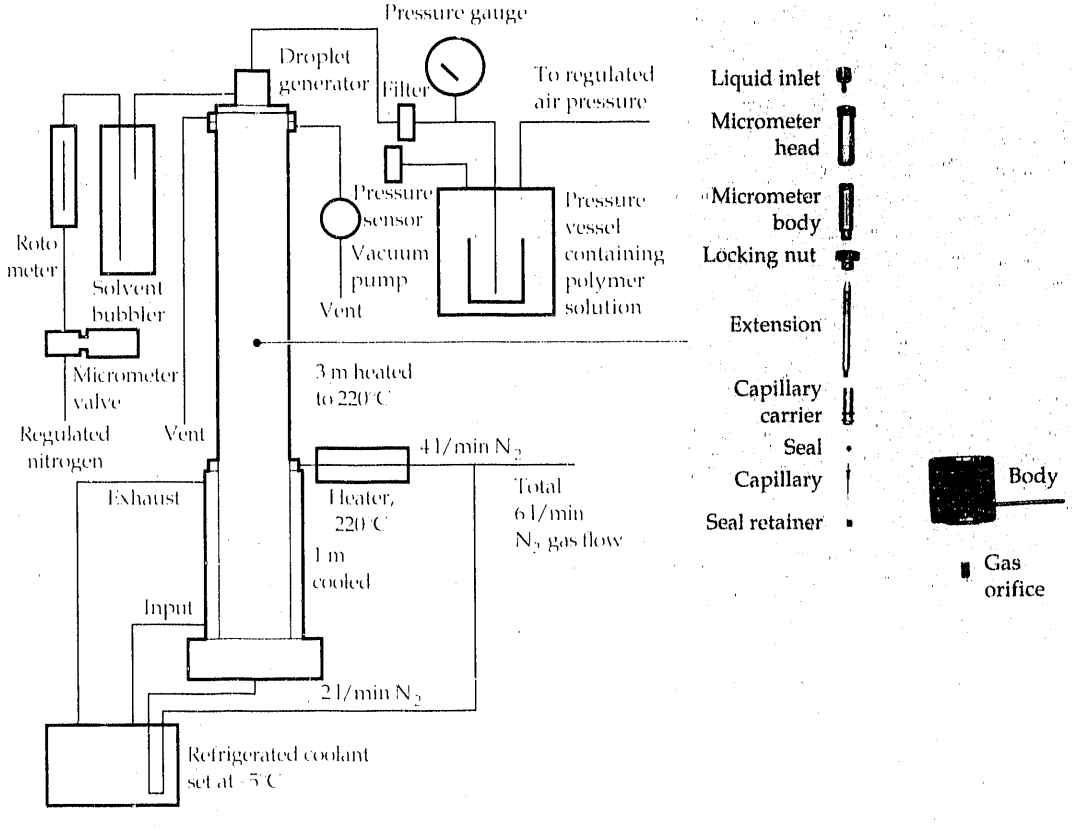


**Figure 2.**

**Schematic of the process used to make polystyrene mandrels.**

The helical resonator is a particular type of tuned resonant cavity that inductively couples energy to the plasma. It is unusual in its capability of producing low-pressure discharges in gases because the magnetic field lines somewhat inhibit the flow of charged species to the walls. The plasma is confined within an interchangeable quartz reaction tube through which a mixture of the monomer gas and hydrogen flows. Changing the reactor tube size provides a means of altering the electron temperature that affects plasma composition. A radiofrequency (RF) shield that varies the length of the discharge region controls the amount of time during which the flowing monomer is subjected to the plasma environment.

**Figure 3.** Schematic of the PVA drop tower.

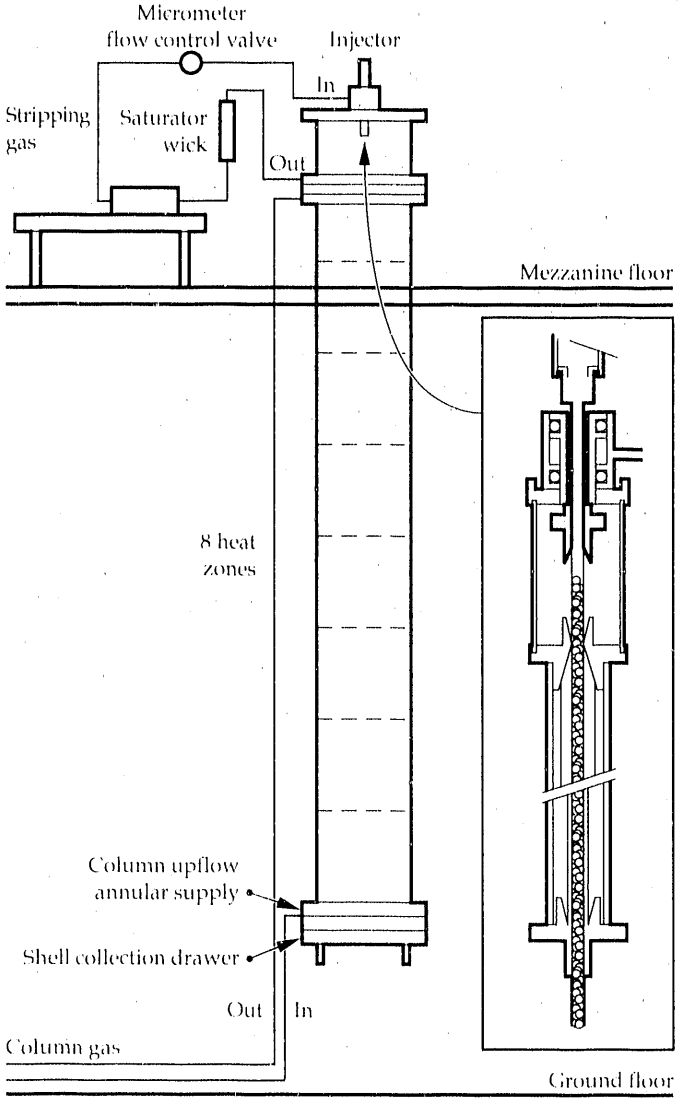


## Characterization of Shells

The coated shells are characterized for inside diameter, wall thickness, layer concentricity, and sphericity.[4] Characterization techniques include interferometry, scanning electron microscopy, radiography, optical microscopy, and x-ray fluorescence. The shells that meet the experimental specifications are filled with $D_2$.

## Filling with $D_2$

The final step in the production of microshell targets is to fill them with the correct amount of $D_2$. The standard procedure for filling the shells with $D_2$ is to put them in a capillary tube and place the capillary tube in a pressure vessel connected to a $D_2$ supply. The pressure in the vessel is increased gradually, in small steps,

**Figure 4.** The helical resonator plasma coater, which is used to apply the CH layer.

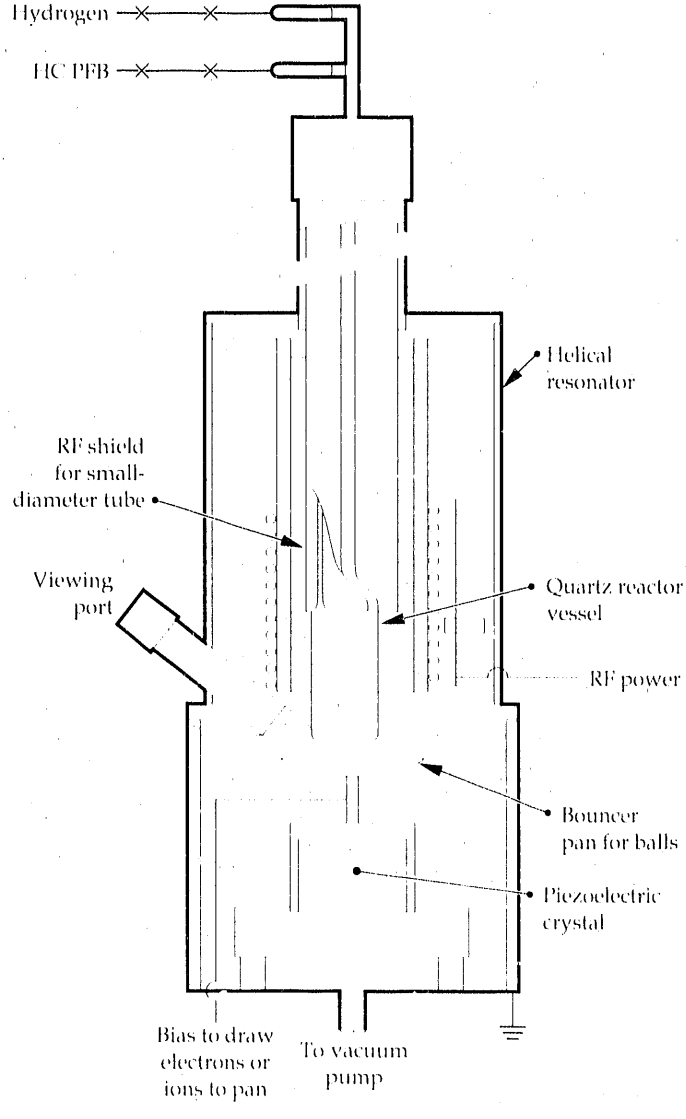

until the desired pressure is reached, following which the shells are heat-treated to reduce the permeability of the PVA to $D_2$. The filled and heat-treated shells are stored in $D_2$ under pressure until needed.

*This work was supported by the ICF Program.*

## References


1. J. H. Campbell, J. Z. Grens, and J. F. Poco, *Preparation and Properties of Hollow Glass Microspheres for Use in Laser Fusion Experiments*, Lawrence Livermore National Laboratory, Livermore, Calif., UCRL-53516 (1983).
2. J. H. Campbell, J. Z. Grens, J. F. Poco, and B. H. Ives, *Preparation and Properties of Polyvinyl Alcohol Microspheres*, Lawrence Livermore National Laboratory, Livermore, Calif., UCRL-53750 (1986).
3. E. M. Lilley and J. Z. Grens, "Production of Polystyrene Microballoons," Lawrence Livermore National Laboratory, Livermore, Calif., draft report (January 22, 1988).
4. E. M. Lilley, "Fabrication, Measurement, Testing, and Pressurization of Polymer Targets," Lawrence Livermore National Laboratory, Livermore, Calif., draft report (July 10, 1987).
5. J. Z. Grens, "Polymer Microspheres—Phenomenology and Modeling of the Production Process," Lawrence Livermore National Laboratory, Livermore, Calif., draft report (1987).
6. K. J. King, *Fabrication and Operation of a System for the PVA Coating of Polymer Microshells with Trace Gas Fill*, Lawrence Livermore National Laboratory, Livermore, Calif., UCID-21435 (1988).
7. W. L. Johnson, S. A. Letts, C. W. Hatcher, L. E. Lorenson, and C. D. Hendricks, "Plasma Polymerization Coating of DT-filled Glass Shells for Laser Fusion Targets," in *Plasma Polymerization, ACS Symposium Series 108*, M. Shen and A. T. Bell, Eds. (American Chemical Society, Washington, D.C., 1979), chapter 20.
8. S. A. Letts, D. W. Myers, and L. A. Witt, "Ultrasmooth Plasma Polymerized Coatings for Laser Fusion Targets," *J. Vac. Sci. Technol.* **19**(3), 739 (1981).

# Nuclear Polarization of Deuterium-Tritium

P. C. Souers,
J. L. Maienschein,
G. W. Collins, and
E. R. Mapoles

*This article describes four years of electron spin resonance (ESR) and nuclear magnetic resonance (NMR) measurements on solid deuterium-tritium (D-T) at 3 K and higher. An adequate number of hydrogen atoms is produced by tritium radioactivity to pump the hydrogen nuclei in dynamic nuclear polarization. The electron relaxation time is too long and the nuclear relaxation times are too short, however, for nuclear polarization. Pure molecular DT and temperatures below 2 K will be needed to pursue nuclear polarization.*

## Introduction

For 10 years, our laboratory has specialized in examining the properties of liquid and frozen D-T in the hope that some special use in hydrogen fusion would result. Such a potential use appeared in the idea of nuclear spin polarization. Kulsrud et al.[1] suggested that D-T fuel with all nuclear magnetic moments aligned parallel would undergo fusion with a 50 percent higher cross section than the usual random mixture. Such a fuel could cut the size, and perhaps the cost, of the inertial confinement fusion driver by as much as 50 percent.

Nuclear polarization has been done for years on special compounds used as targets in nuclear and high-energy physics.[2,3] Temperatures of 0.3 to 0.5 K are routinely used to lengthen the nuclear magnetic relaxation time. Protons have been polarized to virtually 100 percent, but deuterons only to about 40 percent. Polarization of tritons has never been attempted, nor has polarization of radioactive compounds.

One way to polarize nuclei is to cool the sample to millikelvin temperatures in a dilution refrigerator. Honig has used this method for solid hydrogen deuteride (HD).[4] This method requires superlow temperatures, which would not be attainable with the 1 W/mol decay heat of D-T.[5] Almost all polarized high-energy physics targets use a different method in any case: viz, that of dynamic nuclear polarization.[2,3] In this method, unpaired electrons in some "dopant" in the sample are easily polarized in a 3- to 10-T dc magnetic field at 0.3 to 1.4 K. Microwave energy just off the electron spin resonance frequency is then applied, and if all the internal forces are working properly, the electrons will transfer their polarization to the nuclei.

Three basic conditions must hold to cause significant nuclear polarization. First, we must have a large concentration of unpaired electrons. In D-T, these will be supplied by the hydrogen atoms (i.e., deuterium or tritium atoms) constantly being formed by the tritium radioactivity. Second, the electron magnetic relaxation time must be short, because each electron must polarize hundreds to thousands of nuclei sequentially. Third, the nuclear magnetic relaxation times of both the triton and the deuteron must be sufficiently long to retain their polarization while other nuclei are waiting their turn.

**Figure 1.** Total atom-spin count in solid D-T at 3 to 5 K. Five hyperfine lines in the ESR spectrum are added to give these totals. The colder the sample, the more atoms are present. The ESR frequency is 9.4 GHz.

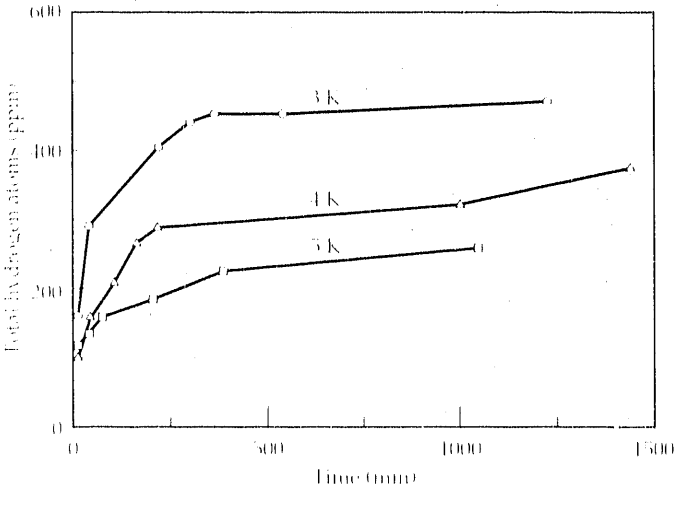


## Results

The years 1986 to 1989 have seen us search for solutions to the above problems in the accessible temperature range of 3 to 5 K. We began, experimentally, with regular D-T, which is a radiation-equilibrated mixture of

25 percent $T_2$, 50 percent molecular DT, and 25 percent $D_2$, but ultimately, a chemically synthesized mixture containing 95 percent molecular DT gave the best results.

The concentration of unpaired electrons was determined by ESR at 9.4 GHz and 0.34 T. They are created by tritium irradiation of solid D-T. The ESR absorption curves were measured without modulation, and the areas were compared with those of ruby standards. Five hyperfine lines spread over 1.6 MHz were added to get the atom total. The total atom-spin counts at 3 to 5 K in solid D-T are shown in Fig. 1. The total amounts to several hundred parts per million, and it increases with decreasing temperature. At lower temperatures, atom diffusion is slowed and recombination back to the diatomic species is reduced.

A different behavior was found below 2 K, as shown by the atom count taken in solid D-T at 1.6 to 1.9 K (Fig. 2). Thermal spikes swept through the system without apparent explanation. The ESR signal decreased following such spikes, and then it built up again with time. The sample temperature rose momentarily to 5 to 8 K, and sample annealing occurred as monitored by the change in thermal conductivity. A burst of light at the ruby frequency of the sapphire window was also seen. We believe that these spikes represent a cooperative atomic recombination—a deflagration wave of released chemical energy. We later found that the spikes could be triggered to order by a quick temperature rise. They could also be suppressed by more intense cooling. At this moment, we do not know the maximum achievable free atom density that can be obtained below 2 K, but we believe that 1000 ppm may be achievable.

We also measured the longitudinal magnetic relaxation time of the electron. This time constant for the loss of magnetic energy to the lattice was measured by the method of "saturation recovery." The ESR signal is reduced to zero by applying high microwave power. We then diminish the power and monitor the return rate of the ESR signal. Below 2 K we found this time to be 85 ± 25 ms. Theoretical calculations by Fedders indicate that this time is as long as it is because the hydrogen atom electron is in the s-state. This spherically symmetric state is close to the nucleus and interacts only weakly with the crystal lattice. In solid HD with 2 percent tritium, however, this time is on the order of 1 s. This means that interaction between the electron moments is reducing the time constant in solid D-T. We believe that increasing the atom density will help to shorten the relaxation time. Also, Solem[6] has reported a time of 1 ms in solid HD doped with molecular oxygen.

The longitudinal (i.e., energy-loss) relaxation of the two nuclei in D-T is the most critical obstacle facing our program. We have spent 4 years measuring these time constants by pulsed NMR using either the $\pi$-$\pi/2$ or $\pi/2$-$\pi/2$ pulse sequence. A large amount of experimental and theoretical work can be summarized[7] as follows. The magnetic moment of the triton is the largest of any nucleus, but that of the deuteron is only one-quarter as large. Any scheme that renders the triton time constant long enough is expected to make the deuteron time constant much longer, because the smaller magnetic moment should not interact as strongly with its surroundings. The short triton relaxation time, then, appears to be our major problem.

The longitudinal relaxation times of solid molecular hydrogen are determined by the electric quadrupole interaction (called the EQQ mechanism). The species causing the triton relaxation time to shorten is the $J = 1$ $T_2$ species, which is the first excited rotational state, often called ortho-$T_2$. It exists as a metastably trapped species at cryogenic temperatures. In the EQQ process, the electric quadrupole moment of the $J = 1$ molecule splits the $J = 1$ rotational energy level into a band of states, which, if separated by energies close to the NMR energy, promote nuclear relaxation with high efficiency. The relaxation is minimized at about 1% $J = 1$ $T_2$. The hydrogen atoms in solid D-T catalyze the transition from $J = 1$ to $J = 0$, but unfortunately, the atom recombination produces new $J = 1$ $T_2$ at a constant rate. One begins with a 0.3-s triton time constant at 30 MHz, and the tritium radioactivity takes it directly to the 0.1-s minimum, where it sticks.

We explored two ways of lengthening the triton relaxation time. One was to eliminate the $J = 1$ $T_2$ by synthesizing 95 percent molecular DT with only a few tenths of a percent $J = 1$ $T_2$, increasing the relaxation time to 1 s. We then added normal $H_2$, and the time constant increased to 10 s. This surprising result was predicted by the EQQ theory. By keeping the $J = 1$ $T_2$ low, but either the $J = 1$ $H_2$ or $J = 1$ $D_2$ high, we push the $T_2$ away from the relaxation time minimum. Using $J = 1$ $D_2$ would, of course, lower the deuteron relaxation time.

A second method was to freeze the solid D-T in silica aerogel and carbon foam. The electric fields on the walls of the foam break the EQQ interaction in the first

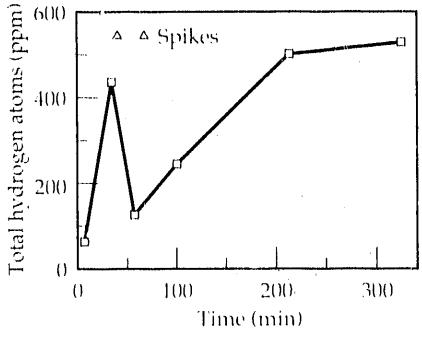


**Figure 2.**

**Effect of thermal spikes on the total atom-spin count in solid D-T at 1.6 to 1.9 K. The decrease in atom concentration after a spike suggests that the spike results from atom recombination.**

two layers of hydrogen molecules. By partly removing the rotational mechanism, the molecule now relaxes more by the much longer spin-lattice mechanism. This technique increases the triton relaxation time for a thin layer of the regular D-T to 18 s.

## The Future

We plan to purify 95 percent molecular DT to 99.99 percent on an adsorption column. A triton relaxation time of 100 to 1000 s is likely. The tritium radiation will, however, produce new $J = 1$ $T_2$ and diminish the advantages of pure DT. The rate for this is seen in Fig. 3, which shows the NMR signal height for 93 percent DT. The decrease in signal represents the conversion of DT to $D_2$ and $T_2$, where the $J = 1$ species is converted fairly quickly to $J = 0$. A "hot-atom" equilibrium with a 140-h time constant is considered to be a likely mechanism. This would translate to a 20-min lifetime for superpure DT.

*This work was supported by the Weapons Program, Institutional Research & Development, and the Inertial Confinement Fusion Program.*

## References

1. R. M. Kulsrud, H. P. Furth, E. J. Valeo, and M. Goldhaber, "Fusion Reactor Plasmas with Polarized Nuclei," *Phys. Rev. Lett.* **49**, 1248 (1982).
2. W. DeBoer, "Dynamic Orientation of Nuclei at Low Temperatures," *J. Low Temp. Phys.* **22**, 185 (1976).
3. W. Meyer, K. H. Althoff, V. Burkert, U. Hartfiel, T. Hewel, O. Kaul, G. Knop, E. Kohlgarth, H. D. Schablitzky, E. Schilling, and W. Thiel, "Tensor Polarization of Deuterons in Irradiated $ND_3$," *Nucl. Instrum. Meth. Phys. Res.* **A244**, 574 (1986).
4. A. Honig, Syracuse University, Syracuse, N.Y., private communication (1988).
5. W. L. Pillinger, J. J. Hentges, and J. A. Blair, "Tritium Decay Energy," *Phys. Rev.* **121**, 232 (1961).
6. J. C. Solem, "Dynamic Polarization of Protons and Deuterons in Solid Deuterium Hydride," *Nucl. Instrum. Meth.* **117**, 477 (1974).
7. P. C. Souers, E. M. Fearon, E. R. Mapoles, J. D. Sater, G. W. Collins, J. R. Gaines, R. H. Sherman, and J. R. Bartlit, "Triton Memory Time in Solid DT and its Nuclear Polarization," *Fusion Tech.* **14**, 855 (1988).

**Figure 3.** **Decrease of the triton NMR signal in 93 percent molecular DT as it decays at 5.1 K to an equilibrium mix of DT with $D_2$ and $T_2$. Two possible chemical equilibration schemes are shown. The hot-atom equilibrium, with the shorter 140-h exchange time constant, is probably the more likely. The experiment was not run long enough to distinguish between the two.**

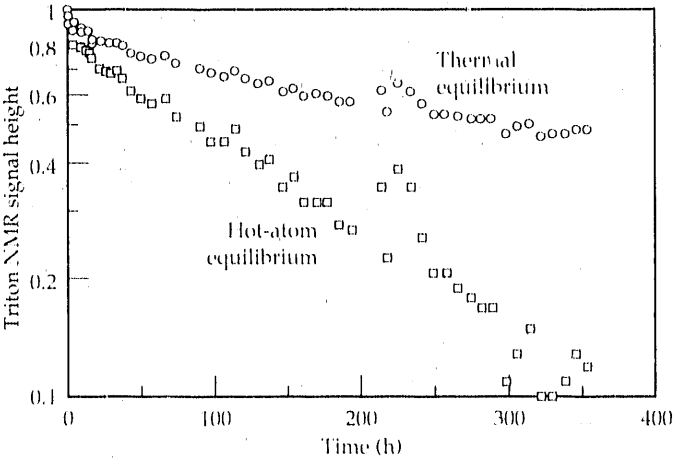

# Development of a High-Level Nuclear-Waste Container for the Yucca Mountain Project

W. L. Clarke

***A program is under way to develop a high-level nuclear-waste disposal container for the proposed Yucca Mountain repository in Nevada. Corrosion appears to be the process most likely to degrade such a waste container. Our studies indicate that Alloy 825 (an austenitic high-nickel alloy) and CDA 715 (Cu-30Ni) are currently the best choices for the metal container in terms of resistance to corrosion. An alternative materials program has been proposed to augment the material selected for the containers, if necessary.***

## Introduction

Iron- and nickel-base austenitic alloys and copper-base alloys are being evaluated as candidate materials for fabrication of metal containers for the Yucca Mountain Project. The containers will be used in disposing of high-level radioactive waste at the proposed Yucca Mountain site in Nevada. The leading candidates[1,2] were selected because of their good corrosion-resistance properties, their wide use in the marine, nuclear, and process industries, and their reasonable cost. These materials are:

- Types 304L and 316L stainless steels,
- Alloy 825,
- CDA 102 (oxygen-free copper),
- CDA 613 (Cu-7Al),
- CDA 715 (Cu-30Ni).

Waste, in the forms of spent fuel assemblies from reactors and borosilicate glass, will be sent to the proposed repository. The containers must be retrievable for 50 yr and exhibit substantially complete containment for 300 to 1000 yr following repository closure.[3,4]

After emplacement of the containers in the repository, the container materials could undergo any of several modes of degradation.[5] Those currently under investigation include atmospheric oxidation; general aqueous corrosion; various forms of localized corrosion and stress-corrosion cracking; microbiological corrosion; the effects of hydrogen; undesirable phase transformations due to a lack of phase stability; and the effects of welding. The material selected for container fabrication will be based on a survey of the literature, corrosion testing at LLNL and subcontractor facilities, predictions from modeling, the ability to fabricate and close (weld) the container, previous experience with the material, and cost.

## Discussion

Our investigation of the various modes of container degradation shows that general corrosion and oxidation do not appear to limit the application of any of the candidate materials.[6] Long-term exposure of the candidate materials to corrosive water at 80°C and steam at 100°C revealed no limitations for a majority of the materials. The significance of these exposures is based on their relevance to repository-emplacement conditions. Radioactive decay of the stored waste will result in substantial heat transfer to the surroundings and in gamma radiation. For waste packages with the highest thermal output, the surface temperature of the containers will rise to a peak of about 250°C. The temperature will drop to about 150°C after 100 yr and will continue dropping slowly.

Pure copper and aluminum bronze did exhibit high general corrosion rates in the water environment for exposures of 1 to 2 yr. However, all of the austenitic alloys and the Cu-30Ni alloy exhibited low general corrosion rates. The observed rates would not result in penetration of 1 mm in 1000 yr under the exposure-test conditions described above.[6]

We identified degradation phenomena in our literature survey[5] that could preclude some of the candidate materials from further consideration. Both Types 304L and 316L stainless steels were noted to be susceptible to stress-corrosion cracking in an oxidizing environment containing chloride ions, as shown in Fig. 1. For oxygen concentrations on the order of a few parts per million (ppm) and chloride concentrations as low as 1 ppm, both Types 304L and 316L exhibited cracking due to chloride-induced stress corrosion. In contrast, Alloy 825 did not fail by stress-corrosion cracking at these concentrations of oxygen and chloride.

Stress-corrosion cracking was also noted in the literature for the copper-base alloys in certain environments. Figure 2 illustrates the effect of alloying-element content on the stress-corrosion resistance of aluminum bronze and copper-nickel alloys. Note that the time-to-failure due to stress-corrosion cracking in an ammoniacal environment decreases dramatically with increasing aluminum content in aluminum bronze. At an aluminum content of about 1 wt%, the time-to-failure reaches a minimum for aluminum bronze. Copper-nickel alloys reveal a similar minimum in time-to-failure due to stress-corrosion cracking in an aqueous ammoniacal environment over a range of nickel content from about 5 to 10 wt%, as shown by the lower curve in Fig. 2. However, the Cu-30Ni alloy (CDA 715) appears to be more resistant to stress-corrosion cracking than are the other copper-base candidate materials (CDA 102 and CDA 613).

There is also a possibility of biological activity in the repository. In such an event, microbes could generate a moist ammoniacal environment having nearly neutral pH.[7] As illustrated in Fig. 3, which gives the Pourbaix diagram (potential vs pH) for the $NH_3$-$H_2O$-Cu system, a singularity exists at a pH of about 7.3 and a potential of about 275 mV (standard hydrogen electrode). The passive film at the tip of stress-corrosion cracks is metastable under these conditions. Consequently, such environments promote stress-corrosion crack propagation. Fortunately, the compositions of CDA 613 and CDA 715 (see Fig. 2) have been optimized to minimize susceptibility to stress corrosion in moist ammoniacal environments.

An extensive study of potential methods of fabrication and closure of the containers has recently been completed.[8,9] The methods identified as practical for fabricating waste containers include roll-and-welded, spin-formed, hot-extrusion, and centrifugal-casting processes. The closure methods include inertial (friction) welding, plasma-arc welding, and electron-beam welding. Methods for nondestructive evaluation of the final closure seal of each container are also under study.

**Figure 1.**

Susceptibility of Types 304L and 316L stainless steels to stress-corrosion cracking in an oxidizing environment containing chloride ions. In contrast to these alloys, Alloy 825 does not fail by stress-corrosion cracking at the concentrations of oxygen and chloride shown.

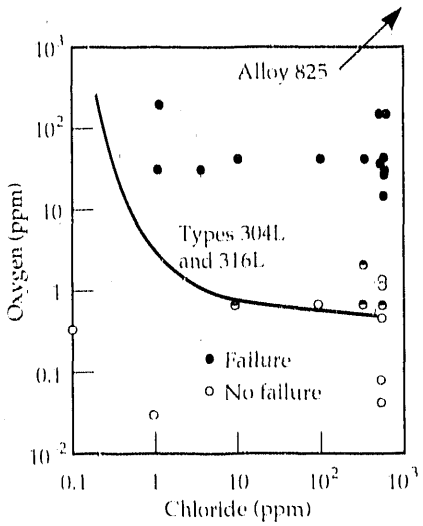


**Figure 2.**

Effect of alloying-element content on resistance to stress corrosion. Of the copper-base candidate alloys, CDA 715 (Cu-30Ni) is the most resistant to corrosion.

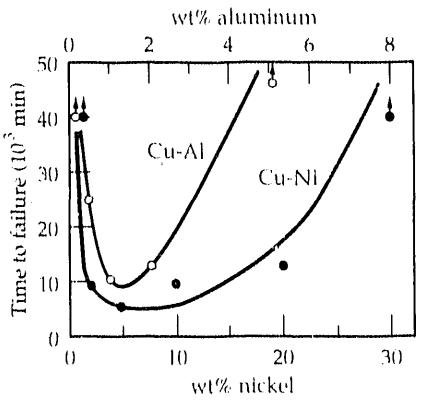


## Alternative Materials Program

Additional design and analysis may suggest the use of an alternative material to augment the metal selected for the containers. Several concepts currently under consideration include ceramic liners, application of monolithic graphite liners, development of a bimetallic container employing galvanic protection, and the use of filler materials in the metal container.

The alternative container concept proposed is an insert within the container shell that will act as a supplement to the shell wall, if needed. The container shell will be selected from the six candidate metals described above and will be chosen to provide protection against the expected site environment. The alternative provides an extra margin should different environmental circumstances be encountered. Such circumstances could include more water than expected, more aggressive water chemistry, higher loads than originally predicted, or new containment and release requirements not met by the container shell.

The alternative materials concept addresses the technical uncertainty in the repository program as well as the uncertainty in meeting the performance goals of the waste container. The alternative materials program also permits the licensing schedule to be maintained by providing licensing conservatism through a redundant design.

## Summary

Corrosion is considered the process most likely to degrade disposal containers for high-level radioactive waste at the proposed repository in Nevada. It has become apparent, from the test data described above and from additional data presented in our literature survey, that the candidate metal barrier materials exhibit limited ranges of resistance to corrosive environments. Types 304L and 316L stainless steels appear unsuitable under both the expected conditions and other, low-probability conditions. Aluminum bronze and pure copper may be usable under the conditions expected, but they do not appear satisfactory for low-probability conditions. Alloys 825 and CDA 715 appear acceptable under the conditions expected and may be suitable for other environments as well.

*This work was supported by the Yucca Mountain Project, which is managed by the Yucca Mountain Project Office of the DOE Nevada Operations Office.*

## References

1. W. G. Halsey and R. D. McCright, *Plan for Metal Barrier Selection and Testing for NNWSI*, Lawrence Livermore National Laboratory, Livermore, Calif., UCID-21262 (1987).
2. R. D. McCright, *An Annotated History of Container Material Selection*, Lawrence Livermore National Laboratory, Livermore, Calif., UCID-21472 (1988).
3. "Disposal of High-Level Radioactive Wastes in Geologic Repositories, Technical Criteria," 10 CFR Part 60, Nuclear Regulatory Agency, Federal Register, Rules and Regulations, Vol. 48, No. 120 (Tuesday, June 21, 1983), pp. 28194–28229.
4. *Site Characterization Plan, Consultation Draft, Yucca Mountain Site, Nevada Research and Development Area*, U.S. Department of Energy, Office of Civilian Radioactive Waste Management, Washington, D.C., DOE/RW-0160 (1988), Secs. 7.5 and 8.3.5.9.
5. D. B. Bullen, J. C. Farmer, G. E. Gdowski, J. N. Kass, R. D. McCright, M. J. Strum, R. A. Van Konynenburg, and H. Weiss, *Survey of Degradation Modes of Candidate Materials for High-Level Radioactive-Waste Disposal Containers*, Lawrence Livermore National Laboratory, Livermore, Calif., UCID-21362 (1988), 8 vols. and Overview.
6. R. D. McCright, W. G. Halsey, and R. A. Van Konynenburg, *Progress Report on the Results of Testing Advanced Conceptual Design Metal Barrier Materials Under Relevant Environmental Conditions for a Tuff Repository*, Lawrence Livermore National Laboratory, Livermore, Calif., UCID-21044 (1987).
7. J. C. Farmer and R. D. McCright, "Localized Corrosion and Stress Corrosion Cracking of Candidate Materials for High-Level Radioactive Waste Disposal Containers in U.S.: A Literature Review," presented at *MRS Conference, Berlin, October 1988*.
8. K. O. Stein, H. A. Domian, R. L. Holbrook, and D. E. LaCount, *Fabrication Development for High-Level Nuclear Waste Containers for the Tuff Repository, Phase 1 Final Report*, Babcock & Wilcox, Alliance, Ohio, BAW-2010 (1987).
9. K. O. Stein, E. W. Roblitz, M. D. McAninch, and D. P. Edmonds, *Closure Development for High-Level Nuclear Waste Containers for the Tuff Repository, Phase 1 Final Report*, Babcock & Wilcox, Alliance, Ohio, BAW-2009 (1987).

**Figure 3.** **Stress-corrosion cracking of copper in moist ammoniacal environments occurs at two pH levels: 7.3 and 11.3. The compositions of candidate alloys CDA 613 (Cu-7Al) and 715 (Cu-30Ni) minimize susceptibility to stress corrosion in such environments.**

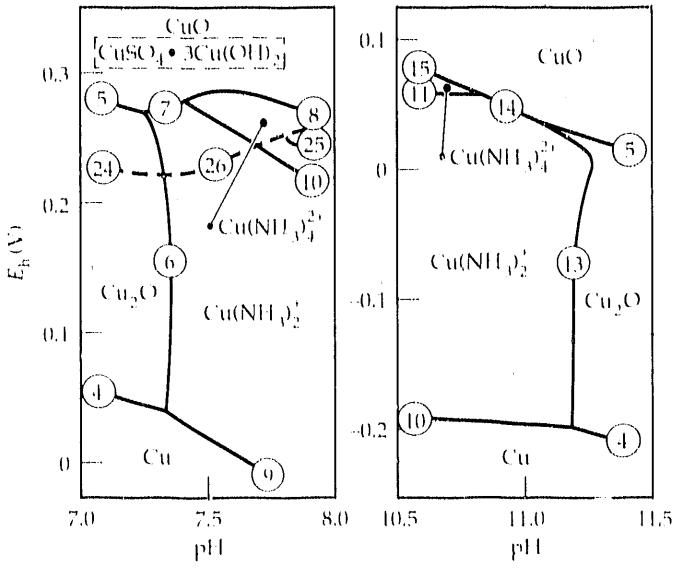

Section 7

# Department Personnel and Professional Contributions

# Personnel

## Chemistry & Materials Science Directorate

C. Catrousis
Associate Director for Chemistry & Materials Science

L. Schwartz
Deputy Associate Director for Administration

D. LaCurtis
Assistant Associate Director for Resources

T. Sugihara
Deputy Associate Director for Research

J. Kolb
Assistant Associate Director for
Weapons Program Support

**Critical Facilities**

M. Singleton
Tritium Facility Manager

A. Toy
Plutonium Facility Manager

**Directorate Staff**

J. Campbell, K. Ernst, J. Johnson, A. Mode, D. Seaton

**Division Leaders**

M. Fluss, Condensed Matter and
Analytical Sciences Division

J. Kass, Materials Division

J. Richardson, Chemical Sciences Division

**Administrative Staff**

L. Brown, G. Maestas, B. Parashis, Y. Villa, E. Waller
M. Altenbach, K. Common, F. Eckert, L. Ellis, E. Gaitan,
M. Governor, S. Woodard

## Chemical Sciences Division

J. Richardson, Division Leader
J. Ackerman, Deputy Division Leader
M. Schwab, Z Division

**Administrative Staff**

E. McArthur, M. Lewis, E. Allen, L. Burke,
D. Coronado, K. Greer, L. Hicks, B. McCollough,
K. Spurlin, R. Treat, C. Ynzunza

### Chemical Engineering Section

C. Thorsness
Section Leader

J. Britten
A. Burnham
D. Camp
R. Cena
C. Chen
J. Creighton
J. Diaz
D. Fields
K. Foster
D. Gregg
R. Hickman
R. Homsy
W. Hui
K. King
M. Kozlowski
E. Lilley
S. Mayer
M. McClelland
L. Murguia
B. Musgrave
M. Oh
R. Quong
R. Taylor
D. Thompson
R. Upadhye
Y. Zundelevich

## High Explosives Technology Section

R. Simpson
Section Leader

E. Lee
R. McGuire
K. Scribner
C. Tarver

**Initiation and Detonation Performance**

L. Green, Group Leader
D. Brolthaupt
T. Cook
F. Helm
C. Lee
S. Rice
P. Urtiew

**Formulation and Processing**

C. Pruneda, Group Leader
W. Black
L. Daniels
K. Fordyce
L. Logoteta
K. Pederson
W. Sunderland
E. von Holtz
C. Walkup
R. Whipple

**Synthesis**

C. Coon, Group Leader
E. Jessop
A. Mitchell
P. Pagoria

**Theory and Modeling**

D. Calef, Group Leader
D. Aidis
P. Crawford
M. Murphy
A. Nichols
J. Walton

**Materials Characterization**

W. Tao, Group Leader
L. Frahm
H. Golopol
G. Moody
D. Ornellas
L. Simpson

## Physical Chemistry Section

P. Shell
Section Leader

R. Alexander
B. Baker
S. Buckley
W. Burks
W. Conaway
A. Cook
P. Cornado
M. Droege
B. Haendler
L. Hair
G. Haugen
B. Holder
L. Hrubesh
D. Jackson
A. Karo
H. Leider
D. Leonard
D. Miller
F. Miller
R. Morrison
D. Olness
J. Poco
J. Roe
R. Sanner
L. Spellman
C. Stevens
S. Steward
N. Stout

## Polymers Section

S. Letts
Section Leader

C. Alviso
J. Carley
I. Chui
R. Cook
J. Harter
M. Hoffman
K. Hong
R. Hopper
S. Hulsey
F-M. Kong
J. LeMay
F. Matthews
B. Mendoza
E. Mones
J. Nielsen
G. Overturf
R. Pekala
M. Riley
J. Satcher
T. Tillotson
L. Weekes

## Tritium and Hydrides Section

C. Souers
Section Leader

P. Barry
J. Bowers
G. Collins
J. Emig
R. Failor
E. Fearon
F. Garcia
R. Garza
R. Hafner
R. Hudson
R. Kanna
J. Maienschein
S. Mayhugh
F. McMurphy
G. Morris
R. Tsugawa

# Condensed Matter and Analytical Sciences Division

M. Fluss, Division Leader
R. Ruzsa, Deputy Division Leader

**Division Staff**

G. Campbell, M. Elder, J. Fischer, A. Hamza, J. Hirschfeld, J. Pyper, J. Tobin, M. Waterman

**Administrative Staff**

K. McDowell, R. Quigley, D. Baker, M. Camacho, R. Coleman, K. Jautaikis, L. McPherson, N. Pogglo, G. Watson

## Analytical Chemistry Section

V. Oversby
Associate Division Leader

**Plutonium**

J. Magana, Group Leader
D. Del Giudice
G. Roberts
P. Wallace
W. Wein
E. Worden

**Lasers/ICP**

P. Miller, Group Leader
J. DeYoreo
T. Duewer
P. Epperson
R. Lim
S. Lombard
W. Morris
C. Otto
D. Pugh
J. Reynolds

**Z Division/Gas Chromatography–Mass Spectrometry**

R. Hawley-Fedder, Group Leader
B. Andresen
L. Foiles
R. Glass
J. Haas
S. Monaco
R. Sanborn

**Energy/Environment**

R. Crawford, Group Leader
A. Alcaraz
R. Bedford
J. Clarkson
T. Coburn
J. Cupps
J. Lindsey
C. Morris
J. Newton
R. Swansiger

**Solutions**

J. Harrar, Group Leader
A. BeLue
N. Butler
A. Conover
J. Deering
L. Rigdon
W. Selig

**Weapons**

H. Gregg, Group Leader
B. Armstrong
W. Boyle
J. Happer
C. Strickland
R. Ward

## Materials Characterization Section

R. Meisenheimer
Acting Associate Division Leader

**Surface Science**

C. Colmenares, Group Leader
M. Balooch
A. Connor
C. Evans
W. Siekhaus

**Particle Laboratory**

H. Newkirk, Group Leader
K. Gels

**X-Ray Diffraction**

G. Smith, Group Leader
Q. Johnson
L. Summers

**Electron Microscopy**

W. King, Group Leader
W. Bell
V. Chen
S. Fadeff
D. McCoy
G. Nutt
P. Perry
M. Sattler
C. Violet
J. Yoshiyama

## Condensed Matter Section

M. Weber
Associate Division Leader

**Synchrotron Radiation**

J. Kinney
J. Wong

**Crystal Growth and Characterization**

J. Atherton
J. Cooper
L. Davis
R. Reibold
F. Wang

**Electron, Magnetic, and Optical Studies**

A. Gonis
M. Guinan
P. Turchi

# Materials Division

J. Kass, Division Leader
A. Lingenfelter, Deputy Division Leader
L. Newkirk, Deputy Division Leader
T. Barbee

**Administrative Staff**

J. Strickland, L. Jones, A. Moser, S. Cowan, J. Gomez, M. Manipis, H. Meredith, J. Prince

## Physical Metallurgy, Joining, and Coating Section

M. Kassner
Section Leader

**Physical Metallurgy**

G. Henshall
R. Musket
N. Nguyen
C. Price
R. Rosen
M. Sluiter
L. Tanner
M. Wall

**Joining**

J. Elmer, Group Leader
M. Gauthier
D. Hoffman
D. Kautz
B. Olsen
T. Ramos
M. Strum
L. Wagner
H. Weiss
B. Westfall

**Coatings**

D. Makowiecki, Group Leader
C. Alford
C. Chen
R. Foreman
R. Juntz
N. Thomas

## Metals Processing Section

G. Gallegos
Section Leader

J. Hanafee
A. Jankowski

**Forming and Processing**

W. Barmore
R. Burns
M. Coops
J. Huang
L. Keene
P. Landon
T. Quick
E. Raymond
E. Sedillo
M. Stratman
W. Thayer
S. Torres
C. Witherell
D. Wood

**Metallography**

R. Kershaw,
Lead Metallographer
J. Canfield
K. Miller
H. Olson

**Deposition**

A. Barfknecht
E. Randich
E. Stiles
R. Wallace

## Plutonium Technology Section

A. Lingenfelter
Section Leader

**SIS Technology**

C. Cate
T. Crawford
D. Hays
D. McAvoy

**Plutonium Technology**

R. Condit, Group Leader
J. Furr
R. Gomez
D. Hagerty
W. Kuhl
R. Krueger
V. Mason-Reed
B. Vallier

## Ceramics and Composites Section

R. Landingham
Section Leader

**Ceramics**

W. Gourdin, Group Leader
S. Aceves
C. Anderson
M. Costantino
P. Curtis
C. Hoenig
B. Holt
O. Krikorian
P. Lewis
B. Lum
T. Maclean
J. Marion
R. Otto
T. Shell
A. Tesar
W. Weinland
K. Wilfinger

**Polymer-Based Fiber Composites**

J. Lepper, Group Leader
L. Chaio
R. Christensen
S. DeTeresa
R. Lyon
J. Matthews
D. Schumann
W. Steele

## Corrosion Section

A. Lingenfelter
Acting Section Leader

**Yucca Mountain Project**

W. Clarke, Group Leader
J. Estill
J. Farmer
D. Fleming
W. Halsey
M. Juhas
D. McCright
R. Van Konynenberg

**Metallurgy**

M. Farris
J. H. DePruneda
J. Mitchell
J. Oldani

## Postdoctoral Research Staff Members

Ph.D. Institution and Fiscal Year of Appointment

| | |
|---|---|
| J. D. Bauer | Columbia University (1990) |
| T. P. Beebe | University of Pittsburgh (1989) |
| T. D. de la Rubia | State University of New York, Albany (1989–1990) |
| J. W. Elmer | Massachusetts Institute of Technology (1989; career employee in 1990) |
| M. E. Foltz | University of California, Berkeley (1990) |
| E. M. Larson | Arizona State University (1989–1990) |
| N. Merk | University of Neuchatel (1988–1989) |
| S. S. Park | University of California, Davis (1989–1990) |
| B. Rupp | University of Vienna (1990) |
| J. D. Sater | Ohio State University (1989) |
| M. H. F. Sluiter | University of California, Berkeley (1990) |
| F. R. Solal | University of Paris (1990) |
| E. C. Sowa | University of California, Berkeley (1989–1990) |
| J. Stephens | Rice University (1990) |
| P. A. Sterne | Cambridge University (1989–1990) |
| P. E. A. Turchi | University of Paris (1987–1989; career employee in 1990) |
| A. L. Wachs | University of Illinois (1989) |
| H. Wallman | University of California, Berkeley (1990) |

## Graduate Students

| | |
|---|---|
| S. Bisson | University of California, Davis |
| S. Bosson | University of California, Davis |
| D. Brown | University of California, Davis |
| M. Connor | University of California, Davis |
| J. Davis | University of California, Santa Barbara |
| S. Dunmead | University of California, Davis |
| J. Mikalopis | University of California, Davis |
| R. Rosen | University of California, Davis |
| M. Schildbach | University of California, Davis |
| T. Summers | University of California, Berkeley |
| E. Suranyi | University of California, Davis |
| A. Sunwoo | University of California, Berkeley |
| R. Tench | University of California, Davis |
| L. Wang | University of California, Davis |

# Consultants

| | |
|---|---|
| H. S. Ahluwalia | Science & Engineering Associates, Inc. |
| J. G. Albright | Texas Christian University |
| A. Alexander | Custom Analytical Engineering Systems, Inc. |
| D. B. Bullen | KMI Energy |
| Y. T. Chou | Lehigh University |
| M. S. Conradi | Washington University |
| P. H. Dederichs | Institüt für Festkorperforschung, W. Germany |
| M. Denn | University of California, Berkeley |
| J. Economy | University of Illinois |
| G. Egan | Aptech Engineering Services, Inc. |
| P. A. Fedders | Washington University |
| L. Feldman | AT&T Bell Laboratories |
| J. F. Fellers | University of Tennessee |
| J. R. Gaines | University of Hawaii |
| R. Gangloff | University of Virginia |
| R. W. Gaver | San Jose State University |
| G. E. Gdowski | KMI Energy |
| W. H. Giedt | University of California, Davis |
| R. Goehner | Nicolet Instrument Corporation |
| R. Golding | Tracer Research Corporation |
| H. T. Hahn | Pennsylvania State University |
| J. R. Hardy | University of Nebraska |
| R. J. Hardy | University of Nebraska |
| R. M. Herman | Pennsylvania State University |
| G. M. Hieftje | Indiana University |
| J. Huizenga | University of Rochester |
| W. L. Johnson | California Institute of Technology |
| R. Jones | Electric Power Research Institute |
| N. Kioussis | California State University, Northridge |
| R. Long | G. P. U. Nuclear |
| F. E. Lytle | Purdue University |
| R. K. Maccrone | Rensselaer Polytechnic Institute |
| T. B. Massalski | Carnegie-Mellon University |
| B. J. Matkowsky | Northwestern University |
| H. J. McQueen | Concordia University |
| M. H. Mehlman | University of California, Riverside |
| D. J. Meier | Michigan Molecular Institute |
| A. K. Miller | Stanford University |
| R. J. Morgan | Michigan Molecular Institute |
| J. W. Morris, Jr. | University of California, Berkeley |
| A. K. Mukherjee | University of California, Davis |
| Z. A. Munir | University of California, Davis |
| P. M. Naghdi | University of California, Berkeley |
| R. J. Naylor | Maryville College |
| B. J. Neuhauser | Stanford University |
| R. E. Norberg | Washington University |
| S. R. Nutt | Brown University |
| D. R. Olander | University of California, Berkeley |
| G. B. Olson | Massachusetts Institute of Technology |
| M. Prager | Materials Property Council |
| W. E. Preeg | Schlumberger Well Services |
| E. A. Rinehart | University of Wyoming |
| D. Schryvers | University of Antwerp |
| J. H. Simmons | University of Florida |
| A. W. Sleeswyk | University of Gröningen |
| D. K. Smith | Pennsylvania State University |
| G. Springer | Stanford University |
| T. D. Thomas | Oregon State University |
| T. A. Tombrello | California Institute of Technology |
| T. Tsakalakos | Rutgers University |
| G. Van Tendeloo | University of Antwerp |
| P. Weinberger | Technical University of Vienna |
| M. Wuttig | University of Maryland |
| R. N. Zare | Stanford University |

## Scientific Advisory Committees

### Chemistry Review Committee

T. A. Tombrello,
California Institute of Technology, Chair
T. Brill, University of Delaware
M. Denn, University of California, Berkeley
J. R. Huizenga, University of Rochester
R. E. Norberg, Washington University
W. E. Preeg, Schlumberger Well Services
T. D. Thomas, Oregon State University

### Materials Review Committee

T. A. Tombrello,
California Institute of Technology, Chair
M. Blume, Brookhaven National Laboratory
D. M. Gruen, Argonne National Laboratory
W. L. Johnson, California Institute of Technology
M. B. Maple, University of California, San Diego
J. W. Morris, University of California, Berkeley

# Collaborations

Research and development programs in the C&MS Department frequently involve collaborations with researchers at universities and other institutions. The following is a partial list of collaborating organizations.

## American Universities

Brown University
University of California
- Berkeley
- Davis
- Irvine
- Los Angeles
- San Diego
- San Francisco
- Santa Barbara

California Institute of Technology
California State University
- Northridge
- San Jose

Carnegie-Mellon University
University of Cincinnati
University of Connecticut
Cornell University
Florida Atlantic University
Georgia Institute of Technology
Harvard University
University of Hawaii
University of Houston
University of Illinois
University of Maryland
University of Massachusetts
Massachusetts Institute of Technology
Miami University (Ohio)
University of Minnesota
University of Missouri at Kansas City
University of Nebraska
North Carolina Agricultural and Technical State University
Northwestern University
Ohio State University
Oregon State University
Princeton University
Rutgers University
University of South Carolina
Stanford University
Syracuse University
University of Texas at Arlington
Texas Christian University
University of Virginia
Washington University (St. Louis)
University of Wisconsin
- Madison
- Milwaukee

## Foreign Universities

University of Antwerp (Belgium)
University of Bristol (U.K.)
Concordia University (Montreal)
Dortmund University (FRG)
University of Gröningen (Netherlands)
University of Guelph (Ontario)
Queen's University (Ontario)
University of Tokyo (Japan)
Technical University of Vienna (Austria)

## American Laboratories

Ames Laboratory
Argonne National Laboratory
Brookhaven National Laboratory
- National Synchrotron Light Source

Department of Defense
- Army Research and Development Center (Picatinny Arsenal)
- Naval Ordnance Station (Indian Head, Md.)
- Naval Surface Weapons Center (White Oak, Md.)
- Naval Warfare Station (Yorktown, Va.)
- Naval Weapons Center (China Lake, Calif.)
- Rocket Propulsion Laboratory (Edwards AFB, Calif.)

## American Laboratories (cont.)

Lawrence Berkeley Laboratory
Los Alamos National Laboratory
National Aeronautics and Space Administration
Oak Ridge National Laboratory
Sandia National Laboratories
  Albuquerque
  Livermore
Stanford Synchrotron Radiation Laboratory

## Foreign Laboratories

Centre National de Recherche Scientifique, Laboratory of Electronic Properties of Solids (Grenoble, France)
European Institute for Transuranium Elements (Karlsruhe, FRG)
HASYLAB, Deutsches Elektronen Synchrotron (Hamburg, FRG)
Kernforschungsanlage Jülich, Institut für Festkörperforschung (Jülich, FRG)
Max Planck Institut für Metallforschung (Stuttgart, FRG)
National Institute for Research in Inorganic Materials (Tsukuba, Japan)
Office National d'Etudes et de Recherches Aérospatiale (Chatillon, France)
Solid State Physics Institute, Academy of Science (Moscow)

# Research Communications

## Journal Publications

J. G. Albright and D. G. Miller, "Nonlinear Regression Programs for the Analysis of Gouy Fringe Patterns from Isothermal Free Diffusion Experiments on Three-Component Systems," *J. Phys. Chem.* **93**, 2169 (1989).

J. G. Albright, R. Mathew, D. G. Miller, and J. A. Rard, "Isothermal Diffusion Coefficients for NaCl-$MgCl_2$-$H_2O$ at 25°C. 1. Solute Concentration Ratio of 3:1," *J. Phys. Chem.* **93**, 2176 (1989).

D. Aldis and D. Gidaspow, "Combustion of a Polydispersed Solid Using a Particle Population Balance," *Power Technology* **57**, 281 (1989).

P. D. Askenazy, E. Kamenetzky, L. E. Tanner, and W. L. Johnson, "Deformation-Induced Amorphization of Crystalline Particles in a Cu-Ti Metallic Glass," *J. Less-Common Metals* **140**, 149 (1988).

R. S. Averback, T. D. de la Rubia, and R. Benedek, "Dynamics and Structure of Energetic Displacement Cascades," *Nucl. Instrum. Meth.* **B33**, 693 (1988).

M. Balooch, D. S. Fischl, D. R. Olander, and W. J. Siekhaus, "The Kinetics of Tungsten Etching by Atomic and Molecular Chlorine," *J. Electrochem. Soc.* **135**, 2090 (1988).

T. W. Barbee and J. Wong, "EXAFS of Near Monolayer Hafnium Film," *Physica B* **158**, 670 (1989).

J. M. Beiriger, R. A. Failor, K. V. Marsh, and G. E. Shaw, "Radioactive Fallout from the Chernobyl Reactor Accident," *J. of Radioanaly. Nucl. Chem.* **123**, 21 (1988).

J. A. Benson, J. C. Hansen, M. T. McEllistrem, W. D. Clendening, and J. G. Tobin, "An Investigation of the Au/Ge(001) Interface," *Surface Science* **193**, L87 (1988).

U. Bonse, R. Nusshardt, F. Busch, Q. Johnson, J. Kinney, R. Saroyan, and M. Nichols, "Optimization of CCD-Based Microtomography," *Rev. Sci. Instrum.* **60**, 2471 (1989).

L. C. Bourne, S. Hoen, M. F. Crommie, W. M. Creager, A. Zettl, M. L. Cohen, L. Bernardez, J. H. Kinney, and D. E. Morris, "Oxygen Isotope Effect in the Superconducting Oxide $La_{1.85}Sr_{0.15}CuO_4$," *Phys. Rev. B* **39**, 2269 (1989).

R. C. Bowman, A. Attalla, P. C. Souers, C. L. Folkers, T. McCreary, G. D. Snider, F. V. Vanderhoofen, and R. T. Tsugawa, "Density of Trapped Gas in Heavily-Irradiated Lithium Hydride," *J. Nucl. Mater.* **154**, 318 (1988).

J. A. Britten, "Extinction Phenomena in Countercurrent Packed-Bed Coal Gasifiers: A Simple Model for Gas Production and Char Conversion Rates," *Ind. Eng. Chem. Res.* **27**, 197 (1988).

J. A. Britten and C. B. Thorsness, "A Model for Cavity Growth and Resource Recovery During Underground Coal Gasification," *In Situ* **13**, 1 (1989).

D. W. Brown, R. G. Musket, and Z. A. Munir, "Formation of a Nearly Pure Aluminum Layer in Beryllium using Ion Implantation," *Appl. Phys. Lett.* **54**, 326 (1989).

A. K. Burnham, M. S. Oh, R. W. Crawford, and A. M. Samoun, "Activation Energy Distributions and Related Chemistry for Pyrolysis of the Argonne Premium Coals," *Energy & Fuels* **3**, 42 (1989).

A. K. Burnham, "On the Validity of the Pristane Formation Index," *Geochim. Cosmochim. Acta* **53**, 1693 (1989).

A. K. Burnham, R. L. Braun, R. W. Taylor, and T. T. Coburn, "Comparison of Isothermal and Nonisothermal Pyrolysis Data with Various Rate Mechanisms: Implications for Kerogen Structure," *ACS Div. Petr. Chem. Preprints* **34**(1), 36 (1989).

D. Calef and A. Nichols, "Polar Solvent Relaxation: The Mean Spherical Approximation Method," *J. Chem. Phys.* **89**, 3783 (1988).

W. R. Cannon and K. Wilfinger, "Particle Interactions in Zirconia Toughened Alumina," *J. Am. Ceram. Soc.* **72**, 256 (1989).

Y. Cao, J. R. Gaines, P. A. Fedders, and P. C. Souers, "The Ortho to Para Conversion in Solid Tritium I. Theoretical Models," *Phys. Rev. B* **37**, 1474 (1988).

D. X. Chen, J. Nogues, K. V. Rao, C. E. Violet, and R. J. Borg, "Effect of Cold-Rolling on the Magnetic Transitions in $Au_{83}Fe_{17}$," *Chinese Phys. Lett.* **5** (1988).

C. W. Chen and C. S. Alford, "Optimization of the Sputter-Deposition Process for Preparing Smooth Coatings of Beryllium on Microspherical Substrates," *J. Vac. Sci. Technol.* **A6**, 128 (1988).

L. Chiao, "Application of Mechanistic Chemical Kinetics to Thermoset Composites Processing," *High Performance Polymers* **1–2**, 109 (1989).

L. Chiao and P. W. Borris, "Honeycomb Cure Modeling," *Soc. Advancement Mater. Proc. Eng. Quarterly* **20-1**, 9 (1988).

L. Chiao and R. G. Rinker, "A Kinetic Study of Ammonia Synthesis: Modeling High-Pressure Steady-State and Forced-Cycling Behavior," *Ch.E. Sci.* **44-1**, 9 (1988).

L. Chiao and R. G. Rinker, "The Simulated Behavior of an Autothermal Reactor Under Relaxed-Steady State Operation," *Ch.E. Comm.* **73**, 163 (1988).

L. Chiao, S. C. Darfler, and P. W. Borris, "Simulation as a Cure Process Design Tool for Aerospace Materials," *Simulation* **53-1**, 15 (1989).

R. M. Christensen, "Tensor Transformations and Failure Criteria for the Analysis of Fiber Composite Materials," *J. Comp. Mater.* **22**, 874 (1988).

R. M. Christensen, "A Two Material Constant, Nonlinear Elastic Stress Constitutive Equation Including the Effect of Compressibility," *Mech. Mater.* **7**, 155 (1988).

P. C. Clapp, J. Rivkin, J. Kenyon, and L. E. Tanner, "Molecular Dynamics Simulation of Tweed as a Precursor to a Martensitic Transformation," *Metall. Trans.* **19A**, 783 (1988).

T. T. Coburn, M. S. Oh, R. W. Crawford, and K. M. Foster, "Water Generation During Pyrolysis of Oil Shales. 1. Sources," *Energy & Fuels* **3**, 216 (1989).

R. C. Cook, "A Molecular View of Bulk Deformation," *ACS Symp. Series* **404**, 107 (1989).

R. C. Cook, "Computer Simulation of Polymeric Materials I. Stress-Strain Behavior," *J. Polym. Sci.* **26**, 1337 (1988).

R. C. Cook, "Energy Storage in Polymer Chains Under Stress," *J. Polym. Sci.* **26**, 1349 (1988).

R. C. Cook, F.-M. Kong, B. L. Haendler, L. M. Hair, and S. A. Letts, "Low-Density Polystyrene Foam Materials For Direct-Drive Laser Inertial Confinement Fusion Target," *J. Vac. Sci. Tech.* **A6**, 1894 (1988).

P. R. Coronado, E. M. Fearon, R. G. Garza, J. F. Shaw, P. C. Souers, R. K. Stump, and R. T. Tsugawa, "He$^3$ Outgassing from Four Working Palladium and Uranium Beds," *Fusion Tech.* **14**, 741 (1988).

R. W. Crawford, A. Alcaraz, and J. G. Reynolds, "Real-Time, On-Line Determination of $CO_2$ Using Charge Exchange with Krypton in a Triple Quadrupole Mass Spectrometer," *Anal. Chem.* **60**, 2439 (1988).

M. W. Crofton, C. G. Stevens, D. Klenerman, J. H. Gutow, and R. V. Zare, "Overtone Spectra of C-H Oscillators in Cold Molecules," *J. Chem. Phys.* **89**, 7100 (1988).

T. Datta, H. M. Ledbetter, C. E. Violet, C. Almasan, and J. Estrada, "Reentrant Softening in Perovskitelike Superconductors," *Phys. Rev. B* **37**, 7502 (1988).

J. J. Derby, L. J. Atherton, and P. M. Gresho, "An Integrated Process Model for the Growth of Oxide Crystals by the Czochralski Method," *J. Cryst. Growth* **97**, 792 (1989).

S. J. DeTeresa, R. S. Porter, and R. J. Farris, "Experimental Verification of a Microbuckling Model for the Axial Compressive Failure of High Performance Polymer Fibers," *J. Mater. Sci.* **23**, 1886 (1988).

S. J. DeTeresa and L. Nicolais, "The Contribution of Thermal Stresses to the Failure of Kevlar® Fabric Composites," *Polym. Comp.* **9**, 192 (1988).

J. J. DeYoreo, "Thermal Models for Granite Genesis Following Crustal Thickening," *Trans. Am. Geophys. U.* **69**, 770 (1988).

J. J. DeYoreo, D. R. Lux, C. V. Guidotti, E. R. Decker, and P. H. Osberg, "The Acadian Thermal History of Western Maine," *J. Met. Geol.* **7**, 169 (1989).

J. J. DeYoreo, D. R. Lux, and C. V. Guidotti, "A Thermal Model for Carboniferous Metamorphism Near the Sebago Batholith in Western Maine," *C.T. Jackson Commemorative Volume: Studies in Maine Geology*, D. Marvinny and M. Loiselle, Eds., Maine Geological Survey, Augusta, Maine (1989), Vol. 3, p. 1.

D. Eimerl, S. Velsko, L. Davis, F. Wang, G. Loiacono, and G. Kennedy, "Deuterated L-Arginine Phosphate: A New Efficient Nonlinear Crystal," *IEEE J. Quantum Electron.* **25**, 179 (1989).

J. W. Elmer, M. E. Kassner, and R. S. Rosen, "The Behavior of Silver-Aided Diffusion-Welded Joints under Tensile and Torsional Loads," *Welding J.* **67**, 157 (1988).

R. A. Failor, P. C. Souers, and S. G. Prussin, "Initial Radiolysis Effects on the $T_2$-$O_2$ Gas Reaction," *J. Phys. Chem.* **92**, 429 (1988).

R. A. Failor, P. C. Souers, and S. G. Prussin, "Comments on the Initial Rate of Tritiated Water Formation," *Fusion Tech.* **14**, 1136 (1988).

E. M. Fearon, R. G. Garza, C. M. Griffith, S. R. Mayhugh, E. R. Mapoles, P. C. Souers, R. T. Tsugawa, J. D. Sater, G. W. Collins, and J. R. Gaines, "Synthesis and Stability of Liquid Molecular DT," *Fusion Tech.* **14**, 864 (1988).

R. H. Fish and J. G. Reynolds, "Molecular Characterization of Non-Porphyrin Trace-Metal Compounds of Geochemical and Process Significance using High-Performance Liquid Chromatography in Combination with Element-Selective Detection," *Trends in Analytical Chemistry* **7**(5), 174 (1988).

M. J. Fluss, Y. C. Jean, P. E. A. Turchi, A. L. Wachs, and R. H. Howell, "Reply to Comment on Evidence for a Common High-Temperature Superconducting Effect in $La_{1.85}Sr_{0.15}CuO_4$ and $YBa_2Cu_3O_7$," *Phys. Rev. Lett.* **61**, 2004 (1988).

H. Fukushima, Y. Shimomura, and M. W. Guinan, "Nature and Stability of TEM Observed Defects in 14-MeV Neutron-Irradiated Au and Cu," *J. Nucl. Mater.* **155–157**, 1205 (1988).

J. R. Gaines, J. D. Sater, E. M. Fearon, P. C. Souers, F. E. McMurphy, and E. R. Mapoles, "The Ortho to Para Conversion in Solid Tritium II. Experimental Values," *Phys. Rev. B* **37**, 1482 (1988).

J. R. Gaines, P. C. Souers, E. M. Fearon, J. D. Sater, and E. R. Mapoles, "The Effects of High Atom Densities on the NMR Relaxation Times in Solid $T_2$ and DT," *Phys. Rev. B* **39**, 3943 (1989).

E. Garcia, R. R. Ryan, N. N. Suer, M. J. Fluss, L. Bernardez, Z. Fisk, and B. Pierce, "Synthesis and Superconducting Critical Temperature of $YBa_2Cu_3{}^{18}O_{7-\delta}$," *Phys. Rev. B* **38**, 2900 (1988).

A. Gonis, X.-G. Zhang, and D. M. Nicholson, "Electronic Structure Method for General Space-Filling Cell Potentials," *Phys. Rev. B* **38**, 3564 (1988).

A. Gonis, X.-G. Zhang, and D. M. Nicholson, "Multiple Scattering Green's Function Method for Space Filling Cell Potentials," *Phys. Rev. B* **40**, 947 (1989).

W. H. Gourdin, S. L. Weinland, and R. M. Boling, "Development of the Electromagnetically Launched Expanding Ring as a High-Strain-Rate Test Technique," *Rev. Sci. Instrum.* **60**, 427 (1989).

W. H. Gourdin, "Analysis and Assessment of Electromagnetic Ring Expansion as a High-Strain-Rate Test," *J. Appl. Phys.* **65**, 411 (1989).

W. H. Gourdin, "VISAR Analysis in the Presence of Large Intensity Changes: Application of the Expanding Ring," *Rev. Sci. Instrum.* **60**, 754 (1989).

R. B. Greegor, F. W. Lytle, M. J. Weber, J. Wong, and W. J. Weber, "Application of Various XAFS Techniques to the Investigation of Structurally Damaged Materials," *Physica B* **158**, 498 (1989).

M. W. Guinan, P. A. Hahn, C. E. Klabunde, and J. R. R. Coltman, "Radiation Imposed Limits on Superconducting Magnets: A Data Base for Copper Stabilizers," *J. Nucl. Mater.* **155–157**, 1315 (1988).

M. W. Guinan, "Fundamental Studies of Irradiation Effects in Fusion Materials," *MRS Bulletin* **14(7)**, 20 (1989).

J. C. Hansen and J. G. Tobin, "ARPES Studies of Surface-Alloying in Au/Cu(001)," *J. Vac. Sci. Technol.* **A7**, 2475 (1989).

J. C. Hansen, J. A. Benson, M. K. Wagner, and J. G. Tobin, "The Electronic Structure of (2x1) Au(110)," *Solid State Commun.* **69**, 1197 (1989).

J. C. Hansen, B. J. Knapp, R. de Souza-Machado, M. K. Wagner, and J. G. Tobin, "Column IB Metal Adsorption on Ge(111): the Growth Mode of Cu," *J. Vac. Sci. Technol.* **A7**, 2083 (1989).

D. R. Harshman, L. F. Schnemeyer, J. V. Waszczak, Y. C. Jean, M. J. Fluss, R. H. Howell, and A. L. Wachs, "Temperature Dependence of the Positron Annihilation Lifetime in Single-Crystal $YBa_2Cu_3O_7$," *Phys. Rev. B* **38**, 848 (1988).

G. A. Henshall, T. G. Tanaka, A. K. Miller, and T. G. Lowe, "Numerical Differentiation for Use in Integrating Unified Constitutive Equations," *Int. J. Numer. Methods Eng.* **28**, 1115 (1989).

H. Hsieh, T. D. de la Rubia, R. S. Averback, and R. Benedek, "Molecular Dynamics Studies of the Temperature Dependence of Atomic Mixing in Cascades," *Phys. Rev. B* **40**, 9986 (1989).

J. S. Huang and E. N. Kaufmann, "Nucleation, Growth, and Glass Formation in an Electron-Beam Surface-Processed $Cu_{47}Zr_{53}$ Alloy," *J. Mat. Res.* **3**, 238 (1988).

J. S. Huang, M. W. Guinan, M. A. Kirk, and P. A. Hahn, "Fusion Neutron Irradiation Induced Ordering and Defect Production in $Cu_3Au$ at High Temperatures," *J. Nucl. Mater.* **155**, 1084 (1988).

J. S. Huang, M. W. Guinan, and P. A. Hahn, "Fusion Neutron Irradiation of Ni-Si Alloys at High Temperature," *J. Nucl. Mater.* **155–157**, 1227 (1988).

J. S. Huang, G. E. Gallegos, M. P. Stratman, and E. M. Sedillo, "Deformation and Failure Mechanisms of Nb and Ta during Tensile Testing in Uranium at 1473 K," *Scripta Metall.* **23**, 103 (1989).

A. F. Jankowski, "Modeling the Supermodulus Effect in Metallic Multilayers," *J. Phys. F: Metal Physics* **18**, 413 (1988).

A. F. Jankowski, "The Strain Wave Approach to Modulus Enhancement and Stability of Metallic Multilayers," *J. Phys. Chem. Solids* **50**, 641 (1989).

A. F. Jankowski, D. M. Makowiecki, M. A. Wall, and M. A. McKernan, "Subnanometer Multilayers for X-Ray Mirror: Amorphous Crystal," *J. Appl. Phys.* **65**, 4450 (1989).

A. F. Jankowski and T. Tsakalakos, "Phase Stability by the Artificial Concentration Wave Method," *Metall. Trans.* **20A**, 357 (1989).

A. F. Jankowski, R. M. Bionta, and P. C. Gabriele, "Optimization of Internal Stresses in Fabricating Transmissive Multilayer X Ray Optics," *J. Vac. Sci. Technol.* **7A**, 210 (1989).

Y. C. Jean, J. Kyle, H. Nakanishi, P. E. A. Turchi, R. H. Howell, A. L. Wachs, M. J. Fluss, R. L. Meng, H. P. Hor, J. Z. Huang, and C. W. Chu, "Evidence for a Common High Temperature Superconducting Mechanism in $La_{1.85}Sr_{0.15}Cu0_4$ and $YBa_2Cu_3O_7$," *Phys. Rev. Lett.* **60**, 1069 (1988).

Y. C. Jean, H. Nakanishi, M. J. Fluss, A. L. Wachs, P. E. A. Turchi, R. H. Howell, Z. Z. Wang, R. L. Meng, P. H. Hor, Z. J. Huang, and C. W. Chu, "A Comparison of the Temperature Dependence of Electron-Positron Momentum Density Characteristics in Tc (2223), Y(123), and La(214) Superconductors," *J. Phys.: Condensed Matter* **1**, 2696 (1989).

M. E. Kassner and J. J. Oldani, "Large-Strain Steady-State Deformation of Silver at Ambient and Near Ambient Temperature," *Scripta Metall.* **22**, 41 (1988).

M. E. Kassner, H. J. McQueen, and M. M. Myshlyaev, "Large-Strain Torsional Deformation of Aluminum at Elevated Temperature," *Mater. Sci. Eng.* **108**, 45 (1989).

M. E. Kassner and D. E. Peterson, "The Al-Np (Aluminum-Neptunium) System," *Bull. Alloy Phase Diagrams* **10**, 111–112 (1989).

M. E. Kassner, "Large-Strain Deformation of Aluminum Single Crystals at Elevated Temperature A Critical Test for Geometric-Dynamic-Recrystallization," *Metall. Trans.* **20A**, 2182 (1989).

M. E. Kassner, "The Rate-Dependence and Microstructure of High-Purity Silver Deformed to Large Strains between 0.16 and 0.30 Tm," *Metall. Trans.* **20A**, 2001 (1989).

M. E. Kassner and D. E. Petersen, "The Al-Am (Aluminum-Americium) System," *Bull. Alloy Phase Diagrams* **10**, 277 (1989).

M. E. Kassner, P. H. Adler, M. G. Adamson, and D. E. Peterson, "Evaluation and Thermodynamic Analysis of Phase Equilibria in the U-Al System," *J. Nucl. Mater.* **167**, 160 (1989).

M. E. Kassner and D. E. Peterson, "The Pu-Al (Plutonium-Aluminum) System," *Bull. Alloy Phase Diagrams* **10**, 459 (1989).

M. E. Kassner and D. E. Peterson, "The Al-Th (Aluminum-Thorium) System," *Bull. Alloy Phase Diagrams* **10**, 466 (1989).

N. K. Kim, K. Kim, D. A. Payne, and R. S. Upadhye, "Fabrication of Hollow Silica Aerogel Spheres by a Droplet Generation Method and Sol-gel Processing," *J. Vac. Sci. Technol.* **A7**, 1181 (1989).

J. H. Kinney, Q. C. Johnson, R. A. Saroyan, U. Bonse, R. Nusshardt, R. Pahl, M. C. Nichols, and J. Brase, "Tomography in Materials Science," *Mater. Res. Soc. Bull.* **13**, 13 (1988).

J. H. Kinney, Q. C. Johnson, R. A. Saroyan, U. Bonse, R. Nusshardt, and M. C. Nichols, "Energy-Modulated X-Ray Microtomography," *Rev. Sci. Instrum.* **59**, 196 (1988).

J. H. Kinney, M. C. Nichols, U. Bonse, Q. C. Johnson, R. A. Saroyan, and R. Nusshardt, "Synchrotron Microtomography on Beam Line X-2 at SSRL," *Rev. Sci. Instrum.* **60**, 2478 (1989).

B. J. Knapp and J. G. Tobin, "KRIPES Investigations of Au and Ag on Ge(111)," *J. Vac. Sci. Technol.* **A6**, 772 (1988).

B. J. Knapp and J. G. Tobin, "The Unoccupied Electronic Structure of Au and Ag on Ge(111)," *Phys. Rev. B* **37**, 8656 (1988).

B. J. Knapp, J. C. Hansen, M. K. Wagner, W. D. Clendening, and J. G. Tobin, "Occupied Electronic Structure of Au and Ag on Ge(111)," *Phys. Rev. B* **40**, 2814 (1989).

O. H. Krikorian and P. G. Curtis, "Synthesis of CeS and Interactions with Molten Metals," *High Temp.-High Press.* **20**, 9 (1988).

O. H. Krikorian, "Thermal Expansivity Correlations for Refractory Materials with the Na Cl-Type Structure," *High Temp.-High Press.* **20**, 169 (1988).

O. H. Krikorian, "Solubilities and Diffusivities of $H_2O$ and $H_2$ in $Li_2O$," *High Temp.-High Press.* **20**, 183 (1988).

J. D. LeMay, "Low-Density Foams from Macroporous Epoxy Gels," *Polym. Mater.* **60**, 695 (1989).

S. A. Letts, S. R. Buckley, C. Chen, A. R. Cook, B. L. Haendler, L. M. Hair, E.-M. Kong, S. C. Mance, G. E. Overturf, and J. C. Thomas, "Characterization of Low-Density Foam Materials for Direct-Drive Laser Inertial Confinement Fusion Targets," *J. Vac. Sci. Technol.* **A6**, 1896 (1988).

J. L. Maienschein, F. E. McMurphy, and V. L. DuVal, "Increase of Tritium Permeation Through Resistant Metals at 323 K by Lattice Defects," *Fusion Tech.* **14**, 701 (1988).

J. L. Maienschein, F. E. McMurphy, and F. S. Uribe, "Tritium Storage in Ion-Exchanged Zeolites," *Fusion Tech.* **14**, 775 (1988).

J. L. Maienschein and J. A. Emig, "Compatibility of Cyanoacrylate Glue with Li(D,T)," *J. Nucl. Mater.* **158**, 283 (1988).

R. Mathew, L. Paduano, J. G. Albright, D. G. Miller, and J. A. Rard, "Isothermal Diffusion Coefficients for NaCl-$MgCl_2$-$H_2O$ at 25°C. 3. Low $MgCl_2$ Concentrations with a Wide Range of NaCl Concentrations," *J. Phys. Chem.* **93**, 4370 (1989).

H. Matsui, H. Shimidzu, S. Takehana, and M. W. Guinan, "Radiation Softening of High Purity Iron by 14 MeV Neutrons," *J. Nucl. Mater.* **155–157**, 1169 (1988).

H. Matsui, S. Takehana, and M. W. Guinan, "Resistivity Recovery in High Purity Iron After Fission- and Fusion-Neutron Irradiation," *J. Nucl. Mater.* **155–157**, 1284 (1988).

D. G. Miller, A. W. Ting, and J. A. Rard, "Mutual Diffusion Coefficients of Various $ZnCl_2$(0.5 m)-KCl-$H_2O$ Mixtures at 298.15°K by Rayleigh Interferometry," *J. Electrochem. Soc.* **135**, 896 (1988).

D. G. Miller, "A Method for Obtaining Multicomponent Diffusion Coefficients Directly from Rayleigh and Gouy Fringe Positions," *J. Phys. Chem.* **92**, 4222 (1988).

R. G. Musket, L. M. Thomas, and J. G. Wilder, "Enhanced Adhesion at Oxide/Oxide Interfaces by Ion Beam Stitching," *Appl. Phys. Lett.* **52**, 410 (1988).

R. G. Musket, C. W. Price, and J. C. Norberg, "Implanted Standards for Ion Microanalysis of Oxygen in Beryllium," *Nucl. Instrum. Meth. Phys. Res.* **B42**, 245 (1989).

R. G. Musket, "Cleaning Surfaces of Sintered Beryllium Oxide," *Appl. Surface Sci.* **37**, 55 (1989).

R. G. Musket, "Applications of Ion Implantation for Modifying the Interactions between Metals and Hydrogen Gas," *Nucl. Instrum. Meth.* **B40/41**, 591 (1989).

A. Nichols and D. Calef, "Polar Solvent Relaxation: The Mean Spherical Approximation Method," *J. Chem. Phys.* **89**, 3783 (1988).

M. C. Nichols, J. H. Kinney, Q. C. Johnson, U. Bonse, R. A. Saroyan, and R. Nusshardt, "Synchrotron Microtomography of Supported Catalysts," *Rev. Sci. Instrum.* **60**, 2475 (1989).

W. Nixon, J. Mitchell, and S. Lederman, "Solute Pairing in fcc Binary and Ternary Cu Alloys," *Physica B* **158**, 25 (1989).

M. S. Oh, R. W. Taylor, T. T. Coburn, and R. W. Crawford, "Ammonia Evolution During Oil Shale Pyrolysis," *Energy & Fuels* **2**, 100 (1988).

K. C. Ott, R. M. Aikin, L. Bernardez, A. Connor, Z. Fisk, M. J. Fluss, E. Garcia, M. Goldblatt, W. B. Hutchinson, G. H. Kwei, C. J. Maggiore, J. A. Martin, R. Meisenheimer, M. Nastasi, E. J. Peterson, E. J. Tesmer, J. D. Thompson, T. E. Walker, J. O. Willis, and P. J. Yvon, "Oxygen Isotope Effects in Yttrium Barium Copper Oxides," *Phys. Rev. B* **39**, 4283 (1989).

L. Paduano, R. Mathew, J. G. Albright, D. G. Miller, and J. A. Rard, "Isothermal Diffusion Coefficients for NaCl-$MgCl_2$-$H_2O$ at 25°C. 2. Low Concentrations of NaCl with a Wide Range of $MgCl_2$ Concentrations," *J. Phys. Chem.* **93**, 4366 (1989).

S. Pei, T. B. Massalski, W. M. Temmerman, P. A. Sterne, and G. M. Stocks, "Phase Stabilities of the $Co_3Ti$ and $Ni_3V$ Alloys," *Phys. Rev. B* **39**, 5767 (1989).

R. W. Pekala and R. E. Stone, "Low-Density Resorcinol-Formaldehyde Foams," *Polym. Preprints* **29**, 204 (1988).

R. W. Pekala and F.-M. Kong, "Resorcinol-Formaldehyde Aerogels and Their Carbonized Derivatives," *Polym. Preprints* **30**, 221 (1989).

R. W. Pekala and F.-M. Kong, "A Synthetic Route to Organic Aerogels—Mechanism, Structure, and Properties," *J. Phys. (Paris)* **Colloque C4**, 33 (1989).

C. T. Peng, R. L. Hua, P. C. Souers, and P. R. Coronado, "Tritium Labeling of Amino Acids and Peptides with Liquid and Solid Tritium," *Fusion Tech.* **14**, 833 (1988).

J. L. Peng, P. Klavins, R. N. Shelton, H. B. Radousky, P. A. Hahn, L. Bernardez, and M. Costantino, "Preparation, Characterization, and Superconducting Properties of Tetragonal $LaBaCaCu_3O_{7+d}$," *Phys. Rev. B* **39**, 9074 (1989).

D. A. Peterson and M. E. Kassner, "The Pu-Ga (Plutonium-Gallium) System," *Bull. Alloy Phase Diagrams* **9**, 261 (1988).

C. W. Price and P. L. McCarthy, "Low-Voltage Scanning Electron Microscopy of Low-Density Materials," *Scanning* **10**, 29 (1988).

K. J. Rao and J. Wong, "L-edge EXAFS Study of Pb Coordination in PbO-$PbF_2$ Glasses," *J. Chem. Soc. Fara. Trans.* **84**, 1773 (1988).

K. J. Rao and J. Wong, "Investigation of Pb Coordination in PbO-$PbF_2$ Glasses by XANES," *J. Chem. Soc. Fara. Trans.* **84**, 1779 (1988).

J. A. Rard and D. G. Miller, "Ternary Mutual Diffusion Coefficients of NaCl-$SrCl_2$-$H_2O$ at 25°C. 2. Total Concentrations of 2.0 and 3.0 mol-$dm^{-3}$," *J. Phys. Chem.* **92**, 6133 (1988).

J. A. Rard and D. G. Miller, "Isopiestic Determination of the Osmotic and Activity Coefficients of $ZnCl_2$(aq) at 298.15°K," *J. Chem. Thermo.* **21**, 482 (1989).

J. G. Reynolds and W. R. Biggs, "Application of Size Exclusion Chromatography Coupled with Element-Specific Detection to the Study of Heavy Crude Oil and Residua Processing," *Accounts Chem. Res.* **21**, 319 (1988).

J. G. Reynolds and S. Beret, "Effect of Prehydrogenation on Hydroconversion of Maya Residuum. 1. Process Characterization," *Fuel Science Technol. Intern.* **7**(2), 165 (1989).

J. G. Reynolds and R. W. Crawford, "Pyrolysis of Sunnyside (Utah) Tar Sand: Characterization of Volatile Compound Evolution II," *Fuel Science Technol. Intern.* **7**(5–6), 823 (1989).

J. G. Reynolds, E. L. Jones, J. A. Bennett, and W. R. Biggs, "Characterization of Nickel and Vanadium Compounds in Tar Sand Bitumen by UV-vis Spectroscopy and Size Exclusion Chromatography Coupled with Element Specific Detection," *Fuel Science Technol. Intern.* **7**(5–6), 625 (1989).

S. F. Rice, "The $A'^2\Delta$ State of ScO: Analysis of the $A'^2\Delta(v = 3) \sim A^2\Pi(v = 1)$ Perturbation," *J. Mol. Spectrosc.* **133**, 22 (1989).

S. F. Rice and M. S. Costantino, "Single Pulse Broad Band CARS of Nitromethane within a Diamond Anvil Cell," *J. Phys. Chem.* **93**, 536 (1989).

J. Roe and T. Hirschfeld, "Fiber Optic Hydrogen Sulfide Detection," *J. Optoelectronics* **3**, 289 (1988).

T. D. de la Rubia, R. S. Averback, H. Hsieh, and R. Benedek, "Molecular Dynamics Simulation of Displacement Cascades in Cu and Ni: Thermal Spike Behavior," *J. Mater. Res.* **4**, 579 (1989).

M. L. Sattler and P. N. Ross, "The Corrosion of Carbon Black Anodes in Alkaline Electrolyte: III. The Effect of Graphitization on the Corrosion Resistance of Furnace Blacks," *J. Electrochem. Soc.* **135**, 1464 (1988).

G. H. Schadler, A. M. Boring, P. Weinberger, and A. Gonis, "Electronic Structure of Stoichiometric and Off-Stoichiometric $TaC_{0.72}$," *Phys. Rev. B* **38**, 5932 (1988).

W. S. Selig, "The Use of Graphite Electrodes in Potentiometric Titrations," *Synth. Mater.* **23**, 503 (1988).

W. S. Selig, "Sequential Titrations of Anions with Cetylpyridinium Chloride," *Z. Anal. Chem.* **330**, 127 (1988).

W. S. Selig, "Potentiometric Microdetermination of Potassium, Rubidium, and Cesium with Tetraphenylborate without Separation of Precipitate," *Microchem. J.* **37**, 141 (1988).

W. J. Selig, "Preliminary Results on a New Potentiometric Method for the Estimation of the Rare Earth Elements. Comments on Other Ions Titratable with Sodium Tetraphenylborate," *Microchem. J.* **37**, 155 (1988).

W. S. Selig, "Final Analysis," *Plating Surf. Fin.* **75**, 10 (1988).

W. S. Selig, "Potentiometric Estimation of Aurocyanide and Molybdate in Mixtures," *Microchem. J.* **38**, 276 (1988).

W. S. Selig, "The Potentiometric Titration of Aluminum and Gallium with Tetraphenylborate," *Fresenius' Z. Anal. Chem.* **332**, 369 (1988).

W. S. Selig, "Potentiometric Titration of Potassium Aurocyanide with Mercuric Ions," *Microchem. J.* **38**, 332 (1988).

W. S. Selig, "Potentiometric Titration and Differentiation of Cyano and Nitrito Complexes of Ir(III), Pt(II), and Pd(II)," *Fresenius' Z. Anal. Chem.* **332**, 795 (1988).

W. S. Selig, "Comments on the Microdetermination of Molybdenum in the Presence of Gold after Conversion to Molybdate," *Microchem. J.* **39**, 133 (1989).

S. M. Shapiro, B. X. Yang, G. Shirane, Y. Noda, and L. E. Tanner, "Neutron Scattering Studies of the Martensitic Transformation in a Ni-Al Beta-phase Alloy," *Phys. Rev. Lett.* **62**, 1298 (1989).

Y. Shimomura, M. W. Guinan, H. Fukushima, P. A. Hahn, and M. Kiritani, "20K Cryo-Transfer TEM Observation of Nascent Displacement Cascade Damage in Low Temperature D-T Neutron-Irradiated Metals at RTNS-II," *J. Nucl. Mater.* **155–157**, 1181 (1988).

A. Silberstein, P. C. Clapp, and L. E. Tanner, "Computer Simulation of Defect-Induced Vitrification," *J. Less-Common Metals* **140**, 245 (1988).

M. F. Singleton, J. F. Cooper, B. D. Andresen, and E. P. Milanovich, "Laser-Induced Bulk Damage in Potassium Dihydrogen Phosphate Crystal," *Appl. Phys. Lett.* **52**, 857 (1988).

M. Sluiter, P. Turchi, F. Zezhong, and D. de Fontaine, "Re-examination of BCC Based Phase Diagrams with Constant First and Second Neighbor Pair Interactions in the Cluster Variation Method," *Physica* **148A**, 61 (1988).

M. Sluiter, P. Turchi, F. Zezhong, and D. de Fontaine, "Tight-Binding Calculation of Ti-Rh-Type Phase Diagram," *Phys. Rev. Lett.* **60**, 716 (1988).

P. C. Souers, E. M. Fearon, E. R. Mapoles, J. D. Sater, G. W. Collins, J. R. Gaines, R. H. Sherman, and J. R. Bartlit, "Triton Memory Time in Solid DT and its Nuclear Polarization," *Fusion Tech.* **14**, 855 (1988).

P. C. Souers, E. M. Fearon, R. K. Stump, and R. T. Tsugawa, "Infrared Analysis of Liquid and Solid D-T," *Fusion Tech.* **14**, 850 (1988).

P. C. Souers, E. J. Ackerman, T. J. Biel, J. Bigwood, V. Brite, L. D. Christensen, C. L. Folkers, V. Gede, C. M. Griffith, E. B. Huss, R. Lindahl, T. McCreary, H. H. Otsuki, R. L. Pond, G. D. Snider, C. Stanhope, R. K. Stump, F. Vanderhoofven, R. T. Tsugawa, J. L. Anderson, D. H. W. Cartens, W. L. Drumhiller, W. B. Lewis, J. E. Nasise, F. E. Pretzel, E. G. Szklarz, D. T. Vier, J. R. C. Bowman, and A. Attalla, "Swelling and Outgassing of Heavily Irradiated Lithium Hydride," *J. Nucl. Mater.* **154**, 308 (1988).

E. C. Sowa, A. Gonis, X.-G. Zhang, and S. M. Foiles, "Electronic Structure of Grain Boundaries," *Phys. Rev. B* **40**, 9993 (1989).

W. Speier, J. C. Fuggle, P. J. Durham, R. Zeller, R. J. Blake, and P. A. Sterne, "Matrix Elements in Inverse X-Ray Photoemission (BIS)," *J. Phys. C: Solid State Phys.* **21**, 2621 (1988).

P. A. Sterne and C. S. Wang, "Dynamical Correlation Corrections to Band Edge Discontinuities in Si/GaP Superlattices," *Phys. Rev. B* **37**, 10436 (1988).

P. A. Sterne and C. S. Wang, "Oxygen Vacancies and Antiferromagnetism in $La_2CuO_4$," *Phys. Rev. B* **37**, 7472 (1988).

P. A. Sterne and C. S. Wang, "Higher $T_c$ Through Metallic Interlayer Coupling in $Bi_2Sr_2CaCu_2O_8$," *J. Phys C: Solid State Phys.* **21**, 949 (1988).

G. M. Stocks, W. M. Temmerman, Z. Szotek, and P. A. Sterne, "Density Functional Theory, Total Energies and Equilibrium Volumes of $La_2CuO_4$ and $La_{1.5}Sr_{0.5}CuO_4$," *Supercond. Sci Technol.* **1**, 57 (1988).

M. J. Strum, "Hot Cracking in Directed-Energy Surface Processing," *MRS Bull.* **13**, 33 (1988).

M. J. Strum, L. T. Summers, and J. R. Miller, "Ductility Enhancement in Unreacted Internal-Sn $Nb_3Sn$ Through Low-Temperature Anneals," *IEEE Trans. Magnetics* **25**(2), 2208 (1989).

P. Sundararaman, W. R. Biggs, J. G. Reynnolds, and J. C. Fetzer, "Vanadylporphyrins, Indicators of Kerogen Breakdown and Generation of Petroleum," *Geochim. Cosmochim. Acta* **52**, 2337 (1988).

Y. Tomota, M. J. Strum, and J. W. Morris, "Tensile Deformation Behavior of Mechanically Stabilized Fe-Mn Austenite," *Metall. Trans. A* **19**, 1563 (1988).

P. E. A. Turchi, G. M. Stocks, W. H. Butler, D. M. Nicholson, and A. Gonis, "First Principles Study of Ordering Properties of Substitutional Alloys Using the Generalized Perturbation Method," *Phys. Rev. B* **37**, 5982 (1988).

P. E. A. Turchi, A. L. Wachs, Y. C. Jean, R. H. Howell, K. H. Wetzler, and M. J. Fluss, "Positron Annihilation in Perovskite Superconductors: Theory and Experiment," *Physica* **C153–155**, 157 (1988).

R. S. Upadhye, M. K. Kong, and E. J. Hsieh, "Analysis of Sputter Coating Uniformity by Computer Modeling," *J. Vac. Sci. Technol.* **A6**(3), 1891 (1988).

A. L. Wachs, P. E. A. Turchi, Y. C. Jean, K. H. Wetzler, R. H. Howell, M. J. Fluss, D. R. Harshman, J. P. Remeika, A. S. Cooper, and R. M. Fleming, "Electronic Structure Studies of $La_2CuO_4$," *Phys. Rev.* **B38**, 913 (1988).

A. L. Wachs, P. E. A. Turchi, R. H. Howell, Y. C. Jean, M. J. Fluss, J. H. Kaiser, R. N. West, K. L. Merkle, and A. Revcolevschi, "Positron-Annihilation Studies of the Electronic Structure of NiO," *Phys. Rev.* **B40**, 1 (1989).

C. S. Wang, P. A. Sterne, P. G. McQueen, and A. Bhattacharya, "Magnetic Interactions in High-$T_c$ Superconductors," *J. de Physique* **49**, 2243 (1988).

M. J. Weber, "Faraday Rotator Materials for Lasers," *J. Appl. Phys.* **63**, 3118 (1988).

P. Weinberger, R. Dirl, A. M. Boring, A. Gonis, and A. J. Freeman, "Fully Relativistic KKR-CPA Embedded Cluster Method Evaluation of Short-Range Order Effects in Substitutional Alloys Containing Heavy Elements," *Phys. Rev. B* **37**, 1383 (1988).

G. O. Williams, T. D. de la Rubia, J. W. Corbett, N. Cue, and J. F. Ziegler, "Fractal Dimension of Ion Cascades in Matter," *Rad. Effects Express* **1**, 175 (1988).

S. W. Wilson, R. J. Borree, D. L. Chambers, Y. Chang, J. T. Merrill, P. C. Souers, and R. K. Wiggins, "A New Box System for a High Pressure Tritium Pump," *Fusion Tech.* **14**, 1005 (1988).

J. Wong and G. A. Slack, "Metals in Beta-Rhombohedral," *Physica B* **158**, 627 (1989).

E. Worden, J. Blaise, and J. G. Conway, "Revisions and Additions to the Energy Levels of Neutral Curium ($^{244}$Cm I)," *J. Opt. Soc. Am.* **B5**, 2093 (1988).

A. C. Wright, A. G. Clare, G. Etherington, M. J. Weber, S. A. Brawer, and R. N. Sinclair, "A Neutron Diffraction and Molecular Dynamics Investigation of the Structure of Vitreous Beryllium Fluoride," *J. Non-Cryst. Solids* **111**, 139 (1989).

A. Zettl and J. H. Kinney, "$O^{18}$ in $YBa_2Cu_3O_{7-x}$: Where Does the Oxygen Go?" *Phys. Rev. Lett.* **60**, 753 (1988).

X.-G. Zhang and A. Gonis, "New, Real Space Multiple Scattering Theory Method for the Determination of Electronic Structure," *Phys. Rev. Lett.* **62**, 1161 (1989).

X.-G. Zhang, A. Gonis, and J. M. MacLaren, "Real-Space Multiple Scattering Theory and the Electronic Structure of Systems with Full or Reduced Symmetry," *Phys. Rev. B* **40**, 3694 (1989).

X.-G. Zhang and A. Gonis, "The Secular Equation of Korringa, Kohn and Rostoker for the Case of Non-Muffin Tin, Space-Filling Potential Cells," *Phys. Rev. B* **39**, 10373 (1989).

## Conference Proceedings

M. Balooch, D. R. Olander, W. J. Siekhaus, and D. E. Miller, "The Kinetics of Molybdenum Etching by Atomic and Molecular Chlorine," in *Tungsten and Other Refractory Metals for VLSI Applications V, Mater. Res. Soc. Proc.*, C. M. McConica and R. S. Blewer, Eds., Materials Research Society, Pittsburgh, Pa. (1988).

R. M. Bionta, A. F. Jankowski, and D. M. Makowiecki, "Creation and Characterization of Transmissive Multilayer Optics for 8 keV X Rays," in *Multilayers: Synthesis, Properties and Nonelectronic Applications, Mater. Res. Soc. Symp. Proc. Vol. 103*, T. W. Barbee, Jr., F. Spaepen, and A. L. Greer, Eds., Materials Research Society, Pittsburgh, Pa. (1988), p. 257.

R. Bionta, E. Ables, K. Cook, O. Edwards, P. Gabriele, A. F. Jankowski, D. Makowiecki, L. Ott, and N. Thomas, "Sputtered-Sliced Multilayers: Zone Plates and Transmission Gratings for 8 keV X Rays," in *SPIE Conf. Proc. Vol. 984*, SPIE, Bellingham, Wash. (1988), p. 247.

R. M. Brusasco, J. A. Britten, C. B. Thorsness, M. S. Scrivener, W. G. Unites, J. H. Campbell, and W. L. Johnson, "A High-Temperature, Plasma-Assisted Chemical Vapor Deposition System," in *Symp. Optical Materials for High Power Lasers* (1989).

A. K. Burnham, R. L. Braun, R. W. Taylor, and T. T. Coburn, "Comparison of Isothermal and Nonisothermal Pyrolysis Data with Various Rate Mechanisms: Implications for Kerogen Structure," in *ACS Preprints*, American Chemical Society, Washington, D.C. (1989), p. 36.

D. W. Camp and R. G.Mallon, "LLNL Mild Coal Gasification Review," in *8th Annual Gasification and Gas-Stream Cleanup Systems Contractors Review Meeting*, V. P. Kothari and J. R. Longabach, Eds., U.S. Department of Energy, Morgantown Energy Technology Center, Morgantown, W. Va. (1988), p. 600.

D. W. Camp, "Enthalpy Relations for Eastern Shales," in *Proc. 1987 Eastern Oil Shale Symposium*, Kentucky Energy Cabinet Laboratory, Lexington, Ky. (1988), p. 353.

D. W. Camp and R. G. Mallon, "Mild Coal Gasification—Development of a Screw Pyrolyzer," in *9th Annual Gasification and Gas Stream Cleanup Systems Contractors Review Mtg.*, U.S. Department of Energy, Morgantown Energy Technology Center, Morgantown, W. Va. (1989).

R. J. Cena, T. T. Coburn, and R. W. Taylor, "LLNL Oil Shale Project Review," in *Third Annual Oil Shale, Tar Sands and Mild Coal Gasification Contractors Review Meeting*, T. C. Bartke, Ed., U.S. Department of Energy, Morgantown Energy Technology Center, Morgantown, W. Va. (1988), pp. 57, 79.

J. Chaudhuri, S. Shah, and A. F. Jankowski, "X Ray Diffraction Analysis of Au/Ni Multilayers," in *Multicomponent Ultrafine Microstructures, Mater. Res. Soc. Symp. Proc. Vol. 132*, D. E. Polk, R. W. Siegel, and B. H. Kear, Eds., Materials Research Society, Pittsbugh, Pa. (1989), p. 231.

T. T. Coburn, R. W. Taylor, C. J. Morris, and V. DuVal, "Isothermal Pyrolysis and Char Combustion of Oil Shales," in *Intern. Conf. Oil Shale and Shale Oil*, Z. Yajie, Ed., Chemical Industry Press, Beijing, China (1988), p. 245.

B. Comaskey, J. G. Conway, C. Haynam, J. Stockdale, and E. Worden, "Branching Ratios of Cerium with the Kitt Peak I-m Fourier Transform Spectroscopy," in *High Resolution Fourier Transform Spectroscopy*, R. Engleman, Jr., Ed., Optical Society of America, Washington, D.C. (1989), p. 38.

R. C. Cook, "A Molecular View of Bulk Deformation," in *Proc. ACS Division of Polymeric Materials*, T. Provder, Ed., American Chemical Society, Washington, D.C. (1988), p. 498.

T. Datta, C. Almasan, J. Estrada, C. E. Violet, D. U. Gubser, and S. A. Wolf, "Magnetic Behavior of Y-Ba-Cu-O Superconductors Prepared Under Different Oxygen Anneals," in *Proc. 32nd Ann. Conf. Magnetism and Magnetic Materials, Chicago, Ill., 1988*, p. 4204.

J. J. DeYoreo, D. R. Lux, and C. V. Guidotti, "The Role of Crustal Anatexis and Magma Migration in Regions of Thickened Continental Crust," in *Geol. Soc. Spec. Pub. No. 43*, J. S. Daly, R. A. Cliff, and B. W. D. Yardley, Eds., Blackwell Scientific Publications, Oxford, U.K. (1988), p. 187.

M. W. Droege, L. M. Hair, W. J. Pitz, and C. K. Westbrook, "Partial Oxidation Reactions of Methane and Oxygen," in *Proc. 1989 SPE Gas Technology Symp.*, Society of Petroleum Engineers, Dallas, Tex. (1989), p. 247.

D. F. Edwards, P. P. Hed, and J. E. Marion, "Subsurface Damage Produced during the Processing of Glass," in *Proc. Glasses for Optoelectronics* (1989).

J. W. Elmer, S. M. Allen, and T. W. Eagar, "The Influence of Cooling Rate on the Ferrite Content of Stainless Steel Alloys," in *Recent Trends in Welding Science and Technology*, S. A. Davis and J. M. Vitek, Eds., American Society for Metals, Metals Park, Ohio (1990).

J. C. Farmer and R. D. McCright, "Localized Corrosion and Stress Corrosion Cracking of Candidate Materials for High-Level Radioactive Waste Disposal Containers in the USA: A Critical Literature Review," in *Scientific Basis for Nuclear Waste Management XII, Mater. Res. Soc. Symp. Proc. Vol. 127*, W. Lutze and R. Ewing, Eds., Materials Research Society, Pittsburgh, Pa. (1988), p. 359.

M. J. Fluss, A. L. Wachs, P. E. A. Turchi, R. H. Howell, Y. C. Jean, J. Kyle, H. Hakanishi, C. W. Chu, R. L. Meng, H. P. Hor, and J. Z. Huang, "Probing the Electronic and Defect Structure of Perovskite Superconductors," in *World Congress on Superconductivity*, C. G. Burnham and R. D. Kane, Eds., World Scientific, Singapore (1988), p. 357.

P. C. Gabriele, R. M. Bionta, and A. F. Jankowski, "Cylindrical X-Ray Multilayer Monochromator," in *SPIE Conf. Proc. Vol. 1160*, SPIE, Bellingham, Wash. (1989), p. 122.

A. Gonis, P. E. A. Turchi, X.-G. Zhang, G. M. Stocks, D. M. Nicholson, and W. H. Butler, "Concentration Dependent Effective Cluster Interactions in Substitutional Alloys," in *Proc. Conf. World Materials Congress, Atomistic Simulation of Materials*, V. Vitek and D. T. Srolovitz, Eds., Plenum Publishing Co., New York, N.Y. (1989), p. 15.

B. L. Haendler, L. M. Hair, and F.-M. Kong, "The Application of Statistical Experimental Design to the Development of Low-Density Polymer Foams," in *Computer Applications in Applied Polymer Science II: Automation, Modeling and Simulation*, T. Provder, Ed., American Chemical Society, Washington, D.C. (1989), p. 74.

W. G. Halsey, J. C. Farmer, R. D. McCright, R. A. Van Konynenburg, and D. B. Bullen, "Localized Corrosion and Stress Corrosion Cracking of Austenitic Candidate Materials for High-Level Radioactive Waste Disposal Containers: Analysis of Data," in *174th Mtg. Electrochemical Society*, Chicago, Ill. (1988), p. 212.

G. A. Henshall and A. K. Miller, "Physically-Based Constitutive Equations for Creep and Plasticity: Cyclic Deformation," in *Proc. Materials '88: Materials and Engineering Design B*, F. Dyson, Ed., The Institute of Metals, London, U.K. (1988), p. 41.

R. Hiskes and A. M. Karo, "Dissociative Recombination of $H_2^+$ and $H_3^+$ Ions on Surfaces," in *Intern. Symp. Dissociative Recombination: Theory, Experiment, and Applications*, B. A. Mitchell, Jr., and S. Guberman, Eds., World Scientific, Teaneck, N.J. (1988), p. 204.

D. M. Hoffman, F. M. Matthews, and C. O. Pruneda, "Dynamic Mechanical and Thermal Analysis of Crystallinity Development in Kel-F 800 and TATB/Kel-F 800 Plastic Bonded Explosives. Pt. 1. Kel-F 800," in *Proc. 17th Conf. North American Thermal Analysis Soc.* (1988), p. 172.

D. M. Hoffman, F. M. Matthews, M. O. Riley, and C. M. Walkup, "Anelastic and Thermal Properties of Ethylene/Acrylic Acid Copolymers Partially Ionized with Transition Metals," in *ACS Polymer Preprints*, American Chemical Society, Washington, D.C. (1988), p. 455.

L. W. Hrubesh and C. T. Alviso, "Optical Characterization of Silica Aerogel," in *Mater. Res. Soc. Symp. Proc.*, Materials Research Society, Pittsburgh, Pa. (1988), p. 703.

L. W. Hrubesh, R. Staffin, D. B. Boercker, and T. Wainright, "Studies of Polymer Foam Morphology with FIR Laser Scattering," in *Proc. 4th Intern. Conf. Infrared Physics* (1988).

J. S. Huang, E. N. Kaufmann, M. A. Wall, and B. L. Olsen, "Crystallization and Glass Formation in Electron and Laser Beam Irradiated Cu-Zr Alloys," in *Fundamentals of Beam-Solid Interactions and Transient Thermal Processing*, M. J. Aziz, L. E. Rehn, and B. Stritzker, Eds., Materials Research Society, Pittsburgh, Pa. (1988), p. 589.

J. S. Huang, R. G. Musket, and M. A. Wall, "Phases and Microstructures of Carbon-Implanted Niobium," in *Processing and Characterization of Materials Using Ion Beams*, L. E. Rehn, J. Greene, and F. A. Smidt, Eds., Materials Research Society, Pittsburgh, Pa. (1989), p. 327.

J. S. Huang and E. N. Kaufmann, "Directed-Energy Electron-Beam Processing of a Hypereutectic $Cr_{90}Ta_{10}$ Alloy," in *Solidification Processing of Eutectic Alloys*, D. M. Stefanescu, G. J. Abbaschian, and R. J. Bayuzick, Eds., The Metallurgical Society, Inc., Warrendale, Pa. (1988), p. 243.

A. F. Jankowski, D. M. Makowiecki, M. McKernan, S. Nutt, and K. Green, "Exploring the Relation Between Interface Structure and Mechanical Properties in Multilayer Structures," in *Multilayers: Synthesis, Properties and Nonelectronic Applications*, T. W. Barbee, Jr., F. Spaepen, and A. L. Greer, Eds., Materials Research Society, Pittsburgh, Pa. (1988), p. 327.

A. F. Jankowski and D. M. Makowiecki, "Manufacture, Structure and Performance of W/B4C Multilayer Mirrors," in *SPIE Conf. Proc., Vol. 984*, SPIE, Bellingham, Wash. (1988), p. 64.

A. F. Jankowski, "W/C Mirror Deposition Optimization," in *SPIE Conf. Proc., Vol. 1160*, SPIE, Bellingham, Wash. (1989), p. 297.

A. F. Jankowski, "Coherency Strain Modeling of Elastic Moduli in Cu/Nb Multilayers," in *Atomic Scale Calculations in Materials Science, Mater. Res. Soc. Symp. Proc. Vol. 141*, J. Tersoff, D. Vanderbilt, and V. Vitek, Eds., Materials Research Society, Pittsburgh, Pa. (1989), p. 147.

Y. C. Jean, H. Nakanishi, P. E. A. Turchi, R. H. Howell, A. L. Wachs, M. J. Fluss, R. L. Meng, P. H. Hor, Z. J. Huang, and C. W. Chu, "Defect Properties of High Temperature Superconductors Probed by Positrons," in *Mater. Res. Soc. Symp. Proc.*, Materials Research Society, Pittsburgh, Pa. (1988), p. 137.

Y. C. Jean, H. Nakanishi, J. Kyle, M. J. Fluss, A. L. Wachs, P. E. A. Turchi, R. H. Howell, R. L. Meng, P. H. Hor, J. Z. Huang, and C. W. Chu, "Positron Annihilation Spectroscopy in High-$T_c$ Superconductors," in *Mater. Res. Soc. Symp. Proc.*, D. W. Capone, II, W. H. Butler, B. Batlogg, and C. W. Chu, Eds., Materials Research Society, Pittsburgh, Pa. (1988), p. 229.

M. E. Kassner, J. J. Oldani, and K. L. Cadwell, "The Variation of Torsional Ductility of High Purity Aluminum with Temperature and Strain-Rate," in *Proc. XXII Intern. Metallurgy Congress—Innovation for Quality*, Association of Italian Metallurgists, Milan, Italy (1988), p. 505.

M. E. Kassner, R. S. Rosen, G. A. Henshall, and W. E. King, "Delayed Failure of Silver-Aided Diffusion Welds," in *Brazing, High-Temperature Brazing and Diffusion Welding*, DVS-Verlag, Düsseldorf, FRG (1989), p. 47.

E. N. Kaufmann, J. S. Huang, A. M. Karo, M. A. Wall, and T. M. Deboni, "Nucleation and Growth in Surface Melted Alloys," in *Powder Preparation/Rapid Quenching*, K. Akashi, Y. Ozaki, T. Takeda, A. Inoue, T. Masumato, and T. Suzuki, Eds., Materials Research Society, Pittsburgh, Pa. (1989), p. 615.

E. F. Lindsey, C. W. Price, E. L. Pierce, and E. J. Hsieh, "SEM Analysis of DC Magnetron Sputtered Beryllium Films," in *Proc. 46th Ann. Mtg. Electron Microscopy Soc. of America*, G. W. Bailey, Ed., San Francisco Press, San Francisco, Calif. (1988), p. 960.

E. F. Lindsey, C. W. Price, R. M. Franks, and M. A. Lane, "Stereoscopic Analyses of Surfaces on Polystyrene Foam," in *Proc. 47th Ann. Mtg. Electron Microscopy Soc. of America*, G. S. Bailey, Ed., San Francisco Press, San Francisco, Calif. (1989), p. 706.

J. E. Marion, "Guidelines for the Estimation and Measurement of Thermomechanical Properties of Optical Materials, Structure-Property Relationships in Optical Materials," in *Mater. Res. Soc. Proc.*, Materials Research Society, Pittsburgh, Pa. (1988).

J. E. Marion, "Advanced Phosphate Glasses for High Average Power Lasers," in *Proc. Glasses for Opto-electronics* (1989).

J. E. Marion, "Materials Development for High Average Power Laser Amplifier Slabs," in *Proc. High Power and Solid State Lasers* (1989), p. 1.

F. M. Matthews, D. M. Hoffman, and S. A. Letts, "Development of Low Viscosity Adhesives for Low-Density Polystyrene Foam Materials for Direct-Drive Laser ICF Targets," in *Soc. Plastics Engineers Ann. Tech. Conf. Proc.*, Society of Plastics Engineers, New York, N.Y. (1988), p. 1552.

F. M. Matthews and D. M. Hoffman, "Low-Density Foams Produced From Sheared Ultra-High-Molecular Weight Polyethylene Gels," in *Soc. Plastics Engineers Ann. Tech. Conf. Proc.*, Society of Plastics Engineers, New York, N.Y. (1989), p. 621.

K. D. McKeegan, D. Phinney, V. Oversby, M. Buchholtzten Brink, and D. K. Smith, "Uranium Transport in Topopah Spring Tuff: An Ion Microscope Investigation," in *Scientific Basis for Nuclear Waste Management XII, Mater. Res. Soc. Symp. Proc. Vol. 127*, W. Lutze and R. Ewing, Eds., Materials Research Society, Pittsburgh, Pa. (1988), p. 813.

R. G. Musket, "Composition and Thickness of Multilayer Foils using MeV Ion-beam Techniques," in *X-Ray and Vacuum Ultraviolet Interaction Data Bases, Calculations, and Measurements, SPIE Vol. 911*, N. K. Delgrande, P. Lee, J. A. R. Samson, and D. Y. Smith, Eds., SPIE, Bellingham, Wash. (1988), p. 177.

R. G. Musket and I. M. Thomas, "Improved Adhesion for $SiO_2$ Particles on Silica Substrates using Helium-ion Irradiation," in *Adhesion in Solids, Mat. Res. Soc. Symp. Proc. Vol. 119*, D. M. Mattox, J. E. E. Baglin, R. J. Gottschall, and C. D. Batich, Eds., Materials Research Society, Pittsburgh, Pa. (1988), p. 121.

D. M. Nicholson, G. M. Stocks, W. M. Temmerman, P. A. Sterna, and D. G. Pettifor, "Structural Twin Differences in $Al_3Ti$: The Role of Tetragonal Distortion in APB and Twin Energies," in *Mat. Res. Soc. Symp. Proc. Vol. 133*, Materials Research Society, Pittsburgh, Pa. (1989), p. 775.

S. R. Nutt, K. Green, W. D. Nix, S. Baker, and A. E. Jankowski, "Gold-Nickel Multilayer Films: Structure-Property Correlations," in *Mater. Res. Soc. Symp. Proc. Vol. 130*, J. C. Bravman, W. D. Nix, D. A. Smith, and D. M. Barnett, Eds., Materials Research Society, Pittsburgh, Pa. (1989), p. 129.

M. S. Oh, T. T. Coburn, R. W. Crawford, and A. K. Burnham, "Study of Gas Evolution During Oil Shale Pyrolysis by Triple Quadrupole Mass Spectrometry," in *Intern. Conf. Oil Shale and Shale Oil*, Z. Yajie, Ed., Chemical Industry Press, Beijing, China (1988), p. 295.

M. S. Oh, A. K. Burnham, and R. W. Crawford, "Evolution of Sulfur Gases during Coal Pyrolysis," in *ACS Preprints*, American Chemical Society, Washington, D.C. (1988), p. 274.

M. S. Oh, R. W. Crawford, K. G. Foster, and A. Alcaraz, "Ammonia Evolution from Western and Eastern Oil Shales," in *ACS Div. of Pet. Chem. Preprints*, American Chemical Society, Washington, D.C. (1989), pp. 94–102.

C. W. Price, "Observations of Dislocation Interactions with Recrystallized Grain Boundaries," in *Proc. 46th Ann. Mtg. Electron Microscopy Soc. of America*, G. W. Bailey, Ed., San Francisco Press, San Francisco, Calif. (1988), p. 628.

C. W. Price, E. F. Lindsey, R. M. Franks, and M. A. Lane, "Characterization of Machined Polystyrene Foam," in *Proc. 47th Ann. Mtg. Electron Microscopy Soc. of America*, G. W. Bailey, Ed., San Francisco Press, Inc., San Francisco, Calif. (1989), p. 372.

J. G. Reynolds, "Programmed Temperature Pyrolysis Comparing Big Clifty (Kentucky) Tar Sand and Asphaltenes from Laboratory and Pilot Plan Extracted Bitumen," in *1988 Eastern Oil Shale Symp.*, IMMR 88-101 (1989), p. 9.

J. G. Reynolds, R. W. Crawford, and T. T. Coburn, "Variable Temperature Pyrolysis of Domestic Tar Sands---Asphalt Ridge (Utah) and Big Clifty (Kentucky)," in *1987 Eastern Oil Shale Symp.*, KECL 87-175 (1988), p. 101.

S. Rice, D. Erskine, N. Holmes, G. Otani, and P. McCandless, "Mie Scattering Spectroscopy in Shocked Benzene," in *APS Topical Conf. Shock Waves in Condensed Matter*, American Physical Society, New York, N.Y. (1989).

M. O. Riley, C. M. Walkup, and E. S. Jessop, "Spectral Filters Based on Ethylene/Acrylic Acid Copolymers Partically Ionized with Transition Metals," in *ACS Polymer Preprints*, American Chemical Society, Washington, D.C. (1988), p. 449.

H. F. Rizzo, L. E. Tanner, M. A. Wall, E. D. McClanahan, and T. B. Massalski, "Formation of Metastable Structures and Amorphous Phases in Cu-W Alloys Using the Triode Sputtering Technique," in *Proc. Mater. Res. Symp. Fundamentals of Beam-Solid Interactions and Transient Thermal Processing*, M. J. Aziz, L. E. Rehn, and B. Stritzker, Eds., Materials Research Society, Pittsburgh, Pa. (1988), p. 81.

D. A. Roylance, L. Chiao, and P. M. McElroy, "A Versatile Finite Element Code for Polymer and Composite Processing," in *Computer Applications in Applied Polymer Sci.*, T. Provder, Ed., ACS Symp. Series 404, American Chemical Society, Washington, D.C. (1989).

T. D. de la Rubia, R. S. Averback, I. M. Robertson, and R. Benedek, "Molecular Dynamics Studies of the Primary State of Radiation Damage," in *Proc. Workshop on Fusion Energy* (1988).

T. D. de la Rubia, K. Smalinskas, R. S. Averback, I. M. Robertson, H. Hsieh, and R. Benedek, "Mechanisms of Cascade Collapse," in *Proc. Mater. Res. Soc. Fall Mtg. Characterization of the Structure and Chemistry of Defects in Metals*, Materials Research Society, Pittsburgh, Pa. (1989), p. 29.

D. L. Sapak, J. M. Ward, and J. E. Marion, "Impurity Absorption Coefficient Measurements in Phosphate Glass Melted under Oxidizing Conditions," in *Proc. Properties and Characteristics of Optical Glass* (1989), p. 107.

D. Schryvers, L. E. Tanner, and G. VanTendeloo, "Premartensitic Microstructures as seen in the High-Resolution Electron Microscope: A Study of a Ni-Al Alloy," in *NATO/ASI Proc. Alloy Phase Stability*, G. M. Stocks and A. Gonis, Eds., Kluwer Academic Publications, Dordrecht, The Netherlands (1988), p. 599.

D. Schryvers, L. E. Tanner, and S. M. Shapiro, "Electron Microscopy and Neutron Scattering Studies of Premartensitic Behavior in a Ni-Al Beta-phase Alloy," in *Proc. Mater. Res. Soc. Symp. Shape-Memory Materials*, K. Otsuka and K. Shimizu, Eds., Materials Research Society, Pittsburgh, Pa. (1989), p. 35.

S. M. Shapiro, B. X. Yang, G. Shirane, J. Z. Larese, L. E. Tanner, and S. C. Moss, "Neutron Scattering Studies of Premartensitic Behavior in a Ni-Al Alloy," in *Proc. Intern. Conf. Neutron Scattering* (1989), p. 59.

M. Sluiter and P. Turchi, "Electronic Theory of Phase Stability in Substitutional Alloys: a Comparison Between the Connolly-Williams Scheme and the Generalized Perturbation Method," in *NATO-ASI Proc.*

*Alloy Phase Stability*, G. M. Stocks and A. Gonis, Eds., Kluwer Academic Publishers, Dordrecht, The Netherlands (1988), p. 521.

E. C. Sowa, A. Gonis, and X.-G. Zhang, "First-Principles Calculations of the Electronic Structure of Grain Boundaries," in *Proc. Intern. Congress Intergranular and Interphase Boundaries in Materials, IIB89*, Les Editions de Physique, Ecole des Mines de Paris, France (1989).

P. A. Sterne, C. S. Wang, G. M. Stocks, and W. M. Temmerman, "Electronic Structure and Antiferromagnetism in $La_2CuO_4$," in *Mater. Res. Soc. Symp. Proc. Vol. 99*, Materials Research Society, Pittsburgh, Pa. (1988), p. 353.

P. A. Sterne, "Electronic Structure of High Temperature Superconductors," in *Proc. 4th Intern. Conf. Supercomputing* (1989), p. 90.

M. J. Strum, S. K. Hwang, and J. W. Morris, Jr., "The Influence of Boron on the Ductile-Brittle Transition in Fe-Mn Steels," in *Proc. Symp. Interfacial Structure, Properties and Design*, W. A. T. Clark, M. H. Yoo, and C. L. Briant, Eds., Materials Research Society, Pittsburgh, Pa. (1988), p. 467.

M. J. Strum and J.W. Morris, Jr., "Influence of Post-Anneal Cooling Treatments on Suppression of Cryogenic Intergranular Fracture in Experimental Ni-Free High-Mn Austenitic Steels," in *Advances in Cryogenic Engineering Materials*, A. F. Clark and R. P. Reed, Eds., Plenum Press, New York, N.Y. (1988), p. 371.

L. T. Summers, M. J. Strum, and J. R. Miller, "The Influence of Liquid Metal Infiltration on the Superconducting Characteristics of Niobium Nitride," in *Advances in Cryogenic Engineering Materials*, A. F. Clark and R. P. Reed, Plenum Press, New York, N.Y. (1988), p. 835.

C. B. Thorsness and J. A. Britten, "Analysis of Material and Energy Balances for the Rocky Mountain I UCG Field Test," in *Proc. Intern. Underground Coal Gasification Symp. 1989* (1989).

T. M. Tillotson, L. W. Hrubesh, and J. M. Thomas, "Partially Hydrolyzed Alkoxysilanes as Precursors for Silica Aerogels," in *Mater. Res. Soc. Symp. Proc.*, Materials Research Society, Pittsburgh, Pa. (1988), p. 685.

T. Tsakalakos and A. F. Jankowski, "Critical Phenomena in Nanoscale Multilayer Materials," in *Multicomponent Ultrafine Microstructures, Mater. Res. Soc. Symp. Proc. Vol. 132*, D. E. Polk, R. W. Siegel, and B. H. Kear, Eds., Materials Resarch Society, Pittsburgh, Pa. (1989), p. 199.

P. E. A. Turchi, A. Gonis, X. G. Zhang, and G. M. Stocks, "Configurational Energies in Terms of Effective Cluster Interactions in Binary Substitutional Alloys: Connection Between the Embedded Cluster Method and the Generalized Perturbation Method," in *NATO-ASI Proc. Alloy Phase Stability*, G. M. Stocks and A. Gonis, Eds., Kluwer Academic Publishers, Dordrecht, The Netherlands (1988), p. 509.

C. E. Violet, R. J. Borg, K. V. Rao, J. Noques, R. D. Taylor, and A. Batra, "Magnetic Behavior of Amorphous Fe-Ni-Zr Alloys and Their Response to Radiation Damage," in *Intern. Conf. Applications of the Mössbauer Effect* (1988), p. 963.

C. E. Violet, T. Datta, H. M. Ledbetter, C. Almasan, and J. Estrada, "Reentrant Softening in Copper-Oxide Superconductors," in *Mater. Res. Soc. Symp. Proc.*, Materials Research Society, Pittsburgh, Pa. (1988), p. 375.

A. L. Wachs, P. E. A. Turchi, Y. C. Jean, K. H. Wetzler, R. H. Howell, D. R. Harshman, J. P. Remeika, A. S. Cooper, R. M. Fleming, and M. J. Fluss, "Electronic Structure Investigations of High-$T_c$ Materials by Positron Annihilation Spectroscopy: Theory and Experiment," in *Materials Research Soc. Mtg. High Temperature Superconductors II*, D. W. Capone, II, W. H. Butler, B. Batlogg, and C. W. Chu, Eds., Materials Research Society, Pittsburgh, Pa. (1988), p. 237.

M. J. Weber, "Survey of Defense Laboratories Needs for Hard X-Rays," in *Proc. 1st Ann. Users Mtg. for Advanced Photon Source*, Argonne National Laboratory, Chicago, Ill. (1988), p. 75.

M. J. Weber, "Optically-Detected X-Ray Absorption Spectroscopy in Luminescent Materials," in *Ann. Mtg. Technical Digest*, Optical Society of America, Washington, D.C. (1989), p. MGG2.

M. J. Weber, "Laser Glass," in *Proc. 2nd Intern. Symp. New Glass*, The Association of New Glass Industries, Tokyo, Japan (1989), p. 55.

M. J. Weber, "Recent Optical Studies of the Local Environment of Rare Earth Ions in Glass," in *Proc. Ultrastructure Processing Conf.*, Wiley, New York, N.Y. (1989).

C. E. Witherell, "Metallurgical Characterization of Wasted Surfaces in In-Bed Carbon Steel Evaporator Tubes," in *Proc. 10th Intern. Conf. Fluidized Bed Combustion*, A. M. Manake, Ed., American Society of Mechanical Engineers, New York, N.Y. (1989), p. 937.

## Articles in Books

R. M. Bionta, A. F. Jankowski, and D. M. Makowiecki, "Sputtered-Sliced Linear Zone Plates for 8 keV X-Rays," in *X-Ray Microscopy II*, D. Sayre, M. Howells, J. Kirz, and H. Rarback, Eds. (Springer-Verlag, Berlin, 1988), p. 142.

D. Calef, "Theoretical Treatments of Solvent Effects," in *Photoinduced Electron Transfer Reactions*, M. A. Fox and M. Chanon, Eds. (Elsevier, Amsterdam, The Netherlands, 1988), p. 362.

R. M. Christensen and S. R. Swanson, "Evaluation of a New Failure Criterion for Fibrous Composite Materials," in *Mechanics of Composite Materials*, G. J. Dvorak and N. Laws, Eds. (American Society of Mechanical Engineers, New York, 1988), p. 63.

J. R. Gaines and P. C. Souers, "The Spin-Lattice Relaxation Time ($T_1$) in Mixtures of Hydrogen Isotopes," in *Mixtures of Hydrogen Isotopes* (Academic Press, Orlando, Fla., 1988), p. 91.

L. W. Hrubesh, and C. T. Alviso, "Optical Characterization of Silica Aerogel," in *Better Ceramics Through Chemistry III*, C. J. Brinker, D. E. Clark, and D. R. Ulrich, Eds. (Materials Research Society, Pittsburgh, Pa., 1988), p. 703.

A. F. Jankowski and T. Tsakalakos, "Phase Stability by the Artificial Concentration Wave Method," in *Alloy Phase Stability*, G. M. Stocks and A. Gonis, Eds. (Kluwer Academic Publishers, Dordrecht, The Netherlands, 1989), p. 585.

M. E. Kassner, R. S. Rosen, G. A. Henshall, and W. E. King, "Delayed Failure of Silver-Aided Diffusion Welds Between Steel," in *Brazing, High Temperature Brazing and Diffusion Bonding* (DVS-Verlag, Düsseldorf, FRG, 1989), p. 47.

H. J. McQueen and M. E. Kassner, "Extended Ductility in α-Iron and Aluminum Alloys," in *Superplasticity in Aerospace*, H. C. Heikkenen and T. R. McNelley, Eds. (AIME, New York, 1988), p. 77.

S. B. Monaco and J. H. Richardson, "Stress-Induced Chemiluminescence of Polymeric Materials," in *Luminescence Techniques in Polymer Research*, L. Zlatkevich, Ed. (Marcel Dekker, New York, 1989), p. 237.

A. J. Pertica, J. E. Marion, and S. E. Stokowski, "Reduction of Tetravalent Chromium-Induced Optical Loss in Nd:Cr:GSGG," in *Advances in Laser Science*, J. L. Gole, D. F. Heller, M. Lapp, and W. Stwalley, Eds. (American Institute of Physics, New York, 1988), p. 103.

## Books Edited

*Alloy Phase Stability*, G. M. Stocks and A. Gonis, Eds. (Kluwer Academic Publishers, Dordrecht, The Netherlands, 1989).

*Unsteady Interaction of Shock and Detonation Waves in Gases*, English translation by P. A. Urtiew; V. P. Korobeinikov, Ed. (Hemisphere Publishers Corp., 1988).

*Glass Lasers*, M. J. Weber, Ed., Supplement 1 to *Handbook of Laser Science and Technology* (CRC Press, Boca Raton, Fla., 1989).

## Reports

A. K. Burnham, M. S. Oh, R. W. Crawford, and A. M. Samoun, *Pyrolysis of the Argonne Premium Coals: Activation Energy Distributions and Related Chemistry*, Lawrence Livermore National Laboratory, Livermore, Calif., UCRL-99738 (1989).

J. C. Thomas, D. L. James, S. A. Letts, and S. C. Mance, *Cryogenic Mechanical Characterization of Low-Density Polymeric Foams Being Developed for Direct-Drive Laser ICF Targets*, Lawrence Livermore National Laboratory, Livermore, Calif., UCRL-98398 (1988).

J. A. Caird, F. P. Milanovich, N. D. Nielsen, H. T. Powell, J. E. Marion, A. J. Pertica, and J. N. Roe, *Passive Optical Losses in Laser Glass*, Lawrence Livermore National Laboratory, Livermore, Calif., UCRL-100012 (1989).

C. Chen, R. C. Cook, B. L. Haendler, L. M. Hair, F. M. Kong, and S. A. Letts, *Target Materials Development*, Lawrence Livermore National Laboratory, Livermore, Calif., UCRL-50021-86 (1988).

C. W. Chen, *Review: Fabrication and Characterization of Thin Films with Perpendicular Magnetic Anisotropy for High-Density Magnetic Recording*, Lawrence Livermore National Laboratory, Livermore, Calif., UCRL-100944 (1989).

C. W. Chen, D. M. Makowiecki, C. S. Alford, M. A. McKernan, and P. B. Ramsey, *Surface-Defect Formation in Graphite Targets during Magnetron Sputtering*, Lawrence Livermore National Laboratory, Livermore, Calif., UCRL-101293 (1989).

L. Chiao and R. E. Lyon, *A Fundamental Approach to Resin Cure Kinetics*, Lawrence Livermore National Laboratory, Livermore, Calif., UCRL-101110 (1989).

L. Chiao, *Mechanistic Kinetics of Diaminodiphenyl Sulfone-Cured Tetraglycidyl 4,4' Diaminodiphenyl Methane Epoxy Resins*, Lawrence Livermore National Laboratory, Livermore, Calif., UCRL-101067 (1989).

L. Chiao, *Application of Mechanistic Chemical Kinetics to Thermoset Composites Processing*, Lawrence Livermore National Laboratory, Livermore, Calif., UCRL-101272 (1989).

L. Chiao, *Mechanistic Modeling of Epoxy Resins*, Lawrence Livermore National Laboratory, Livermore, Calif., UCRL-101108 (1989).

I. L. Chiu and D. M. Hoffman, *Anaerobic Adhesion to Depleted Uranium*, Lawrence Livermore National Laboratory, Livermore, Calif., UCRL-101007-ABST (1989).

R. M. Christensen, *A Critical Evaluation for a Class of Micro-Mechanics Models*, Lawrence Livermore National Laboratory, Livermore, Calif., UCRL-100169 (1989).

R. M. Christensen, *Tensor Transformations and Failure Criteria for the Analysis of Fiber Composite Materials, Part II: Necessary and Sufficient Conditions for Laminate Failure*, Lawrence Livermore National Laboratory, Livermore, Calif., UCRL-96196 Part II (1989).

R. M. Christensen and E. Zywicz, *A Three-Dimensional Constitutive Theory for Fiber Composite Laminates*, Lawrence Livermore National Laboratory, Livermore, Calif., Livermore, CA, UCRL-100947 (1989).

W. E. Conaway, D. S. Leonard, and C. G. Stevens, *State-to-State Photodissociation from Highly Excited Vibrational States of $H_2O$*, Lawrence Livermore National Laboratory, Livermore, Calif., UCRL-100041 (1989).

M. S. Costantino, J. F. Lakner, and R. Bastasz, *Synthesis of Monolithic Uranium Hydride and Uranium Deuteride*, Lawrence Livermore National Laboratory, Livermore, Calif., UCRL-101022 (1989).

M. W. Droege, L. M. Hair, W. J. Pitz, and C. K. Westbrook, *The Thermal Gas Phase Reactions of Methane and Oxygen: A Comparison of Model Calculations and Experimental Results*, Lawrence Livermore National Laboratory, Livermore, Calif., UCRL-100568 (1989).

J. W. Elmer, *The Influence of Cooling Rate On the Microstructure of Stainless Steel Alloys*, Sc.D. thesis, Department of Materials Science and Engineering, Massachusetts Institute of Technology, Cambridge, Mass. (1988).

L. Erickson, P. A. Urtiew, and R. Simpson, *High Explosive Diagnostics*, Lawrence Livermore National Laboratory, Livermore, Calif. (1988).

R. A. Failor, *Kinetics of the Gas-Phase Tritium Oxidation Reaction*, Lawrence Livermore National Laboratory, Livermore, Calif., UCRL-53922 (1989).

A. Goldberg, O. D. Sherby, and M. J. Strum, *Steel Initiative, Semi-Annual Progress Report, Development of Superplastic Steel Processing*, Office of Industrial Programs, Office of Conservation and Renewable Energy, U. S. Department of Energy, Washington, D.C., DOE/CE-0256 (1989).

R. P. Gonzales, M. S. Staggs, M. F. Singleton, D. George, C. L. Weinzapfel, and S. Weinzapfel, *Variations with Laser Pulse Duration of the Thresholds at 350 nm and 1064 nm for Bulk Damage in Crystals of KCP*, Lawrence Livermore National Laboratory, Livermore, Calif., UCRL-95284 (1988).

B. L. Haendler, R. C. Cook, D. L. James, F.-M. Kong, S. A. Letts, S. C. Mance, I. G. E. Overturf, D. L. Schumann, and J. C. Thomas, *Low-Density Polystyrene Foams for Direct-Drive Laser ICF Targets*, Lawrence Livermore National Laboratory, Livermore, Calif., UCRL-98350 (1988).

G. Haugen and C. G. Stevens, *Atom Detection by Sideband Spectroscopy*, Lawrence Livermore National Laboratory, Livermore, Calif., UCRL-53689 (1988).

J. R. Hiskes and A. M. Karo, "Recombination and Dissociative Recombination of $H_2^+$ and $H_3^+$ Ions on Surfaces with Application to Volume Sources," in *NPB Annual Program Review*, Los Alamos National Laboratory, Los Alamos, N. Mex. (1988).

J. R. Hiskes and A. M. Karo, *Recombination and Dissociation of $H_2^+$ and $H_3^+$ Ions on Surfaces to Produce Vibrationally Excited $H_2$: Direct H⁻ Production on Low-Work Function Surface*, Lawrence Livermore National Laboratory, Livermore, Calif., UCRL-100536 and UCRL-100536, Rev. 1 (1989).

J. R. Hiskes and A. M. Karo, *Interpretation and Analysis of the $H_2$ Vibrational Distribution in a Hydrogen Discharge*, Lawrence Livermore National Laboratory, Livermore, Calif., UCRL-101070 (1989).

A. F. Jankowski, L. R. Schrawyer, M. A. Wall, and D. M. Makowiecki, *Interfacial Bonding in W/C and W/$B_4$C Multilayers*, Lawrence Livermore National Laboratory, Livermore, Calif., UCRL-99378 (1988).

A. F. Jankowski and M. A. Wall, *Transmission Electron Microscopy of Ni/Ti Neutron Mirrors*, Lawrence Livermore National Laboratory, Livermore, Calif., UCRL-99853 (1989).

A. F. Jankowski, *Origin of the Supermodulus Effect: Artificial Ordering Considerations*, Lawrence Livermore National Laboratory, Livermore, Calif., UCRL-99380 (1989).

M. E. Kassner, D. E. Peterson, M. G. Adamson, and P. H. Adler, *The Al-U (Aluminum-Uranium) System*, Lawrence Livermore National Laboratory, Livermore, Calif., UCRL-97992 (1988).

M. E. Kassner, *A Case for Taylor Hardening During Primary and Steady-State Creep in Aluminum and Type 304 Stainless Steel*, Lawrence Livermore National Laboratory, Livermore, Calif., UCRL-98619 (1988).

M. E. Kassner, *The Effects of Temperature and Strain-Rate in the Elevated Temperature Ductility of Aluminum in Torsion*, Lawrence Livermore National Laboratory, Livermore, Calif., UCRL-101245 (1989).

M. E. Kassner, R. S. Rosen, G. A. Henshall, and K. D. Challenger, *Time-Dependent Failure of Silver Interlayer Diffusion Bonds Between Non-Deforming Base Metals*, Lawrence Livermore National Laboratory, Livermore, Calif., UCRL-102284 (1989).

E. N. Kaufmann, J. S. Huang, A. M. Karo, M. A. Wall, and T. M. Deboni, *Nucleation and Growth in Surface Melted Alloys*, Lawrence Livermore National Laboratory, Livermore, Calif., UCRL-97716 (1989).

E-M. Kong, S. R. Buckley, L. Caley, B. L. Haendler, L. M. Hair, and S. A. Letts, *Low-Density Resorcinol-Formaldehyde Foams for Direct-Drive Laser ICF Targets*, Lawrence Livermore National Laboratory, Livermore, Calif., UCRL-98349 (1988).

E-M. Kong, *Low-Density Carbonized Composite Foams for Direct-Drive Laser ICF Targets*, Lawrence Livermore National Laboratory, Livermore, Calif., UCRL-100798 (1989).

O. H. Krikorian and D. Y. Lai, *Modeling of Heat Capacities of Metals*, Lawrence Livermore National Laboratory, Livermore, Calif., UCRL-98496 (1989).

S. A. Letts, S. R. Buckley, C. Chen, A. R. Cook, R. C. Cook, B. L. Haendler, B. C. Johnston, E-M. Kong, S. C. Mance, I. G. E. Overturf, and J. C. Thomas, *Characterization of Low-Density Materials and Their Precursors*, Lawrence Livermore National Laboratory, Livermore, Calif., UCRL-98351 (1988).

R. E. Lyon, *Physical Basis for a Pressure-Dependent Yield Criterion for Polymers*, Lawrence Livermore National Laboratory, Livermore, Calif., UCRL-99196 (1988).

A. R. Mitchell, *Synthesis of Dense Energetic Materials Using Polymer Supports*, Lawrence Livermore National Laboratory, Livermore, Calif., UCRL-53689-88 (1989).

R. G. Musket and I. M. Thomas, *Proton Stitching of Layers of $SiO_2$ Particles to Fused Silica*, Lawrence Livermore National Laboratory, Livermore, Calif., UCRL-101289 (1989).

D. J. Nikkel and R. M. Christensen, *A Micro-Mechanical Model for Aligned Fiber Elastic-Plastic Composites*, Lawrence Livermore National Laboratory, Livermore, Calif., UCRL-101221 (1989).

D. U. Olness, *Sensors for In-Situ Monitoring of Elastic Properties*, Lawrence Livermore National Laboratory, Livermore, Calif., UCRL-53924 (1989).

R. W. Pekala, *Organic Aerogels from the Polycondensation of Resorcinol with Formaldehyde*, Lawrence Livermore National Laboratory, Livermore, Calif., UCRL-98645 (1988).

R. W. Pekala, *Aerogels and Xerogels from Organic Precursors*, Lawrence Livermore National Laboratory, Livermore, Calif., UCRL-100423 (1989).

R. S. Rosen, J. J. Oldani, and M. E. Kassner, *An Analysis of Materials Selected for Mocking High Strain-Rate Mechanical Behavior of Uranium Alloys*, Lawrence Livermore National Laboratory, Livermore, Calif., UCRL-53884 (1988).

R. S. Rosen, M. E. Kassner, and J. J. Oldani, *Simple Constitutive Relationships for the Yield and Ultimate Strengths of Alloyed Plutonium in Tension, Compression, and Torsion*, Lawrence Livermore National Laboratory, Livermore, Calif., UCRL-53897 (1989).

R. S. Rosen and M. E. Kassner, *Diffusion Welding of Silver Interlayers Coated onto Base Metals by Planar Magnetron Sputtering*, Lawrence Livermore National Laboratory, Livermore, Calif., UCRL-101168 (1989).

R. S. Rosen, S. Beitscher, and M. E. Kassner, *Stress Corrosion Cracking of Uranium-Silver Interfaces in Silver-Aided Diffusion Welds*, Lawrence Livermore National Laboratory, Livermore, Calif., UCRL-97917, Rev. 1 (1989).

R. S. Rosen and M. E. Kassner, *Diffusion Welding of Silver Interlayers Coated onto Base Metals by Planar Magnetron Sputtering*, Lawrence Livermore National Laboratory, Livermore, Calif., UCRL-101168 (1989).

K. J. Scribner, E. von Holtz, and R. Simpson, *High Performance, Extrusion Cast Explosives with Low Sensitivity, Interim Report No. 1*, Lawrence Livermore National Laboratory, Livermore, Calif., UCRL-53890 (1989).

W. S. Selig, *The Determination of Calcium Phosphate in Sodium Chloride*, Lawrence Livermore National Laboratory, Livermore, Calif., UCRL-100643 (1989).

W. S. Selig, *The Complexiometric Microdetermination of Divalent Copper and Cobalt*, Lawrence Livermore National Laboratory, Livermore, Calif., UCRL-101095 (1989).

F. J. D. Serduke, C. G. Stevens, M. Friedman, and G. Grutmann, *Evaluation of a Proposed Electron Density Diagnostic for NOVA X-Ray Transmission Experiments*, Lawrence Livermore National Laboratory, Livermore, Calif., UCRL-99735 (1989).

R. L. Simpson, K. J. Scribner, and E. H. von Holtz, *High Performance, Extrusion Cast Explosives with Low Sensitivity, Interim Report No. 2*, Lawrence Livermore National Laboratory, Livermore, Calif., UCRL-53890 (1989).

D. K. Smith, G. S. Smith, and R. L. Landingham, *Hysteresis in the Orthorhombic-Tetragonal Phase Transition of 123 Superconductor Materials as a Function of Oxygen Fugacity*, Lawrence Livermore National Laboratory, Livermore, Calif., UCRL-98403 (1988).

C. M. Walkup, I. L. Chiu, E. M. Matthews, and D. M. Hoffman, *Adhesives for Special Foams*, Lawrence Livermore National Laboratory, Livermore, Calif., UCRL-96601 (1988).

M. A. Wall and A. F. Jankowski, *Atomic Imaging of Au/Ni Multilayers*, Lawrence Livermore National Laboratory, Livermore, Calif., UCRL-99854 (1989).

C. E. Witherell and R. G. Meisenheimer, *Tubing Wastage in Fluidized-Bed Coal Combustors—Test Series 2 NCB (IEA Grimethorpe) Ltd.*, Lawrence Livermore National Laboratory, Livermore, Calif., UCRL-21039 (1988).

C. E. Witherell, *Tubing Wastage in Fluidized-Bed Coal Combustors (TVA20 Megawatt AFBC Pilot Plant)*, Lawrence Livermore National Laboratory, Livermore, Calif., UCRL-21163 (1989).

## Lectures by Staff

M. G. Adamson, "Liquid Metal Containment Research at LLNL," at Sandia National Laboratory, Livermore, Calif., May 18, 1989.

L. Chiao, (1) "Basics of Honeycomb and Bonded Panels," and (2) "Application of Cure Modeling to Aerospace Materials," at Beijing Institute of Aeronautical Materials, The People's Republic of China, October 1988; Changsha Institute of Technology, 5th Department, Hunan Province, The People's Republic of China, October 1988.

L. Chiao, "Composite Materials and the Chemical Engineer," at Department of Chemical & Nuclear Engineering, University of California, Santa Barbara, Calif., December 1988.

R. M. Christensen, "Failure Mechanics of Composite Materials," at Notre Dame University, Notre Dame, Ind., October 10, 1988; at Illinois Institute of Technology, Chicago, Ill., October 11, 1988; at University of Illinois, Urbana, Ill., October 13, 1988; at Purdue University, West Lafayette, Ind., October 14, 1988.

R. M. Christensen, "A Two Material Constant Nonlinear Elastic Stress Constitutive Equation Including the Effect of Compressibility," at University of Massachusetts, Boston, Mass., May 31, 1989; University of Michigan, Ann Arbor, Mich., April 17, 1989; Michigan State University, East Lansing, Mich., April 18, 1989; University of Wisconsin, Madison, Wis., April 20, 1989; University of Minnesota, Minneapolis, Minn., April 21, 1989.

G. W. Collins, "Magnetic Resonance Study of Atomic Excitations in Solid Molecular Hydrogen," at Ohio State University, Columbus, Ohio, May 24, 1989.

R. C. Cook, "Polyisocyanates, Stiff or Flexible? — A Historical Perspective," at IBM, San Jose, Calif., May 2, 1989.

C. L. Coon, "Synthesis of Energetic Materials at Lawrence Livermore National Laboratory," at Naval Weapons Center, China Lake, Calif., January 1988.

C. L. Coon, "Problems of Waste Disposal in Organic Synthesis Laboratories," at Y-12 Plant, Oak Ridge, Tenn., March 1989.

M. Costantino, "Synthesis of Monolithic Uranium Hydride," at Sandia National Laboratories, Livermore, Calif., January 1989.

L. Davis, "Crystals for Frequency Doubling of Fusion Lasers," at Modesto Junior College Science Club, Modesto, Calif., March 1989.

T. D. de la Rubia, "Molecular Dynamics Studies of Atomic Collisions in Solids," at University of New Mexico, Albuquerque, N. Mex., October 27, 1989.

M. W. Droege, "The Interaction of Gas Phase Reactions with Methane Conversion Catalysts," at Catalytica Associates, Inc., Mountain View, Calif., May 31, 1989.

R. A. Failor, "Radioactive Fallout from the Chernobyl Reactor Accident," at University of Alabama, Huntsville, Ala., April 1988.

R. A. Failor, "Nuclear Power, Environmental Radioactivity and Activation Analysis," at University of Alabama, Huntsville, Ala., April 1988.

R. A. Failor, "Environmental Radioactivity," at Oakland University, Rochester, Mich., May 1988.

A. Gonis, "Electronic Structure Method for Systems with Full or Reduced Symmetry," at Physics Department, Imperial College, London, U.K., June 30, 1989; University of Bristol, Bristol U.K., June 31, 1989.

M. W. Guinan, "Recent Developments in Irradiation Effects in Metals," at Faculty of Engineering, Hiroshima University, Hiroshima, Japan, February 1989; Department of Nuclear Engineering, Kyushu University, Kyushu, Japan, January 1989.

M. W. Guinan, "Cold Fusion—85 Days Later," at Lockheed Research Colloquium, Lockheed Research and Development Division, Palo Alto, Calif., June 1989.

B. L. Haendler, "The Development of Low-Density Polymer Foams for Laser Inertial Confinement Fusion," at California Section, ACS Technician Affiliates Group Meeting, Dublin, Calif., May 1989.

J. E. Harrar, "Raman Spectroscopy and Electrochemistry of Nitric Acid, Nitrogen Oxide Solutions," at University of Nottingham, Nottingham, U.K., May 1988.

R. Hawley-Fedder, "FTIR—Fancy Techniques in Infrared Spectrometry," at Alabama A&M University, Normal, Ala., April 6, 1989.

D. M. Hoffman, "Bonding Aerogels with Urethanes," at Pantex Plant, Amarillo, Tex., June 21, 1988.

D. M. Hoffman, "The Physics of Poly (ethylene oxide)/Poly (methyl methacrylate)," at Edi Chem-Americas, Inc., Princeton, N.J., March 28, 1988.

D. M. Hoffman, "Dynamic Mechanical and Thermal Analysis of Crystallinity Development in Kel-F 800 and TATB/Kel-F 800 Plastic Bonded Explosives. Pt. I. Kel-F 800," at Sandia National Laboratories, Albuquerque, N. Mex., October 12, 1988.

J. B. Holt, "Fundamentals of Combustion Synthesis and Applications of Combustion Synthesis Research," at National Research Institute for Metals, Tokyo, Japan, February 1989.

J. B. Holt, "Applications of Combustion Synthesis Research," at Kyoritsu Ceramic Materials Co., Ltd., Nagoya, Japan, February 1989.

J. B. Holt, "Combustion Synthesis in USA," at Osaka University, Osaka, Japan, February 1989.

J. B. Holt, "Basics of Combustion Reactions," at Japanese Fine Ceramics Center, Nagoya, Japan, February 1989.

A. F. Jankowski, "Elastic Anomalies of Metallic Superlattices," at University of Michigan, Department of Materials Science and Engineering–Applied Physics Program, Ann Arbor, Mich., February 20, 1989; Rutgers University, Department of Mechanics and Materials Science, New Brunswick, N.J., February 16, 1989.

M. E. Kassner, "Deformation of Aluminum and Iron Alloys to Ultra-Large Strains," at Lockheed Research Center, Palo Alto, Calif., February 1988.

J. H. Kinney, "Novel Methods for Dentin Characterization using Synchrotron Radiation," at University of California, San Francisco, Department of Restorative Dentistry, February 1989.

J. H. Kinney, "Applications of 3D Chemical X-ray Microscopy," at Argonne National Laboratory, Chicago, Ill., January 1989.

R. E. Lyon, "Strain-Induced Crystallization of Elastomers," at Department of Pharmacy, University of San Francisco, San Francisco, Calif., February 1988.

J. E. Marion, "Laser Materials Research at Livermore," at Department of Mechanical Engineering and Materials Science, University of California, Santa Barbara, Calif., January 1988; Department of Materials Science, University of California, Berkeley, Calif., January 1988; Department of Chemistry and Ceramics, Ohio State University, Columbus, Ohio, February 1988; Department of Materials Science, Case Western Reserve University, Cleveland, Ohio, February 1988.

J. E. Marion, "Fracture of Brittle Materials," at Johnson & Johnson, San Diego, Calif., August 1988.

J. E. Marion, "Advanced Lasers Materials Requirements for Inertial Confinement Fusion and High Average Power Lasers," at E. Merck, Darmstadt, FRG, November 1988.

J. E. Marion, "Optics Requirements for a Multimegajoule Laser Research Facility," at Johnson/Matthey, Royston, U.K., November 1988.

J. E. Marion, "Large Scale Laser Crystal Growth," at Wacker Chemitronic, Burghausen, FRG, May 1989.

J. E. Marion, "Development of High Average Power Lasers at Livermore," at Dutch National Energy Research Center, Amsterdam, Holland, May 1989.

J. E. Marion, "Laser Optics Requirements for Inertial Confinement Fusion," at Cranfield Institute of Technology, Cranfield, U.K., May 1989.

J. E. Marion, "Fracture of Solid State Laser Materials," at Coherent, Inc., Palo Alto, Calif., August 1989.

F. M. Matthews, "Compounds and Solutions," at Claremont Middle School, Oakland, Calif., July 10, 1988.

F. M. Matthews, "College Readiness Program Scientific Participation," at California State University, Hayward, Calif., May 17, 1988 and March 11, 1989.

D. G. Miller, (1) "The International Collaboration on the Study of the System NaCl-$MgCl_2$-$H_2O$" and (2) "Pierre Duhem, An Extraordinary Figure of Turn of the Century Science," at Texas Christian University, Fort Worth, Tex., March 1989.

D. G. Miller, (1) "The Surprising Complexity of Binary and Ternary Diffusion Data for Electrolyte Solutions," (2) "New Methods for Analyzing Gouy Fringe Data from Individual Diffusion Experiments," and (3) "Solutions of the Diffusion Equations for Equal Eigenvalues of the Diffusion Coefficient Matrix," at Technische Hochschule, Aachen, FRG, October 1988.

D. G. Miller, "The Theory and Practice of Diffusion Measurements," at University of Naples, Naples, Italy, September 28, 1988.

E. T. Mones, "Topaz System," at Rockwell International, Microelectronics Sector, Anaheim, Calif., April 4, 1989.

E. T. Mones, "Overview of the Connoisseur Coating Systems," at National Semiconductor, Tucson, Ariz., August 10, 1988.

R. G. Musket, "Applied and Fundamental Ion-beam Modification of Materials," at Physics Department, Alabama A&M University, Normal, Ala., November 1988.

V. M. Oversby, "Uranium and Actinide Transport in Topopah Spring Tuff," at SCK/CEN/Mol, Belgium, January 16, 1989.

P. F. Pagoria, "Synthesis of K-6 and D-56," at University of New Orleans, New Orleans, La., September 1988.

P. F. Pagoria, "Synthesis of K-6, K-56 and Notes on CL-20 Synthesis," at Los Alamos National Laboratory, Los Alamos, N. Mex., September 1988.

R. W. Pekala, "The Synthesis of Organic Aerogels," at Sandia National Laboratories, Albuquerque, N. Mex., April 21, 1989; 3M Company, St. Paul, Minn., May 23, 1989.

C. W. Price, "Some Applications of Ion Microanalysis of Beryllium and Beryllium Films," at Charles Evans and Associates, Redwood City, Calif., October 18, 1988.

M. L. Sattler and S. Hulsey, "Modern Alchemy, the Metallurgist and the Chemist," at Chabot College, Livermore, Calif., March 1988.

M. L. Sattler and S. Hulsey, "Modern Alchemy, Changing Metal into Gold?" at Los Positas College, Livermore, Calif., March 1989.

K. Scribner, "Extrusion Cast Explosives Processing Technology," at Naval Ordnance Station, Indian Head, Md., April 1989.

W. S. Selig, "Magic of Chemistry," at Renaissance Camp, Santa Cruz County, Calif., August 26, 1988.

E. C. Sowa, "The Electronic Structure of Grain Boundaries: A New, First-Principles Approach," at Max Planck Institüt für Metallforschung, Stuttgart, FRG, September 11, 1989.

P. A. Sterne, "Electronic Structure of High Temperature Superconductors," at Florida Atlantic University, Boca Raton, Fla., May 1988.

C. G. Stevens, "Two-Step Photodissociation of Molecules via Overtone States: A Route to Bond Selective Chemistry," at University of Southern California, Los Angeles, Calif., March 1989.

L. E. Tanner, "The Systematics of Phase Transformations in Metallic Alloys," at University of California Materials Engineering Colloquium, San Diego, Calif., December 19, 1988.

L. E. Tanner, "TEM Observations of the Pretransformation Behavior in Metallic Alloys," at Stanford University, Department of Materials Science, Annual Symposium on Contemporary Electron Microscopy, Stanford, Calif., February 15, 1988.

L. E. Tanner, "Displacive Phase Transformations in Alloys," at University of California Physics Colloquium, Berkeley, Calif., September 28, 1988.

J. G. Tobin, "The Reversible Formation of a Surface Alloy: Au/Cu(001)," at University of California, Berkeley, Calif., October 1988; Stanford University, Stanford, Calif., October 1988.

K. Wilfinger, "Cermet Processing," at Rutgers University, New Brunswick, N.J., November 22, 1988.

J. Wong, "Experimental X-Ray Absorption Spectroscopy Using Synchrotron Radiation," at National Taiwan University, Taipei, Taiwan, July 1989.

## Technical Presentations at Conferences and Meetings, 1988 and 1989

**Gordon Research Conference on Composites, Ventura, Calif., January 11–15, 1988**

S. J. DeTeresa, "Compression of Carbon Fibers."

**American Institute of Mechanical Engineers Annual Meeting, Phoenix, Ariz., February 25–27, 1988**

M. E. Kassner and J. J. Oldani, "Large-Strain Steady-State Deformation of Silver at Ambient and Near-Ambient Temperatures."

H. J. McQueen and M. E. Kassner, "Extended Ductility in Aluminum and α-Iron Alloys."

**National Teleconference on Superconductivity, Sandia National Laboratories, Albuquerque, N. Mex., January 25–26, 1988**

R. L. Landingham, "Superconducting Materials Research."

**World Congress on Superconductivity, Houston, Tex., February 22–24, 1988**

M. J. Fluss, A. L. Wachs, P. E. A. Turchi, R. H. Howell, Y. C. Jean, J. Kyle, H. Nakanishi, C. H. Chu, R. L. Meng, H. P. Hor, and J. Z. Huang, "Probing the Electronic and Defect Structure of Perovskite Superconductors."

**Pittsburgh Conference, New Orleans, La., February 24, 1988**

W. S. Selig, "A New Potentiometric Method for the Estimation of the Rare Earth Elements."

**International Conference on High-Temperature Superconductors and Materials and Mechanisms of Superconductivity, Interlaken, Switzerland, Feb. 29–March 4, 1988**

P. E. A. Turchi, A. L. Wachs, Y. C. Jean, R. H. Howell, K. H. Wetzler, and M. J. Fluss, "Positron Annihilation in Perovskite Superconductors, Theory and Experiment."

C. E. Violet, K. V. Rao, D.-X. Chen, and R. L. Landingham, "Density, Microstructure, and High-$T_c$ Superconductivity."

**American Physical Society Spring Meeting, New Orleans, La., March 21–25, 1988**

D. Calef, "Structure of Molecular Fluids."

A. Gonis, X.-G. Zhang, D. Nicholson, and C. L. Fu, "Multiple Scattering Theory for General Space-Filling Cell Potentials."

W. J. Nellis and R. L. Landingham, "Shock Compaction of High-$T_c$ Oxide Powders in a Metal Matrix."

J. D. Sater, J. R. Gaines, E. M. Fearon, P. C. Souers, and E. E. McMurphy, "Self-Diffusion Measurements on Solid Hydrogens."

P. A. Sterne and C. S. Wang, "Higher $T_c$ Through Metallic Interlayer Coupling in $Bi_2Sr_2CaCu_2O_8$."

P. A. Sterne and C. S. Wang, "Oxygen Vacancy Induced Antiferromagnetism in $La_2CuO_4$."

C. E. Violet, T. Datta, J. Estrada, C. Almasan, and J. H. Kinney, "Derivative Analysis of Magnetic and Resistive Measurements of Superconducting $YBa_2Cu_3O_{7-x}$"

C. E. Violet, H. M. Ledbetter, and T. Datta, "Low-Temperature Shear Modulus of the Metal-Oxide Superconductor Ho-Ba-Cu-Fe-O."

X.-G. Zhang and A. Gonis, "Reformulation of Scattering Theory in Terms of the Complete Scattering Matrix of an Assembly."

L. E. Tanner, "Direct Observations of Premartensitic Structural Modulations by TEM."

**Workshop on Fusion Energy, Lugano, Switzerland, March 24–29, 1988**

M. W. Guinan, "Electrical Resistivity Studies at RTNS-II."

**National Organization for the Professional Advancement of Black Chemists and Chemical Engineers, Philadelphia, Pa., April 4–8, 1988**

E. M. Matthews, C. M. Walkup, I. L. Chiu, and D. M. Hoffman, "Adhesives for Special Foams."

**Materials Research Society Spring Meeting, Reno, Nev., April 5–9, 1988**

L. W. Hrubesh and C. T. Alviso, "Optical Characterization of Silica Aerogel."

R. G. Musket and I. M. Thomas, "Improved Adhesion for $SiO_2$ Particles on Silica Substrates using Helium-ion Irradiation."

M. J. Strum, S. K. Hwang, and J. J. W. Morris, "The Influence of Boron on the Ductile-Brittle Transition in Fe-Mn Steels."

T. M. Tillotson, L. W. Hrubesh, and I. M. Thomas, "Partially Hydrolyzed Alkoxysilanes as Precursors for Silica Aerogels."

R. A. Van Konynenburg, "Radiation Effects in Glass, Ceramics, and Minerals."

C. E. Violet, P. A. Hahn, Z. Mei, T. Datta, C. Almasan, and J. Estrada, "High $T_c$ Superconducting $HoBa_2(Cu_{1-x}Fe_x)_3O_{7-x}$"

**American Chemical Society, Dallas, Tex., April 9–14, 1988**

M. S. Oh, R. W. Crawford, K. G. Foster, and A. Alcaraz, "Ammonia Evolution from Western and Eastern Oil Shale."

**Optical Society of America 4th Topical Meeting on Optical Interference, Tucson, Ariz., April 12–15, 1988**

N. L. Thomas, R. M. Bionta, P. C. Gabriele, A. E. Jankowski, and D. M. Makowiecki, "Young's Experiment at 1.54 Angstroms Using Sputtered Sliced Multilayers."

**American Welding Society Annual Meeting, New Orleans, La., April 19–22, 1988**

J. W. Elmer, "Measuring The Residual Ferrite Content of Rapidly Solidified Stainless Steel Alloys."

**Conference on Lasers and Electro-Optics, Anaheim, Calif., April 25–29, 1988**

J. E. Marion, "Optical Quality High Strength Laser Slabs."

H. Toratani, Y. Lee, H. Meissner, and J. E. Marion, "Ion Exchange Strengthening of Slab Lasers."

**SUBWOG 12C Meeting, Los Alamos, N. Mex., April 26, 1988**

W. S. Selig, "Determination of Gold and Molybdenum in Special Materials."

**3rd Topical Meeting on Tritium Technology in Fission, Fusion and Isotopic Applications, Toronto, Ontario, Canada, May 1–6, 1988**

P. R. Coronado, E. M. Fearon, R. G. Garza, J. E. Shaw, P. C. Souers, R. K. Stump, and R. T. Tsugawa, "$He^3$ Outgassing from Four Working Palladium and Uranium Beds."

R. A. Failor, P. C. Souers, and S. G. Prussin, "Comments on the Gas-Phase Initial Rate of Tritiated Water Formation."

E. M. Fearon, "Infrared Analysis of Liquid and Solid D-T."

E. M. Fearon, R. Garza, C. M. Griffith, S. R. Mayhugh, E. R. Mapoles, P. C. Souers, R. T. Tsugawa, J. D. Sater, G. W. Collins, and J. R. Gaines, "Synthesis and Stability of Liquid Molecular DT."

E. M. Fearon, "Triton Memory Time in Solid DT and its Nuclear Polarization."

J. L. Maienschein, F. E. McMurphy, and F. S. Uribe, "Tritium Storage in Ion-Exchanged Zeolites."

J. L. Maienschein, F. E. McMurphy, and V. L. DuVal, "Increase of Tritium Permeation Through Resistant Metals at 323 K by Lattice Defect."

C. T. Peng, R. L. Hua, P. C. Souers, and P. R. Coronado, "Tritium Labeling of Amino Acids and Peptides with Liquid and Solid Tritium."

P. C. Souers, E. M. Fearon, E. R. Mapoles, J. D. Sater, G. W. Collins, J. R. Gaines, R. H. Sherman, and J. R. Bartlit, "Triton Memory Time in Solid DT and its Nuclear Polarization."

P. C. Souers, E. M. Fearon, R. K. Stump, and R. T. Tsugawa, "Infrared Analysis of Liquid and Solid D-T."

W. Wilson, R. J. Borree, D. I. Chambers, Y. Chang, J. T. Merrill, P. C. Souers, and R. K. Wiggins, "A New Box System for a High Pressure Tritium Pump."

**American Ceramics Society, Cincinnati, Ohio, May 2–5, 1988**

M. J. Weber, "Laser Spectroscopy and Glass Structure."

J. Wong, "X-Ray Absorption Spectroscopy of Glasses."

J. Wong, and M. J. Weber, "XANES and EXAFS Studies of Glass."

**Materials '88: Materials and Engineering Design, London, England, May 9–13, 1988**

G. A. Henshall and A. K. Miller, "Physically-Based Constitutive Equations for Creep and Plasticity: Cyclic Deformation."

**ITER Magnet Specialists Meeting, Max Planck Institute for Plasma Physics, Garching, FRG, May 9–13, 1988**

M. W. Guinan, "Radiation Damage to Superconductors."

**American Geophysics Union Conference, Baltimore, Md., May 13–14, 1988**

J. J. DeYoreo and A. Navrotsky, "Thermochemistry of Framework Silicate Glasses in the Systems $NaM_3 + O_2$–$SiO_2$ ($M$ = Al, B, Fe, Ga)."

**U.S. Army Ballistics Research Laboratory Workshop on Composite Materials, Aberdeen, Md., May 24–25, 1988**

R. M. Christensen, "Failure of Composite Materials."

**International Symposium on Dissociative Recombination: Theory, Experiment, and Applications, Chateau Lake Louise, Alberta, Canada, May 28–31, 1988**

J. R. Hiskes and A. M. Karo, "Dissociative Recombination of $H_2^+$ and $H_3^+$ Ions on Surfaces."

**Workshop on Computational Methods for the Electronic Structure and Related Properties of Alloys, University of Kentucky, Lexington, Ky., May 30–June 10, 1988**

P. A. Sterne, "Electronic Structure of High Temperature Superconductors."

**3rd Chemical Congress of North America, Toronto, Ontario, Canada, June 5–11, 1988**

R. C. Cook, "A Molecular View of Bulk Deformation."

B. L. Haendler, L. M. Hair, and E-M. Kong, "The Application of Statistical Experimental Design to the Development of Low-Density Polymer Foams."

R. W. Pekala and R. E. Stone, "Low-Density Resorcinol-Formaldehyde Foams."

J. G. Reynolds, "Pyrolysis of Sunnyside (Utah) Tar Sand: Characterization of Volatile Compound Evolution."

J. G. Reynolds, "Characterization of Nickel and Vanadium Compounds in Tar Sand Bitumen by Petroporphyrin Quantitation and Size Exclusion Chromatography Coupled with Element Specific Detection."

**International Conference on Ion Beam Modification of Materials, Tokyo, Japan, June 12–17, 1988**

D. W. Brown, Z. A. Munir, and R. G. Musket, "Formation of a Nearly Pure Aluminum Layer in Beryllium using Ion Implantation and Post-implant Annealing."

**6th Target Fabrication Specialists Meeting, Los Alamos, N. Mex., June 20–24, 1988**

B. L. Haendler, R. C. Cook, D. L. James, F.-M. Kong, S. A. Letts, S. C. Mance, G. E. Overturf, III, D. L. Schumann, and J. Clarence Thomas, "Low-Density Polystyrene Foams for Direct-Drive Laser ICF Targets."

E. J. Hsieh and R. S. Upadhye, "An Integrated Model for Sputter Coating Uniformity."

K. Kim and R. S. Upadhye, "Formation of Spherical-Shell $SiO_2$ Aerogel Pellets Using the Sol-Gel Method."

F.-M. Kong, "Low-Density Resorcinol-Formaldehyde Foam for Direct-Drive Laser ICF Targets."

H. D. Kramer and R. S. Upadhye, "Development of a Die System for Molding Target Parts from Polystyrene."

E. F. Lindsey, C. W. Price, P. L. McCarthy, and M. A. Lane, "SEM Analyses of Machined Surfaces on Polystyrene Foam."

G. E. Overturf, "Drying Studies on Inverse Emulsion PS Foams."

C. W. Price, "Ion Microanalysis of Beryllium."

C. W. Price, P. L. McCarthy, and M. A. Lane, "Defects in Machined Aerogel Surfaces."

C. W. Price and P. L. McCarthy, "Low-Voltage Scanning Electron Microscopy of Target Materials."

**JOWOG-9, Albuquerque, N. Mex., June 20–24, 1988**

C. L. Coon, R. McGuire, P. F. Pagoria, and W. C. Tao, "Synthesis and Characterization of CL-20."

K. Scribner, "Th Effects of Process Variables on the Performance Characteristics of TATB."

R. L. Simpson, "Shock Initiation of Heterogeneous Explosives an Development of Imbedded Gauges."

P. A. Urtiew, "Shock Initiation of Heterogeneous Explosives and Development of Imbedded Gauges."

**Society of Engineering Science Annual Meeting, Berkeley, Calif., June 20–25, 1988**

R. M. Christensen, "Evaluation of a New Failure Criterion for Fibrous Composite Materials."

**American Crystallographic Association Annual Meeting, Philadelphia, Pa., June 26–July 1, 1988**

D. K. Smith, G. S. Smith, and R. L. Landingham, "Hysteresis in the Orthorhombic-Tetragonal Phase Transition of 123 Superconductor Materials as a Function of Oxygen Fugacity."

L. E. Tanner, "Premartensitic Microstructures."

**Combustion & Detonation Phenomena, Karlsruhe, FRG, June 29–July 1, 1988**

P. C. Crawford, R. L. Simpson, F. Helm, and J. Kury, "Shock Initiation Studies on Heterogeneous Explosives."

**Gordon Conference on Fuel Science, New Hampton, N.H., July 4–8, 1988**

A. K. Burnham, "Modeling the Kinetics of Petroleum Generation."

**International Conference on the Calculation of Phase Diagrams, Berkeley, Calif., July 7–10, 1988**

L. E. Tanner, "The Systematics of Phase Transformations in Metallic Alloys."

**Gordon Research Conference on Electronic Spectroscopy, Wolfeboro, N.H., July 17–22, 1988**

J. G. Tobin, "Spectroscopic Observation of the Formation and Deformation of a Surface Alloy."

**4th International Conference on the Structure of Non-Crystalline Materials, Oxnard, Calif., July 18–21, 1988**

M. J. Weber and J. Wong, "EXAFS/XANES Determination of the Rare Earth Environment in Fluoroberyllate Glasses: Comparison with Molecular Dynamics Simulations."

**Gordon Conference on Physical Metallurgy, Meriden, N.H., July 18–22, 1988**

A. F. Jankowski, "Strain Wave Effects in Metallic Multilayers."

**19th Annual Meeting of the Fine Particle Society, Santa Clara, Calif., July 19–22, 1988**

W. L. Barmore, L. W. Hrubesh, L. E. Keene, and E. L. Raymond, "RF Induction-Plasma Apparatus for Generating Submicron Particles of Metals."

C. W. Price, "Microstructural Characterization of Low-Density Foams."

**International Conference on Magnetism, Paris, France, July 25–29, 1988**

C. S. Wang, P. A. Sterne, P. G. McQueen, and A. Bhattacharya, "Magnetic Interactions in High-$T_c$ Superconductors."

**23rd Inter-Society Energy Conversion Engineering Conference, Denver, Colo., July 31–August 5, 1988**

W. A. Steele, P. B. Mohr, H. R. Leider, and T. B. Hirschfeld, "A Novel Approach to Abrasion Resistance."

**Denver X-Ray Conference, Steamboat Springs, Colo., August 1–5, 1988**

J. H. Kinney, M. C. Nichols, Q. C. Johnson, U. Bonse, R. A. Saroyan, R. Nusshardt, and R. Pahl, "Advances in Two and Three Dimensional Chemical State Imaging using Synchrotron Radiation."

**Gordon Conference on Water and Aqueous Solutions, Plymouth, N.H., August 1–5, 1988**

D. G. Miller, "Transport Properties in Mixed Electrolyte Solutions: Results from the International Collaboration on the $NaCl$-$MgCl_2$-$H_2O$ System."

**International Conference on Synchrotron Radiation Instrumentation, SRI-88, Tokyo, Japan, August 1988**

J. Cerino and J. Wong, "Beam Line 10: A Multipole Wiggler Beamline at SSRL."

**Quantitative Nondestructive Evaluation Conference, La Jolla, Calif., August 2–3, 1988**

J. H. Kinney, M. C. Nichols, Q. C. Johnson, U. Bonse, R. A. Saroyan, and R. Nusshardt, "Synchrotron Microtomography: The 'Inside' Story."

**Gordon Research Conference on Glass, Tilton Academy, N.H., August 1–5, 1988**

M. J. Weber, "Optical Studies of the Structure of Glass."

**Microbeam Analysis Society, San Francisco, Calif., August 7–12, 1988**

J. H. Kinney, Q. C. Johnson, M. C. Nichols, U. Bonse, R. A. Saroyan, R. Nusshardt, and R. Pahl, "Three-Dimensional X-Ray Microtomography: Principles and Applications."

**Gordon Conference on Physical Electrochemistry, New London, N.H., August 8–12, 1988**

J. C. Farmer, "Physical Electrochemistry."

**46th Annual Meeting of the Electron Microscopy Society of America, Milwaukee, Wis., August 8–12, 1988**

E. F. Lindsey, C. W. Price, E. L. Pierce, and E. J. Hsieh, "SEM Analysis of DC Magnetron Sputtered Beryllium Films."

M. L. Sattler and M. A. O'Keefe, "Identification of Periodic Structure Characterized from Amorphous Support by Simulation and Processing Techniques."

**International Society for Optical Engineering, Meeting on X-Ray Multilayers for Diffractometers, Monochromators and Spectrometers, San Diego, Calif., August 14–19, 1988**

R. Bionta, E. Ables, K. Cook, O. Edwards, P. Gabriele, A. F. Jankowski, D. Makowiecki, L. Ott, and N. Thomas, "Sputtered-Sliced Multilayers: Zone Plates and Transmission Gratings for 8 keV X-Rays."

A. F. Jankowski, and D. M. Makowiecki, "Manufacture, Structure and Performance of $W/B_4C$ Multilayer Mirrors."

**14th Underground Coal Gasification Symposium, Chicago, Ill., August 15–18, 1988**

G. A. Metzger and J. A. Britten, "Data Acquisition System and Instrumentation for the Rocky Mountain I Coal Gasification Test."

**5th International Conference on X-Ray Absorption Fine Structure, Seattle, Wash., August 21–26, 1988**

R. B. Greegor, F. W. Lytle, D. R. Sdanstrom, M. J. Weber, and J. Wong, "Site Selectivity in Mn Glass Using Optical XANES."

R. B. Greegor, F. W. Lytle, B. C. Chakoumakos, R. C. Ewing, R. J. Livak, F. W. C. Jr., E. D. Crozier, N. Alberding, A. J. Seary, G. W. Arnold, M. J. Weber, J. Wong, and W. J. Weber, "Application of Various EXAFS Techniques to the Investigation of Structurally Damaged Materials."

J. Wong, "Metal Sites and Bonding in Beta-Boron."

J. Wong, "EXAFS on Near Monolayer of Hafnium."

J. Wong, "Solute Pairing in Solution Hardened FCC Alloys."

**4th International Conference on Infrared Physics, Zurich, Switzerland, August 22–26, 1988**

L. W. Hrubesh, R. Staffin, D. B. Boercker, and T. Wainright, "Studies of Polymer Foam Morphology with FIR Laser Scattering."

**European Electron Microscopy Conference, York, England, September 4–9, 1988**

D. Schryvers, "High-Resolution Observations in the Omega Phase Structure in Ti-Mo Alloys."

**Symposium on Synchrotron Radiation-Photon Beam Lines, Taipei, Taiwan, September 10–12, 1988**

U. Bonse, J. H. Kinney, and M. C. Nichols, "Chemically Specific Microtomography Using Synchrotron Radiation."

**2nd International Symposium on Aerogels, Montpellier, France, September 21–23, 1988**

R. W. Pekala and F.-M. Kong, "A Synthetic Route to Organic Aerogels—Mechanism, Structure, and Properties."

T. M. Tillotson, L. W. Hrubesh, R. W. Pekala, and J. D. LeMay, "Properties of Partially Condensed Silica Derived Aerogels."

**Metallurgical Society/American Institute of Mechanical Engineers Fall Meeting, Chicago, Ill., September 25–29, 1988**

A. F. Jankowski and R. M. Bionta, "Multilayer X Ray Optics."

M. E. Kassner, P. H. Adler, M. G. Adamson, and D. E. Peterson, "Evaluation and Thermodynamic Analysis of Phase Equilibria in the U-Al System."

L. E. Tanner, "Phase Transformations in Rapidly Solidified Al-Be and Al-Be-Li Alloys."

**National Meeting of the American Chemical Society, Los Angeles, Calif., September 25–30, 1988**

D. M. Hoffman, "Anelastic and Thermal Properties of Ethylene/Acrylic Acid Copolymers Partially Ionized with Transition Metals."

J. G. Reynolds, "Real-Time, On-Line Determination of Carbon Monoxide in Fossil Energy Research using Charge Exchange with Krypton in a Triple Quadrupole Mass Spectrometer."

M. O. Riley, C. M. Walkup, and E. S. Jessop, "Spectral Filters Based on Ethylene/Acrylic Acid Copolymer Ionomers."

J. G. Tobin, "Using Core Skirt Measurements to Follow Surface Alloying and Mixing."

**7th International Symposium on the Thermodynamics of Nuclear Materials, Chicago, Ill., September 26–29, 1988**

O. H. Krikorian and D. Y. Lai, "Modeling of Heat Capacities of Metals."

**World Materials Congress, "Atomistic Modeling: Beyond Pair Potentials," Chicago, Ill., September 26–30, 1988**

A. Gonis, X.-G. Zhang, P. E. A. Turchi, G. M. Stocks, W. H. Butler, and D. M. Nicholson, "Symposium on Concentration Dependent Effective Interactions in Substitutional Alloys."

A. Gonis, P. E. A. Turchi, X.-G. Zhang, G. M. Stocks, D. M. Nicholson, and W. H. Butler, "Concentration and Temperature Dependent Effective Cluster Interactions in Substitutional Disordered Alloys."

A. Gonis, X.-G. Zhang, G. M. Stocks, W. H. Butler, and D. M. Nicholson, "Concentration Dependent Effective Interactions in Substitutional Alloys."

**American Vacuum Society, Atlanta, Ga., October 3-4, 1988**

A. F. Jankowski, L. R. Schrawyer, M. A. Wall, and D. M. Makowiecki, "Interfacial Bonding in W/C and W/$B_4C$ Multilayers."

J. G. Tobin, "Column 1B Metal Adsorption on Ge(111) = the Growth Mode of Cu(001)."

**JOWOG 22, Pu SUBWOG, Los Alamos, N. Mex., October 4–6, 1988**

R. S. Rosen, M. E. Kassner, and J. J. Oldani, "Simple Constitutive Relationships for the Yield and Alternate Strengths of Alloyed Plutonium in Compression Tension and Torsion."

**JOWOG 22D, AWE Aldermaston, U.K., October 4–11, 1988**

J. W. Elmer and T. W. Eagar, "Measuring the Ferrite Content of Stainless Steel Alloys Using a Vibrating Sample Magnetometer."

**Workshop on Applications of Copper as a Nuclear Waste Containment Material, Paris, France, October 5–7, 1988**

R. D. McCright, "Status of Yucca Mountain Project Container Work."

R. D. McCright, "General, Localized and Stress Corrosion of Copper-Based Materials."

R. D. McCright, "Fabrication and Welding Processes for Copper-Based Materials."

**Commissariat a l'Energie Atomique, Fontenay-aux-Roses, France, October 7, 1988**

R. D. McCright, "Status of Yucca Mountain Project Container Work (Copper, Iron, and Nickel-Based Materials)."

**Festkolloquium Anlasslich des 70. Geburtstages von Prof. Dr. Rolf Haase, Technische Hochschule, Aachen, FRG, October 7, 1988**

D. G. Miller, "Application of Irreversible Thermodynamics to Electrolyte Mixtures: Results from the International Collaboration on the Transport Properties of NaCl-$MgCl_2$-$H_2O$."

**XIIth Materials Research Society Symposium on the Scientific Basis for Nuclear Waste Management, Berlin, FRG, October 9–13, 1988**

J. C. Farmer, "Status of Yucca Mountain Project Container Work (Copper, Iron, and Nickel-Based Materials)."

V. M. Oversby, "Uranium Transport in Topopah Spring Tuff: An Ion Microscope Investigation."

**17th Annual North American Thermal Analysis Society Meeting, Buena Vista, Fla., October 10, 1988**

D. M. Hoffman, "Dynamic Mechanical and Thermal Analysis of Crystallinity Development in Kel-F 800 and TATB/Kel-F 800 Plastic Bonded Explosives. Pt. I. Kel-F 800."

**International Seminar on High Energy Working of Rapidly Solidified Materials, Novosibirsk, U.S.S.R., October 10–14, 1988**

W. J. Nellis, R. L. Landingham, and J. B. Holt, "Shock Compaction of Superconductors."

**JOWOG 28/12th DOE Ceramics Workshop, Albuquerque, N. Mex., October 10–14, 1988**

M. S. Costantino and B. Holt, "Combustion Synthesis under High Gas Pressure."

M. S. Costantino, "High Pressure Processing of Oxide Superconductors."

P. G. Curtis and O. H. Krikorian, "Development of Oxidation-Resistant Coatings for Refractory Metals at 1200–1800°C."

O. H. Krikorian and P. G. Curtis, "Development of Ceramic Coatings for Molten Metal Containment."

H. R. Leider, "A Retrospective Discussion of LLNL's Approach to Materials Aging."

J. D. LeMay, "Low-Density, Fine Morphology Foams from Macroporous Epoxy Gels."

J. D. LeMay, T. M. Tillotson, and L. W. Hrubesh, "Mechanical Properties of Aerogels Derived from Partially Condensed Silica."

R. W. Pekala, "The Structure and Properties of Organic Aerogels."

A. A. Tesar, "Advanced Laser Glass Development."

**2nd Annual Connoisseur Users Meeting, Ft. Meade, Md., October 11, 1988**

E. T. Mones, "Recommended Belt Furnace Sealing of Microelectronic IC's."

**Conference of the American Association for Crystal Growth, Atlantic City, N.J., October 19–21, 1988**

L. J. Atherton, R. W. Martin, D. H. Roberts, and J. F. Cooper, "Induction Heating for Bridgman Crystal Growth: Model Predictions and Experimental Results."

J. F. Cooper, H. Lugg, M. Shinn, D. Roberts, and L. J. Atherton, "Growth of Yttrium Aluminum Garnet by Gradient Freeze Technique."

**Neutral Particle Beam Annual Program Review, Los Alamos, N. Mex., October 19–21, 1988**

J. R. Hiskes, and A. M. Karo, "Recombination and Dissociative Recombination of $H_2^+$ and $H_3^+$ Ions on Surfaces with Application to Volume Sources."

**1st International Symposium on Combustion and Plasma Synthesis of High Temperature Materials, San Francisco, Calif., October 23–26, 1988**

J. B. Holt and Z. A. Munir, "Symposium on Combustion and Plasma Synthesis."

**15th DOE Compatibility, Aging and Service Life Conference, Miamisburg, Ohio, October 25–26, 1988**

A. Alcaraz, R. W. Crawford, and K. G. Foster, "Determination of Water in $Er_2O_3$ Using On-Line Mass Spectrometry."

**30th Annual Meeting of the Division of Plasma Physics of the American Physical Society, Hollywood, Fla., October 31–Nov. 4, 1988**

J. R. Hiskes and A. M. Karo, "Recombination and Dissociative Recombination of $H_2^+$ and $H_3^+$ Ions on Surfaces."

J. R. Hiskes and A. M. Karo, "Studies of Relaxation and Recombination Processes During $H^+$ Bombardment of Metal Surfaces at Low and Intermediate Energies."

**Welding Research Council Subcommittee on the Welding of Stainless Steels, New York, N.Y., November 2, 1988**

J. W. Elmer and T. W. Eagar, "Measuring the Ferrite Content of Rapidly Solidified Stainless Steel Alloys."

**15th DOE Surface Studies Conference, Clearwater Beach, Fla., November 1–3,1988**

C. W. Price, C. W. Hatcher, and P. J. Wegner, "Analysis of Surface Deposits and Films on Nova Debris Shields."

C. W. Price, "Calculations of Surface Energies and Surface-Force Tensors from Simulated Crystal Surfaces."

**American Ceramics Society, Glass Division, Tucson, Ariz., November 6–9, 1988**

J. P. Campbell, A. Tesar, L. Weinzapfel, and M. Weber, "Effect of Composition on the Spectroscopic Properties of Nd-doped Fluoride Glasses."

J. Campbell, A. Tesar, C. Weinzapfel, M. Weber, Y. Lin, H. Meissner, and H. Toratani, "Effect of Composition on the Spectroscopic Properties of $Nd^{3+}$-Doped Fluoride Laser Glasses."

A. A. Tesar and M. Suscavage, "Concentration Quenching in Nd-doped Fluoride Glasses."

**American Physical Society, Conference on the Applications of Accelerators in Research and Industry, Denton, Tex., November 7–9, 1988**

R. G. Musket, "Applications of Ion Implantation for Modifying Interactions between Metals and Hydrogen Gas."

**DOE Integrated Contractors Meeting and SUBWOG 12A Meeting on Coatings, Sandia National Laboratories, Livermore, Calif., November 8–10, 1988**

A. F. Jankowski, D. M. Makowiecki, and R. M. Bionta, "Multilayer X Ray Optics for Reflection and Transmission."

J. C. Farmer, W. D. Bonivert, and J. T. Hachman, "Tuned Frequency Reversible Impedance Probe for the Measurement of Dilute Organic Additives for Electroplating Baths."

**25th Semi-Annual Bay Area Conference on High Temperature Science and Technology, Lawrence Berkeley Laboratory, Berkeley, Calif., November 9, 1988**

O. H. Krikorian, "Modeling of Heat Capacity of Metals."

**International Symposium on Multiphase Macromolecular Systems, at the 14th Biennial Meeting of the ACS Division of Polymer Chemistry, San Diego, Calif., November 19–23, 1988**

J. D. LeMay, "Low-Density, Ultra-Fine Morphology Foams from Macroporous Epoxy Gels."

**Fall Meeting of the Materials Research Society, Boston, Mass., November 28–December 3, 1988**

J. Chaudhuri, S. Shah, and A. F. Jankowski, "X Ray Diffraction Analysis of Au/Ni Multilayers."

S. J. DeTeresa and R. J. Farris, "The Prime Importance of Second-Order Effects in Rigid-Rod Polymers."

J. S. Huang, R. G. Musket, and M. A. Wall, "Phase and Microstructures of Carbon-Implanted Niobium."

A. F. Jankowski, "Coherency Strain Modeling of Elastic Moduli in Cu/Nb Multilayers."

D. M. Nicholson, G. M. Stocks, W. M. Temmerman, P. A. Sterne, and D. G. Pettifor, "Structural Twin Difference in $Al_3Ti$: The Role of Tetragonal Distortion in APB and Twin Energies."

S. R. Nutt, R. Green, W. D. Nix, S. Baker, and A. F. Jankowski, "Gold-Nickel Multilayer Films: Structure-Property Correlations."

T. Tsakalakos and A. F. Jankowski, "Critical Phenomena in Nanoscale Multilayer Materials."

**1988 Eastern Oil Shale Symposium, Lexington, Ky., November 30, 1988**

T. T. Coburn, R. W. Taylor, and C. J. Morris, "Laboratory Studies of New Albany Shale Flash Pyrolysis Under Solid-Recycle Conditions: Chemistry and Kinetics."

J. G. Reynolds, "Programmed Temperature Pyrolysis Comparing Big Clifty (Kentucky) Tar Sand and Asphaltene from Laboratory and Pilot Plant Extracted Bitumen."

**American Geophysical Union Conference, San Francisco, Calif., December 6–10, 1988**

J. J. DeYoreo and A. Navrotsky, "The Heat Contents of Partial Melts: Theoretical Considerations and Preliminary Experimental Data."

**DOD/DOE Coordination Meeting on Advanced Armor/Anti-Armor Materials and Advanced Computational Methods, Alexandria, Va., December 13–15, 1988**

R. L. Landingham, "Processing and Mechanical Behavior of Advanced Ceramics."

**French-Israeli Workshop on Solid State Lasers, Jerusalem, Israel, December 12–15, 1988**

M. J. Weber, "The Search for Solid State Fusion Lasers."

**Livermore–Los Alamos High Explosives Information Exchange Meeting, Los Alamos, N. Mex., December 13–14, 1988**

A. Nichols, "Structure and Dynamics of Molecular Fluids under High Density Conditions."

**Joint AAAS–APT Symposium on Synchrotron Radiation, San Francisco, Calif., January 1989**

J. Wong, "Materials Studies Using X-Ray Absorption Spectroscopy."

**Gordon Research Conference on Composites, Ventura, Calif., January 9–13, 1989**

S. J. DeTeresa and R. J. Farris, "The Prime Importance of Second-Order Effects in Anisotropic Materials."

**XVIII Informal Conference on Photochemistry, Santa Monica, Calif., January 9–13, 1989**

W. E. Conaway and C. G. Stevens, "State-to-State Photodissociation from Highly Excited Vibrational States of $H_2O$."

**Acta/Scripta Conference on Metal/Ceramic Interfaces, Santa Barbara, Calif., January 15–19, 1989**

Z.-G. Zhang, E. C. Sowa, and A. Gonis, "A First-Principles Method for the Determination of the Electronic Structure of Grain Boundaries."

**SPIE's OE/LASE '89 Meeting on Optics, Electro-Optics and Laser Applications in Science and Engineering, Los Angeles, Calif., January 18–20, 1989**

J. R. Hiskes and A. M. Karo, "Recombination and Dissociative Recombination of $H_2^+$ and $H_3^+$ Ions on Surfaces with Application to Hydrogen Negative Ion Sources."

J. E. Marion and A. J. Pertica, "Materials for High Average Power Lasers."

E. Milanovich, J. Hunt, and J. Roe, "Measurement of Optical Loss in Transparent Solids Using a Novel Spectrometer Based on Optical Cavity Decay."

**Japan/U.S. Workshop on Radiation Damage: Theory and Calculation, Tsukuba, Japan, January 18–20, 1989**

M. W. Guinan, "The Role of Molecular Dynamics in the Study of High Energy Cascades."

**12th Golden Gate Polymer Forum Asilomar Conference on Polymeric Materials, Pacific Grove, Calif., February 12–15, 1989**

S. J. DeTeresa, "High Performance Fibers in Compression."

**The WATTEC Conference, Knoxville, Tenn., February 14–17, 1989**

F. M. Matthews, C. M. Walkup, I. L. Chiu, and D. M. Hoffman, "Adhesives for Special Foams."

**Annual Meeting of the Adhesion Society, Hilton Head Island, S.C., February 20–22, 1989**

R. G. Musket, "Ion-beam Stitching at Oxide/Oxide Interfaces."

**4th International Conference on Ultrastructure Processing of Ceramic, Glasses and Composites, Tucson, Ariz., February 20–24, 1989**

R. W. Pekala, "Aerogels and Xerogels from Organic Precursors."

M. J. Weber, "Optical Studies of the Local Environment of Rare Earth Ions in Glass."

**U.S./U.S.S.R. Exchange on Irradiation and Post-Irradiation Testing of Fusion Materials, Santa Barbara, Calif., February 21–23, 1989**

M. W. Guinan, "Role of Molecular Dynamics in Radiation Effects Modeling."

**Metallurgical Society, American Institute of Mechanical Engineers, Las Vegas, Nev., February 27–March 3, 1989**

J. S. Huang and C. F. Gallegos, "Tensile Behaviors of Group VB and VIB Refractory Metals and Alloys in Liquid U: Strain Rate Effects."

S. R. Stock, T. M. Breunig, S. D. Antolovich, A. Guvenilir, J. H. Kinney, Q. C. Johnson, M. C. Nichols, U. Bonse, D. J. Bowen, and J. C. Elliot, "Microtomography of Damage in SiC/Al Continuous Fiber Composites."

**5th Tank Automotive Command Armor Coordinating Conference for Combat Vehicles, Monterey, Calif., March 7–9, 1989**

R. L. Landingham, "Advanced Lightweight Armor Projects (ALAP) at LLNL."

**4th International Conference on Mechanical Properties of Material at High Rates of Strain, Oxford, England, March 20–22, 1989**

W. G. Gourdin, "Constitutive Properties of Copper and Tantalum at High Rates of Tensile Strain: Expanding Ring Results."

**American Physical Society Annual Meeting, St. Louis, Mo., March 20–24, 1989**

G. W. Collins, P. C. Souers, E. R. Mapoles, and J. R. Gaines, "Properties of H and D Atoms in Solid Molecular HD."

A. Gonis, X.-G. Zhang, J. M. MacLaren, R. C. Albers, S. Crampin, and D. D. Vveddensky, "An Alternative Layer-Korringa-Kohn-Rostoker (LKKR) Approach to Surface and Interface Electronic Structure."

M. S. Costantino, H. B. Radousky, J. L. Peng, and R. L. Shelton, "Superoxygenation of $Pr_xY_{(1-x)}Ba_2Cu_3O_{(7+y)}$."

D. M. Nicholson, G. M. Stocks, W. M. Temmerman, and P. A. Sterne, "Total Energy Calculations of NiAl and FeAl: Implication for Slip Behavior."

P. C. Souers, E. M. Fearon, E. R. Mapoles, J. R. Gaines, and P. A. Fedders, "Nuclear Relaxation Time of Tritiated Solid Hydrogen Adsorbed onto Silica Aerogel."

E. C. Sowa, A. Gonis, X.-G. Zhang, and S. M. Foiles, "The Electronic Structure of Unrelaxed and Relaxed Grain Boundaries."

C. E. Violet, R. G. Bedford, P. A. Hahn, N. W. Winter, and Z. Mei, "Local Oxygen Configurations Relative to Fe-Probe Ions in $HoBa_2(Cu_{0.95}Fe_{0.05})_3O_{7-x}$."

X.-G. Zhang, A. Gonis, and J. M. MacLaren , "A New Method for the Determination of Electronic Structure."

**1989 Mössbauer Spectroscopy Institute, Ft. Worth, Tex., March 27–31, 1989**

C. E. Violet, "Application of Mössbauer Spectroscopy to Metallurgy."

C. E. Violet, "Application of Mössbauer Spectroscopy to High $T_c$ Superconductors."

**Conference on Lasers and Electro-Optics, Baltimore, Md., April 1, 1989**

J. A. Caird, J. E. Marion, F. P. Milanovich, N. D. Nielsen, A. J. Pertica, and J. N. Roe, "Passive Optical Losses in Laser Glass."

M. Shinn, F. Milanovich, and J. Roe, "Determination of the Stimulated Emission Cross Section for the Laser Transition in YAG: Nd."

**American Institute of Chemical Engineers National Meeting, Houston, Tex., April 2–6, 1989**

M. W. Droege, L. M. Hair, W. J. Pitz, and C. K. Westbrook, "The Thermal Gas Phase Reactions of Methane and Oxygen: A Comparison of Model Calculations and Experimental Results."

**American Welding Society Annual Meeting, Washington, D.C., April 2–7, 1989**

J. W. Elmer and T. W. Eagar, "Variations in the Geometric Shape of Electron Beam Welds."

**Scanning 89/Electron Microscopy West Conference, Long Beach, Calif., April 5–7, 1989**

P. L. Perry and M. L. Sattler, "Orientation Procedures for TEM Characterization of Interfaces in X-Ray Beamsplitters."

C. W. Price, "Low-Voltage Scanning Electron Microscopy of Beryllium."

**American Chemical Society, Dallas, Tex., April 10–14, 1989**

R. W. Pekala and F.-M. Kong, "Resorcinol-Formaldehyde Aerogels and the Carbonized Derivatives."

J. G. Reynolds, "Can the D 2007-80 with Asphaltene Precipitation (SARA) Separation, Size Exclusion Chromatography with Element Specific Detection, and Hydrogen Distribution by NMR Help at all Predicting Residuum Processability?"

**National Association of Corrosion Engineers, New Orleans, La., April 14–21, 1989**

J. C. Farmer and R. D. McCright, "A Review of Models Relevant to the Prediction of Performance of High-Level Radioactive Waste Disposal Containers."

**16th International Conference on Metallurgical Coatings, San Diego, Calif., April 17–21, 1989**

A. F. Jankowski and M. A. Wall, "Transmission Electron Microscopy of Ni/Ti Neutron Mirrors."

**25th JOWOG-12, Los Alamos, N. Mex., April 17–21, 1989**

C. Colmenares, R. L. Smith, and S. Torres, "Effect of Alpha Irradiation on Fluorocarbons."

O. H. Krikorian and P. G. Curtis, "Development of Oxidation-Resistant Coatings for Niobium."

C. Pruneda, "Insensitive Munitions Efforts at LLNL."

**Corrosion/89, National Association of Corrosion Engineers, New Orleans, La., April 17–21, 1989**

J. C. Farmer and R. D. McCright, "A Review of Models Relevant to the Prediction of Performance of High-Level Radioactive Waste Disposal Containers."

**1989 Natural Gas R&D Contractors Review Meeting, Morgantown, W.Va., April 18–19, 1989**

M. W. Droege, "The Conversion of Methane to Liquid Hydrocarbons."

**DOE Workshop on HT Detection Technologies, Savannah River, S.C., April 18–19, 1989**

F. Magnotta, B. Failor, A. Ramponi, and C. G. Stevens, "Advanced Lasers and Cryogenic Targets for Ultra Trace Detection of HT."

**International Congress on Optical Science and Engineering, Paris, France, April 24–28, 1989**

D. F. Edwards, P. P. Hed, and J. E. Marion, "Subsurface Damage Produced During the Processing of Glass."

J. E. Marion, "Advanced Phosphate Glasses for High Average Power Lasers."

**Materials Research Society, San Diego, Calif., April 24–29, 1989**

H. B. Radousky and M. S. Costantino, "Superoxygenation Studies of $Y_{(1-x)}Pr_xBa_2Cu_3O_7$."

M. L. Sattler, "Characterization of Highly Dispersive Multilayer Mirrors for Amplitude Modulation of Soft X-Rays Using High Resolution Electron Microscopy."

C. E. Violet, C. I. Merzbacher, B. P. Bonner, R. G. Bedford, and P. A. Hahn, "Diffuse Reflectance Infrared Spectroscopy as an Indicator of Oxygen Content and Annealing History of $YBa_2Cu_3O_{7-y}$."

C. E. Violet and N. W. Winter, "Quantum Chemistry Calculation of the Electric Field Gradients in $YBa_2Cu_3O_{7-x}$."

**2nd International Conference on Trends in Welding Research, Gatlinburg, Tenn., May 14–18, 1989**

J. W. Elmer, S. M. Allen, and T. W. Eagar, "Microstructural Development During Rapid Solidification of Stainless Steel Alloys."

**2nd Workshop on Computational Methods for the Electronic Structure and Related Properties of Alloys, Lexington, Ky., May 14–26, 1989**

P. A. Sterne, "Band Theory of Rare Earth Metals."

**The Golden Gate Polymer Forum Asilomar Conference on Composites: Structure, Function and Analysis, Pacific Grove, Calif., May 14–16, 1989**

S. J. DeTeresa, "High Performance Fibers in Compression."

**Bay Area 26th High Temperature Science and Technology Symposium, Sandia National Laboratories, Livermore, Calif., May 18, 1989**

J. S. Huang and G. F. Gallegos, "Behaviors of Refractory Metals in Liquid U."

**ASMS Conference on Mass Spectrometry and Allied Topics, Miami Beach, Fla., May 21–26, 1989**

R. W. Crawford, T. T. Coburn, and A. Alcaraz, "The On-Line Determination of Water by Mass Spectrometry."

**Societe National des Poudres et Explosifs, Sourges, France, May 26, 1989**

J. E. Harrar, "Electrochemistry and Analytical Chemistry of Dinitrogen Pentoxide/Nitric Acid Solutions."

**Gas Research Institute, Joint Physical Sciences and Chemical Process, Methane Reaction Science and Methane Processes Contracts Review Meeting, Chicago, Ill., May 31, 1989**

M. W. Droege, "The Conversion of Methane to Hydrocarbons."

**Society of Petroleum Engineers National Meeting, Dallas, Tex., June 7–9, 1989**

M. W. Droege, L. M. Hair, W. J. Pitz, and C. K. Westbrook, "Partial Oxidation Reactions of Methane and Oxygen."

**Gas Research Institute Annual Review Meeting, Houston, Tex., June 9, 1989**

M. W. Droege, "The Gas Phase Reactions of Methane and Oxygen."

**44th Symposium on Molecular Spectroscopy, Columbus, Ohio, June 14, 1989**

C. E. Violet, N. W. Winter, R. M. Pitzer, C. I. Merzbacher, and D. K. Temple, "Spectroscopy of High Temperature Superconductors."

**1st Symposium on Advances in Coal Spectroscopy, Salt Lake City, Utah, June 14, 1989**

M. S. Oh, R. W. Crawford, T. T. Coburn, A. Alcaraz, and A. K. Burnham, "The On-Line Determination of Water by Mass Spectrometry."

**2nd International Conference on Materials and Mechanisms of Superconductivity, Stanford, Calif., June 23–28, 1989**

R. H. Howell, H. B. Radousky, A. L. Wachs, M. J. Fluss, P. E. A. Turchi, Y. C. Jean, C. S. Sundar, C. W. Chu, R. N. Shelton, and D. G. Hinks, "Systematics in Positron Annihilation Lifetime Analysis of High $T_c$ Superconducting Transitions."

C. Sundar, A. Bharathi, Y. C. Jean, D. G. Hinks, B. Dabrowksi, Y. Zheng, A. W. Mitchell, J. C. Ho, R. H. Howell, A. L. Wachs, P. E. A. Turchi, M. J. Fluss, R. L. Meng, P. H. Hor, Z. J. Huang, and C. W. Chu, "The Electronic Properties of High $T_c$ Superconductors Probed by Positron Annihilation."

C. E. Violet, R. G. Bedford, P. A. Hahn, N. W. Winter, and Z. Mei, "Local Oxygen Configurations Relative to Fe-Probe Ions in $HoBa_2(Cu_{0.95}Fe_{0.05})O_{7-x}$."

C. E. Violet and N. W. Winter, "Calculation of the Nuclear Quadrupole Resonance Spectra of $YBa_2Cu_3O_{7-x}$."

C. E. Violet, H. M. Ledbetter, J. D. Thompson, and S. A. Kim, "Low-Temperature Elastic Constants of Polycrystalline $La_2CuO_4$ and $La_{1.85}Sr_{0.15}CuO_4$."

A. L. Wachs, P. E. A. Turchi, R. H. Howell, Y. C. Jean, M. J. Fluss, R. N. West, J. H. Kaiser, S. Rayner, H. Hahgighi, K. L. Merkle, and A. Revcolevschi, "Electron-Positron Momentum Distribution Measurements of High-$T_c$ Superconductors and Related Systems."

**49th Annual Physical Electronics Conference, Seattle, Wash., June 26–28, 1989**

E. C. Sowa, A. Gonis, and X.-G. Zhang, "First-Principles Calculations of the Electronic Structure of Grain Boundaries."

**Taiwan Synchrotron Radiation Research Center Users Meeting, Taipei, Taiwan, July 1989**

J. Wong, "Applications of EXAFS and XANES to Materials Science."

**XV International Congress on Glass, Leningrad, U.S.S.R., July 2–7, 1989**

M. J. Weber, "Science and Technology of Laser Glasses."

**Gordon Research Conference on Thermosetting Polymers, Plymouth, N.H., July 3–7, 1989**

L. Chiao, "Mechanistic Modeling of Epoxy Resins."

J. D. LeMay, "Low-Density, Ultrafine Morphology Foams from Macroporous Epoxy Gels."

**JOWOG 28A, Aldermaston, England, July 10–14, 1989**

L. W. Hrubesh, J. F. Poco, W. E. Sunderland, T. M. Tillotson, and S. A. Steward, "Process Optimization for Silica Aerogels."

J. D. LeMay, "Mechanical Structure-Property Relationships of Organic and Inorganic Low-Density Aerogels."

J. D. LeMay, "Mechanical Structure-Property Relationships of Microcellular Low-Density Foams."

**3rd Annual "Thick Composites in Compression" Workshop, Knoxville, Tenn., July 11–12, 1989**

S. J. DeTeresa, "Compressive Failure of Graphite Fibers."

**American Crystallographic Association Annual Meeting, Seattle, Wash., July 23–28, 1989**

A. F. Jankowski, "Short Period Multilayers: Interface Dominated Structures."

E. M. Larson, J. Wong, and M. J. Weber, "The Determination of the Near Neighbor Environment of $Nd^{3+}$ in a Series of $BeF_2$ Laser Glasses Using X-Ray Absorption Spectroscopy."

J. Wong, "Coordination of Nd in Binary Alkali $BeF_2$ Glasses."

**ASNT Topical Meeting on Industrial Computed Tomography, Seattle, Wash., July 25–27, 1989**

J. H. Kinney, "X-Ray Tomographic Microscopy."

**6th International Conference on Synchrotron Radiation Instrumentation, Berkeley, Calif., August 1989**

J. Wong, "$YB_{66}$: A New Soft X-Ray Monochromator for Synchrotron Radiation."

**47th Annual Meeting of the Electron Microscopy Society of America, San Antonio, Tex., August 6–11, 1989**

E. F. Lindsey, C. W. Price, R. M. Franks, and M. A. Lane, "Stereoscopic Analyses of Surfaces on Polystyrene Foam."

C. W. Price, E. F. Lindsey, R. M. Franks, and M. A. Lane, "Characterization of Machined Polystyrene Foam."

M. L. Sattler, "HRTEM Simulation of Interfacial Structure in Amorphous Multilayers."

**International Society for Optical Engineering Meeting on X-Ray/EUV Optics for Astronomy and Microscopy, San Diego, Calif., August 6–11, 1989**

P. C. Gabriele, R. M. Bionta, and A. F. Jankowski, "Cylindrical X-Ray Multilayer Monochromator."

A. F. Jankowski, "W/C Mirror Deposition Optimization."

**LABCOM SHS Working Group, U.S. Army Materials Technology Laboratory, Watertown, Mass., August 8–9, 1989**

M. S. Costantino and C. Firpo, "High Pressure Combustion Synthesis of $Si_3N_4$ and AlN."

**American Physical Society, Topical Conference on Shock Compression of Condensed Matter, Albuquerque, N. Mex., August 14–17, 1989**

L. G. Green and D. Erskine, "VISAR Measurements of Explosive Reaction Zones."

**9th Symposium (International) on Detonation, Portland, Oreg., August 27–September 1, 1989**

D. Aldis, E. Lee, R. Simpson, and A. Weston, "Model Calculations for the Response of HMX Porous Beds to Deflagration and Shock."

D. Aldis, P. Urtiew, L. Erickson, and C. Tarver, "Effects of Initial Temperature on Shock Initiation of LX-17."

R. D. Breithaupt, M. Murphy, R. Simpson, and C. Tarver, "Reactive Flow Measurements and Model Development for Composite Explosives."

R. D. Breithaupt, K. Bahl, C. Tarver, and W. V. Holle, "Fabry-Perot Velocimetry on Detonating LX-17 in Planar Spherically Divergent Geometries."

R. D. Breithaupt, J. Kury, and C. Tarver, "Detonation Product Equation of State for Baratol."

P. Crawford, E. H. Helm, R. Simpson, and J. Kury, "Particle Size Effects in the Initiation of Explosives Containing Reactive and Non-Reactive Continuous Phases."

L. Erickson, D. Aldis, C. Tarver, and P. A. Urtiew, "Shock Initiation of LX-17 as a Function of Its Initial Temperature."

L. G. Green and C. Tarver, "Failure Diameter from One-Dimensional Lab Scale Tests."

L. G. Green, C. Tarver, and D. Erskine, "Reaction Zone Structure in Supracompressed Detonating Explosives."

D. Ornellas, "The Effect of the Pentafluorothio (SF5) Group on the Properties of Explosive Nitro Compounds: New SF5 Explosives."

S. E. Rice, N. Holmes, G. Otani, and P. McCandless, "Absorption Spectroscopy of Shocked Benzene."

R. L. Simpson, "Particle Size Effects in the Initiation of Explosives Containing Reactive and Non-Reactive Continuous Phases."

R. Simpson, D. Aldis, L. Lee, and A. Weston, "Model Calculations for the Response of HMX Porous Beds to Deflagration and Shock."

C. M. Tarver and P. A. Urtiew, "Shock Initiation of LX-17 as a Function of its Initial Temperature."

**DOE Conference on Technology R&D for Arms Control Verification, Los Alamos, N. Mex., August 29–31, 1989**

D. Gritton, P. Pearson, S. Monaco, and E. Raber, "Electronic Tags."

**SIMS VII, Monterey, Calif., September 3–8, 1989**

C. W. Price and J. C. Norberg, "Analysis of Nitrogen-Pulsed Sputtered Beryllium."

C. W. Price and J. C. Norberg, "Analyses of Particles in Beryllium by Ion Imaging."

**International Conference on the Applications of the Mössbauer Effect, Budapest, Hungary, September 4–8, 1989**

C. E. Violet, S. R. Bohlen, S. Martin, and Z. Mei, "Fe Spin State in Fayalite at High Pressure."

**American Chemical Society Meeting, Miami Beach, Fla., September 10-15, 1989**

C. Wong, M. Rudokas, R. Yost, and R. S. Upadhye, "Opportunities for Using Expert Systems in Design Monitoring and Control of Advanced Life Support Systems on Manned Space Missions."

**14th International Meeting on Organic Geochemistry, Paris, France, September 18-22, 1989**

A. K. Burnham and R. L. Braun, "A Detailed Kinetic and Thermodynamic Model of Petroleum Formation, Destruction and Expulsion."

**American Ceramics Society, Glass Division, Orlando, Fla., September 18–20, 1989**

R. Adair, L. L. Chase, S. A. Payne, and M. J. Weber, "Nonlinear Refractive Index of Optical Materials for High Power Lasers."

**2nd International Conference on Brazing, High Temperature Brazing and Diffusion Welding, Essen, FRG, September 19–20, 1989**

M. E. Kassner, R. S. Rosen, G. A. Henshall, and W. E. King, "Delayed Failure of Silver-Aided Diffusion Welds Between Steel."

**Workshop on Radiation Damage Correlation for Fusion Conditions, Silkeborg, Denmark, September 27–October 3, 1989**

M. W. Guinan and T. de la Rubia, "Progress in the Development of a Molecular Dynamics Code for High Energy Cascade Studies."

**American Conference for Crystal Growth, East Coast Meeting, October 1989**

L. J. Atherton, D. H. Roberts, R. W. Martin, and J. E. Cooper, "Growth of $LiCaAlF_6$: Cr (LiCAF) by the Bridgman Process."

**JOWOG-9, Aldermaston, England, October 9–13, 1989**

K. Scribner, "The Effects of Process Variables on the Performance Characteristics of TATB."

**3rd Users Meeting of the Advanced Photon Source, Argonne National Laboratory, Chicago, Ill., October 12–13, 1989**

J. H. Kinney, "X-Ray Tomographic Microscopy using Synchrotron Radiation."

**Optical Society of America, Orlando, Fla., October 15–20, 1989**

M. J. Weber, J. Wong, R. B. Greegor, F. W. Lytle, and D. R. Sandstrom, "Optically-Detected X-Ray Absorption Spectroscopy in Luminescent Materials."

**DOI Nuclear Weapons Complex Conference on Electron Microscopy, Miamisburg, Ohio, October 17–19, 1989**

M. L. Sattler, "Characterization of Micron-sized Be Powders."

**American Vacuum Society, Boston, Mass., October 25, 1989**

K. Y. Jang, K. Kim, and R. S. Upadhye, "Study of Sol-gel Processing for Fabrication of Hollow Silica Aerogel Sphere."

J. G. Tobin, "Probing Bimetallic Surfaces With Photoelectron Diffraction: Au/Cu(001) and Fe/Cu(001)."

R. S. Upadhye and E. J. Hsieh, "A Unified Integrated Model for Sputter Coating Uniformity."

**15th Annual SSRL User's Group Meeting, Stanford, Calif., October 27-28, 1989**

V. Karpenko, K. Neufeld, K. G. Tirsell, E. R. Holdener, G. L. Johnson, R. K. Wiggins, S. Kulkarni, C. Poppe, L. Wilson, J. H. Kinney, M. J. Weber, J. Wong, T. Troxel, J. Yang, J. Cerino, E. Hoyer, D. Humphries, and D. Plate, "Beam Line 10-2: Specification, Characterization and Experimental Capabilities."

J. G. Tobin, "The Dynamic Equilibrium Between Overlayer & Surface Alloy: Au/Cu(001)."

M. J. Weber, "UC/National Laboratories PRT and Beam Lines: Whence and Whereto."

**American Institute of Chemical Engineers Annual Meeting, San Francisco, Calif., November 6–8, 1989**

L. J. Atherton, D. H. Roberts, R. W. Martin, and J. E. Cooper, "Bridgman Growth of $LiCaAlF_6$: Cr (LiCAF)."

E. Cantwell, P. Robinson, T. Shenk, and R. S. Upadhye, "Design Assistant Workstation."

L. Chiao, "Mechanistic Modeling of Epoxy Cure."

**Materials Research Society Meeting, Boston, Mass., November 27–Dec. 2, 1989**

E. C. Sowa, A. Gonis, and X.-G. Zhang, "The Electronic Structure of S5 Grain Boundaries in Cu."

J. Wong, "Coordination of Ti and V in Dispersed Catalysts and Model Compounds."

J. Wong, "High Resolution Electron Microscopic and Spectroscopic Studies of SIPOS and Its Interface with Si."

J. Wong, "Metal Interactions in the Beta-Boron Lattices."

**34th Annual Conference on Magnetism and Magnetic Materials, Boston, Mass., November 28–December 1, 1989**

D. C. Chrzan, L. M. Falicov, J. M. MacLaren, X.-G. Zhang, and A. Gonis, "Magnetic Structure of {111} Stacking Faults in Nickel."

C. E. Violet, F. W. Oliver, and L. May, "Eu Mössbauer Study of the High $T_c$ Superconductor $BiCa_{0.5}Eu_{0.5}Sr_2Cu_2O_x$."

**2nd International Symposium on New Glass, Tokyo, Japan, November 29–30, 1989**

M. J. Weber, "Laser Glass."

# Patents

B. Andresen and E. Fought, *Interface for Liquid Chromatograph–Mass Spectrometer*, U.S. Patent 4,867,947 (1989).

M. Balooch, F. Askary, and M. Farnaam, *Large Cross-Sectional Beam for Deposition and Etching*, U.S. Patent 4,774,416 (1988).

T. T. Coburn, *A High Liquid Yield Process for Retorting Various Organic Materials Including Oil Shale*, DOE Patent Application S-67,224 RL-10,247 IL-7964 (submitted 1988).

J. E. Harrar, R. Quong, L. P. Rigdon, and R. R. McGuire, *Method and Apparatus for Large-Scale Production of Nitric Acid and Nitric-Acid Solutions of Dinitrogen Pentoxide*, U.S. Patent 4,443,308 (1988).

O. H. Krikorian and P. G. Curtis, *Method of Coating Metal Surface to Form Protective Metal Coating Thereon*, DOE Patent Application S-68,268, RL-10, 491 (submitted 1989).

J. G. Reynolds, *Decalcification of Hydrocarbonaceous Feedstocks using Citric Acid and Salts Thereof*, U.S. Patent 4,778,589 (1988).

J. G. Reynolds and T. F. Flinger, *Decalcification of Hydrocarbonaceous Feedstocks using Amino-Carboxylic Acids and Salts Thereof*, U.S. Patent 4,778,590 (1988).

J. G. Reynolds, *Demetalation of Hydrocarbonaceous Feedstocks using Carbonic Acid and Salts Thereof*, U.S. Patent 4,778,591 (1988).

J. G. Reynolds, *Demetalation of Hydrocarbonaceous Feedstocks using Amino-Carboxylic Acids and Salts Thereof*, U.S. Patent 4,778,592 (1988).

J. G. Reynolds, *Demetalation of Hydrocarbonaceous Feedstocks using Hydroxo-Carboxylic Acids and Salts Thereof*, U.S. Patent 4,779,463 (1988).

L. P. Rigdon, J. E. Harrar, S. J. E. Bullock, and R. R. McGuire, *Reference Electrode for Strong, Oxidizing, Acid Solutions*, U.S. Patent 7,355,523 (1989).

R. Tench, M. Balooch, and W. J. Siekhaus, *SiC Film Deposition by us Pulse Ablation*, DOE Patent Application S-70,733, RL-10856, IL-8390 (submitted 1989).

Section 8

# Budget Information

**Table 1.** Distribution of effort and funds for the C&MS Department in FY 1989.

| | Number of FTE | | |
|---|---|---|---|
| | C&MS | Other | $K |
| C&MS Cost Center | | | |
| Direct Programs | | | |
| Weapons Supporting Research | 21.3 | 7.9 | $6,502 |
| Departmental IR&D | 3.6 | 3.7 | 1,578 |
| Laboratory IR&D | 2.7 | 0.6 | 718 |
| DOE/Basic Energy Sciences | 2.0 | 6.9 | 1,420 |
| DoD | 6.7 | 2.1 | 3,149 |
| Other WFO | 1.8 | 1.8 | 310 |
| | 38.1 | 23.0 | $13,677 |
| Distributed Services | | | |
| Plutonium Facility | 5.9 | 26.9 | 5,387 |
| Tritium Facility | 3.0 | 6.7 | 1,526 |
| | 8.9 | 33.6 | $6,913 |
| Indirect Activities | | | |
| Support Burden | 51.0 | 3.7 | 4,822 |
| Maintenance/Noncapital | 7.4 | 27.3 | 5,357 |
| Construction/Equipment | 0.3 | 10.6 | 1,659 |
| | 58.7 | 41.6 | $11,838 |
| Subtotal C&MS Cost Center | 105.7 | 98.2 | $32,428 |
| Support to Other Programs | | | |
| Defense Systems | 107.6 | | |
| Laser Program | 48.9 | | |
| Energy Program | 27.6 | | |
| Misc. DOE | 33.3 | | |
| Reimbursables/WFO | 34.4 | | |
| IR&D | 4.1 | | |
| | 255.9 | | |
| **Total C&MS Department** | **361.6** | | |

**Figure 1.** FTE distribution in FY 1989. (a) and (b) show the C&MS Cost Center. (a) Direct Programs, 38.1 FTE. (b) Distributed Services and Indirect Activities, 67.6 FTE. (c) Support to Other Programs, 255.9 FTE.

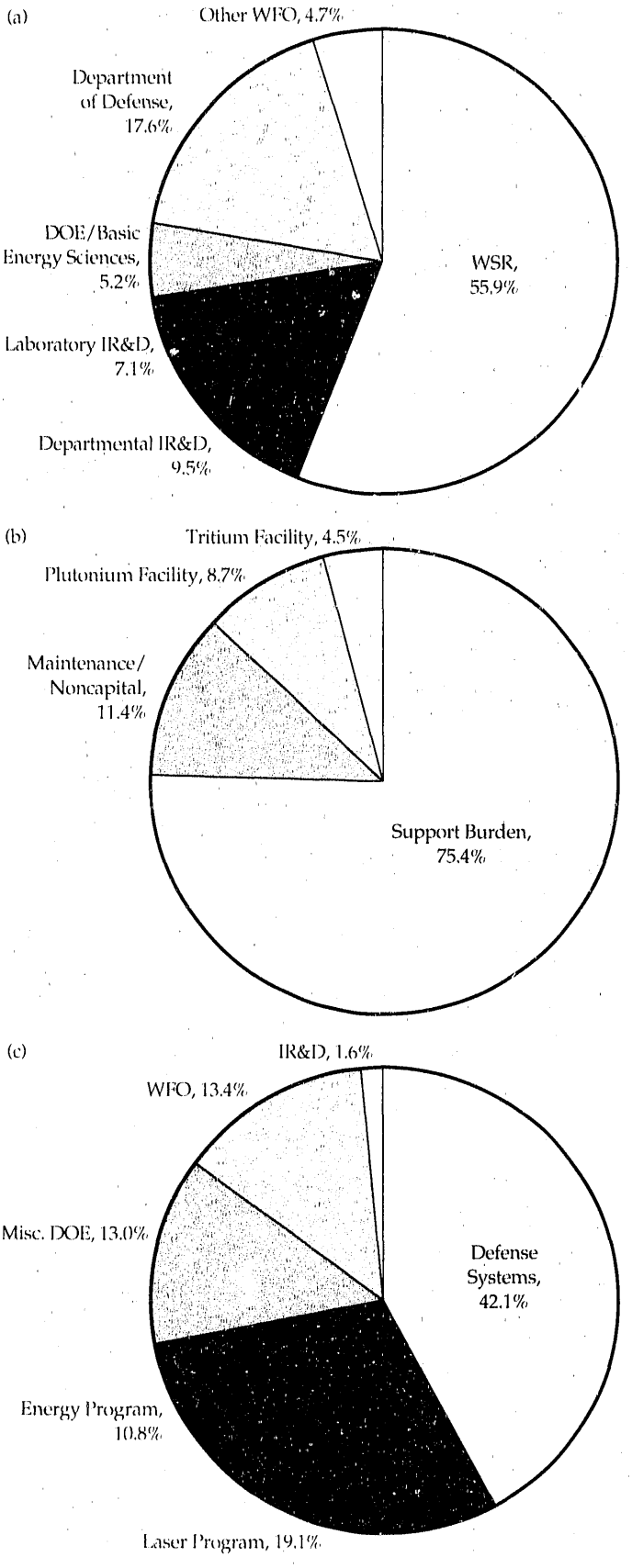

**Table 2.** C&MS Department WSR programs and budgets for FY 1988 and FY 1989.

| Thrust Area | Leader | $K FY 1988 | $K FY 1989 |
|---|---|---|---|
| High Explosives Technology | R. McGuire | $600 | $600 |
| Tritium and Light Hydrides | C. Souers | 840 | 800 |
| Advanced Characterization | S. Perone | 530 | — |
| Superconductors | M. Fluss | 900 | 800 |
| Adhesion and Bonding | W. King | 559 | 600 |
| Plutonium and Actinides | G. Gallegos | 815 | 800 |
| Advanced Synthesis and Processing | M. Adamson | 615 | — |
| Mechanisms of Metal Processing | M. Kassner | — | 760 |
| Synchrotron Radiation–Based Materials Science | J. Wong | — | 450 |
| **Total** | | **$4,859** | **$4,810** |

| Individual Project | Principal Investigator | FY 1988 | FY 1989* |
|---|---|---|---|
| Transition Metal Fluorides | R. Sanner | $100 | — |
| Laser-Induced Chemistry | C. Stevens | 150 | 100 |
| Film Adhesion | S. DeTeresa | 35 | — |
| Actinide Catalysis | C. Colmenares | 180 | — |
| Capillary Structures | R. Hopper | 100 | — |
| Dislocations and Strains | M. Kassner | 180 | * |
| Pretransformation Phase Studies | L. Tanner | 175 | * |
| Material Behavior and Failure | W. Gourdin | 225 | * |
| Low-Density Foams | S. Letts/R. Pekala | — | 150 |
| Ultratrace Analysis | B. Andresen | — | 150 |
| Enzyme Models | M. Droege | — | 150 |
| Reduction of Plutonium Oxide | M. Coops | — | 80 |
| Thermal/Shock Sensitivity of TATB | W. Tao | — | 100 |
| Electronic Structure and Phase Stability | A. Jankowski | — | 60 |
| Electronic Structure of Plutonium | A. Gonis | — | 60 |
| **Total** | | **$1,145** | **$850** |

*Incorporated into Thrust Areas in FY 1989.

**Table 3.** C&MS Department IR&D projects and budgets for FY 1988 and FY 1989.

| Departmental Project | Investigator | $K FY 1988 | $K FY 1989 |
|---|---|---|---|
| Synchrotron Radiation Studies | J. Wong | $180 | $197 |
| Catalysis by Aerogels | C. Colmenares | 100 | — |
| Superconductor Research | M. Fluss | 230 | 987 |
| X-Ray Thin-Film Studies | T. Barbee | 160 | — |
| Calculation of Electronic Structures | A. Gonis | 150 | 148 |
| Diffusion at Grain Boundaries | W. King | 180 | — |
| Laser-Produced Molecular Plasmas | C. Stevens | — | 138 |
| Subnanometer Materials | A. Jankowski | — | 109 |
| **Total** | | **$1,000** | **$1,579** |

| Director's Initiative | Investigator | FY 1988 | FY 1989 |
|---|---|---|---|
| Nuclear Spin Polarization | C. Souers | — | $494 |

| Laboratory-wide Projects | Principal Investigator | FY 1988 | FY 1989 |
|---|---|---|---|
| Synthesis of Dense, Energetic Materials | A. Mitchell | $149 | — |
| Scanning Tunneling Microscopy | W. Bell | 148 | — |
| Ceramic Laser Host | J. Marion | 99 | — |
| $\Delta_n = 0$ Spectroscopy | T. Barbee | 166 | * |
| Material Structure/ Short Time Periods | Q. Johnson | — | 138 |
| Injection of Ceramic Powders | K. Wilfinger | — | 102 |
| **Total** | | **$562** | **$240** |

*Continued in FY 1989 under Physics Department, funded at $176K.

# Acronyms

| | |
|---|---|
| ACPAR | angular correlation of positron annihilation radiation |
| bcc | body-centered cubic |
| bct | body-centered tetragonal |
| C&MS | Chemistry & Materials Science |
| CARS | coherent anti-Stokes Raman scattering |
| CCD | charge-coupled device |
| CDA | Copper Development Association |
| CPA | coherent potential approximation |
| CPU | central processing unit |
| CSM | coherency strain model |
| CT | computed tomography |
| CTEM | contrast TEM |
| CVM | cluster variation method |
| DET | divorced-eutectoid transformation |
| DETWAD | DET with associated deformation |
| DME | 1,2-dimethoxyethane |
| DMSO | dimethylsulfoxide |
| DNA | deoxyribonucleic acid |
| DoD | Department of Defense |
| DOE | Department of Energy |
| DOS | density of states |
| DVB | divinylbenzene |
| EAM | embedded atom method |
| EB | electron beam |
| ECI | effective cluster interaction |
| EPI | effective pair interaction |
| EQQ | electric quadrupole interaction |
| ESR | electron spin resonance |
| EXAFS | extended x-ray absorption fine structure |
| fcc | face-centered cubic |
| FEFO | 1,1'-[methylenebis oxy ]bis[2-fluoro-2,2'-dinitroethane] |
| GC/MS | gas chromatographic/mass spectrometric |
| GPM | generalized perturbation method |
| hcp | hexagonal close-packed |
| HEL | Hugoniot elastic limit |
| HMX | octahydro-1,3,5,7-tetranitro-1,3,5,7-tetrazocine |
| HOPG | highly ordered pyrolytic graphite |
| HREM | high-resolution TEM |
| HRS | hot recycled solid |
| ICF | inertial confinement fusion |
| ICP | Inductively coupled plasma (–mass spectrometry or –emission spectroscopy) |
| IR&D | Institutional Research & Development |
| LCAO/MO | linear combination of atomic orbitals/molecular orbital |
| LIF | laser-induced fluorescence |
| LLNL | Lawrence Livermore National Laboratory |
| MTS | mechanical threshold stress |
| NMR | nuclear magnetic resonance |
| NSLS | National Synchrotron Light Source |
| OFE | oxygen-free electronic |
| PAS | photoacoustic spectroscopy |
| PETN | 2,2-bis[(nitroxy)methyl]-1,3-propanediol,dinitrate |
| PICVD | plasma-initiated chemical vapor deposition |
| ppm | parts per million |
| psi | pounds per square inch |
| PSM | primary solidification mode |
| PVA | polyvinyl alchohol |
| PVD | physical vapor deposition |
| RDX | hexahydro-1,3,5-trinitro-1,3,5-trizine |
| RF | radio frequency |
| RF | resorcinol-formaldehyde |
| RH | relative humidity |
| RSMST | real-space multiple-scattering theory |
| SCC | stress-corrosion cracking |
| STM | scanning tunneling microscopy |
| TATB | 2,4,6-trinitro-1,3,5-benzenetriamine |
| TB-CPA | tight binding coherent potential approximation |
| TEA | thermal-energy analysis |
| TEM | transmission electron microscopy |
| TFAA | trifluoroacetic anhydride |
| TFMSAA | trifluoromethanesulfonic acid anhydride |
| TIGER | a thermodynamic-hydrodynamic code |
| TMOS | tetramethoxysilane |
| TQMS | triple quadrupole mass spectrometer |
| UHCS | ultrahigh-carbon steel |
| VISAR | velocity interferometer system for any reflector |
| WFO | Work for Others |
| WSR | Weapons Supporting Reseach |
| XAFS | x-ray absorption fine structure |
| XANES | x-ray absorption near edge structure |
| XTM | x-ray tomographic microscopy |
| YBCO | $YBa_2Cu_3O_{7-\delta}$ |
| Z | atomic number |

# END

# DATE FILMED

11 / 1 / 90